Ph.D. Program in Science and Marine Technology
Curriculum in Engineering for Marine and Coastal Environments

Department of Civil, Chemical and Environmental Engineering
Polytechnic School, University of Genoa, Italy.

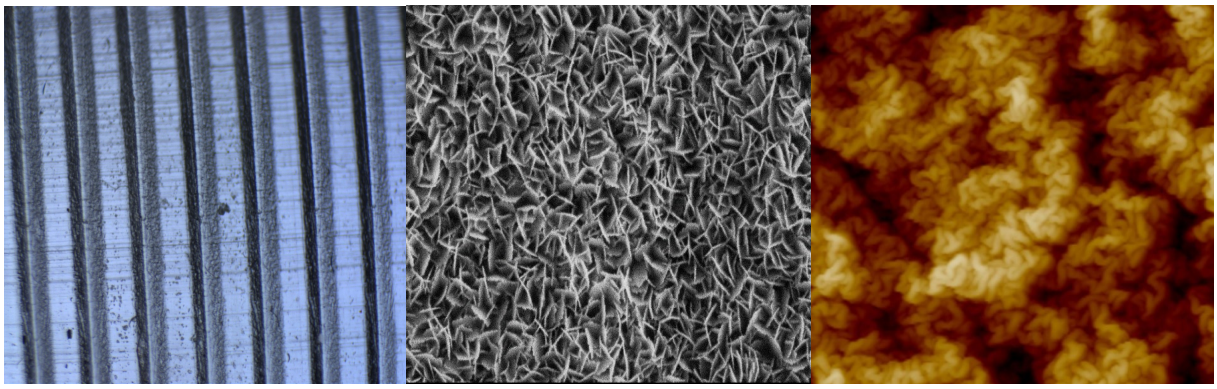

Slippery Surfaces and Materials for Skin-Friction Drag Reduction

Giulia Innocenti

SLIPPERY SURFACES AND MATERIALS FOR DRAG REDUCTION

BY

GIULIA INNOCENTI

Dissertation discussed in partial fulfillment of
the requirements for the Degree of

DOCTOR OF PHILOSOPHY

Civil, Chemical and Environmental Engineering
Curriculum in Engineering for Marine and Coastal Environments,
Department of Civil, Chemical and Environmental Engineering, University of Genoa, Italy

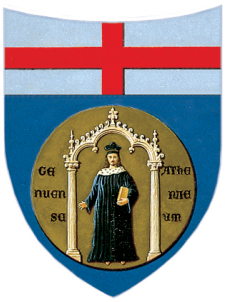

April, 2026

Scientific adviser:
Prof. Alessandro Bottaro - Department of Civil, Chemical and Environmental Engineering, Università degli Studi di Genova (Italy)

External Reviewers:
Prof. Shervin Bagheri - Department of Mechanics, KTH Royal Institute of Technology, Stockholm (Sweden)
Prof. Christophe Clanet - Department of Mechanics and Energetics, École Polytechnique, Paris (France)

Examination Committee:
Prof. Christophe Clanet - Department of Mechanics and Energetics, École Polytechnique, Paris (France)
Prof. Maria Vittoria Salvetti - Department of Civil and Industrial Engineering, Università degli Studi di Pisa (Italy)
Prof. Agnese Seminara - Department of Civil, Chemical and Environmental Engineering, Università degli Studi di Genova (Italy)

Ph.D. program in Civil, Chemical, and Environmental Engineering
Curriculum in Engineering for Marine and Coastal Environments
Cycle XXXVIII

ACKNOWLEDGEMENTS

The PhD journey is a rollercoaster of ups and downs, and it requires great companions to navigate it. After more than three years, I am glad to say that I have been incredibly lucky to have the most motivating and inspiring people around me who have been part of my entire path.

First of all, my deepest and most sincere thanks go to my supervisor, Prof. Alessandro Bottaro. He introduced me to the world of research, expertly guiding me in exploring and enjoying this journey. His passion and dedication to science are truly inspiring. Along the way, I have deeply appreciated his positivity in facing every difficulty.
Along my journey, I had the opportunity to spend some time in Sydney, Australia. Moving to the other side of the world and facing a completely new environment was a challenging experience that could have been daunting. However, I found the most amazing group of people who made me feel at home and turned the university into a safe space, even during difficult times. My deepest gratitude goes to Prof. Chiara Neto for believing in me and allowing me to live such an unforgettable and significant experience, both for my career and my personal growth. I truly admire her passion for scientific research, her ability to foster a wonderful work environment, and the invaluable guidance she provided.
A special thanks goes to Dr. Reza Azadi, who was my guide through one of the most challenging, exciting, and gratifying research experiences. He taught me how to manage experimental work: to be resilient, to appreciate small daily advancements, to stay calm, and, above all, to enjoy the journey.

The research was funded by the European Union - NextGenerationEU (Piano Nazionale di Ripresa e Resilienza, Missione 4 Componente 2 Investimento 1.4 “Potenziamento strutture di ricerca e creazione di “campioni nazionali di R&S” su alcune Key Enabling Technologies”). (CN00000023)— Title: “Sustainable Mobility Center (Centro Nazionale per la Mobilità Sostenibile - CNMS)”.

ABSTRACT

Over the past two decades, **passive drag reduction** technologies have emerged as promising solutions to enhance surface performance, offering advantages in efficiency, environmental compatibility, and long-term sustainability. The growing demand for integrated strategies that improve the performance of engineering systems has stimulated extensive research into innovative approaches to minimize energy consumption and mitigate environmental impact.
Within the maritime sector, this need has become particularly urgent. In recent years, increasingly stringent international regulations have been introduced, reflecting a global awareness of environmental protection and the necessity to reduce emissions and fuel consumption. These regulations have intensified the pressure on researchers and industrial and technological development to implement advanced solutions that can be effectively integrated into existing infrastructures and current technologies.
Consequently, significant efforts are being directed toward the adaptation and optimization of surface treatment methods and drag reduction techniques that are both compliant with modern regulatory standards. In this context, passive technologies represent a key area of investigation, as they offer the potential to achieve substantial performance improvements without additional energy input or complex system modifications.
Inspired by the natural world and by the evolution of animals and plants over millions of years, researchers have increasingly investigated biological designs and mechanisms, drawing from them to develop and enhance technologies aimed at reducing drag. This field of study is referred to as **biomimetics**.
Numerous natural systems highlight surface adaptations, demonstrating the relevance of fluid-surface interactions: the lotus leaf and the Coleoptera's wings (e.g., lady beetles) exhibit pronounced water-repellent properties, thanks to its micro and nanostructure; the leading-edge structures of owls enable stabilized airflow and reduced aerodynamic noise; whale tubercles are known to delay stall, enhance lift, and reduce drag; the pitcher plant (Nepenthes) generates a highly slippery interface through the formation of a stable liquid–liquid boundary with an immiscible fluid; and shark skin, characterized by microstructured riblets-like, facilitates efficient motion through water by reducing frictional resistance. These examples, among many others, highlight the diversity of evolutionary solutions that inspire drag-reduction technologies.
Starting from these biological designs, rough and regular patterned surfaces, superhydrophobic coatings, and liquid-impregnated materials have become a wide range of physical mechanisms and technical complexities to be investigated.
This research aims to provide a comprehensive overview of slippery surfaces, progressing from idealized, regularly textured geometries to more realistic hierarchical materials, thereby enabling a deeper understanding and detailed analysis.
The study focuses on small-scale phenomena occurring in the near-wall region, investigated through an integrated theoretical, numerical, and experimental approach.
First, a research activity on riblet surfaces has been conducted, leading to the development of a novel model capable of describing the behavior of patterned walls under turbulent flow conditions beyond the viscous regime. In this context, a multiscale homogenization approach has been formulated to derive effective boundary conditions that capture the influence of surface

roughness on the overlying flow. The predictive capability of the proposed model has to be subsequently assessed and validated through direct numerical simulations.
Extending this framework, the investigation has been extended to more complex configurations through the design and implementation of a high-precision Taylor–Couette experimental apparatus. This facility enabled systematic hydrodynamic resistance measurements and flow visualization studies. Experiments have been conducted on riblet-textured surfaces, progressively modified through the application of superhydrophobic coatings and subsequent impregnation with lubricant oils. These investigations provided insight into the influence of surface functionalization on drag reduction as well as the onset of flow instabilities, such as the formation of Taylor-Couette vortical structures. Moreover, a linear stability analysis has been developed to theoretically and numerically define the critical parameters of the study, through the definition of effective slippery boundary conditions.
Finally, the study has been further advanced toward realistic, complex, and anisotropic surfaces by addressing the critical issue of lubricant depletion. A custom-built mesoscale Taylor–Couette device has been designed, built, and then employed to investigate the progressive loss of lubricant and the associated degradation of surface performance. Despite its practical relevance, the underlying physical mechanisms governing lubricant depletion and the consequent loss of functionality remain only partially understood. This work, therefore, aims to provide a comprehensive analysis of lubricant loss processes, identifying the key governing parameters and describing their role in the long-term effectiveness of slippery surfaces.

INDEX

List of Figures

List of Tables

Introduction

1.1. Environmental motivation

Climate change represents one of the most pressing global challenges of our time, and mitigating its impacts is essential to ensure a sustainable future for the next generation. When considering anthropogenic activities across the main economic sectors, the transport sector accounts for approximately 15–20% of global greenhouse gas emissions. Consequently, regulating and reducing emissions from road transport, aviation, and maritime shipping is of critical importance. In particular, maritime transport plays a significant role as a contributor to atmospheric emissions. Historically, environmental regulations in the shipping sector were relatively limited, as priority was often given to maintaining the efficiency and competitiveness of international trade, for which maritime transport remains the dominant mode in terms of cargo volume. However, over the past few decades, the International Maritime Organization (IMO) has introduced a broad range of regulatory measures aimed at reducing pollution from ships. These initiatives have culminated in the adoption of an ambitious strategy targeting net-zero emissions from international shipping by 2050.
Several methods and technologies have been developed to minimize emissions, following two main strategies: using low or no-carbon fuels or reducing the required power on board by decreasing speed or reducing drag while keeping speed constant. Concerning the second strategy, various methods can be employed to achieve the objective. These include the optimization of the propeller thrust, the minimization of the hull resistance (e.g., modifying the hull's shape), the installation of energy-saving devices to improve hydrodynamic interaction around the hull or the propeller, and the implementation of measures designed to reduce drag through active and passive drag reduction solutions. The present study highlights the significance of passive drag reduction technologies as pioneering, effective, environmentally friendly, and sustainable solutions to enhance the performance of corrugating or treating surfaces. This is a particularly attractive and appealing solution considering its fully passive nature and its long-term utilization.

1.1.1. Sustainable challenges in marine transport

Comparing shipping emissions against aviation, maritime transport produces about 9 times more NO_x emissions than aviation, but due to the high sulfur concentration in the fuel SO_x emissions exceed about 80 times. Shipping emits approximately 1200 times more particulate matter than aviation. The comparison of total emissions from different transport modes demonstrates that clear information is needed on the climate impact of ship emissions to allow the industry to incorporate, with greater confidence, environmental considerations into its design

and development work. The total amount of emitted particulate matter and SO_x from shipping could modify existing clouds in the marine boundary layer and could contribute to the indirect aerosol effect.[1]
Environmental regulations on emissions from aviation and road transport have generally been enforced more strictly, largely because these sectors have more immediate and visible impacts on human health and the environment in densely populated areas. For example, exhaust emissions from road vehicles can rapidly degrade urban air quality, directly affecting the health of city residents. As a result, these sectors have historically received greater regulatory attention, driven by stronger political and social pressure to monitor and reduce emissions. In contrast, the shipping industry has long faced less stringent regulations, and for many years, it was not subject to international emission regulations comparable to those applied to road transport and aviation. This situation has arisen for several reasons. First, maritime transport is fundamental to global commerce, facilitating approximately 90% of international trade by volume. When its productive value is considered, it is also statistically one of the least environmentally damaging modes of transport. In addition, shipping is among the most energy-efficient forms of transportation on a per-ton-mile basis, making it indispensable for large-scale, long-distance trade. Furthermore, the inherently international nature of maritime transport—where ships frequently operate across multiple jurisdictions and regulatory frameworks—has historically complicated the establishment and enforcement of unified emissions regulations, contributing to their delayed implementation.
The volume of maritime activity has exhibited a gradual increase over the past two decades and is projected to persist in the foreseeable future.
The results of the scenario calculations illustrate the necessity for substantial technological advancements to counterbalance the rise in emissions caused by the expansion of seaborne trade and the intensification of energy consumption for cargo.
In the absence of rigorous emission reduction strategies, the emissions of CO_2 and SO_2 from ships are projected to exceed their current levels by a factor of two. Furthermore, the emissions of NO_x could reach levels that surpass those of the present-day global road transport sector.[2]
Over the past few decades, there has been a notable increase in the interest of shipowners, manufacturers, and investors in the shipping industry in methods and technologies to reduce emissions, largely due to the increasingly stringent and restrictive regulations on the environment established by IMO.
Consequently, compliance with these emissions regulations through technological enhancements has exerted considerable influence over maritime transport, prompting a focus on developing more sophisticated, energy-efficient technology and modifying production and operational processes in the maritime industry.
In particular, there are two ways to reduce greenhouse gas emissions:

- choosing low- or no-carbon fuels;
- reducing the required power on board.

Considering the first option, the maritime shipping sector is pursuing various technological solutions to decarbonise, including advanced biofuels, electrofuels, hydrogen and electric propulsion. This will require new systems, facilities, supply chains, business models and alliances. Many solutions have the potential to contribute to the mid and long-term decarbonisa-

tion of the marine industry. These include liquid natural gas (LNG), green hydrogen, advanced biofuels, methanol, ammonia, battery-electric propulsion, wind-based (Fig. 6) and solar-based propulsion. In the context of innovative fuels, the well-to-wake emissions analysis, also known as life-cycle assessment (LCA), is essential. This methodology involves assessing emissions at each stage of the fuel's life cycle. The emergence of novel fuels and technologies presents a significant opportunity to overcome carbon lock-in and path dependency, thereby disrupting the existing regime and potentially fostering the development of new technological trajectories. However, maritime shipping's decarbonisation options are more complex than those in other transport sectors, as it involves a wider range of functions and segments. The main goal is to provide solutions that guarantee safety, reliability and operational performance, thus allowing industry stakeholders to successfully incorporate advanced technologies into their energy transition strategies.

Focusing on the second alternative, namely reducing the on-board power requirements, many different approaches are proposed and lead to a lower level of installed power. As mentioned before, a wide domain of research investigation is the optimization and efficiency improvement of hull geometry, ship propeller, and their mutual interaction; several solutions are possible. One of the main technologies is the installation of a high-energy-efficient propulsion system, with better performance that guarantees the same output with a lower installed power. Hydrodynamic Energy Saving Devices (EDSs) are advanced and cost-effective tools that increase vessel propulsion efficiency by reducing hull resistance and improving propeller thrust. They reduce fuel consumption by improving the flow around the hull or propeller.

Another innovative approach arises from the idea of reducing overall power consumption not only through improvements in the technical efficiency of devices, but also by fundamentally redesigning systems so that they require less energy to operate. This perspective shifts the focus from optimizing performance within existing constraints to minimizing the intrinsic energy demand of the system. In this sense, it reflects a deeper vision of sustainability, which aims not only at improving the efficiency of existing technologies but also at adapting and redesigning systems so that their fundamental resource requirements are significantly reduced.

When applied to the maritime sector, this concept suggests that a vessel navigating through the ocean could significantly reduce the energy required for propulsion if it were able to effectively *slip* over the water surface. By optimizing the interaction between the hull and the surrounding fluid, hydrodynamic drag can be substantially reduced, allowing the vessel to move through the water with lower resistance. This reduction in resistance directly translates into lower propulsion power requirements and, consequently, reduced fuel consumption.

Recent advances in fields such as microfluid dynamics, materials and chemical science, and biomimetics have led to substantial progress in the development of marine drag-reduction technologies. These disciplines have provided new insights into how surfaces interact with fluids and how natural systems - such as the skin structures of certain marine animals - can inspire engineering solutions. As a result, drag-reduction strategies are increasingly regarded as one of the most promising avenues for improving the energy efficiency of maritime transportation. To fully understand the principles behind these solutions, it is first necessary to examine the physical mechanisms that generate hydrodynamic resistance. A clear description of the nature of drag and of its different components is essential.

1.1.2. Ship resistance: effects of hull roughness and biofouling on hydrodynamic resistance.

Ship resistance represents a fundamental aspect of marine engineering, exerting a direct impact on the performance, fuel efficiency, and environmental sustainability of vessels. It is very crucial to improve operating performance, both increasing the traveling speed, especially for warships and reducing the energy consumption, considering the commercial vessels, directly correlated to saving fuel and thus money.
From a physics perspective, the motion of a body (ship) through a fluid (water) requires propulsive energy to counteract and overcome the resistance exerted by the fluid against the movement. The Buckingham π theorem is employed to assess the resistance, measuring it using a comprehensive model of the full-scale ship.

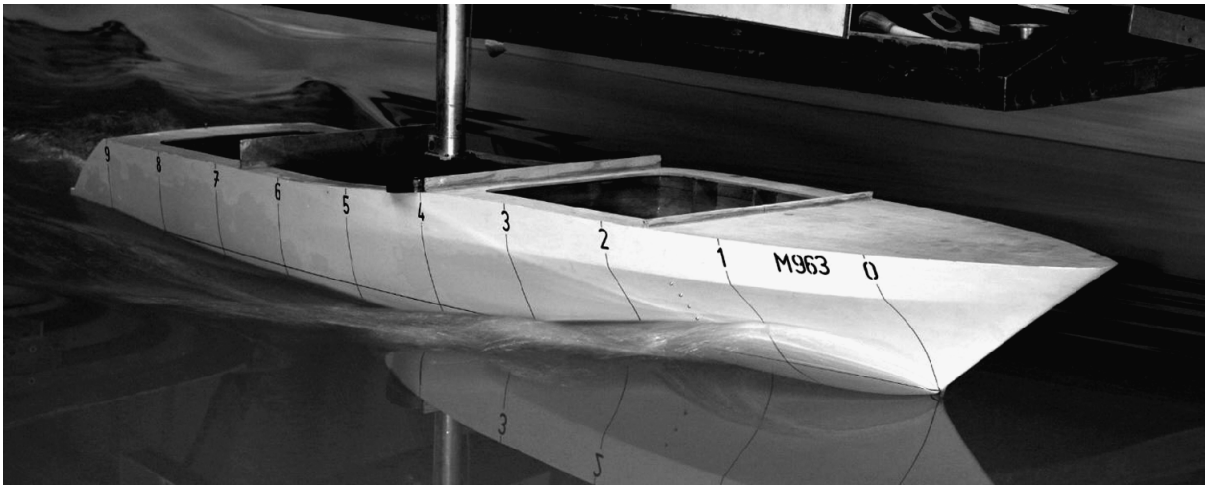

Figure 1.1: Scaled ship model.[3]

As a ship moves through calm water, many factors combine to form the total resistance force R_T acting on the hull, and it can be defined as:

$$R_t = R_V + R_W + R_A$$

where R_V is the viscous resistance, R_W is the wave making resistance and R_A is the air resistance.
The viscous resistance depends on the dimensions of the wetted area on the ship's speed, surface roughness, and water viscosity. In the case of low-speed vessels ($Fr < 0.2$ [1]), such as bulk carriers and tankers, this resistance typically accounts for 70-80% of the ship's total resistance. Conversely, in the context of high-speed vessels, including containers and passenger ships, this resistance may fall below 40%. The wave resistance can be attributed to the energy lost by waves created by the vessel, and it can be reduced by optimizing hull shape.

[1] In marine hydrodynamic applications, the Froude number is the ratio of the flow inertia to the external force field, and it is related to the ship's resistance. $Fr = \frac{V_0}{\sqrt{g\,l_0}}$

Typically, air resistance accounts for approximately 2% of the total resistance. However, in the case of loaded container ships navigating against a headwind, air resistance may increase to as much as 10%. To mitigate and minimize the air resistance, the design and the exposed surfaces must be optimized.[3,4]
Figure 1.2 presents the magnitude of each resistance component at different ship speeds. It is notable how the velocity regime plays a crucial role in shaping the distribution of drag forces and altering the relative contribution of various types of resistance.

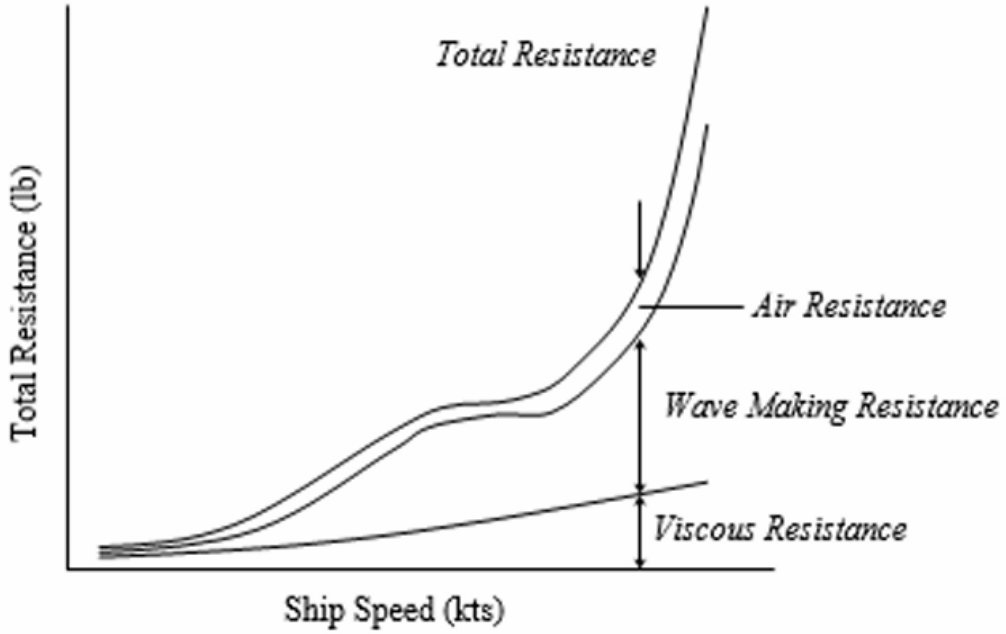

Figure 1.2: Components of Hull Resistance.[3]

This effect also helps determine the relative contribution of each resistance component within the overall system, thereby enabling the selection of appropriate emission-reduction strategies according to the vessel's operating speed regime. In particular, it can be observed that at low speeds, viscous resistance represents the dominant component of total resistance. As speed increases, however, the total resistance curve rises significantly due to the growing influence of wave-making resistance, which progressively becomes the predominant factor.
Similar to the previous figure, the next one illustrates the distribution of the individual resistance components within the total resistance. It highlights that at low speeds, viscous resistance—primarily represented by frictional resistance (R_F)—is greater than wave resistance, which is included in the residual resistance component (R_R).

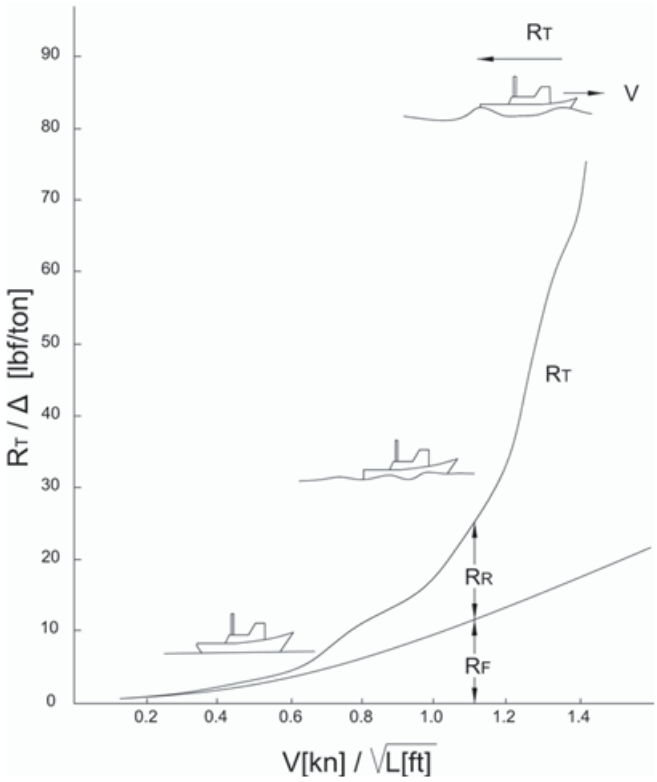

Figure 1.3: Total resistance curve as a function of the speed - length ratio.[5]

As previously mentioned, viscous resistance is also strongly influenced by surface roughness and biofouling. In ships operating over time, an increase in hydrodynamic drag is commonly observed, which can largely be attributed to the combined effects of hull roughness and the accumulation of marine organisms on the surface. Depending on operational conditions—such as service time, navigation area, vessel type, and operational profile—ships must periodically be taken out of service to undergo hull maintenance. During these operations, the hull is cleaned to remove fouling and new coatings and protective paints are applied in order to restore the surface condition, thereby improving hydrodynamic efficiency. However, taking a vessel out of operation for maintenance entails high economic costs. For this reason, ship owners are increasingly interested in long-term technologies capable of protecting the hull from degradation, limiting fouling accumulation, and maintaining low surface roughness over extended operational periods.

On a rough surface, the presence of peaks and valleys leads to an expansion of the overall area, which is in direct contact with water, which in turn increases viscous resistance due to the greater surface exposed to fluid friction. This effect becomes even more pronounced with the occurrence of fouling, a process in which marine organisms - such as algae, barnacles, and mussels - attach themselves to the hull of the vessel. Fouling not only increases resistance but also compromises the structural integrity of protective coatings. If the paint film on the hull begins to deteriorate, erosion can occur, providing an ideal surface for marine plant attachment and growth.

This degradation can spread beyond the hull, potentially affecting other submerged components, including the surface of the propeller, further impeding performance and increasing maintenance demands. The total resistance caused by fouling may increase by 25-50% throughout the lifetime of a ship.

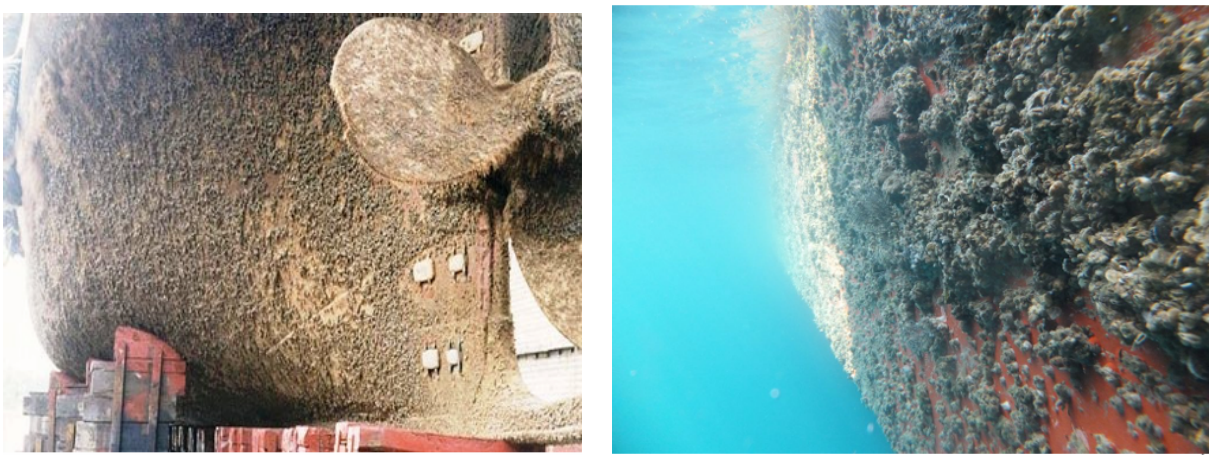

Figure 1.4: Pictures of biofouling impact on the hull of a vessel.

Periodic cleaning, combined with the use of antifouling coatings and treatments, is crucial to avoid and mitigate surface degradation. These practices help remove accumulated marine growth and contaminants, while also providing a new protective layer to prevent further fouling. Regular maintenance not only preserves the vessel's performance by reducing drag but also extends the lifespan of the hull and other submerged components, ultimately reducing long-term repair needs and associated costs.

Figure 1.5: Application of antifouling and protective coatings.

1.1.3. Marine drag reduction solutions

As discussed in Section 1.1.2., viscous resistance represents a significant portion of the total hydrodynamic resistance experienced by ships. For high-speed vessels, it typically accounts for approximately 40–50% of the total resistance, while for low-speed ships this contribution can increase to around 70–80%. Each year, Equasis (Electronic Quality Shipping Information System) provides an overview of the world's merchant fleet based on the data contained in its database. This analysis examines the structure and characteristics of the fleet, as well as its operational performance.

Ship type	Small[1]		Medium[2]		Large[3]		Very large[4]		Total	
Bulk carriers	279	0.5%	3,901	8.1%	7,103	52.7%	1,937	26.6%	13,220	10.4%
Container ships	19	0.0%	2,409	5.0%	1,684	12.5%	1,624	22.3%	5,736	4.5%
Fishing vessels	20,124	34.5%	5,806	12.1%	4	0.0%	1	0.0%	25,935	20.4%
Gas tankers	34	0.1%	1,182	2.5%	475	3.5%	619	8.5%	2,310	1.8%
General cargo ships	4,105	7.0%	12,181	25.4%	288	2.1%	0	0.0%	16,574	13.1%
Offshore vessels	2,871	4.9%	5,097	10.6%	122	0.9%	319	4.4%	8,409	6.6%
Oil and chemical tankers	1,985	3.4%	7,513	15.7%	2,827	21.0%	2,291	31.4%	14,616	11.5%
Other tankers	448	0.8%	776	1.6%	16	0.1%	0	0.0%	1,240	1.0%
Passenger ships	4,417	7.6%	2,945	6.1%	299	2.2%	205	2.8%	7,866	6.2%
Ro-ro cargo ships	1,025	1.8%	1,111	2.3%	553	4.1%	277	3.8%	2,966	2.3%
Service ships	3,801	6.5%	3,810	7.9%	38	0.3%	8	0.1%	7,657	6.0%
Specialized cargo ships	8	0.0%	287	0.6%	63	0.5%	9	0.1%	367	0.3%
Tugs	19,131	32.8%	920	1.9%	0	0.0%	0	0.0%	20,051	15.8%
Total	**58,247**	100%	**47,938**	100%	**13,472**	100%	**7,290**	100%	**126,947**	100%

Source: Equasis [1] GT<500 - [2] 500≤GT<25,000 - [3] 25,000≤GT<60,000 - [4] GT≥60,000

Figure 1.6: Word fleet: total number of ships, by type and size.[6]

Table 1.6 shows the word fleet in 2022, in terms of ship count, classified by type and size. Considering the comments made regarding the impact of viscous resistance on ships traveling at low speeds, it is notable that large ships are predominantly composed of bulk carriers and tankers, which are typically slow-moving vessel types. These vessels account for almost 90% of very large ships and approximately 28% of the world fleet.
This highlights the fundamental importance of reducing viscous resistance for these types of vessels, as improvements in this area can produce significant benefits at a global scale. Given the large number of ships operating worldwide and the substantial share of viscous resistance in total ship resistance, even small reductions in drag can translate into considerable energy savings and lower fuel consumption across the maritime sector.
In order to control, prevent, and reduce drag, a wide range of technologies and strategies have been developed. Hydrodynamic drag can be understood as the force associated with the transfer of momentum between the fluid and the body moving through it. This interaction generates a velocity gradient within the boundary layer that forms between the surface of the object and the surrounding fluid. The energy required to sustain this momentum exchange ultimately manifests as resistance to motion. These approaches are generally classified into three main categories:

active drag reduction, passive drag reduction, and composite drag reduction. Active techniques involve the continuous input of external energy to modify the flow conditions around the body, while passive methods rely on surface modifications or structural design features that reduce drag without additional energy input. Composite approaches combine elements of both strategies to further enhance drag-reduction performance. (Fig.1.7).

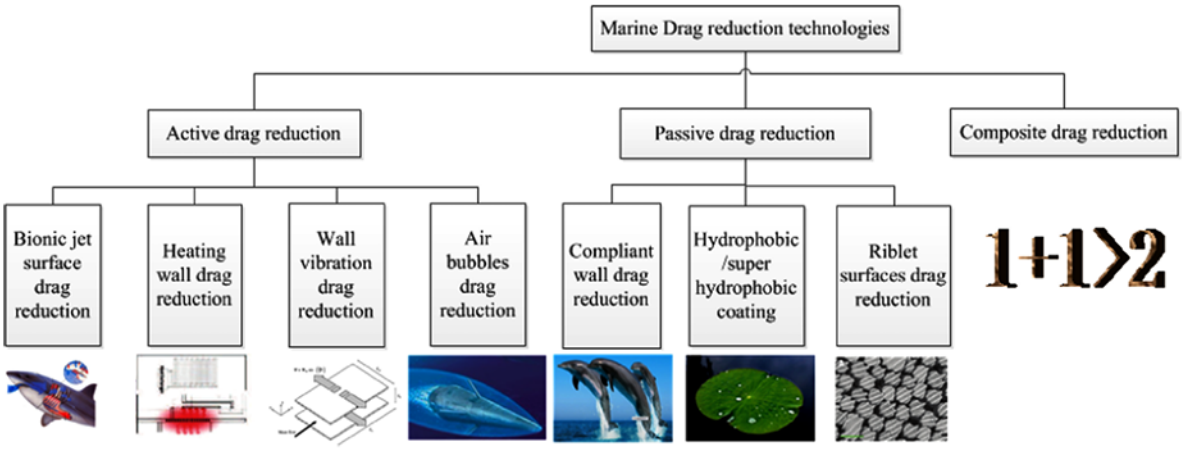

Figure 1.7: Different marine drag reduction technologies.[7]

Active and passive drag reduction technology

Active drag-reduction methods require the input of external energy to initiate and sustain the mechanism responsible for modifying the flow around the surface. This additional power may be needed, for example, to operate air compressors, heating systems, or vibrating devices. The supplied energy enables the generation of specific flow conditions—such as air jets, wall vibrations, temperature gradients, or air bubbles—that can significantly reduce hydrodynamic drag. Three main approaches have been investigated in research aimed at reducing surface friction in both internal and external flows. The first involves delaying boundary layer separation by inducing an early transition to turbulent flow or by actively influencing the boundary layer through fluid injection or suction. This can be achieved by delaying or modifying boundary-layer separation, for instance, through the early transition to turbulent flow, or by directly influencing the boundary layer through fluid injection or suction.
The second strategy focuses on modifying the viscosity of the fluid within the boundary layer, either by injecting a fluid with different properties or by altering its temperature.[8] Within this context, air lubrication has emerged as a particularly promising technique for reducing viscous resistance in marine vessels. This method relies on the injection of air beneath the hull, creating either a bubbly flow or a continuous layer of gas that partially separates the hull surface from the surrounding water. By reducing the direct contact between the hull and the liquid, the frictional component of resistance can be significantly decreased. In the last decade, air lubrication has attracted renewed interest in the maritime industry, and a considerable amount of research has been conducted to evaluate its technical feasibility as well as its economic and environmental benefits. Studies suggest that, under favourable conditions, the application of air lubrication

systems can reduce a ship's fuel consumption by approximately 5–20%, making it a promising strategy for improving energy efficiency and reducing emissions in maritime transport.[9]
The behaviour of the air–water mixture along the hull depends strongly on the airflow rate and the vessel speed. As these parameters vary, three distinct flow regimes can typically be observed. The first is the bubble regime, in which the injected air breaks into small bubbles that travel downstream along the hull surface. As the airflow increases, a transitional regime may occur, where partially broken bubbles begin to coalesce, forming localized patches of air while some bubbles still remain dispersed in the flow. Finally, under suitable conditions, a continuous air-layer regime can develop, in which the bubbles merge to form a stable gas layer covering the hull surface.

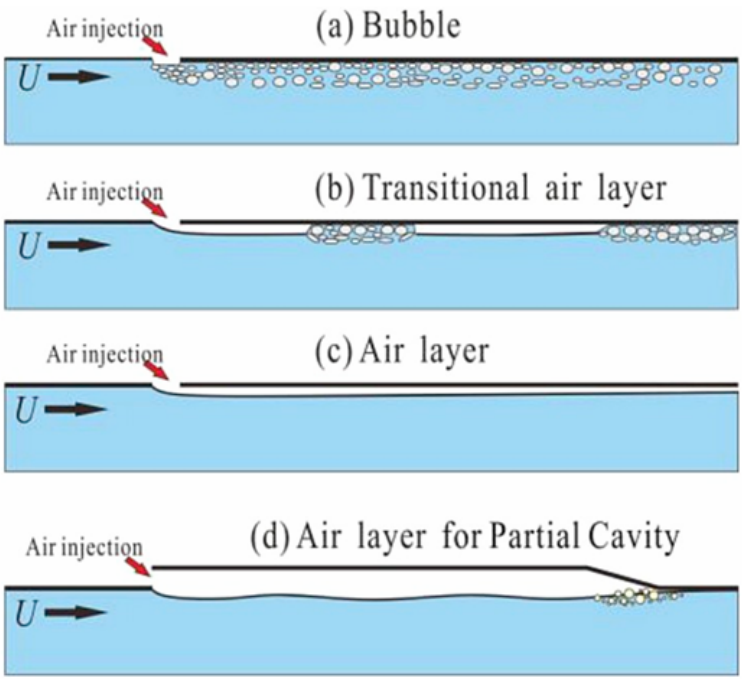

Figure 1.8: Schematic figure of drag reduction with air layer.[10]

For the technology to be effective, it is essential that the energy required to generate and maintain the air layer remains lower than the energy savings achieved through the reduction of frictional resistance; otherwise, the method would not be energetically advantageous. More generally, the external power required to operate the active system must be lower than the power saved to justify the use of an additive solution.
Ensuring this balance is crucial for guaranteeing the overall cost-effectiveness, technical feasibility, and operational viability of air-lubrication systems.
Finally, the third approach consists of modifying the wall geometry by introducing small surface grooves or ribs, commonly referred to as riblets.
It is a passive resistance reduction methods, based on an innovative and straightforward concept: modifying the surface in contact with the fluid so that it performs better from a fluid dynamic perspective, without powering the system with external energy.
Biomimetic studies - based on the observation of how nature adapts and improves itself to obtain

optimal properties - have led researchers to develop passive technologies that, in the absence of ”supplementary” energy, can alter the interaction between a fluid and a surface.
Passive technologies are based on the introduction of modifications to the surface, including the creation of a new micro/nanostructure, thereby redefining the roughness, the application of coatings to modify wettability properties, and the design of a textured pattern (e.g., grooves, pillars, ...). The underlying premise of these passive methods is the concept that by implementing a permanent alteration to the surface, a 'long-term' benefit can be attained.

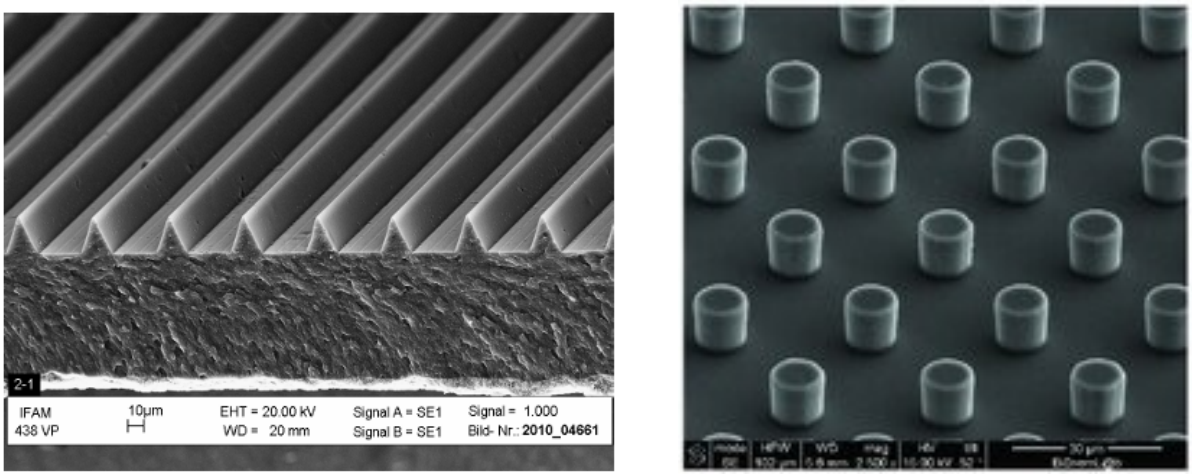

Figure 1.9: Left image courtesy of Fraunhofer IFAM: trapezoidal riblets. Right image: SEM image of micropillar surface.[11]

To achieve a higher reduction, 3D riblets have also been studied, in which the cross-section does not remain constant in the flow direction. It takes inspiration from the shark skin, in which the microgrooves present different alignment directions, based on the position of the shark's body and the local interaction it has with the outer flow. These new configurations have been inspired by active control, from which large amounts of reduced of resistance. One of the new methods proposed in the literature dedicated to reducing turbulent surface friction consists of inducing high-frequency oscillations at the wall in the transverse direction (Wall vibration drag reduction - Fig. 1.7). However, it leads to an active method, which requires more complex systems to implement and manage, and high maintenance costs.
It is possible to imitate such oscillatory motion by employing some passive devices. By modifying the shape of the riblets from straight to sinusoidal, the flow can be guided in an oscillatory motion, thereby combining the two mechanisms of surface friction reduction of surface friction (riblets and oscillatory flow motion).
Another fully passive technique largely studied is superhydrophobic and liquid-infused surfaces. Both inspired by animals and plants, present a hierarchical surface structure that allows, in the case of superhydrophobic surface to develop an air plastron trapped into the microroughness elements and, in the case of liquid-infused surfaces, a thin lubricant layer to be retained within micro and nano-cavities. A fluid-fluid interface is created, allowing the outer flow to slip and slide onto the textured surface easily and with low friction.

Composite drag reduction solution

Finally, composite drag reduction technology combines the effectiveness of the active methods with the reliability of the passive ones, looking for an optimization of the performance.
From an engineering perspective, the utilization of integrated tools can yield outcomes that are more effective than those achieved through the use of a single tool.
In this field, composite technology provides a wider range of applications, since passive solutions exhibit optimal performance when employed in a low-speed regime; conversely, active tools are more versatile and adaptable, thereby enabling them to compensate for each other.
The capacity to grasp the operational characteristics of natural surfaces and to represent their interaction with the surrounding fluid will furnish insight into the engineering design coupling of both passive and active flow systems for technological applications.

The following sections explore and analyse passive technologies, focusing on their intrinsic, energy-independent characteristics. Starting from the inspiration of developing these technologies, by observing nature and plant worlds, leading to theoretical and conceptual explanations of these methods, continuing with a comprehensive review of existing literature, and concluding with an identification of the primary knowledge gaps and the main unexplained phenomena in the field.

1.2. Biomimetic: nature inspires engineering

In the past few decades, scientific and technological research has been increasingly oriented toward the development of innovative, efficient, and sustainable solutions capable of addressing complex challenges. Biomimetics, from the Greek *bios* - life - and *mimesis*, which stands for imitation, firstly introduced by Otto Schmitt in 1957, has emerged as a promising field, oriented towards the observation of natural phenomena and the emulation of models, systems, and elements of biological designs and systems into engineering applications. It is a source of inspiration to mimic nature to solve complex human problems. Nature, through millions of years of evolution, has indeed developed highly effective mechanisms for survival and adaptation, in which every form, structure, or behavior is designed to maximize performance while minimizing energy and resource dissipation. The next figure shows various examples of plants and animals with micro and nanostructures, that promotes their slippery properties.

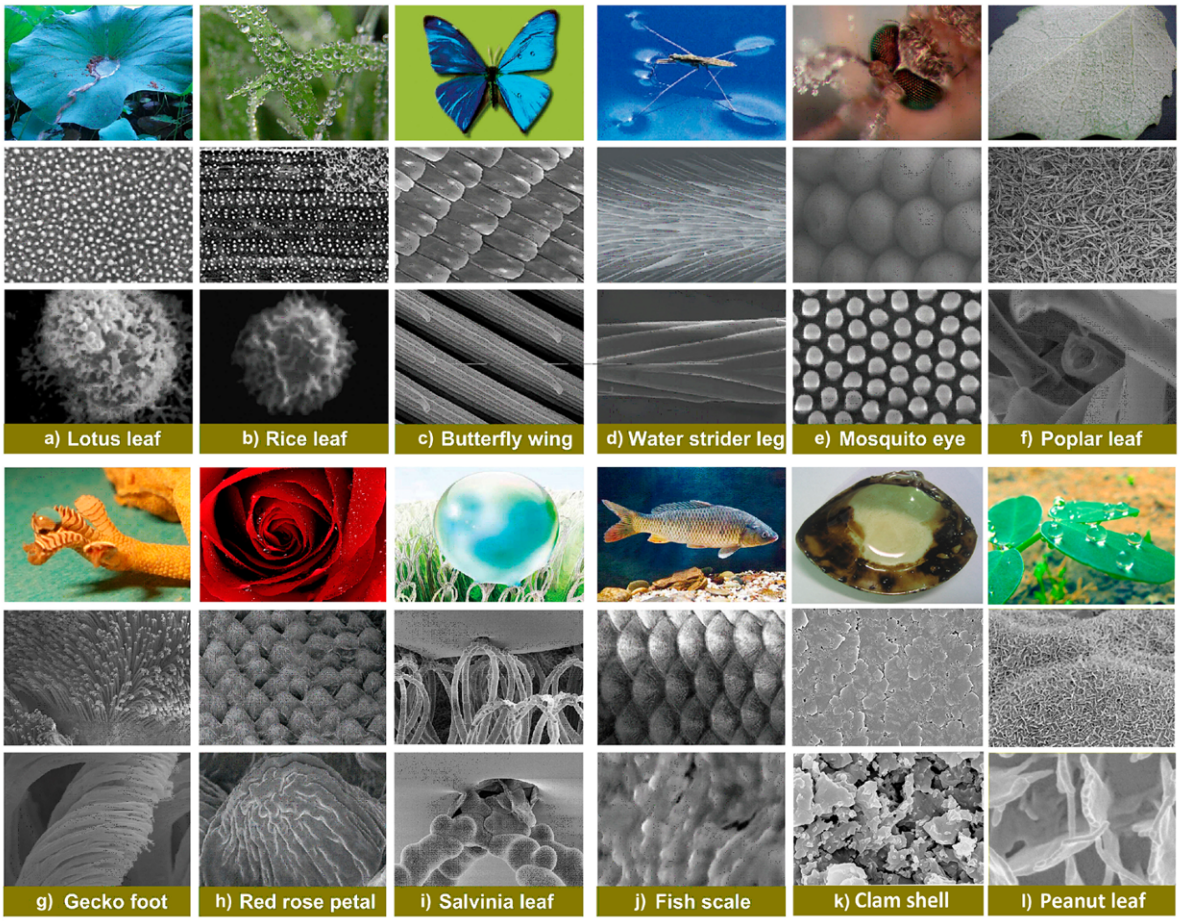

Figure 1.10: Examples of biological surfaces (e.g., lotus leaf, butterfly wing, gecko foot) showing superwettability arising from hierarchical micro/nanostructures, enabling properties like self-cleaning, adhesion, and drag reduction.[12]

Biomimetics goes beyond the mere imitation of forms, placing at its centre the study of the physical, mechanical, and functional principles that govern natural systems, to translate them into practical applications in the field of engineering. The history of biomimetics is connected with scientific and technical progress. What makes biomimetics a field of great interest to mechanical engineering is nature's ability, developed and optimized over millions of years, to provide solutions that simultaneously meet multiple requirements. By studying and understanding these natural mechanisms, humans may be able to replicate these phenomena.[13]
One of the most well-known examples of a naturally slippery surface is the lotus leaf. Its surface exhibits remarkable superhydrophobic properties, resulting in anti-wetting and self-cleaning behavior. This effect arises from its microstructured texture, which traps a thin air layer—known as a plastron—across the surface. As a result, water droplets roll off effortlessly. This phenomenon has inspired the development of advanced self-cleaning coatings.

Figure 1.11: Lotus effect: a water droplet forms a near-spherical shape thanks to the superhydrophobic properties of the lotus leaf.[14]

Another well-known example is shark skin (Figure 1.12). While it appears smooth at the macroscopic scale, a closer inspection at the microscopic level reveals aligned microgrooves that reduce drag and enable sharks to swim efficiently through water[7].
This biological structure has inspired the design of aerodynamic, drag-reducing textured surfaces known as riblets.
In the plant kingdom, the *Nepenthes* pitcher plant (Figure 1.13) provides another interesting example. It creates an exceptionally slippery surface by trapping a thin layer of viscous liquid within its microstructured texture. When an insect steps on the plant's surface, the lubricating film repels the oils on its feet, causing it to slip into the plant. This mechanism has inspired the development of Liquid-Infused Surfaces (LIS).
In the animal world, fish and other aquatic species experience resistance when their body and the surrounding water are in relative motion. The release of mucus by fish, it leads to a reduction in drag, thanks to this liquid-liquid interface. This is another example of adaptation to the environment.[15,16]

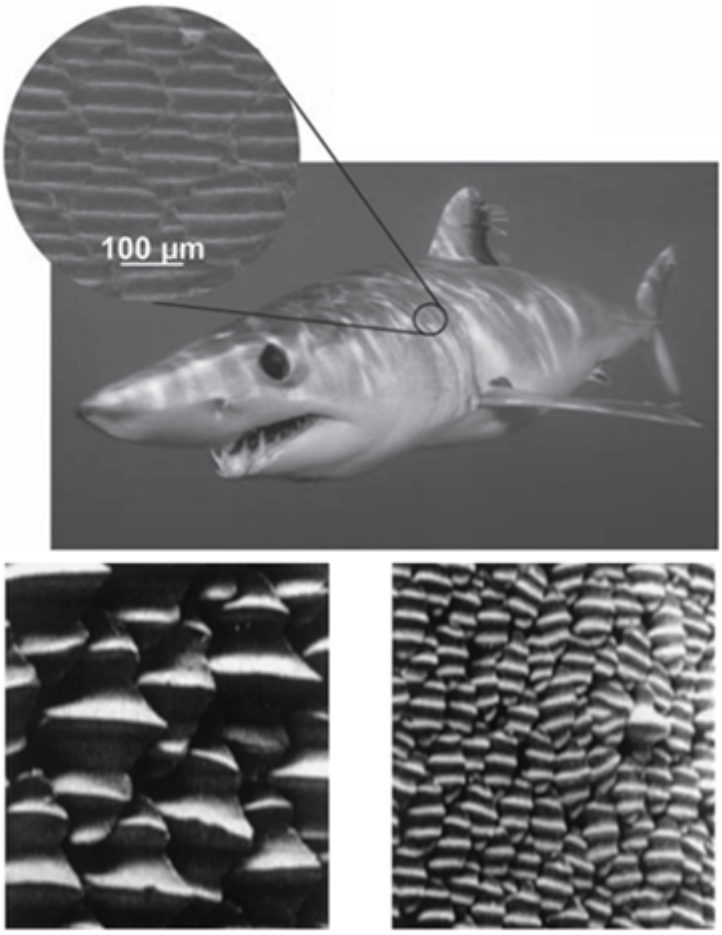

Figure 1.12: Images of different ribleted surfaces on shark skin.[17]

Figure 1.13: Nepenthes Pitcher plant. (Taken from https://gardenerspath.com/plants/houseplants/grow-nepenthes-pitcher-plants/)

1.3. Riblet surfaces

1.3.1. Shark skin: drag reduction mechanism

Shark skin exhibits a microstructured morphology characterized by the presence of longitudinal grooves that are predominantly aligned with the direction of the external water flow.
The surface is covered by microscopic scales, known as *dermal denticles*, which form a repeating pattern of small, flattened V-shaped structures. These denticles generate a grooved texture that resembles engineered riblet surfaces, producing a quasi-periodic pattern across the skin. Depending on their location on the shark's body, dermal denticles vary in both size and shape, reflecting their specific functional role.
Furthermore, their distribution and morphology differ among shark species, indicating a high level of biological specialization. [18]

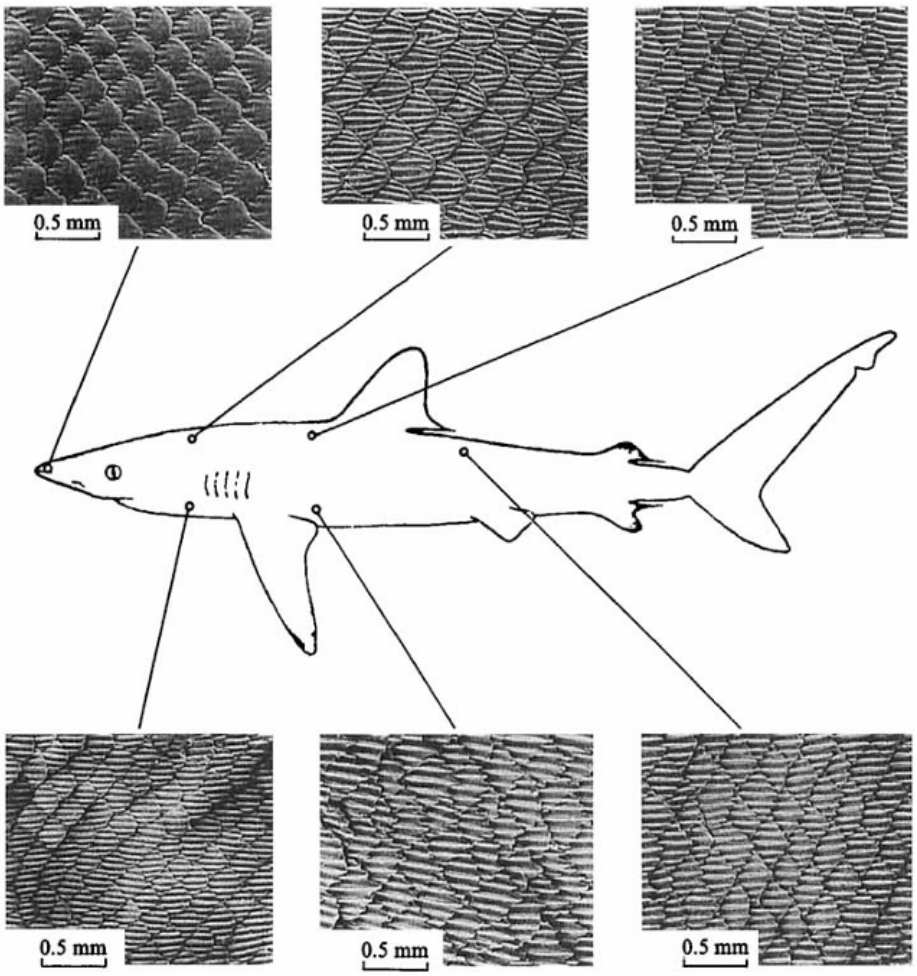

Figure 1.14: Images of different ribleted surfaces on shark skin. [17]

The unique structure of shark skin provides several functional advantages that contribute to the evolutionary success of these animals. The morphology of sharks allows the development of multiple mechanisms that work together to minimize hydrodynamic drag. Through the interaction between microstructure, material properties, and biological functions, shark skin is capable of adapting to different flow conditions and optimizing its performance during swimming. Several key features contributing to drag reduction have been identified in the literature and are summarized below.[19]

- The characteristic depth of the denticle grooves, typically on the order of 20 μm, is comparable to the thickness of the viscous sublayer of the turbulent boundary layer (approximately 10 μm). This allows the viscous sublayer to be partially inserted within the surface structure, reducing momentum transfer close to the wall and consequently decreasing turbulence intensity in the near-wall region.

- Dermal denticles are not perfectly aligned with the direction of the flow. Instead, they are oriented at a small angle relative to the incoming flow, typically ranging from about 10° to 50°. This inclination influences the local flow field, promoting more stable flow structures and generating localized backflow regions that contribute to a reduction in overall resistance.

- Sharks secrete a thin layer of mucus composed primarily of proteins, which acts as a natural lubricant on the skin surface. This lubricating layer reduces friction between the skin and the surrounding water, enhancing the overall slip effect and contributing to drag reduction.

- The flexibility of the underlying tissue allows continuous micro-adjustments of the denticle orientation during swimming. This adaptive capability helps optimize the effective angle of interaction with the flow, further enhancing hydrodynamic efficiency.

- The vertically protruding scales can also contribute to propulsion. Their shape generates additional thrust and reduces viscous forces, enhancing swimming efficiency.

Moreover, the denticles act as a protective layer, offering resistance against mechanical damage and interactions with competitors. In addition, they play a significant role in limiting biofouling. By modifying the surface topography at the microscale, the denticles hinder the adhesion, attachment, and proliferation of marine organisms such as bacteria and algae, thereby preserving the functionality of the skin surface. In general, rough surfaces tend to provide a larger effective area due to the presence of peaks and valleys, which can create favorable conditions for the settlement of marine organisms. However, on smooth surfaces, the initial fouling layer often spreads uniformly, covering the entire surface and eliminating the beneficial characteristics associated with smoothness. The microstructured geometry of shark skin instead interferes with this process, reducing the ability of microorganisms to establish stable attachment.

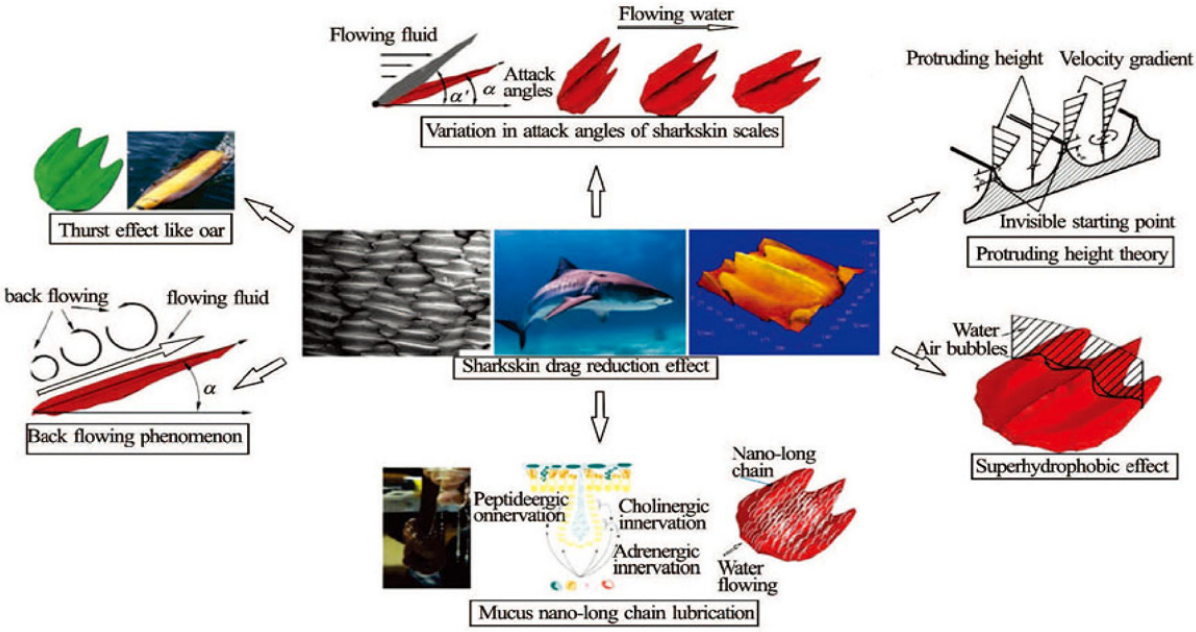

Figure 1.15: Different factors generating shark skin drag reduction.[19]

The primary hydrodynamic function of this specialized surface structure is the reduction of skin-friction drag during swimming. The aligned microgrooves interact with the near-wall flow structures of the boundary layer, leading to a reduction in momentum transfer toward the surface. This effect enables sharks to swim more efficiently, achieving higher speeds while minimizing energy expenditure.
The drag-reducing capability of shark skin has attracted significant attention in engineering research. In particular, the microscopic grooves have inspired the development of artificial riblet surfaces designed to reproduce similar hydrodynamic effects.

1.3.2. Physical mechanism and numerical/experimental review

As discussed in the previous section, riblets are streamwise-aligned microscopic grooves engineered on surfaces to reduce skin-friction drag in turbulent flows. These periodic structures mimic the natural morphology of dermal denticles of shark skin, whose unique microtexture inspired the development of riblets for fluid-dynamic applications by creating riblet-like patterns capable of interacting with the near-wall flow structures[17].
The study of riblets dates back several decades. The aviation and aerospace sector, marine transportation, and industry and energy are the main fields of application.
Early experiments conducted at NASA by Walsh and collaborators[20,21,22] demonstrated that the application of riblet surfaces on aircraft could produce measurable reductions in aerodynamic drag, highlighting their potential for large-scale use in commercial and military aviation. Subsequent experimental investigations[23] confirmed that, when properly designed and dimensioned,

riblets can reduce skin-friction drag by up to approximately 10%. This makes them a promising passive technology in applications where fuel efficiency and aerodynamic performance are critical. In the aeronautical sector, riblets have been investigated for application on aircraft fuselages, wings, and turbine blades. Even modest drag reductions can lead to significant fuel savings over long-distance flights, resulting in lower operational costs and reduced environmental impact through decreased carbon emissions. This aspect is particularly relevant for the aviation industry, where even small improvements in aerodynamics can lead to substantial economic benefits.

Riblets have also attracted considerable interest in the maritime sector. When applied to the hulls of ships and submarines, these microstructured surfaces can reduce hydrodynamic resistance, thereby improving propulsion efficiency. As in aeronautical applications, drag reduction in marine environments leads to lower fuel consumption and potentially higher cruising speeds. A well-known example is the 1987 America's Cup yacht *Stars & Stripes*, which successfully employed riblet surfaces to enhance hydrodynamic performance[24]. In modern sailing competitions, the use of riblets is prohibited. Ongoing research continues to explore the potential of riblet technologies for commercial shipping and naval vessels, including innovative concepts such as riblet-like microstructures impregnated with lubricating liquids to further reduce friction[25].

From a fluid-mechanical perspective, riblets influence the near-wall turbulence structure. In turbulent boundary layers over ribleted surfaces, longitudinal vortices form along the grooves, generating a secondary cross-flow that interacts with the surface corrugations. This interaction tends to weaken the intensity of the near-wall vortical structures, dampening and reducing turbulent momentum transfer toward the wall. As a result, turbulent diffusion decreases, leading to a reduction in eddy viscosity and consequently in skin-friction drag.

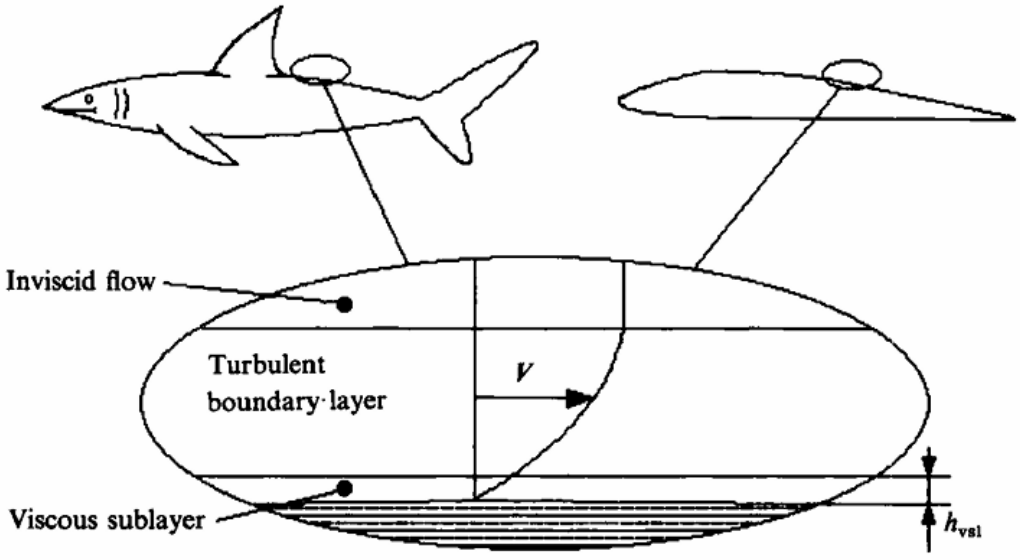

Figure 1.16: The phenomenon of drag reduction is produced by grooves (or riblets) interacting with the viscous sublayer, in a turbulent boundary layer.[8]

Experimental studies conducted by Bechert and collaborators provided a deeper understanding of the relationship between riblet geometry and drag reduction. In particular, it was observed that the effectiveness of riblets strongly depends on their characteristic dimensions, especially the spacing and height of the grooves. These geometric parameters must be of the same order of magnitude as the thickness of the viscous sublayer of the turbulent boundary layer to produce optimal drag reduction.
From a physical perspective, the velocity profile that develops close to the ribleted surface presents an asymptotically linear trend within the adjacent viscous layer. On a regular and periodic textured surface, the velocity zero is reached below the tip level by a certain quantity that depends on the shape and the dimensions of the grooves. So the effective point where the velocity tends to zero, named *virtual origin* of the flow, is displaced. The riblet surface can therefore be interpreted as an equivalent fictitious smooth wall that produces the same effect on the external flow but appears shifted relative to the riblet tips. This shift is commonly referred to as the *protrusion height* (Fig. 1.17).
By considering a small domain near the wall and solving the governing equations numerically, both longitudinal and transverse protrusion heights can be evaluated. These quantities depend on the riblet shape and geometric parameters. Importantly, the difference between the longitudinal and transverse protrusion heights provides a quantitative measure of riblet efficiency in terms of drag reduction.

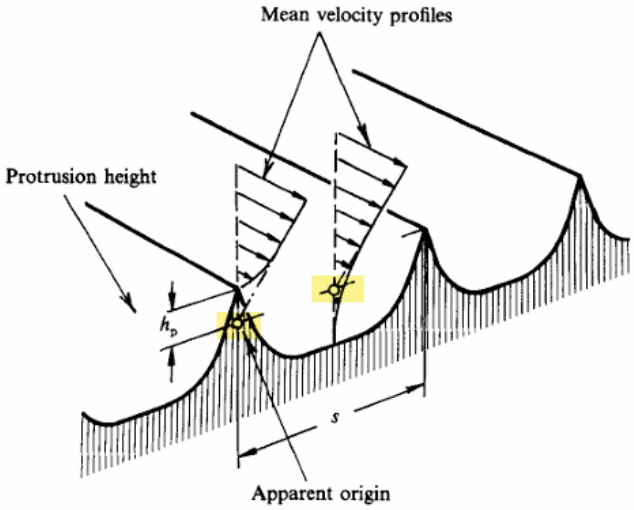

Figure 1.17: Apparent origin of a riblet surface.[17]

In general, randomly rough or textured surfaces tend to increase the overall resistance compared to smooth walls. However, riblets represent a particular case: by damping cross-stream velocity fluctuations and suppressing secondary vortical structures, they can effectively reduce drag. This beneficial effect is closely related to the characteristic size of the grooves relative to the viscous length scale of the turbulent boundary layer. An alternative interpretation of drag reduction considers the total drag force as the integral of the shear stress over the total area. Both the magnitude of the shear stress and the effective contact area must therefore be taken into account. Many studies have focused on suppressing turbulence intensity to reduce the average wall shear stress. Although the introduction of riblets increases the total surface area due to the

presence of peaks and valleys, the resulting distribution of shear stress is highly non-uniform. The riblet tips, which represent a relatively small portion of the surface area, are exposed to higher shear stress levels because they interact with faster-moving fluid structures. In contrast, the majority of the surface area lies within the riblet valleys, where the flow velocity is significantly lower, resulting in reduced shear stresses. By keeping the near-wall vortices above the riblet tips, cross-stream velocity fluctuations within the grooves are substantially smaller than those observed above a smooth flat plate. This reduction in cross-stream momentum transfer near the wall compensates for the increase in surface area and ultimately leads to a net reduction in drag.

One of the most comprehensive experimental investigations of riblet performance was conducted by Bechert et al.[23]. Several riblet geometries—including sawtooth, scalloped, blade, and trapezoidal shapes, as well as adjustable slits and ribs — were tested with different spanwise wavelengths. The drag-reduction parameter is defined as:

$$DR = \frac{\Delta\tau_w}{\tau_{w_0}} \approx \frac{\Delta C_f}{C_{f_0}} \tag{1.1}$$

where τ_w is the wall shear stress. C_f is the skin-friction coefficient,

$$C_f = \frac{2\,\tau_w}{\rho \hat{u}_{bulk}^2} \tag{1.2}$$

with $\hat{u}_{bulk}$ denoting the bulk velocity and ρ the fluid density. The subscript "0" refers to the corresponding smooth-wall value. The drag-reduction parameter was plotted against the non-dimensional riblet spacing

$$\ell^+ = \ell\,\frac{u_\tau}{\nu} \tag{1.3}$$

where u_τ is the friction velocity and ν the kinematic viscosity.

The results demonstrated the existence of a *viscous regime* for very small spacings, characterized by a linear decrease in skin friction. This regime is followed by a maximum drag reduction, after which drag begins to increase, eventually resulting in a drag penalty for ℓ^+ values exceeding approximately 30. For ℓ^+ values smaller than about 5–10 (depending on riblet geometry), the viscous regime is well described by the Stokes-based theory proposed by Luchini et al.[8]. Their analysis showed that riblets provide greater resistance to transverse flow than to streamwise motion. This anisotropic resistance can be quantified through two slip lengths: the longitudinal slip length λ_x and the spanwise slip length λ_z. Luchini et al.[8] further argued that these slip lengths represent distances measured from the riblet tips, which are themselves an arbitrary reference point along the wall-normal coordinate. Consequently, the absolute values of λ_x and λ_z do not directly influence the macroscopic flow behavior. Instead, the physically meaningful quantity is their difference,

$$\Delta\lambda = \lambda_x - \lambda_z \tag{1.4}$$

This concept was later confirmed by Luchini[26] and Jiménez[27], who derived an expression for the drag reduction:

$$\frac{C_f - C_{f_0}}{C_{f_0}} = -\frac{\Delta U^+}{(2\,C_{f_0})^{-1/2} + (2\,\kappa)^{-1}} = -\frac{\mu_0\,\Delta\lambda^+}{(2\,C_{f_0})^{-1/2} + (2\,\kappa)^{-1}}, \tag{1}$$

where ΔU^+ represents the velocity shift in the logarithmic layer (positive when drag is reduced), and κ is the von Kármán constant. The coefficient μ_0 depends on the riblet geometry and spacing; reported values include approximately 0.66 (Jiménez[27]), 0.785 (Bechert et al.[23]), and 1 (Luchini[26]).
In particular, Luchini showed that the equality $\Delta U^+ = \Delta\lambda^+$ arises from an effective upward displacement of the origin of the turbulent mean velocity profile in the presence of riblets. The increase in mean streamwise velocity compensates for this shift, leading to a reduction in wall shear stress. This theoretical framework, however, remains valid only within the viscous regime, typically for ℓ^+ values below approximately 10.

1.3.3. Manufacturing of riblets

As explained in the previous section, the characteristic dimensions of the riblets—such as height, spacing, and shape—must be carefully selected to correspond to the typical length scales of the turbulent structures they are intended to control. If the riblets are either too large or too small relative to these scales, their drag-reduction capability is significantly impacted, making the design and optimization process a critical aspect of their practical implementation.
There are several manufacturing techniques, including microfabrication processes, laser etching, and additive manufacturing, such as 3D printing[28]. These technologies enable the production of highly precise surface textures, allowing engineers to design riblet patterns tailored to specific operating conditions.
In the maritime sector, riblets can be implemented on ship propellers to improve propulsion efficiency, as well as on the hull surface to reduce hydrodynamic friction during navigation. In addition to drag reduction, riblet surfaces may also exhibit antifouling properties, which further enhance their potential benefits for naval applications by limiting the adhesion and growth of marine organisms. Despite their promising performance, a significant challenge in materials science lies in the development of manufacturing techniques that are both efficient and economically viable for large-scale applications, particularly for extensive surfaces such as ship hulls. The fabrication methods must therefore be adaptable, durable, and compatible with existing coating and surface-treatment technologies.
Several approaches have been proposed to produce riblet microstructures, among which the most widely investigated are laser-based surface structuring, textured films, and specialized coating treatments[29]. Laser technology, for instance, uses optically focused beams to locally modify the surface and generate the desired micro-scale geometry. Laser machining allows the creation of complex three-dimensional riblet patterns with high precision and can be applied even on curved or irregular surfaces, where the use of prefabricated textured films would be impractical.
Another promising approach is the roll-to-roll (R2R) film coating technology, which enables the production of functional films incorporating riblet structures. The rolling technique, described by Stille et al.[30], employs two rolls—one structured and one smooth—between which large metallic sheets are passed. A fine, high-strength steel wire is tightly wound around the upper work roll, imprinting a negative riblet pattern onto the roll surface. This structured roll then transfers the riblet geometry onto the passing material, enabling the efficient manufacturing of

riblet textures over large surface areas, as illustrated in Fig. 1.19.

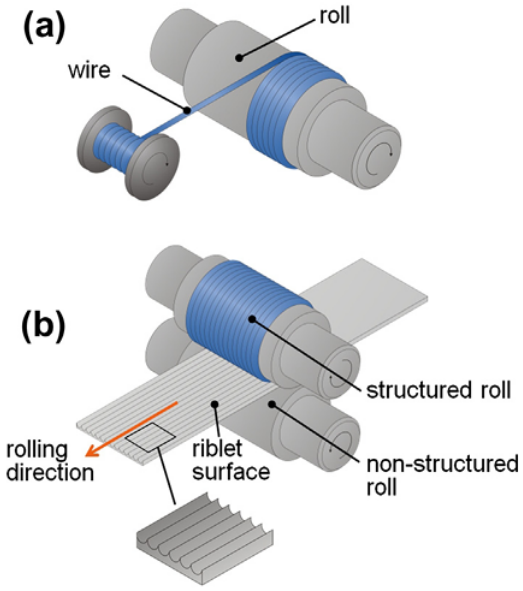

Figure 1.18: Roll structuring method (a) and riblet rolling process (b).[30]

The third application method is coating. There are two main components: the application system and the coating system. The coating process is done using a specially designed roller device and a silicone film, a soft-negative mold, embosses the coating with the microscopic shapes. The grooves are then cured using an ultraviolet light source.[31]

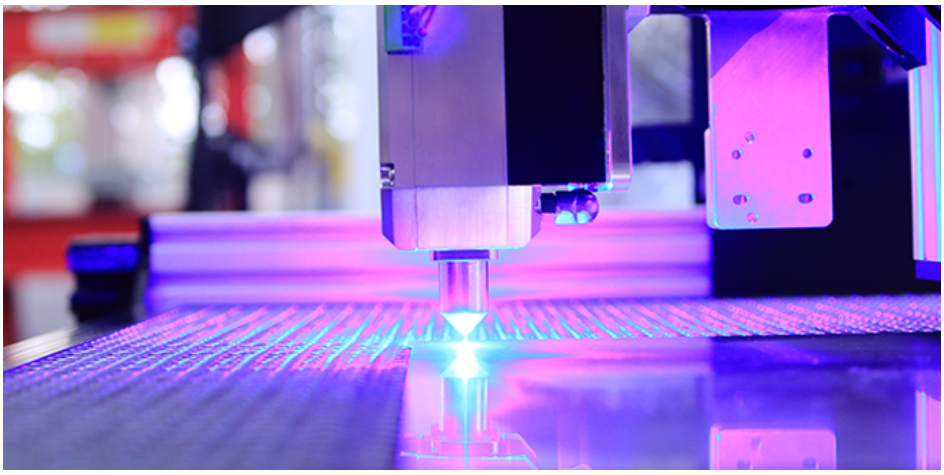

Figure 1.19: Ultraviolet process of curing of a grooved surface.

A similar method technology for the fabrication of micro-riblets utilizes laminate transfer molding, which enables the modification of paint morphology to accommodate the replication of micro-riblets on a ship's hull. Using a laminate mold, made of nylon wire to reproduce

pattern materials, it forms a cavity of the micro-riblets structure on the silicon rubber; then a painting process is done and finally, the outcome is applied to the ship model's hull.[32]

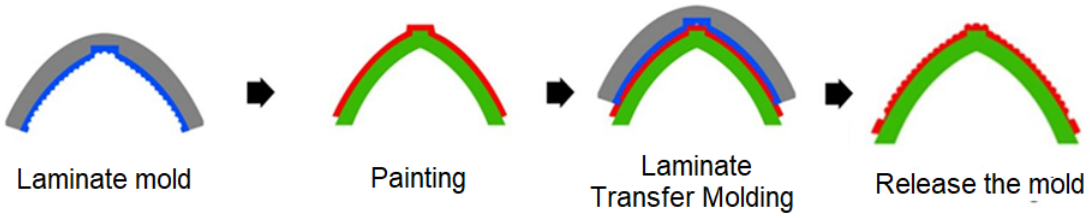

Figure 1.20: Procedure of laminate transfer molding.[32]

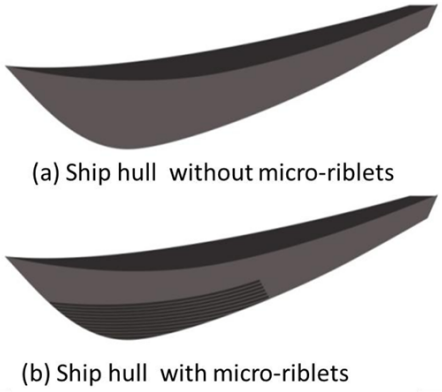

Figure 1.21: Application of micro-riblets on the ship's hull.[32]

With regard to the technological maturity of riblet surfaces in maritime applications, their industrial implementation has so far been limited to relatively small-scale and specialized uses within the shipping sector. One notable example is their application in high-performance sailing and racing boats, where riblet foils are applied to the hull in order to reduce hydrodynamic drag and enhance overall performance. In these contexts, the effectiveness of the microstructured surface can be maintained because the hull is regularly cleaned after each race, preventing the accumulation of contaminants that would otherwise degrade the drag-reduction capability of the riblets[29,33]. When considering broader commercial maritime applications, several challenges emerge. One of the primary limitations is related to surface maintenance. Unlike vessels for competition purpose, commercial ships cannot undergo frequent cleaning operations, and the accumulation of fouling on the surface can significantly reduce the effectiveness of riblet textures. Furthermore, the application of riblet structures over very large surfaces, such as ship hulls, remains a significant technological and manufacturing challenge, both in terms of scalability and long-term durability.

Despite these limitations, riblet technology remains a promising solution for improving the hydrodynamic efficiency of marine vessels. As a passive drag-reduction technique that does not require additional energy input, riblets could contribute to reducing fuel consumption in maritime transport. This improvement in propulsion efficiency would consequently lead to a decrease in CO_2 emissions, supporting current efforts to enhance the environmental sustainability of the shipping industry.

1.4. Slippery surfaces

1.4.1. Superhydrophobic surfaces

In the first decades of the previous century, Robert N. Wenzel[34] and A. B. D. Cassie & S. Baxter[35] developed pioneering studies, investigating the fundamental understanding of wettability on rough and porous surfaces, introducing one of the most important models in surface wettability theory.
In 1936, Wenzel demonstrated that surface roughness strongly influences the wetting behavior of solids by amplifying their intrinsic wettability. In the so-called Wenzel state, the liquid completely penetrates the surface asperities, increasing the effective solid–liquid contact area. The apparent contact angle is described by the Wenzel relation:

$$\cos\theta_W = r\ \cos\theta_Y \tag{1.5}$$

where θ_W is the apparent contact angle on a real rough surface in a Wenzel state, θ_Y is Young's contact angle on an ideal and smooth surface, and r is the roughness ratio, defined as the ratio of the actual surface and the geometrical one (it is larger than 1 because of roughness elements).
In 1944, Cassie and Baxter expanded this theory by studying porous and heterogeneous surfaces. They proposed that, under certain conditions, air can remain trapped beneath a liquid droplet, creating a solid-air interface. In this Cassie–Baxter state, the liquid contacts only a fraction of the solid surface, resulting in reduced adhesion and significantly enhanced water repellency. Their model is expressed as:

$$\cos\theta_{CB} = f_s\,(\cos\theta_Y + 1) - 1 \tag{1.6}$$

where θ_{CB} is the apparent contact angle in Cassie-Baxter state, f_s represents the fraction of solid surface area wetted by the liquid. The next figure shows a schematic representation of both Wenzel and Cassie-Baxter states.

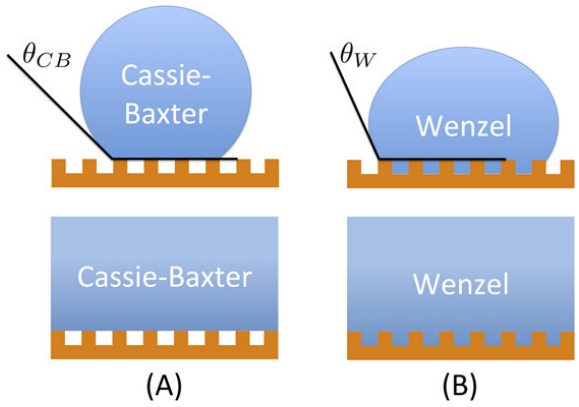

Figure 1.22: (A) Cassie–Baxter state: a drop (top) and bulk liquid (bottom) rest on a rough surface without fully wetting it, remaining suspended on surface asperities. (B) Wenzel state: the liquid fully follows and wets the surface roughness.[36]

The Wenzel and Cassie–Baxter models constitute the theoretical foundation of modern superhydrophobic surface (SHS) research. These surfaces constitute a prominent class of bioinspired engineered interfaces, drawing inspiration from natural systems to achieve anti-wetting, anti-icing, self-cleaning, and low-friction functionalities.
These theories explain how combining two key elements:

I. micro- and nano-scale surface textures, a hierarchically structured roughness

II. low-surface-energy chemical functionalization.

It can produce extremely high water contact angles and low sliding angles, designed to minimize liquid–solid contact and thereby alter interfacial transport phenomena.
The first element is essential for generating surface asperities - such as microgrooves, cavities, and micropillars - that can entrap air pockets. In contrast, a perfectly smooth surface is inherently incapable of sustaining superhydrophobic behavior.
The interdependence between surface roughness, reduced particle adhesion, and water repellency has been widely observed in many biological systems[37]. This coupled problem is recognized as a key mechanism governing self-cleaning surfaces and is schematically illustrated in the figure below.
Bico et al. established fundamental theoretical frameworks describing how surface roughness

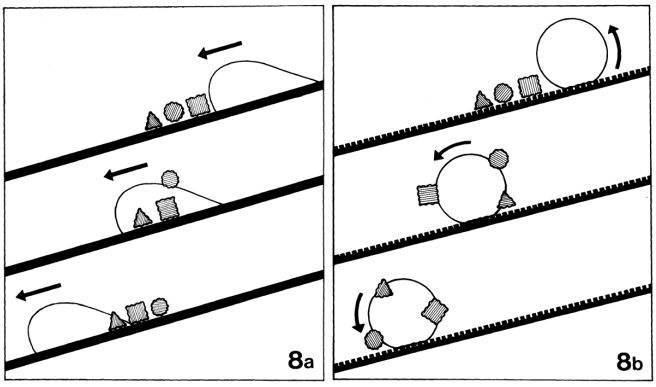

Figure 1.23: Illustration of the connection between surface roughness and self-cleaning: on smooth surfaces, particles are redistributed by water (8a), whereas on rough surfaces they adhere to droplets and are removed as the droplets roll off (8b).[37]

and texture topology dictate the transition between distinct wetting states, specifically analyzing the conditions under which a liquid either spreads into a texture or remains suspended on top of it.[38] In particular, they found out that the wettability property can be described by the apparent contact angle as a function of two dimensionless parameters, the surface roughness and a surface fraction.
In a comprehensive review, Quéré (2008) examined the influence of surface roughness on wettability, highlighting that both the apparent contact angle and contact angle hysteresis are strongly affected by roughness and emphasizing the importance of establishing well-defined measurement protocols[39].
Lafuma and Quéré[40] concluded that microtextured hydrophobic surfaces can exhibit both metastable Cassie states, where air remains trapped beneath the drop, and Wenzel states, where

the liquid penetrates the texture; although both states show similarly high contact angles, the Wenzel state produces dramatically larger hysteresis and much stronger droplet adhesion. They also highlight that superhydrophobicity can fail when water penetrates the surface texture and induces a transition from the Cassie to the Wenzel state, but that highly rough, hierarchical textures—such as those found in plants - can stabilize the Cassie regime and preserve strong water repellency.[40]

A defining macroscopic manifestation of superhydrophobicity is the formation of nearly spherical liquid droplets upon contact with the surface. These droplets exhibit high mobility: even slight inclinations induce rolling, during which contaminants are collected and removed. This self-cleaning mechanism, often referred to as the "lotus effect," has motivated the development of multifunctional surfaces. Water droplets impacting a superhydrophobic surface do not spread or adhere. This behavior reflects the extremely low wettability of such interfaces. Static and dynamic contact angles represent two fundamental metrics for quantifying superhydrophobic performance.[41]

When air is stably trapped within the surface asperities, the liquid partially rests on a composite interface of solid and air, thereby reducing the effective contact area. This regime is described by the Cassie–Baxter model (also known as the "fakir" state). Conversely, if the entrapped air layer is displaced by the liquid, the system transitions to the Wenzel state, characterized by complete wetting of the nano- and microstructures. In this latter condition, the slip effect is suppressed, and the surface behaves as a conventional rough substrate with increased adhesion. The synergistic combination of surface texturing and chemical functionalization enables the stabilization of a thin air layer between the solid substrate and the external fluid, which is the hallmark of SHS performance. Quantitatively, superhydrophobicity is typically assessed via static contact angle measurements. This involves placing a liquid droplet, typically a water droplet, on the surface and determining the angle formed between the solid baseline and the tangent to the droplet profile at the three-phase contact line (solid–liquid–gas). Surfaces exhibiting a static contact angle equal to or greater than 150° are conventionally classified as superhydrophobic.

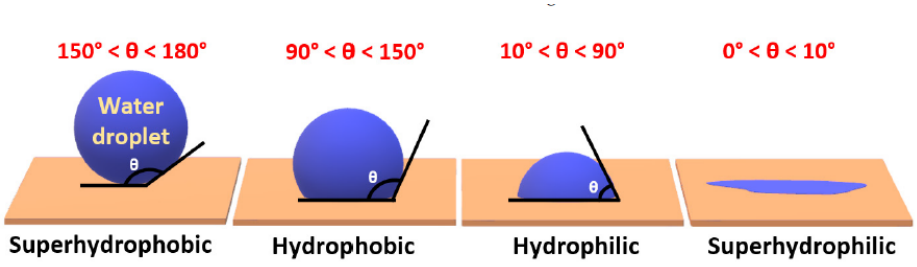

Figure 1.24: Surface characterization through static contact angle measurement.[42]

From a fluid-dynamic perspective, classical viscous flow over a solid boundary is governed by the no-slip condition, whereby the fluid velocity at the interface vanishes (Fig. 1.25a). The velocity profile linearly decreases from an outer velocity U_∞ to zero, when it touches the surface. But this condition is not reliable for all materials, such as rough, superhydrophobic, and liquid-infused surfaces. In Fig. 1.25b, there is a scheme of two immiscible fluids, which could

be air-water or oil-water.

In SHSs, the air entrapped within surface cavities forms a so-called plastron layer, effectively

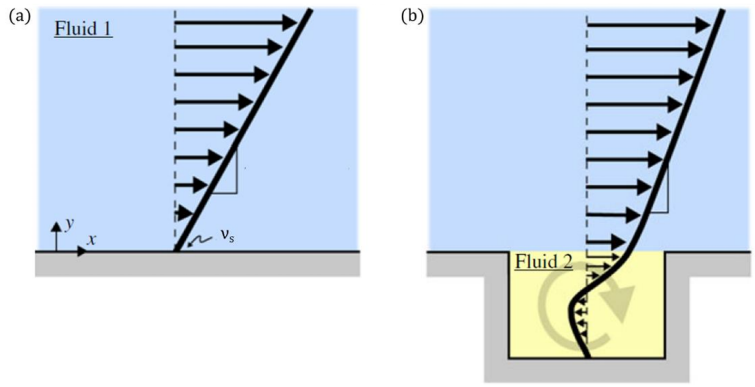

Figure 1.25: Schematic of the near-wall velocity. a) Single-fluid system flows on a solid surface. b) Two immiscible fluid systems on a solid surface with a roughness element. The presence of the second fluid creates a recirculation region, reducing the near-wall shear and drag induced by the flow.[43]

altering the boundary condition and enabling partial slip of the external liquid over the gas layer. At this interface, a finite slip velocity arises, which can be quantified through an effective slip length—a key parameter for characterizing drag-reducing performance. So the interaction between the micro properties of the surface and the flow has a crucial role in determining drag reduction performance. Extensive experimental and numerical studies have demonstrated that SHSs can significantly reduce skin friction in both laminar and turbulent flow regimes. Under favorable conditions, drag reduction exceeding 20% has been reported, highlighting their potential for applications in fluid transport and energy efficiency. The surface energy of a solid provides a measure of its propensity to be wetted. More precisely, wettability arises from the interplay between adhesive forces at the solid–liquid interface and cohesive forces within the liquid phase. In the case of water, strong intermolecular cohesion (due to hydrogen bonding) favors droplet formation, and the extent of spreading on a surface is therefore governed primarily by the surface energy of the solid. Materials with high surface energy promote stronger adhesive interactions with the liquid, resulting in enhanced wetting. Conversely, low-surface-energy materials inhibit such interactions, leading to reduced wettability. This distinction is evident across material classes. Metals, glasses, and ceramics, characterized by strong chemical bonding, exhibit high surface energy and are typically hydrophilic. In contrast, fluoropolymers, whose molecular structure is dominated by weak van der Waals interactions and highly electronegative fluorine atoms, possess intrinsically low surface energy and are therefore hydrophobic. Despite their advantageous properties, a critical limitation of superhydrophobic surfaces emerges under external flow conditions. The shear stresses can destabilize or entirely remove the entrapped gas plastron, leading to partially or totally liquid penetration into the surface texture. This transition effectively suppresses the slip behavior and results in a loss of superhydrophobic functionality, with important implications for their durability and performance in practical applications.

Considering the limited robustness of superhydrophobic surfaces to failure under harsh operating conditions, an alternative strategy consists of replacing the fragile air plastron with a more

stable lubricating phase. In this approach, the entrapped gas is substituted by a viscous, immiscible liquid — typically a lubricating oil — that is retained within the surface texture through capillary forces. This configuration gives rise to so-called liquid-infused surfaces (LIS).
In particular, superhydrophobic surfaces (SHSs) exhibit significant limitations in maritime applications, primarily due to the difficulty of maintaining a stable gas plastron within surface cavities and the near-total loss of their slippery properties in the presence of surfactants[44]. In contrast, liquid-infused surfaces (LIS) represent a promising alternative, owing to their greater resilience to external fluid interactions. However, a key challenge for large-scale implementation lies in the need for simple and scalable application methods over extensive surface areas. At present, both superhydrophobic and liquid-infused surface technologies remain at a low technology readiness level, with development largely confined to the research stage and only limited progress toward industrial deployment.

1.4.2. Liquid-Infused surfaces

The concept of bioinspired, self-repairing Slippery Liquid-Infused Porous Surfaces (SLIPS), commonly referred to as liquid-infused surfaces (LIS), was introduced by Wong et al.[45]. In particular, a novel class of omniphobic materials exhibits superior resistance and significantly greater stability to pressure-driven depletion and diffusive loss mechanisms compared to superhydrophobic surfaces, which commonly compromise the integrity of air-based plastrons. They demonstrated that locking a lubricant within a micro/nanostructured substrate creates a self-healing, high-pressure-resistant interface capable of repelling diverse complex fluids and preventing ice or biofouling accumulation.

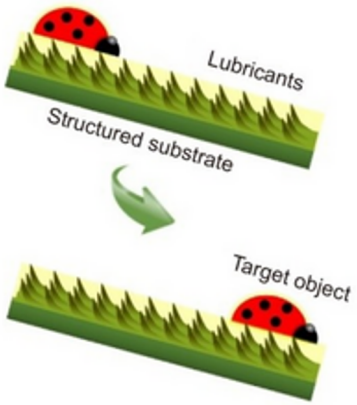

Figure 1.26: Schematic of a liquid-infused surface, illustrating surface asperities impregnated with lubricant oil and an insect sliding across it, highlighting the natural inspiration behind the design.

Liquid-Infused surfaces trap the lubricant within the micro- and nanoscale asperities, forming a continuous liquid layer that effectively separates the solid substrate from the external fluid.
Owing to its higher viscosity, the infused liquid exhibits enhanced resistance to external perturbations. Capillary forces further contribute to stabilizing the lubricant within surface cavities,

preventing its displacement under moderate shear or pressure gradients.
As a result, LIS demonstrates improved robustness compared to conventional superhydrophobic surfaces, emerging as a promising alternative to SHS for certain applications in harsh conditions. This increased stability has positioned LIS as a promising alternative for applications involving extreme flow conditions, where maintaining interfacial slip and low drag is otherwise challenging.
As previously discussed, similarly to superhydrophobic surfaces, liquid-infused surfaces are defined by two primary components: a rough/porous, micro- and nanostructured scaffold, and a lubricating liquid that impregnates and fills the surface cavities. The combined effect of these elements results in the formation of a stable, immobilized lubricant layer, which imparts low interfacial shear and confers the characteristic slippery behavior of the surface. Thanks to the presence of the oil, the fluid above the surface slips, reducing the liquid-solid contact area. The oily film must show affinity with the porous scaffold and be immiscible with the outer liquid, i.e., the liquid-liquid interactions must be minimal for the SLIPS to serve their purpose.
Slippery surfaces are typically characterized under static conditions, similar to SHSs, by placing a water droplet on the surface and measuring the static contact angle. Liquid-infused surfaces (LIS) generally exhibit lower static contact angles compared to SHSs.

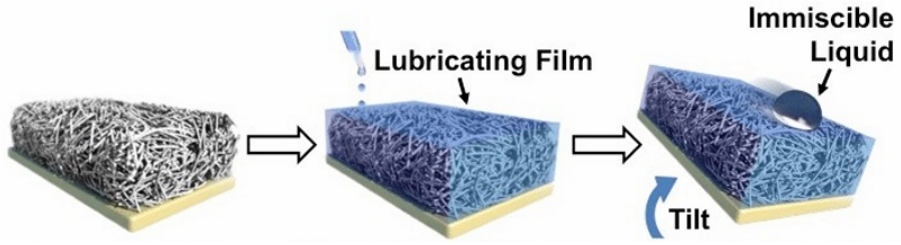

Figure 1.27: Schematic of LIS: porous solid scaffold, characterized by micro and nanocavities, then impregnated with a lubricating oil. By tilting, a water droplet rolls off the surface almost frictionlessly.[45]

While static contact angle measurements provide an initial indication of wettability, they do not fully capture droplet mobility or interfacial friction. For this reason, dynamic characterization is equally important. Two main strategies are commonly employed to assess dynamic performance. The first involves placing a droplet on the surface and gradually inclining it until the droplet begins to roll or slide. An alternative approach, illustrated in the following figure, consists of forming a droplet held by a needle and increasing its volume at a constant rate. In this method, the advancing and receding contact angles are measured when the contact line respectively advances and recedes while the contact angle remains stable (boxes c & e in the next Fig.1.28). The difference between these angles, known as contact angle hysteresis, should be minimal to ensure robust surface performance.
Considering droplet mobility, Smith et al. (2013) established a fundamental thermodynamic framework on lubricant-impregnated surfaces, focusing on the complex physico-chemical hydrodynamics of these immiscible, four-phase systems.[46] The authors demonstrated that a novel contact line morphology emerges, characterized by a finite annular lubricant ridge pulled above the surface texture that forms up to three distinct three-phase contact lines. Crucially, they showed that these unique morphologies dictate not only the initial contact line pinning and resistance to motion, but also the subsequent level of viscous dissipation that governs droplet

sliding velocity once movement begins.

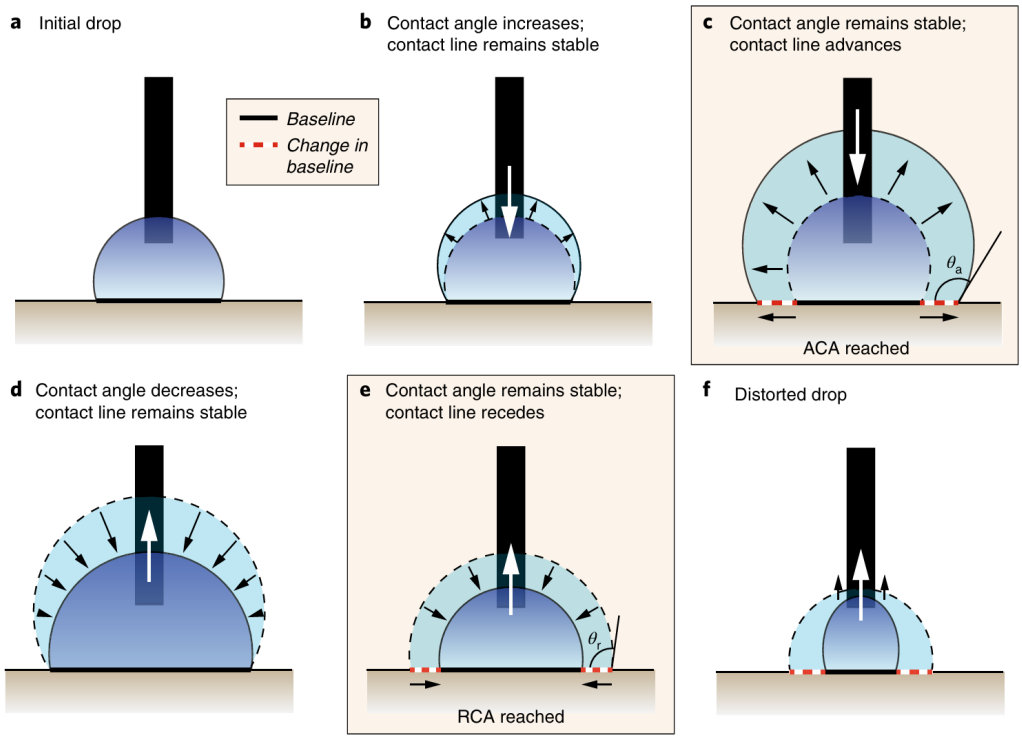

Figure 1.28: Different stages of advancing (ACA) and receding (RCA) contact angle measurements. White arrows indicate water added for ACA and removed for RCA.[47]

However, the effectiveness of skin-friction drag reduction progressively deteriorates as the lubricating layer becomes depleted. This depletion increases the pressure imbalance between the lubricant-filled cavities and the external flow, progressively destabilizing the infused layer. As the lubricant is removed, portions of the textured substrate become exposed to the outer liquid, promoting wetting transitions toward a Wenzel-like state and reducing interfacial slip. The degradation or removal of the lubricant, therefore, represents one of the main limitations of LIS. Once the infused layer becomes unstable, interfacial slip is progressively lost, and drag-reduction performance rapidly deteriorates, making lubricant retention a critical design parameter for practical applications in external and internal flows.[48]

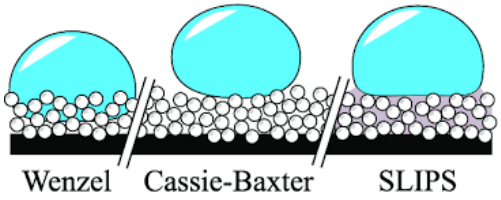

Figure 1.29: The manifestation of Wenzel and Cassie-Baxter states on a surface coated with nanoparticles. In SLIPS, the Cassie-Baxter state is favored due to oil-filled pores.[49]

1.5. Comparison between laboratory and real application scales

In this introductory chapter, section 1.1. is dedicated to the environmental motivation of the study, looking in the direction of applying passive green technologies to the maritime world, reducing the environmental impact. The link with maritime transport has been presented as a motivation for the thesis; there is no intention of proposing a solution to apply in the real world, ready to be durable, effective, and green. The aim is to model and define novel approaches to deeply understand the behaviour of slippery surfaces beyond ideal operating conditions.
However, this section aims to provide an estimation of the comparison between laboratory and real-world application scales, without the purpose of giving a detailed naval calculation, but trying to assess the fundamental parameter scale to better understand the relation of the activities that will be described in the following chapters, compared with the real-world application.
The following calculations have been suggested by Prof. Christophe Clanet, reviewer of this thesis.

1.5.1. Global parameters scale

In ship hydrodynamics, the ITTC-1957 model-ship correlation line is the standard empirical formula used to estimate skin-friction resistance (the viscous drag caused by water sliding along the hull surface).[50] The skin-friction coefficient can be evaluated from the following equation:

$$c_F = \frac{0.075}{(\log_{10} Re_L - 2)^2} \tag{1.7}$$

with Re_L that is the Reynolds number based on the ship length, defined as $Re_L = UL/\nu$.
As previously discussed, see figure 1.6, the use of drag reduction technologies can significantly and positively impact, in particular, large and slow ships, such as bulk carriers and tankers. Considering the word fleet, these ships cover a broad range of dimensions and operating conditions. To consider representative values for the principal tanker classes, some geometrical data need to be defined. L denotes the ship length, B the beam, T the loaded draft, and U the cruising velocity; average values have been taken from "Typical ship principal dimensions" under the section Tankers.[51]

$$L = 300\,m, \quad B = 60\,m, \quad T = 20\,m, \quad U = 7.7\,m/s$$

The seawater properties are assumed $\rho = 1025\,\mathrm{kg\,m^{-3}}$ and $\nu = 10^{-6}\,\mathrm{m^2\,s^{-1}}$, where ρ is the fluid density and ν is the kinematic viscosity. The Reynolds number based on ship length can be calculated, obtaining:

$$Re_L = \frac{UL}{\nu} = \frac{7.7 \times 300}{10^{-6}} \simeq 2.3 \times 10^9. \tag{1.8}$$

The corresponding Froude number is:

$$Fr = \frac{U}{\sqrt{gL}} = \frac{7.7}{\sqrt{9.81 \times 300}} \simeq 0.14. \tag{1.9}$$

With these two dimensionless numbers, the skin-friction coefficient can be estimated from equation 1.7, and it gives:

$$c_F \simeq 1.4 \times 10^{-3}. \tag{1.10}$$

To obtain an order-of-magnitude estimate of the viscous drag force and the corresponding power dissipation, the hull wetted surface area is approximated as a simplified rectangular prism:

$$S \simeq L(B + 2T) = 300, \big(60 + 2 \times 20\big) \simeq 3.0 \times 10^4 \ \mathrm{m}^2. \tag{1.11}$$

The resulting viscous drag force and the related power dissipation become:

$$F_F = \frac{1}{2}\,\rho\, S\, c_F\, U^2 \simeq 1.3 \times 10^6 \ \mathrm{N}, \qquad P_F = F_F U \simeq 9.7 \times 10^6 \ \mathrm{W}. \tag{1.12}$$

To understand the impact of a reduction in the viscous power dissipation on the overall engine power cost, it is crucial to take into account all the effects. The global resistance coefficient includes multiple factors: wave-making resistance, residual resistance, appendages, and aerodynamic drag. For a tanker, a representative estimate of the global resistance coefficient can be taken as:

$$C_T \simeq 2.5 \times 10^{-3}, \tag{1.13}$$

This yields an overall hydrodynamic drag force and required hydrodynamic power of:

$$F_T = \frac{1}{2}\,\rho\, S\, c_T\, U^2 \simeq 2.3 \times 10^6 \ \mathrm{N}, \qquad P_T = F_T\, U \simeq 1.8 \times 10^7 \ \mathrm{W}. \tag{1.14}$$

Assuming a global propulsive efficiency η in the range 0.6-0.7, the corresponding engine power is estimated as:

$$P_E = \frac{P_T}{\eta} \simeq (2.5\text{–}3.0) \times 10^7 \ \mathrm{W}. \tag{1.15}$$

Considering, for instance, a 5% or 10% decrease in viscous drag would correspond to an approximate power saving of:

$$P_R = (0.05\text{–}0.10)\, P_F \ \simeq \ (4.9\text{–}9.7) \times 10^5 \ \mathrm{W}, \tag{1.16}$$

which in terms of percentage corresponds to:

$$P_S = \frac{P_R}{P_E} \times 100 \simeq 1.6\text{–}3.2\% \tag{1.17}$$

Although the potential energetic benefit is substantial, practical implementation at full scale requires the drag-reducing mechanism to remain effective over very large wetted surfaces under seawater exposure, fouling, abrasion, aging, and operational maintenance constraints. But even a small reduction leads to a strong impact overall the system.
The two experimental activities described in this thesis have been conducted in Taylor-Couette configurations, described in the following chapters. This geometry provides a typical framework for studying hydrodynamic instabilities and interfacial flow phenomena: it is very sensitive to small changes, for example, roughness elements, and it can be modeled accurately. However, it does not reproduce the full turbulent boundary layer developing along a ship hull.

In Chapter 3, the flow is under laminar conditions, so it is far from a real application; the study links wall texture, slip length, and flow instabilities, proposing the use of effective boundary conditions to predict the flow behaviour of a rough-patterned cylinder.
In Chapter 4, lubricant-depletion experiments are performed in a custom-built mesoscale Taylor-Couette apparatus, able to reach the following Reynolds number:

$$Re_{TC,\max} = \frac{\Omega_i \, R_i \, d}{\nu} \simeq 4.7 \times 10^4 \tag{1.18}$$

The experiment presented in Chapter 4 is the one that studies the most harsh conditions, in terms of global parameters related to flow speed. However, the global quantities are different from the case of a real tanker.
It is also crucial to point out that in Taylor-Couette flow, the absence of a free surface makes gravitational wave generation negligible. In contrast, for marine applications, the presence of a free surface introduces wave-making effects that contribute directly to the total drag.
Consequently, the comparison between laboratory and full-scale conditions should not be interpreted as a strict dynamic similarity. Rather, the Taylor-Couette experiments provide access to specific local flow mechanisms - such as interfacial stability, lubricant depletion, and viscous transport - that are relevant to the physical processes governing drag reduction, while the ship-scale estimates establish the corresponding order of magnitude and practical engineering significance.

1.5.2. Local parameters scale

To compare maritime applications, it is relevant to consider also the local near-wall flow parameters: wall shear stress τ_w, the friction velocity $u_\tau = \sqrt{\frac{\tau_w}{\rho}}$, the viscous length scale $\delta_\nu = \frac{\nu}{u_\tau}$. From a geometrical point of view, the texture dimensions ℓ is the texture spacing and k is the texture height or characteristic roughness, that can be expressed in wall units: $\ell^+ = \frac{\ell u_\tau}{\nu}$ and $k^+ = \frac{k u_\tau}{\nu} = \frac{k}{\delta_\nu}$. For the representative tanker, wall shear stress is estimated from:

$$\tau_w = \frac{1}{2} \rho \, U^2 \, c_F. \tag{1.19}$$

Using the previous reference data, $U = 7.7 \, \mathrm{m\,s^{-1}}$ and $c_F = 1.4 \times 10^{-3}$, it yields to:

$$u_\tau = U \sqrt{\frac{C_F}{2}} \simeq 2.0 \times 10^{-1} \, \mathrm{m\,s^{-1}}, \quad \tau_w \simeq 42 \, \mathrm{Pa}. \tag{1.20}$$

For the Chapter 4 lubricant-depletion experiments, a laminar cylindrical Couette estimate gives at the maximum rotation rate:

$$u_\tau \simeq 4.0 \times 10^{-2} \, \mathrm{m\,s^{-1}}, \qquad \tau_w \simeq 2.6 \, \mathrm{Pa}. \tag{1.21}$$

Under these conditions, riblets in the classical optimal range $\ell^+ \simeq 10$–20, would correspond to physical spacings of order:

$$\ell \simeq 5.0 \times 10^{-5}\text{–}1.0 \times 10^{-4} \, \mathrm{m}. \tag{1.22}$$

Considering the nanostructure of the Teflon-wrinkles surface, the LIS tested and completely described in Chapter 4, it exhibits characteristic dimensions approximately in the range $k \simeq 0.2 - 1\,\mu m$ which corresponds to $k^+ \lesssim 10^{-2}$, indicating that the nanostructure remains deeply sub-viscous throughout the laboratory experiments.
This comparison is included in the present thesis to highlight that neither local nor global quantities are directly comparable to those of a full-scale tanker hull.

1.5.3. Antifouling field evaluation and real-world challenges

To bridge the gap between laboratory-scale characterization and real-world marine deployment, prior field studies have evaluated the environmental resilience, durability limits, and biofouling resistance of hierarchical structured surfaces by exposing them to ocean conditions. Notably, Ware et al. (2018) examined the marine antifouling efficacy of Teflon-Wrinkle surfaces - LIS described and tested in Chapter 4. Their field tests compared three distinct surface configurations: an untreated control, a superhydrophobic surface (SHS), and a liquid-infused surface (LIS).[52] After seven weeks in the ocean, the untreated substrate fouled rapidly, and the SHS showed only marginal improvement. In contrast, the LIS exhibited excellent initial resistance to biofouling, see the next figure. Long-term immersion up to six months, however, revealed that the LIS eventually became completely covered by algae as a direct consequence of progressive lubricant depletion.
The response of Teflon-wrinkle surfaces has been addressed by immersing the samples under static conditions in the ocean, exposing them to contaminants and marine life. The anti-fouling property is not yet ready for immediate application on an operational ship hull; several practical engineering aspects need to be systematically addressed. However, this preliminary study provides strong motivation for systematically investigating the antifouling performance and drag-reduction behavior of these nanostructured surfaces. Upscaling the technology will require optimizing key factors that need to be completely understood to find the best combination.

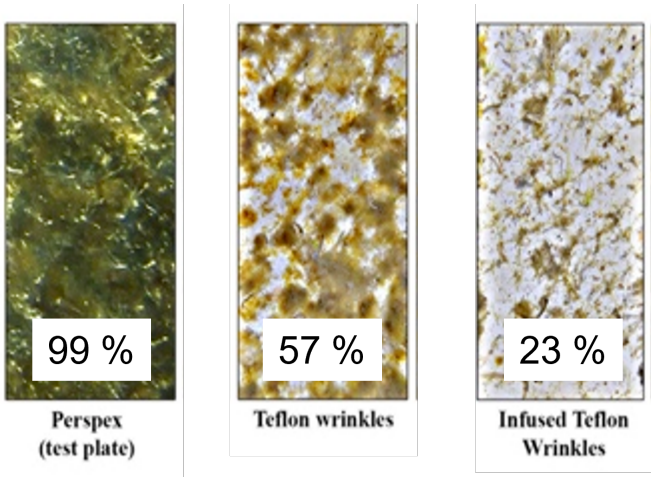

Figure 1.30: Optical images of fouled surfaces, after 7 weeks of testing in the ocean. From left to right: untreated plate, Teflon-Wrinkles plate (SHS), and Infused Teflon-Wrinkles plate (LIS).[52]

1.6. From regular to complex materials: thesis structure

Several key aspects still need to be addressed to bridge the knowledge gap surrounding slippery surfaces for drag-reduction applications. From a numerical perspective, accurately resolving the flow physics in the immediate vicinity of slippery interfaces remains a major challenge. The governing mechanisms are dominated by small-scale, near-wall phenomena that require fully resolved simulations, which are computationally demanding, and intrinsically complex of slippery surfaces, which involve multiphase flow interactions and geometrically intricate textures. From an experimental perspective, a comprehensive understanding of the failure mechanisms is still lacking. In particular, the critical conditions at which a slippery surface begins to lose its effectiveness remain largely unknown.
The present thesis addresses these challenges through a progressive and multi-perspective investigation, starting from idealized textured geometries to more complex, hierarchical materials, as visually represented in the following image.

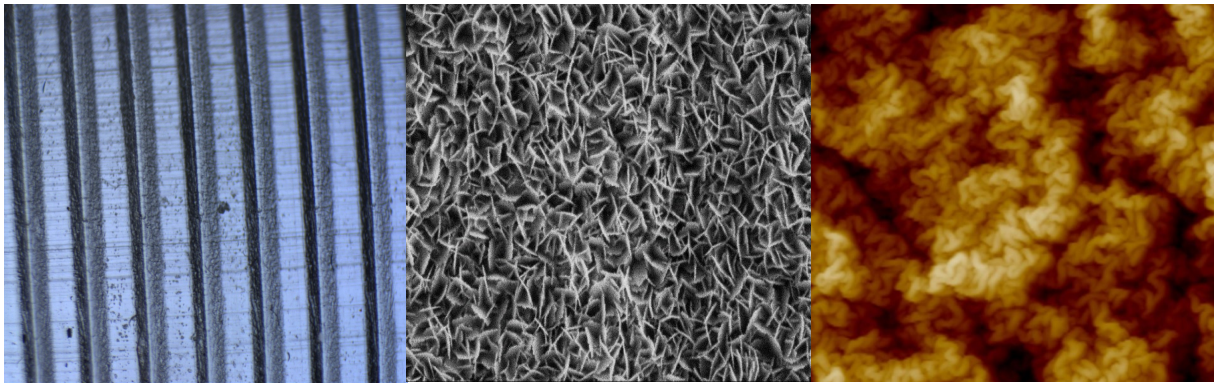

Figure 1.31: From simple to complex surface architectures: periodic trapezoidal grooves (left), an inorganic alumina layer with flower-like microstructures (centre), and nanowrinkled surface features (right).

A novel theoretical model is developed to predict flow characteristics over riblet-textured surfaces, capturing the essential physics while reducing computational cost.
Complementarily, the experimental investigation focuses on periodically grooved surfaces to assess how specific surface patterns influence the onset and evolution of vortical structures in a Taylor–Couette system.
Finally, in order to bridge the gap toward practical applications, lubricant depletion in liquid-infused surfaces is investigated experimentally. A custom-designed meso-scale Taylor–Couette facility is developed to enable direct visualization and quantitative characterization of lubricant dynamics under high-shear conditions. This combined approach provides insight into the coupling between surface morphology, flow structures, and durability, thereby contributing to the development of more reliable and effective drag-reducing surfaces.

Slip-transpiration vortex model for riblets

"There is a need for a universal roughness scale that can describe every type of roughness and be used in any roughflow regimes, including fully rough and transitionally rough regimes".[53]
The interaction between the microscale properties of a slippery surface and the outer flow plays a critical role in determining the overall drag-reduction performance. However, the full numerical resolution of flow features within micro-ribbed geometries entails high computational demands and complexity.
To address this limitation, a novel modeling approach is proposed, enabling the rapid optimization of a wide class of wall-texture configurations without the need for fully resolved simulations.
The method is designed to capture near-wall flow characteristics **beyond the viscous regime**. To this end, a new boundary condition is introduced at a fictitious wall, representing the effective influence of **streamwise-aligned riblets** without explicitly resolving their geometry.
The approach combines a multiscale homogenization technique, properly treating and combining macroscopic and micro-domains, while accounting for advective effects, with a synthetic vortex model that reproduces the transverse flow structures in the near-wall region.
The resulting wall model successfully captures the non-monotonic dependence of skin-friction drag on the riblet spacing, ℓ^+ (defined as riblets' periodicity - in viscous units), including the regime of drag reduction, the subsequent performance degradation, and the eventual drag increase beyond a critical ℓ^+ threshold.

2.1. Introduction

Riblet surfaces represent a well-established and extensively studied passive drag-reduction technology. A wide range of examples of experimental and numerical research has consistently demonstrated their ability to reduce skin-friction drag under turbulent flow conditions. For a given riblet geometry, the drag-reduction performance is typically characterized by a non-monotonic, approximately parabolic dependence on the dimensionless spacing ℓ^+, expressed in viscous units. The existence of an optimal spacing corresponding to maximum drag reduction is therefore well documented and has been extensively investigated over the past decades.
However, the physical mechanisms responsible for the breakdown of the viscous regime and the associated deterioration in performance as ℓ^+ increases beyond its optimal value remain only partially understood.
In particular, recent studies have emphasized the crucial role of advective processes in governing this transition. Advection facilitates the penetration of outer-flow disturbances into the riblet grooves, progressively weakening the ability of the riblet sidewalls to suppress secondary crossflow fluctuations. This process promotes the development of streamwise-oriented vortical structures and enhances momentum exchange in the wall-normal direction, ultimately leading to a degradation of drag-reduction performance.
A particularly insightful analysis of the role of advection in the degradation of drag-reduction performance was proposed by Goldstein and Tuan[54]. Through direct numerical simulations of turbulent flow over surfaces patterned with scalloped riblets, they demonstrated that, as the spanwise spacing of the microstructures increases, a larger ℓ^+ value, the effectiveness to reduce the fluctuation intensity is progressively dampened. This loss of confinement promotes the penetration of transverse motions into the grooves and favors the formation of a stronger secondary streamwise vortical structures both within and above the riblets. The resulting enhancement of vertical momentum transport leads to increased mixing and, consequently, higher drag. Similar counter-rotating vortex pairs were later observed experimentally by Endrikat[55], further supporting this physical interpretation.
These findings provide the primary motivation to develop the present study, improving it by the inclusion of both advective effects and transpiration velocity component in the modeling of flow over riblet surfaces.
In particular, the inspiration has been taken from the approach of Luchini et al.[8], which is adopted and extended. The novel model incorporates a zero-net-mass-flux transpiration boundary condition imposed at a virtual plane located above the riblet tips, enabling the representation of advective exchange between the groove region and the outer flow without resolving the detailed geometry.
The inclusion of advection through the innovative upscaling technique, named adjoint homogenization[15], is a crucial ingredient when the periodicity of the wall texture is sufficiently large. In the very recent work, by Ahmed and Bottaro[56], advection was primarily taken into consideration in porous media and textured walls.
The present work aims to expand and extend the theoretical framework by incorporating the effects of near-wall streamwise vortical structures into the classical concepts of slip length and interfacial permeability. The novel approach seeks to provide a more comprehensive representation of the underlying flow physics at textured surfaces.

2.2. Model description

This section is dedicated to providing the details of the derivation of effective boundary conditions at the fictitious interface between a channel flow and a regularly microstructured wall. A description of the channel flow model is provided, with a discussion of the scales adopted, followed by normalization of the equations in the two domains considered: the inner, or near-wall, domain, and the outer, or bulk, domain.

2.2.1. The upscaling approach

The objective is to develop an approach capable of accurately reproducing near-wall flow features without explicitly resolving the underlying surface microstructure. To this end, a multiscale homogenization technique is employed. It relies on two fundamental ingredients. First, the problem is formulated in terms of two well-separated domains: a microscopic domain, associated with the characteristic length scale of the surface features, and a macroscopic domain, characterized by a larger scale. The clear separation between these scales enables the definition of a small perturbation parameter, called $\delta \ll 1$. It is used to perform a formal expansion of the governing equations of the inner variables by performing an inner-outer matching. This procedure systematically links the microscale physics to the macroscale flow behavior. The central idea is to replace a geometrically complex rough or porous surface with an equivalent smooth, fictitious interface, upon which effective boundary conditions are imposed. These conditions are designed to mimic the net effect of the real surface on the outer flow, thereby significantly reducing computational complexity.
At the microscopic level, the flow is resolved by solving a forced Stokes problem, in which advective effects are incorporated through a modeled representation of near-wall dynamics, namely a synthetic pair of streamwise vortices. This formulation allows the inclusion of key physical mechanisms while maintaining computational tractability. The auxiliary problems are solved for different riblet geometries, yielding effective parameters such as the Navier slip coefficients and the interfacial permeability, which depend explicitly on the shape and size of the surface features.
These microscale solutions are then upscaled to the macroscopic domain through an appropriate matching procedure, leading to a set of effective boundary conditions imposed at the fictitious wall. A crucial aspect of this formulation is that the influence of the microstructure is entirely embedded in these coefficients, allowing complex geometrical effects to be accounted for without direct resolution. Furthermore, the model introduces a wall-normal velocity component in the boundary conditions, thereby capturing transpiration effects. This represents a key improvement over classical approaches, as neglecting wall-normal velocity fluctuations at the virtual interface can lead to significant inaccuracies, particularly when riblets operate beyond the viscous regime.

2.2.2. Domain decomposition and governing equations

The flow configuration considered is a channel flow bounded by a riblet-textured bottom wall and a smooth upper wall. The computational domain corresponds to the free-fluid region above the riblet tips, defining the macroscopic domain of interest. Its dimensions are $L_X \times L_Y \times L_Z = 2\pi H \times 2H \times \pi H$, where H denotes the half-height of the channel. The riblet-textured surface is bounded by black dashed lines that define a virtual plane representing a fictitious smooth wall. At this interface, effective boundary conditions are imposed to account for the presence of the riblets without explicitly resolving their geometry. In this way, the complex microstructure is replaced by an equivalent boundary formulation acting on the outer flow. The microscopic domain is indicated by the red dashed region, which characterizes the riblet geometry and defines the relevant length scale ℓ_g. The surface features are characterized by a spanwise periodicity ℓ and a height H, which govern the texture's geometric properties and ultimately determine the effective coefficients in the macroscopic boundary conditions.

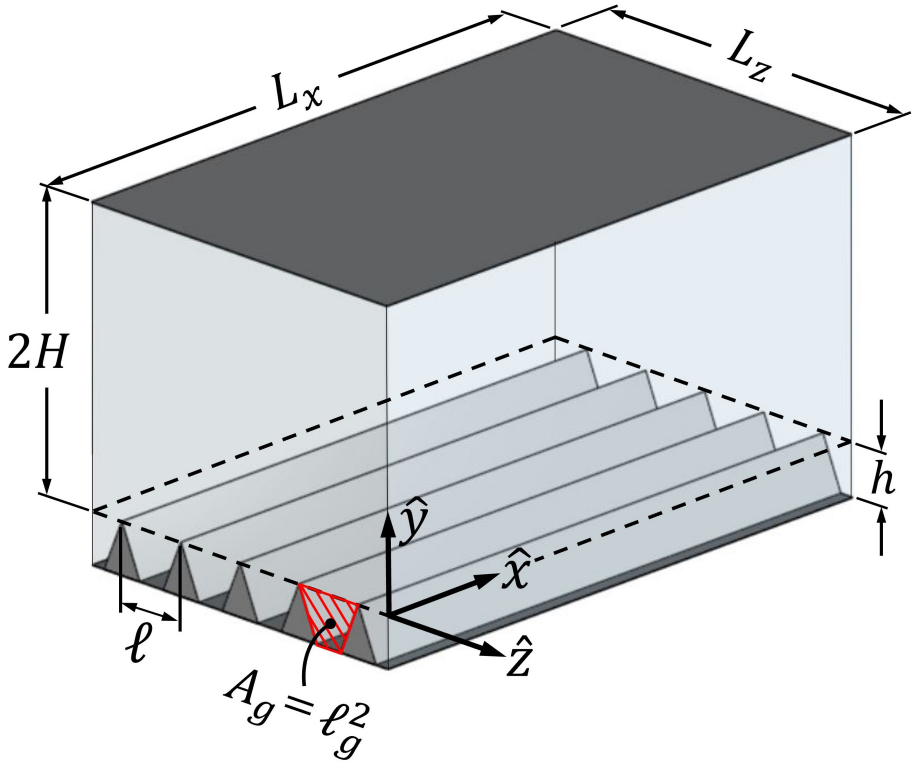

Figure 2.1: Sketch of the macroscopic domain of this study. Streamwise, wall-normal, and spanwise directions correspond to the x-, y-, and z-axes, respectively.

Considering the corrugated wall with regular grooves, they are aligned along the streamwise direction, with a certain periodicity in the spanwise direction, $\hat{x}_3 = \hat{z}$. The other dimensional spatial variables are $\hat{x}_1 = \hat{x}$, streamwise direction, and $\hat{x}_2 = \hat{y}$, wall-normal direction. The longitudinal velocity component is denoted by $\hat{u}_1 = \hat{u}$, the wall-normal component is $\hat{u}_2 = \hat{v}$, and the spanwise velocity component is $\hat{u}_3 = \hat{w}$.

Considering a fully developed turbulent channel flow of total height $2H$, driven by a constant mean pressure gradient $\partial\hat{p}/\partial\hat{x}_1$ applied in the streamwise direction. This pressure gradient balances the total shear stress at the walls and sustains the flow under statistically steady conditions.
The bulk velocity of the flow is denoted by $\hat{u}_{\text{bulk}}$, while a characteristic velocity scale is provided by the friction velocity,

$$u_\tau = \sqrt{\frac{\tau_w}{\rho}} \tag{2.1}$$

where τ_w is the total wall shear stress and ρ is the fluid density. Although in the presence of surface texturing such as riblets, the local wall stress distribution differs from that of a smooth wall, the friction velocity u_τ remains an appropriate scaling parameter for describing the flow dynamics in the outer region, sufficiently far from the wall.
In turbulent channel flows, the mean streamwise velocity profile exhibits a linear behavior in the immediate vicinity of the wall (i.e., within the viscous sublayer). For sufficiently small values of the wall-normal coordinate $\hat{y}$, the streamwise velocity component can therefore be approximated as

$$\hat{u} = \hat{y}\,\frac{\tau_w}{\mu} + \text{constant}, \tag{2.2}$$

where μ is the dynamic viscosity of the fluid. This linear scaling provides the basis for defining inner (viscous) units and serves as a reference for assessing deviations induced by surface modifications such as riblets. The constant in eq. (2.2) is related to the position chosen for the $\hat{y} = 0$ plane whenever the solid surface is micro-textured; for a smooth wall, the constant vanishes on account of the no-slip condition.

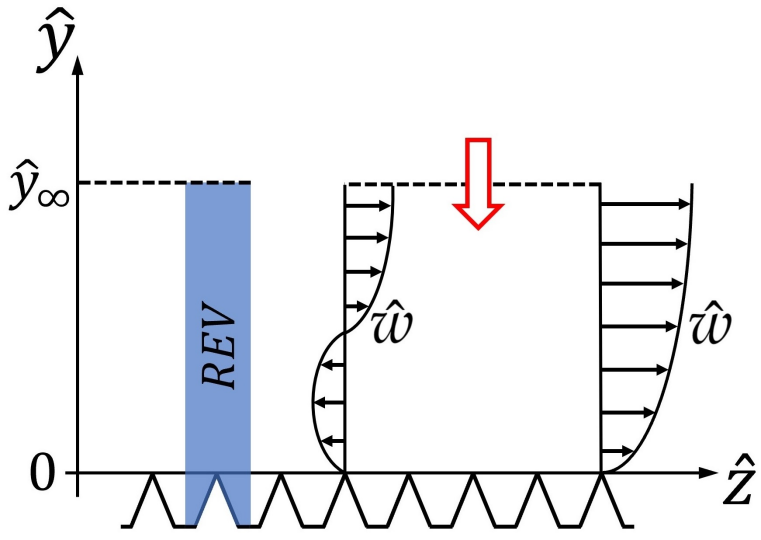

Figure 2.2: Schematic of the representative elementary volume (*REV*), highlighted in blue. It determines the coefficients of the effective boundary conditions. The red arrow illustrates a wall-normal velocity component at $\hat{y}_\infty$

The microscopic domain is schematically illustrated in Fig. 2.2. The blue rectangle denotes the representative elementary volume (REV), which corresponds to the fundamental periodic unit of the riblet geometry and is assumed to be representative of the entire textured surface. The governing equations of the microscopic problem are solved within this domain, enabling the systematic extraction of the coefficients entering the effective boundary conditions.
The REV domain simplified the complex geometrical features of the riblets to be accounted for at the microscale, while their net effect on the outer flow is transferred to the macroscale through homogenization. In this framework, the effective parameters (e.g., slip and permeability coefficients) are directly linked to the geometry and size of the surface features.
The sketch illustrates the emergence of a wall-normal velocity component at $\hat{y} \to \infty$ (indicated by the red arrow). This effect arises from spanwise gradients of the velocity component $\hat{w}$ and/or streamwise gradients of $\hat{u}$ within the microscopic domain. These gradients induce a net vertical flux, which results at the macroscopic level as a transpiration velocity in the effective boundary conditions.
The next step in the upscaling procedure consists of introducing the relevant physical length scales of the problem, which is essential to formally establish the separation of scales. This allows for a consistent estimation of the relative magnitude of the various terms appearing in the governing equations. On this basis, an appropriate non-dimensionalization can be carried out, ensuring that the equations are properly rescaled and amenable to asymptotic analysis.

Definition of scale

A qualitative identification of an appropriate microscopic length scale can be approached based on the interaction between the textured surface and the outer turbulent flow, in order to point out the limitations and validity of the proposed scaling.
As discussed previously, the near-wall dynamics are characterized by quasi-streamwise vortical structures, which may partially penetrate into the riblet grooves. The penetration depth of these overlying coherent structures can be reasonably assumed to be of an order of magnitude of the transverse slip length. For a wide range of textured surfaces, this characteristic length is significantly smaller than the spanwise periodicity ℓ of the pattern. Aiming for scaling arguments, the microscopic characteristic length $\tilde{\ell}$ one may therefore assume:

$$\tilde{\ell} \sim \frac{\ell}{\alpha}, \tag{2.3}$$

where α is a constant that can be taken to be approximately 15.
The macroscopic length scale, denoted by $\tilde{\mathcal{L}}$, is instead associated with the characteristic size of the near-wall coherent structures, typically corresponding to quasi-streamwise vortices. These structures have a length scale of about 15-20 units of length in viscous units[57,58], and can therefore be expressed as:

$$\tilde{\mathcal{L}} \sim \alpha \, \frac{\nu}{u_\tau}, \tag{2.4}$$

where ν is the kinematic viscosity and u_τ the friction velocity.
The ratio between the microscopic and macroscopic scales then reads

$$\frac{\tilde{\ell}}{\tilde{\mathcal{L}}} \sim \frac{\ell^+}{\alpha^2} = \alpha^{-2}\,\frac{\ell}{h}\,h^+, \tag{2.5}$$

where the superscript $(\cdot)^+$ denotes normalization in wall units, and h is the riblet height (see Fig. 2.1). In the present study, the geometric ratio ℓ/h does not exceed 2, implying that its product with α^{-2} remains typically below 10^{-2}.
The parameter $h^+ = hu_\tau/\nu$ represents the roughness Reynolds number, which is commonly used to distinguish between different flow regimes: hydrodynamically smooth ($h^+ \lesssim 5$), transitional ($5 \lesssim h^+ \lesssim 70$), and fully rough ($h^+ \gtrsim 70$). Restricting attention to the so-called *lower transitional roughness* regime[59], with $h^+ \lesssim 15$, the scale separation parameter $\tilde{\ell}/\tilde{\mathcal{L}}$ remains bounded by approximately 0.1. This value is sufficiently small to justify the applicability of a multiple-scale homogenization approach.
Under these conditions, the riblet spacing should be limited to approximately $\ell^+ \lesssim 30$ to preserve a clear separation of scales.
Based on direct numerical simulations results of the present study, employing model interface conditions, a *a posteriori* validation in combination with an experimental comparison and fully resolved simulations, remains a requirement to assess the validity of this assumption up to $\ell^+ \approx 30$.
After having quantified the characteristic length scales, the next step involves an assessment of the velocity magnitude in the proximity of the patterned wall and at some distance from it. This constitutes the basis for evaluating the relative contributions of viscous and advective terms in the microscopic Navier–Stokes equations, thereby providing a rigorous justification for the possible neglect of one of these terms in the subsequent modeling.
The outer velocity magnitude can be evaluated by equation (2.2) as being of order $\tilde{\mathcal{L}}\,\frac{\tau_w}{\mu} = \alpha u_\tau$. For shear stress to match at the outer boundary $\hat{y}_\infty$ of the representative elementary volume (cf. fig. 3.5) the inner velocity scale must be equal to about $\frac{\tilde{\ell}}{\tilde{\mathcal{L}}}\,\alpha\,u_\tau$. The microscopic advective term $\hat{u}_j \dfrac{\partial \hat{u}_i}{\partial \hat{x}_j}$ is thus $\mathcal{O}(\alpha^2 \dfrac{\tilde{\ell}\,u_\tau^2}{\tilde{\mathcal{L}}^2})$, while the viscous term $\nu\,\hat{\nabla}^2\hat{u}$ is $\mathcal{O}(\alpha\,\dfrac{\nu u_\tau}{\tilde{\mathcal{L}}\,\tilde{\ell}})$. Normalization of the Navier-Stokes equation yields a dimensionless number in front of the advective term, which is given by:

$$\alpha^{-2}\,\left[\frac{\ell\,u_\tau}{\nu}\right]^2 = \left[\frac{1}{\alpha}\left(\frac{\ell}{h}\right)\,h^+\right]^2. \tag{2.6}$$

The quantity above remains sufficiently small only for values of h^+ on the order of a few viscous length units, meaning that the conventional approach based on the Stokes approximation of the equations for the derivation of slip lengths[8] loses validity outside the hydrodynamically smooth regime. When h^+ reaches the value of 15, the dimensionless parameter in equation (2.6) is of order one. This implies that, although a separation of scales may still be used, the nonlinear advective term can no longer be considered negligible.
After this qualitative discussion on scales, crucial for a preliminary evaluation of the limitations and validity of the proposed approach, the formal analysis can be developed, eliminating the

empirical coefficient α from the scaling parameters, but keeping in mind the estimated magnitude of the different terms in the equations.
In practice, the microscale is typically on the order of one viscous unit or smaller, while the macroscale is of the order of 15–20 viscous units; therefore, a clear separation of scales can be expected. However, for the purpose of implementing a multiple-scale approach, it is convenient to simply identify ℓ as the "small scale" and $\mathcal{L} = \nu/u_\tau$ as the "large scale", and to expand the inner dependent variables in terms of the gauge factor δ, defined as follows:

$$\delta = \frac{\ell}{\mathcal{L}} = \frac{u_\tau \ell}{\nu}, \tag{2.7}$$

with ν the kinematic viscosity.
Two velocity scales should also be introduced. The tangential velocity of the quasi-streamwise vortices is of the order of the friction velocity; thus, we fix $\hat{u}_{outer} = u_\tau$. Finally, since the near-wall velocity scales as

$$\hat{u}_{inner} \sim \ell \frac{\tau_w}{\mu} \;\rightarrow\; \hat{u}_{inner} = \delta\, u_\tau. \tag{2.8}$$

The tangential velocity of near-wall quasi-streamwise vortices is of the order of the friction velocity; thus, by setting $\hat{u}_{outer} = u_\tau$, it is immediate to recover the dimensionless gauge factor δ to be used in the expansion of the inner dependent variables:

$$\delta = \frac{u_\tau \tilde{\ell}}{\nu} = \frac{\tilde{\ell}}{\mathcal{L}}, \tag{2.9}$$

with ν the kinematic viscosity of the fluid. This shows that the outer scale $\mathcal{L}$ coincides with the usual + unit-of-length of wall-bounded turbulence.
To summarise, the governing scales can be explicitly delineated as follows:
Macroscopic scales

- $\dfrac{\nu}{u_\tau}$ length scale
- u_τ velocity scale
- $\rho\, u_\tau^2$ pressure scale
- $\dfrac{\nu}{u_\tau^2}$: time scale

Microscopic scales

- ℓ: length scale
- u_{inner}: velocity scale
- $\dfrac{\mu\, u_{inner}}{\ell}$: viscous pressure scale
- $\dfrac{u_{inner}}{\ell}$: time scale

To define the outer region of the domain, the so-called macroscopic domain, the following variables are indicated with the superscript "$\mathcal{O}$". Using the superscript "$\mathcal{I}$", on the other hand, denotes the inner region - microscopic domain. The normalized variables in the two regions, based on the previous scales, are the following:

Outer region $^{\mathcal{O}}$*:*

$$X_i = \frac{\hat{x}_i u_\tau}{\nu}, \quad U_i^{\mathcal{O}} = \frac{\hat{u}}{u_\tau}, \quad P^{\mathcal{O}} = \frac{\hat{p}}{\rho u_\tau^2}, \quad t^{\mathcal{O}} = \frac{\hat{t} u_\tau^2}{\nu}. \tag{2.10}$$

Inner region $^{\mathcal{I}}$*:*

$$x_i = \frac{\hat{x}_i}{\ell}, \quad U_i^{\mathcal{I}} = \frac{\hat{u}}{\hat{u}_{inner}}, \quad P^{\mathcal{I}} = \frac{\hat{p}\,\ell}{\mu\,\hat{u}_{inner}}, \quad t^{\mathcal{I}} = \frac{\hat{t}\,\hat{u}_{inner}}{\ell}, \tag{2.11}$$

Governing equations

The differential equations relevant to this study are summarized below. The flow of a viscous, incompressible, Newtonian fluid is governed by the mass and momentum conservation equations:

$$\frac{\partial \hat{u}_i}{\partial \hat{x}_i} = 0, \quad \left(\frac{\partial \hat{u}_i}{\partial \hat{t}} + \hat{u}_j \frac{\partial \hat{u}_i}{\partial \hat{x}_j}\right) = -\frac{1}{\rho}\frac{\partial \hat{p}}{\partial \hat{x}_i} + \nu \frac{\partial^2 \hat{u}_i}{\partial \hat{x}_j^2}. \tag{2.12}$$

where $\hat{t}$ is the dimensional time variable.
The normalization described above leads to the following dimensionless systems for the two subdomains:

$$\frac{\partial U_i^{\mathcal{O}}}{\partial X_i} = 0, \quad \frac{\partial U_i^{\mathcal{O}}}{\partial t} + U_j^{\mathcal{O}} \frac{\partial U_i^{\mathcal{O}}}{\partial X_j} = -\frac{\partial P^{\mathcal{O}}}{\partial X_i} + \frac{\partial^2 U_i^{\mathcal{O}}}{\partial X_j^2}, \tag{2.13}$$

$$\frac{\partial U_i^{\mathcal{I}}}{\partial x_i} = 0, \quad Re_{inner}\left(\frac{\partial U_i^{\mathcal{I}}}{\partial t} + U_j^{\mathcal{I}} \frac{\partial U_i^{\mathcal{I}}}{\partial x_j}\right) = -\frac{\partial P^{\mathcal{I}}}{\partial x_i} + \frac{\partial^2 U_i^{\mathcal{I}}}{\partial x_j^2}. \tag{2.14}$$

In the outer region of the flow, far from the microgrooved wall, all information related to the microstructural details is effectively lost. In contrast, variables in the inner region are assumed to depend on both ℓ and $\mathcal{L}$. The factor that multiplied the convective term in Eq. (2.14) is the microscopic Reynolds number,

$$Re_{inner} = \frac{\hat{u}_{inner}\,\ell}{\nu}; \tag{2.15}$$

it coincides with the square of the gauge factor $\delta = \ell/\mathcal{L}$ which can also take the form

$$\delta = \epsilon Re_\tau = \ell^+, \tag{2.16}$$

with $\epsilon = \ell/H$, $Re_\tau = u_\tau H/\nu$ the friction Reynolds number in the plane channel and ℓ^+ the riblets' spacing measured in viscous units.
Inner velocity and pressure fields are now expanded in powers of δ as

$$\Phi^{\mathcal{I}} = \phi^{(0)} + \delta\,\phi^{(1)} + \delta^2\,\phi^{(2)} + ..., \tag{2.17}$$

with $\Phi^{\mathcal{I}}(t, x_i, X_i)$ which represents either $P^{\mathcal{I}}$ or $U_i^{\mathcal{I}}$. The inner variables are functions of both microscopic and macroscopic spatial coordinates; the chain rule $\dfrac{\partial}{\partial x_i} \rightarrow \dfrac{\partial}{\partial x_i} + \delta \dfrac{\partial}{\partial X_i}$ must be adopted when expressing spatial derivatives.

2.3. The microscopic model

In the present model, the microscopic Reynolds number is treated as an independent parameter, deliberately neglecting in Eq. (2.14) the fact that Re_{inner} can be expressed as the product of δ times ℓ^+.
This choice reflects the formal definition of $\ell\, u_\tau/\nu$; in practice, an arbitrary scaling factor α could be introduced to ensure δ remains small. The reason behind this approach is analogous to the methodology employed in the linear stability analysis of slowly spatially evolving flows; a more detailed description is in the relative paper[60].
As argued in Section 2.2.2., convective terms become non-negligible when h^+ and ℓ^+ exceed a few viscous units.
Accordingly, as a primary innovative aspect of the model, advective effects are considered in the inner-region equations. Governing equations at the leading order become as follows:

$$\frac{\partial u_i^{(0)}}{\partial x_i} = 0, \qquad \delta\ell^+ \left(\frac{\partial u_i^{(0)}}{\partial t} + u_j^{(0)} \frac{\partial u_i^{(0)}}{\partial x_j} \right) + \frac{\partial p^{(0)}}{\partial x_i} - \frac{\partial^2 u_i^{(0)}}{\partial x_j^2} = 0. \tag{2.18}$$

By setting $\delta\ell^+ = 0$ and neglecting the convective term, the governing equations reduce to a Stokes-like system, which has already been solved by Bottaro and Naqvi[61].
The system of equations (2.18) defines the microscopic boundary-value problems to be solved numerically within the representative elementary volume (*REV*) shown in Fig. 2.2.
These problems are addressed using COMSOL Multiphysics, where an appropriate computational domain is defined to examine a range of riblet geometries. The boundary conditions consist of periodicity along the directions parallel to the surface (at $y = 0$), together with a no-slip condition imposed at the impermeable wall located at $y = y_{\text{wall}}$.
Particular attention must be devoted to the asymptotic conditions as $y \to \infty$, as these ultimately determine the macroscopic effective boundary conditions applied at the virtual wall ($Y = 0$).
The subsequent section details the remaining steps of the multiscale procedure. First, a rigorous matching between the inner (microscopic) and outer (macroscopic) equations is established, ensuring that the influence of the microgrooved surface is consistently considered. Next, the macroscopic problem is developed, accounting in particular for the transpiration velocity. Finally, this procedure leads to the derivation of effective boundary conditions expressed in terms of microscopically coefficients.

2.4. Matching between inner and outer domains

Velocity conditions

Continuity of the domains between the $\bullet^{\mathcal{O}}$ and $\bullet^{\mathcal{I}}$ regions, across the interface, is imposed by matching both velocity and traction vectors at a virtual surface over the riblets' tip. Denoting by y_∞ the inner vertical coordinate of this surface (see Fig. 2.2), the corresponding position in outer variables is given by $Y_\infty = \delta\, y_\infty$.
In nondimensional form, accounting for the respective scalings of inner and outer variables, the velocity matching conditions can be expressed as follows, considering the gauge factor δ:

$$\langle U_i^{\mathcal{I}} \rangle \big|_{y=y_\infty} = \frac{1}{\delta}\, U_i^{\mathcal{O}}(t, X, Y_\infty, Z), \tag{2.19}$$

By using Taylor expansion of the outer variable $U^{\mathcal{O}}$ around $Y = 0$, the matching condition (2.19) can be further modified to eventually yield the macroscopic velocity at the virtual wall,

$$U_i^{\mathcal{O}}(t, X, Y_\infty, Z) = U_i^{\mathcal{O}}(t, X, 0, Z) + \delta\, y_\infty \frac{\partial U_i^{\mathcal{O}}}{\partial Y}\bigg|_{Y=0} + \delta^2\, \frac{y_\infty^2}{2} \frac{\partial^2 U_i^{\mathcal{O}}}{\partial Y^2}\bigg|_{Y=0} + ..., \tag{2.20}$$

eventually, rewriting the equation by collecting terms of the same order, it leads to the following expression:

$$U_i^{\mathcal{O}}(t, X, 0, Z) = \delta \left(\langle u_i^{(0)} \rangle \big|_{y=y_\infty} - y_\infty \frac{\partial U_i^{\mathcal{O}}}{\partial Y}\bigg|_{Y=0} \right) + \delta^2 \left(\langle u_i^{(1)} \rangle \big|_{y=y_\infty} - \frac{y_\infty^2}{2} \frac{\partial^2 U_i^{\mathcal{O}}}{\partial Y^2}\bigg|_{Y=0} \right) + ... \tag{2.21}$$

Shear conditions

The shear stress matching conditions, properly defined to account for the respective scalings of inner and outer variables, can be expressed as follows:

$$\langle -P^{\mathcal{I}}\, \delta_{i2} + \frac{\partial U_2^{\mathcal{I}}}{\partial x_i} + \frac{\partial U_i^{\mathcal{I}}}{\partial y} \rangle \bigg|_{y=y_\infty} = \mathcal{S}_{i2}(t, X, Y_\infty, Z), \tag{2.22}$$

with δ_{ij} the Kronecker index and $\mathcal{S}_{i2} = \boldsymbol{\sigma} \cdot \boldsymbol{e}_2 = -P^{\mathcal{O}} \delta_{i2} + \dfrac{\partial U_2^{\mathcal{O}}}{\partial X_i} + \dfrac{\partial U_i^{\mathcal{O}}}{\partial Y}$ the outer traction vector, $\boldsymbol{\sigma}$ being the stress tensor. The symbol $\langle \cdot \rangle$ denotes surface averaging over x and z, across the microscopic *REV*, at any given y. However, assuming that y_∞ is sufficiently far from y_{wall} for the order zero, it becomes invariant in x and z; it can be simplified, yielding to the following matching boundary conditions:

$$-p^{(0)}\, \delta_{i2} + \frac{\partial u_2^{(0)}}{\partial x_i} + \frac{\partial u_i^{(0)}}{\partial y}\bigg|_{y=y_\infty} = \mathcal{S}_{i2}\big|_{Y=Y_\infty}. \tag{2.23}$$

This equation (2.23) is used along the direction $i = 1$ and $i = 3$, i.e., to evaluate the slip components of the velocity at the virtual wall. For the wall-normal component (the so-called *transpiration velocity* at $Y = 0$), a different approach is employed, as discussed later.
Summarizing, the microscopic problem to be solved in the *REV* is thus formed by equations (2.18) with no-slip conditions at the wall, periodicity along x and z, plus condition (2.23) at y_∞.

2.4.1. Adjoint homogenization

Adjoint homogenization procedure is a multiscale technique that introduces an inner product between two functions a and b , over the representative element of volume, following this definition:

$$\int_{y_{wall}}^{y_\infty} \langle\, a\, b \,\rangle \, \mathrm{d}y. \tag{2.24}$$

The inner–outer matching conditions were introduced in the previous section; to ensure a consistent and rigorous coupling between the two fields, an adjoint homogenization framework[15] is employed.
This approach enables the systematic closure of the matching problem by linking the microscale solutions to the macroscopic description through appropriately defined adjoint fields.
By considering the inner product of the continuity equation in (2.18) with the test vector $p_j^\dagger$ and subtracting this from the inner product of the test tensor $u_{ji}^\dagger$ with the momentum equation, the following system of equations is obtained:

$$\begin{aligned} 0 &= \int_{y_{wall}}^{y_\infty} \langle\, p_j^\dagger \frac{\partial u_i^{(0)}}{\partial x_i} - u_{ji}^\dagger \left[\delta\ell^+ \left(\frac{\partial u_i^{(0)}}{\partial t} + u_k^{(0)} \frac{\partial u_i^{(0)}}{\partial x_k} \right) + \frac{\partial p^{(0)}}{\partial x_i} - \frac{\partial^2 u_i^{(0)}}{\partial x_k^2} \right] \rangle \, \mathrm{d}y \\ &= \int_{y_{wall}}^{y_\infty} \langle\, \frac{\partial u_{ji}^\dagger}{\partial x_i} p^{(0)} + \left[\delta\ell^+ \left(\frac{\partial u_{ji}^\dagger}{\partial t} + u_k^{(0)} \frac{\partial u_{ji}^\dagger}{\partial x_k} \right) - \frac{\partial p_j^\dagger}{\partial x_i} + \frac{\partial^2 u_{ji}^\dagger}{\partial x_k^2} \right] u_i^{(0)} \rangle \, \mathrm{d}y \\ &\qquad - \frac{\mathrm{d}}{\mathrm{d}t} \int_{y_{wall}}^{y_\infty} \langle\, u_{ji}^\dagger \, u_i^{(0)} \,\rangle \, \mathrm{d}y + \text{“boundary terms”}. \end{aligned} \tag{2.25}$$

Considering the test functions $u_{ji}^\dagger$ and $p_j^\dagger$ as solutions of

$$\frac{\partial u_{ji}^\dagger}{\partial x_i} = 0, \qquad -\delta\ell^+ \left(\frac{\partial u_{ji}^\dagger}{\partial t} + u_k^{(0)} \frac{\partial u_{ji}^\dagger}{\partial x_k} \right) = -\frac{\partial p_j^\dagger}{\partial x_i} + \frac{\partial^2 u_{ji}^\dagger}{\partial x_k^2}, \tag{2.26}$$

with the normalizing constraint that the term $\int_{y_{wall}}^{y_\infty} \langle\, u_{ji}^\dagger \, u_i^{(0)} \,\rangle \, \mathrm{d}y$ is time-invariant[62].
Appropriate boundary conditions are imposed: periodicity in the horizontal directions, zero velocity at the wall, and a closure condition at the outer boundary. This formulation provides an explicit relation between the averaged microscopic velocity and the macroscopic strain rate, consistent with standard homogenization assumptions. In the Stokes limit, the problem simplifies significantly and can be solved numerically, yielding auxiliary (adjoint) fields that determine the effective macroscopic behavior.

In the limit $Re_{inner} = \delta\ell^+ = 0$, the flow reduces to the creeping flow condition. Taking into account the streamwise invariance of the riblet geometry, the problem can be formulated as two-dimensional in the (y, z) plane, and system (2.26) simplifies to an uncoupled Stokes–Laplace problem.
The numerical solution can be obtained using a finite-element approach (e.g., FreeFEM++) and/or COMSOL Multiphysics. By employing FreeFEM++, a piecewise quadratic (P_2) element

for the velocity components and linear elements for the adjoint pressure $p_j^\dagger$. The computational domain is discretized with an unstructured mesh of up to 2×10^5 triangular elements, with local refinement near the solid boundary to ensure grid convergence. To guarantee the uniqueness of the solution, a normalization condition is imposed by enforcing a zero spatial average of $p_j^\dagger$ over the domain.
On the other hand, the coefficient form PDE interface in COMSOL Multiphysics is a versatile tool for defining linear and nonlinear partial differential equations, including diffusion and convection terms. It allows the user to specify the coefficients that activate a specific part of the differential equations, providing a flexible control over model parameters and dependent variables. An *extremely fine* mesh is chosen to resolve equations in the domain accurately.

For equilateral triangular riblets extending infinitely in the streamwise direction, the computed adjoint (auxiliary) fields display a clear asymptotic behavior at the outer boundary y_∞. Specifically, the components $\langle u_{11}^\dagger \rangle$ and $\langle u_{33}^\dagger \rangle$ approach uniform values that match their pointwise values at y_∞, while all other components of $u_{ji}^\dagger$ decay to zero, provided the computational domain height satisfies $y_\infty \gtrsim 2$. The following table shows only the non-zero auxiliary fields' values in the Stokes approximation, evaluated at the upper boundary of the representative element of volume in the case of equilateral triangular riblets. The values of $u_{11}^\dagger$ and $u_{33}^\dagger$ are uniformly increasing with y_∞ value. Each value differs from one spanwise position to any other one only in the sixth significant digit, which doesn't have a physical meaning. These numbers reported are obtained by evaluating $u_{11}^\dagger$ and $u_{33}^\dagger$ through z-averaging along the domain, at each $y = y_\infty$. These numerical values show and prove the independence from the height of the microscopic domain.

Table 2.1: Non-zero ${u_{ji}}^\dagger$ components evaluated at different y_∞, showing that a domain larger than 2 units provides sufficient distance from the micro-element to correctly solve microscopic equations.

$u_{11}^\dagger\big\vert_{y_\infty=4}$	$u_{11}^\dagger\big\vert_{y_\infty=5}$	$u_{11}^\dagger\big\vert_{y_\infty=6}$	$u_{11}^\dagger\big\vert_{y_\infty=7}$	$u_{33}^\dagger\big\vert_{y_\infty=4}$	$u_{33}^\dagger\big\vert_{y_\infty=5}$	$u_{33}^\dagger\big\vert_{y_\infty=6}$	$u_{33}^\dagger\big\vert_{y_\infty=7}$
4.170660	5.170675	6.170678	7.170673	4.080549	5.080515	6.080529	7.080513

With the above results, the variables of the problem at first order can be defined as:

$$\langle\, u_1^{(0)} \,\rangle\Big|_{y_\infty} = u_1^{(0)}\Big|_{y_\infty} = u_{11}^\dagger\Big|_{y_\infty} S_{12}\big|_{Y_\infty}, \tag{2.27}$$

$$\langle\, u_2^{(0)} \,\rangle\Big|_{y_\infty} = u_2^{(0)} = 0, \tag{2.28}$$

$$\langle\, u_3^{(0)} \,\rangle\Big|_{y_\infty} = u_3^{(0)}\Big|_{y_\infty} = u_{33}^\dagger\Big|_{y_\infty} S_{32}\big|_{Y_\infty}, \tag{2.29}$$

when y_∞ is sufficiently far from the tip of the ribs.

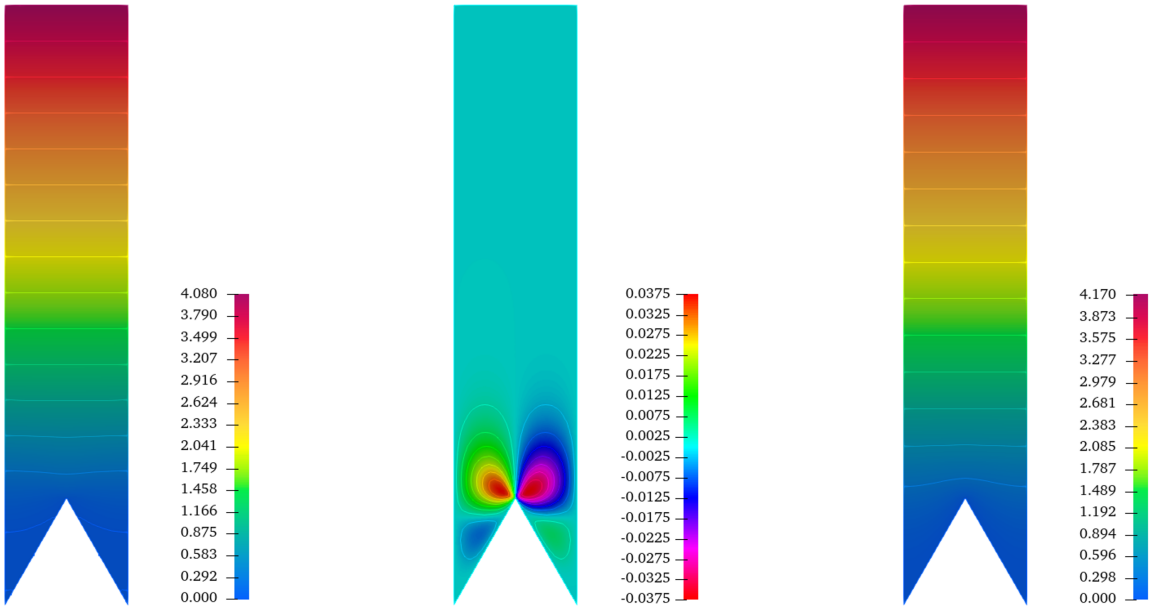

Figure 2.3: Some steady auxiliary fields for equilateral triangular riblets. From left to right, isocontours of $u^\dagger_{33}$, $u^\dagger_{23}$ and $u^\dagger_{11}$.

2.4.2. Navier slip lengths and Interface permeability coefficients

Based on the previously derived microscopic equations, the complete solution of the inner problem allows for the systematic characterization of the microscale behavior within the domain. In particular, this procedure enables the identification and quantification of the effective microscopic properties governing the local dynamics. These properties can be consistently upscaled and incorporated into the macroscopic formulation, thereby establishing a rigorous coupling between the microscopic and macroscopic descriptions of the problem.
The *Navier slip lengths* are defined as the difference between the non-zero auxiliary components $u^\dagger_{11}$ and $u^\dagger_{33}$ and the height of the microscopic domain y_∞. The definitions are the following:

$$\begin{aligned} \lambda_x &= u^\dagger_{11}|_{y_\infty} - y_\infty \\ \lambda_z &= u^\dagger_{33}|_{y_\infty} - y_\infty \end{aligned} \tag{2.30}$$

The *interface permeability coefficients* are defined as follows:

$$\begin{aligned} \mathcal{K}^{itf}_{xy} &= [m_{11}(y_\infty + \lambda_x) - y_\infty \lambda_x - y^2_\infty/2] \\ \mathcal{K}^{itf}_{zy} &= [m_{33}(y_\infty + \lambda_z) - y_\infty \lambda_z - y^2_\infty/2] \end{aligned} \tag{2.31}$$

with m_{11} and m_{33} that represent the average of the auxiliary variables along the whole microdomains,

$$m_{11} = \frac{1}{u^\dagger_{11}|_{y_\infty}} \int_{y_{wall}}^{y_\infty} \int_0^1 u^\dagger_{11}\, dz\, dy, \qquad m_{33} = \frac{1}{u^\dagger_{33}|_{y_\infty}} \int_{y_{wall}}^{y_\infty} \int_0^1 u^\dagger_{33}\, dz\, dy. \tag{2.32}$$

Section 2.5.1. provides a detailed derivation of the governing equations leading to the definition of the interface permeability coefficients. It clarifies their role and physical interpretation, highlighting how they characterize wall-normal fluctuations as a function of the underlying microstructural properties of the surface.
The microscopic problem has been addressed by systematically analysing seven distinct riblet geometries, which are illustrated in Fig. 2.4.
A schematic representation of these configurations is provided in the y–z plane, highlighting the characteristic cross-sectional profiles of the surface patterns. For all the considered geometries, the base dimension of the groove along the z-direction is kept constant and is denoted by ℓ, which defines the periodicity of the roughness element.
The remaining geometrical parameters are expressed in a dimensionless form relative to ℓ, thereby ensuring a consistent parametrization and facilitating a direct comparison among the different riblet shapes.

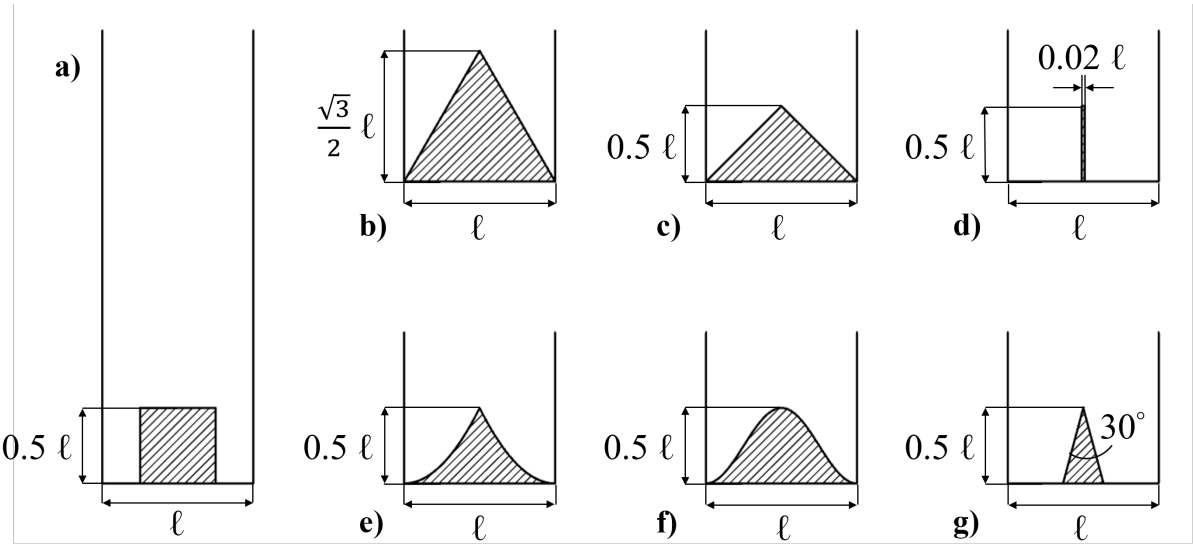

Figure 2.4: Riblets' shapes: square (a), equilateral triangle (b), right triangle (c), blade (d), parabolic/scalloped (e), cosine (f), trapezoidal (g).

Table 2.2: Effective coefficients for the riblets' shapes in figure 2.4, in the Stokes limit ($Re_{inner} = 0$).

Riblets' shape	λ_x	λ_z	$\mathcal{K}_{xy}^{itf}$	$\mathcal{K}_{zy}^{itf}$	$\Delta\lambda = \lambda_x - \lambda_z$	ℓ_g/ℓ
Square	0.0415	0.0179	0.0058	0.0004	0.0236	0.5000
Equilateral triangle	0.1707	0.0805	0.0282	0.0058	0.0901	0.7530
Right triangle	0.1397	0.0779	0.0168	0.0058	0.0618	0.5000
Blade	0.1915	0.0784	0.0379	0.0046	0.1131	0.7000
Parabolic/scalloped	0.1699	0.0804	0.0259	0.0060	0.0894	0.5773
Cosine	0.1141	0.0638	0.0140	0.0042	0.0503	0.4262
Trapezoidal	0.1912	0.0820	0.0348	0.0054	0.1091	0.6830

The coefficients of interest are reported in Table 2.2. The results are believed to be accurate up to the last significant digit reported.
The parameter ℓ_g reported in Table 2.2 is defined as the square root of the groove cross-sectional area A_g, as illustrated in Fig. 2.4.
This quantity represents a purely geometrical parameter, originally introduced by Garc'ia-Mayoral and Jim'enez[63], to simultaneously account for the effects of both riblet spacing and shape within a single characteristic length scale.
In more recent experimental and numerical studies, it has become standard practice to express drag reduction as a function of ℓ_g^+, i.e., the groove length scale normalized in viscous units. This choice is motivated by the observation that such a scaling leads to an improved collapse of the data onto a nearly universal curve across a wide range of conventional riblet geometries. In particular, this behavior is most evident for configurations characterized by well-defined, open grooves that are fully exposed to the outer flow.
The parameter $\Delta\lambda^+$ is calculated in the table 2.2, as the difference between the two slip lengths $\lambda_x^+ - \lambda_z^+$. The skin-friction drag is known to be linearly proportional to riblets periodicity, in the viscous regime, so when ℓ^+ has only a few viscous units.[23]
As mentioned before, Luchini[26] has shown that the reduction in skin friction coefficient DR with respect to the smooth-wall value is proportional to $\Delta\lambda^+$, according to (1):

$$DR = \frac{C_f - C_{f_0}}{C_{f_0}} = -\frac{\Delta U^+}{(2\,C_{f_0})^{-1/2} + (2\,\kappa)^{-1}} = -\frac{\mu_0\,\Delta\lambda^+}{(2\,C_{f_0})^{-1/2} + (2\,\kappa)^{-1}} \tag{2.33}$$

with μ_0 a constant close to one.
From the numerical results reported in Table 2.2, it is evident that the highest value of $\Delta\lambda^+$, which directly correlates with the maximum drag reduction, is obtained for the blade riblet configuration among the geometries considered. This observation is consistent with the experimental results of Bechert et al.[23]. It can therefore be inferred that, at least within the viscous regime, riblets characterized by smaller thickness exhibit superior drag-reducing performance.
However, to accurately assess the flow behaviour for values of ℓ^+ exceeding approximately 10 - particularly in the regime where drag reduction progressively deteriorates and may eventually transition into drag increase[63] - it becomes necessary to account for additional terms. In this context, the effects of advection and transpiration within the grooves play a crucial role and must be properly incorporated into the analysis.
The approach for resolving the microscopic domain has been described in detail. The next step is to formulate the macroscopic boundary conditions that account for the transpiration velocity component at the interface. By developing these boundary relations, one can obtain complete and consistent definitions of effective microscopic coefficients, such as the Navier slip lengths and the interface permeability coefficients.

2.5. Macroscopic boundary conditions

The equation (2.34), reported below, describes the outer variables $U^{\mathcal{O}}$, by accounting for the microscopic properties:

$$U_i^{\mathcal{O}}(t,X,0,Z) = \delta\left(\langle u_i^{(0)}\rangle\big|_{y=y_\infty} - y_\infty \frac{\partial U_i^{\mathcal{O}}}{\partial Y}\bigg|_{Y=0}\right) + \delta^2\left(\langle u_i^{(1)}\rangle\big|_{y=y_\infty} - \frac{y_\infty^2}{2}\frac{\partial^2 U_i^{\mathcal{O}}}{\partial Y^2}\bigg|_{Y=0}\right) + ... \tag{2.34}$$

In particular, this is achieved by evaluating the inner variables at the interface between the two domains and by explicitly expanding the macroscopic boundary conditions to be imposed at $Y = 0$ up to $\mathcal{O}(\delta)$.
By considering the definitions of the components $\langle u_i^{(0)}\rangle$ provided in equations 2.27, 2.28, and 2.29, these expressions are substituted into the previously derived relations. Consequently, the leading-order macroscopic boundary conditions are obtained and can be formulated as follows:

$$U_1^{\mathcal{O}}(t,X,0,Z) = \delta\left[u_{11}^{\dagger}\,\mathcal{S}_{12}\big|_{Y=\delta y_\infty} - y_\infty \frac{\partial U_1^{\mathcal{O}}}{\partial Y}\bigg|_{Y=0}\right] + \mathcal{O}(\delta^2), \tag{2.35}$$

$$U_2^{\mathcal{O}}(t,X,0,Z) = \mathcal{O}(\delta^2), \tag{2.36}$$

$$U_3^{\mathcal{O}}(t,X,0,Z) = \delta\left[u_{33}^{\dagger}\,\mathcal{S}_{32}\big|_{Y=\delta y_\infty} - y_\infty \frac{\partial U_3^{\mathcal{O}}}{\partial Y}\bigg|_{Y=0}\right] + \mathcal{O}(\delta^2). \tag{2.37}$$

The first and third equations can be further developed by using the Taylor expansion around $Y = 0$ for all the shear stress terms $\mathcal{S}_{ij}$, evaluated at $Y = \delta y_\infty$.
For example, $\mathcal{S}_{12}\big|_{Y=\delta y_\infty}$ can be manipulated, becoming:

$$\mathcal{S}_{12}\big|_{Y=\delta y_\infty} = \mathcal{S}_{12}\big|_{Y=0} + \delta y_\infty \left(\partial \mathcal{S}_{12}/\partial Y\right)\big|_{Y=0} + ... \tag{2.38}$$

and, furthermore, also $S_{12}\big|_{Y=0}$ can be expanded to leading order in δ, becoming:

$$S_{12}\big|_{Y=0} = \left(\partial U_1^{\mathcal{O}}/\partial Y\right)\big|_{Y=0}. \tag{2.39}$$

Combining these two expansions, it leads to:

$$\mathcal{S}_{12}\big|_{Y=\delta y_\infty} = \left(\partial U_1^{\mathcal{O}}/\partial Y\right)\big|_{Y=0} + \delta y_\infty \left(\partial \mathcal{S}_{12}/\partial Y\right)\big|_{Y=0} + ... \tag{2.40}$$

and if substituted in the boundary conditions, the macroscopic equation becomes:

$$\begin{aligned} U_1^{\mathcal{O}}(t,X,0,Z) &= \delta\left[u_{11}^{\dagger}\left[\frac{\partial U_1^{\mathcal{O}}}{\partial Y} + \delta y_\infty \frac{\partial \mathcal{S}_{12}}{\partial Y}\big|_{Y=0} + ...\right] - y_\infty \frac{\partial U_1^{\mathcal{O}}}{\partial Y}\bigg|_{Y=0}\right] + \mathcal{O}(\delta^2) \\ &= \delta\left(u_{11}^{\dagger} - y_\infty\right)\frac{\partial U_1^{\mathcal{O}}}{\partial Y} + \delta^2 y_\infty \left(\frac{\partial \mathcal{S}_{12}}{\partial Y}\right)\big|_{Y=0} + \mathcal{O}(\delta^2) \end{aligned} \tag{2.41}$$

Same procedure for the third component.
By renaming these terms $U^{\mathcal{O}} = U_1^{\mathcal{O}}$ and $W^{\mathcal{O}} = U_3^{\mathcal{O}}$, the macroscopic slip boundary conditions at the virtual wall up to the leading order and neglecting the higher order terms, become:

$$U^{\mathcal{O}}(t, X, 0, Z) = \delta\, \lambda_x \frac{\partial U^{\mathcal{O}}}{\partial Y}\bigg|_{Y=0} + \mathcal{O}(\delta^2), \tag{2.42}$$

$$W^{\mathcal{O}}(t, X, 0, Z) = \delta\, \lambda_z \frac{\partial W^{\mathcal{O}}}{\partial Y}\bigg|_{Y=0} + \mathcal{O}(\delta^2), \tag{2.43}$$

with $\lambda_x = u_{11}^{\dagger}|_{y_\infty} - y_\infty$ and $\lambda_z = u_{33}^{\dagger}|_{y_\infty} - y_\infty$.
As mentioned before, an inspection of Table 3.1 demonstrates that the two slip lengths, λ_x and λ_z, are independent of the choice of y_∞. It is, however, essential that $y_\infty > 2$ to ensure that the microscopic equations are adequately captured and properly resolved within the computational domain.

2.5.1. The transpiration velocity

Based on previous studies[64,65,66], it has been observed that the normal wall velocity component plays a crucial role in turbulent flow, especially in the case when the interaction between outer flow and near wall fluctuations accounts for.
The present study aims to study the behaviour of turbulent flow in the near-wall region of a rough and ribleted wall, so knowing the importance of the transpiration velocity at the fictitious boundary at $Y = 0$, is addressed to be included in the model.
The equation 2.36 shows that the vertical component vanishes at the leading order; only second-order terms remain in the equation. Considering the physics of the problem, it is justified by accounting for the impermeability of the real wall.
However, it has been demonstrated that neglecting vertical (wall-normal) velocity fluctuations at the virtual wall can introduce significant inaccuracies in the prediction of drag variation. This limitation becomes particularly critical when modeling riblet configurations that operate beyond the viscous regime, where the interaction between the flow structures and the surface geometry is no longer confined to the immediate near-wall region. In such cases, the neglect of wall-normal fluctuations leads to an inaccurate estimation of drag reduction or increase.[15,56]
Considering the interface between inner and outer domains, at $Y_\infty = \delta y_\infty$, referring to Fig. 2.2, an estimation of $V^{\mathcal{O}}$ is obtained by manipulating the following equations. The first condition enforces velocity matching at the interface:

$$\langle U_i^{\mathcal{I}} \rangle\big|_{y=y_\infty} = \frac{1}{\delta}\, U_i^{\mathcal{O}}(t, X, Y_\infty, Z) \tag{2.44}$$

Then the second equation, which arises from homogenization theory and represents a standard ansatz for defining the problem variables in the presence of a single forcing term in the direct formulation.

$$u_j^{(0)} = u_{ji}^{\dagger}\, S_{i2}\big|_{Y_\infty} \tag{2.45}$$

By combining these equations, the following one is obtained:

$$\left.\frac{\partial U_j^{\mathcal{O}}}{\partial Y}\right|_{Y_\infty} = \frac{\mathcal{C}_{jk}}{\delta}\, U_k^{\mathcal{O}}\big|_{Y_\infty}\,, \tag{2.46}$$

with j and k equal to 1 and 3, and the 2×2 diagonal matrix $\mathcal{C}$ defined as

$$\mathcal{C} = \begin{pmatrix} \dfrac{1}{u_{11}^{\dagger}\big|_{y_\infty}} & 0 \\ 0 & \dfrac{1}{u_{33}^{\dagger}\big|_{y_\infty}} \end{pmatrix}. \tag{2.47}$$

Expression (2.46) can be combined with Eq. 2.45 yielding to:

$$u_j^{(0)} = \delta^{-1}\, u_{ji}^{\dagger}\, \mathcal{C}_{ik}\, U_k^{\mathcal{O}}\Big|_{Y_\infty} \tag{2.48}$$

with the index i, which can also take only the values 1 and 3.
Accounting the order δ in the microscopic y-velocity component at the upper edge of the *REV*, and integrating first on the vertical direction:

$$u_2^{(1)}\big|_{y_\infty} = v^{(1)}\big|_{y_\infty} = -\frac{\partial}{\partial x_i}\int_{y_{wall}}^{y_\infty} u_i^{(1)}\, dy - \frac{\partial}{\partial X_i}\int_{y_{wall}}^{y_\infty} u_i^{(0)}\, dy, \tag{2.49}$$

and subsequently integrating in z from 0 to 1 gives:

$$\int_0^1 v^{(1)}\big|_{y_\infty}\, dz = -\frac{\partial}{\partial X_i}\int_{y_{wall}}^{y_\infty}\int_0^1 u_i^{(0)}\, dz\, dy = -\delta^{-1}\left[\int_{y_{wall}}^{y_\infty}\int_0^1 u_{ij}^{\dagger}\, dz\, dy\right]\mathcal{C}_{jk}\frac{\partial U_k^{\mathcal{O}}}{\partial X_i}\bigg|_{Y_\infty}, \tag{2.50}$$

so that the macroscopic transpiration velocity, now defined up to the second-order terms at Y_∞, is:

$$V^{\mathcal{O}}\big|_{Y_\infty} = \delta^2\int_0^1 v^{(1)}\big|_{y_\infty}\, dz + \mathcal{O}(\delta^3) = -\delta\, m_{ik}\left.\frac{\partial U_k^{\mathcal{O}}}{\partial X_i}\right|_{Y_\infty} + \mathcal{O}(\delta^3). \tag{2.51}$$

with $m_{ik} = \left[\displaystyle\int_{y_{wall}}^{y_\infty}\int_0^1 u_{ij}^{\dagger}\, dz\, dy\right]\mathcal{C}_{jk}$.

The two components of the matrix can be defined as:

$$m_{11} = \frac{1}{u_{11}^{\dagger}\big|_{y_\infty}}\int_{y_{wall}}^{y_\infty}\int_0^1 u_{11}^{\dagger}\, dz\, dy, \qquad m_{33} = \frac{1}{u_{33}^{\dagger}\big|_{y_\infty}}\int_{y_{wall}}^{y_\infty}\int_0^1 u_{33}^{\dagger}\, dz\, dy. \tag{2.52}$$

The effective condition (2.51) must now be transferred to $Y = 0$; this is easily accomplished by expanding $V^{\mathcal{O}}$ around $Y = 0$, i.e.

$$V^{\mathcal{O}}\big|_{Y_\infty} = V^{\mathcal{O}}\big|_{Y=0} + \delta y_\infty \frac{\partial V^{\mathcal{O}}}{\partial Y}\bigg|_{Y=0} + \delta^2 \frac{y_\infty^2}{2} \frac{\partial^2 V^{\mathcal{O}}}{\partial Y^2}\bigg|_{Y=0} + \mathcal{O}(\delta^3) =$$

$$V^{\mathcal{O}}\big|_{Y=0} + \delta y_\infty \left[-\frac{\partial U^{\mathcal{O}}}{\partial X} - \frac{\partial W^{\mathcal{O}}}{\partial Z} \right] \bigg|_{Y=0} + \delta^2 \frac{y_\infty^2}{2} \frac{\partial}{\partial Y} \left[-\frac{\partial U^{\mathcal{O}}}{\partial X} - \frac{\partial W^{\mathcal{O}}}{\partial Z} \right] \bigg|_{Y=0} + \mathcal{O}(\delta^3) =$$

$$V^{\mathcal{O}}\big|_{Y=0} - \delta y_\infty \left\{ \frac{\partial}{\partial X} \left[\delta \lambda_x \frac{\partial U^{\mathcal{O}}}{\partial Y} \right] + \frac{\partial}{\partial Z} \left[\delta \lambda_z \frac{\partial W^{\mathcal{O}}}{\partial Y} \right] \right\} \bigg|_{Y=0} - \delta^2 \frac{y_\infty^2}{2} \left[\frac{\partial^2 U^{\mathcal{O}}}{\partial Y \partial X} + \frac{\partial^2 W^{\mathcal{O}}}{\partial Y \partial Z} \right] \bigg|_{Y=0} + \mathcal{O}(\delta^3). \tag{2.53}$$

Expanding in a similar manner the term on right hand side of Eq. (2.51) it is obtained:

$$V^{\mathcal{O}}\big|_{Y_\infty} = -\delta\, m_{11} \left[\frac{\partial U^{\mathcal{O}}}{\partial X} + \delta y_\infty \frac{\partial^2 U^{\mathcal{O}}}{\partial Y \partial X} \right] \bigg|_{Y=0} - \delta\, m_{33} \left[\frac{\partial W^{\mathcal{O}}}{\partial Z} + \delta y_\infty \frac{\partial^2 W^{\mathcal{O}}}{\partial Y \partial Z} \right] \bigg|_{Y=0} + \mathcal{O}(\delta^3) =$$

$$-\delta\, m_{11} \left\{ \frac{\partial}{\partial X} \left[\delta \lambda_x \frac{\partial U^{\mathcal{O}}}{\partial Y} \right] + \delta y_\infty \frac{\partial^2 U^{\mathcal{O}}}{\partial Y \partial X} \right\} \bigg|_{Y=0} - \delta\, m_{33} \left[\frac{\partial}{\partial Z} \left[\delta \lambda_z \frac{\partial W^{\mathcal{O}}}{\partial Y} \right] + \delta y_\infty \frac{\partial^2 W^{\mathcal{O}}}{\partial Y \partial Z} \right] \bigg|_{Y=0} + \mathcal{O}(\delta^3). \tag{2.54}$$

Putting together (2.53) and (2.54) it is finally found:

$$V^{\mathcal{O}}(t, X, 0, Z) = -\delta^2 \left[\mathcal{K}_{xy}^{itf} \frac{\partial^2 U^{\mathcal{O}}}{\partial Y \partial X} + \mathcal{K}_{zy}^{itf} \frac{\partial^2 W^{\mathcal{O}}}{\partial Y \partial Z} \right] \bigg|_{Y=0} + \mathcal{O}(\delta^3), \tag{2.55}$$

with $\mathcal{K}_{xy}^{itf} = [m_{11}(y_\infty + \lambda_x) - y_\infty \lambda_x - y_\infty^2/2]$ and $\mathcal{K}_{zy}^{itf} = [m_{33}(y_\infty + \lambda_z) - y_\infty \lambda_z - y_\infty^2/2]$ playing the role of interface permeability coefficients[15,61]. Another form, more convenient for computational purposes, of (2.55) can be found by using (2.42) and (2.43), and this is:

$$V^{\mathcal{O}}(t, X, 0, Z) = -\delta\, n_{11} \frac{\partial U^{\mathcal{O}}}{\partial X}\bigg|_{Y=0} - \delta\, n_{33} \frac{\partial W^{\mathcal{O}}}{\partial Z}\bigg|_{Y=0} + \mathcal{O}(\delta^3), \tag{2.56}$$

with $n_{11} = \mathcal{K}_{xy}^{itf}/\lambda_x$ and $n_{33} = \mathcal{K}_{zy}^{itf}/\lambda_z$. It is important to stress the fact that n_{11} and n_{33}, just like the Navier slip coefficients λ_x and λ_z and the interface permeability coefficients, are independent of the choice of y_∞ of the *REV*. Boundary condition (2.56) at the effective surface in $Y = 0$, together with (2.42) and (2.43), allow the model in (2.13) for the macroscopic variables $(U^{\mathcal{O}}, V^{\mathcal{O}}, W^{\mathcal{O}}, P^{\mathcal{O}})$ to be closed.

The formal derivation of the macroscopic boundary conditions has now been completed; the next section 2.6. describes one of the most original contributions of the present paper, where it is assumed the presence of longitudinal vortices, on top of a streamwise-homogeneous mean flow.

2.6. A vortex model for advection

As previously noted, one of the most innovative features of the present model lies in the explicit inclusion of the advective term within the microscopic formulation. In particular, the streamwise vortex is modeled as a function of the cross-stream coordinates, with a periodicity corresponding to that of the riblet geometry.
This idea is motivated by prior numerical investigations - performed by Goldstein and Tuan[54], Endrikat[55], and Modesti et al.[67] - which examined flows over ribleted surfaces. These studies consistently report the emergence of coherent vortical structures above the riblet tips, which in turn induce significant wall-normal velocity fluctuations in the near-wall region.
Considering the convective term, defined in equation (2.26),

$$-\delta\ell^+ \left(u_k^{(0)} \frac{\partial u_{ji}^\dagger}{\partial x_k} \right) \tag{2.57}$$

This term must be appropriately approximated, building upon insights from previous studies.
In particular, the presence of counter-rotating vortical structures has been clearly documented by Modesti et al.[67]. Their analysis of ensemble-averaged secondary flow fields reveals a pair of symmetric vortices, characterized by an upwash region located above the riblet tips. Moreover, the intensity of this upwash is observed to increase with the spanwise periodicity of the surface geometry.
In order to estimate the advective term, previous studies have been analyzed. For instance, in the case of trapezoidal riblets with height $h = \ell/2$, the maximum upwash velocity v^+, expressed in viscous units, attains values of approximately 0.04 for $\ell^+ = 18$ and 0.15 for $\ell^+ = 36$[68,67]. As the spacing between adjacent riblets increases, the mean downward secondary flow more effectively transports streamwise momentum into the grooves, thereby contributing to an increase in drag. Nevertheless, even at $\ell^+ = 63$, the vortical structures do not penetrate the grooves but instead remain above them, with each vortex in the pair centered slightly above the riblet tips.
Similarly, numerical simulations conducted by Goldstein and Tuan[54] for scalloped, short riblets show that the streamwise vortex pair reaches a maximum wall-normal velocity of about 0.03 at $\ell^+ = 23$ and $h^+ = 8.7$, which increases to approximately 0.12 as ℓ^+ rises to 62.8 (for $h^+ = 8.9$).
Based on these results, a synthetic pair of streamwise vortices is introduced for the case of blade riblets, which are selected as the most promising configuration and, at the same time, the most challenging to simulate. In this configuration, both the transpiration effects and the convective term associated with the wall-normal fluctuations of the streamwise vortex pair along the riblets become increasingly significant due to the intrinsic geometry of the grooves.
The procedure to consider the synthetic pair of streamwise vortices is now described. First, the system described in equation (2.26) is solved for blade riblets by neglecting the convective term, reducing it to the Stokes equations. Subsequently, building on this solution, a microscale forced Stokes problem is formulated in which the convective term is reintroduced as a function of a parameter $\mathcal{P}$. This parameter is then calibrated to produce a vortex background flow consistent with previous studies.
The boundary conditions of the problem are: periodicity conditions at $z = 0$ and $z = 1$, no-slip at the solid walls, and a velocity boundary condition at the top of the domain that rapidly goes

to zero outside of the roughness sublayer.
By imposing $\delta = 0$ to the equations (2.26) and starting from its solution, to create a vortex with the velocity components (v_V^+, w_V^+) in the $(y, z) = (x_2, x_3)$ plane.

$$\begin{aligned} \frac{\partial v_V^+}{\partial x_2} + \frac{\partial w_V^+}{\partial x_3} &= 0 \\ -\frac{\partial p_V^+}{\partial x_2} + \frac{\partial^2 v_V^+}{\partial x_i^2} &= \mathcal{P}\left[u_{j3}^\dagger \frac{\partial u_{23}^\dagger}{\partial x_j}\right] \\ -\frac{\partial p_V^+}{\partial x_3} + \frac{\partial^2 w_V^+}{\partial x_i^2} &= \mathcal{P}\left[u_{j3}^\dagger \frac{\partial u_{33}^\dagger}{\partial x_j}\right] \end{aligned} \tag{2.58}$$

with indices i and j taking values 2 and 3.
Clearly, the parameter $\mathcal{P}$, which represents the intensity of the vortex pair, leaves a degree of arbitrariness and flexibility in the problem, which allows tuning and calibrating the background (v_V^+, w_V^+) vortex field to obtain similar secondary flow, in terms of size and intensity, compared to reference cases.
It has been found that $\mathcal{P}$ value close to 160 yields secondary flows of size and upwash velocity in the range of those quoted by Goldstein and Tuan[54], Endrikat[55] and Modesti et al.[67].

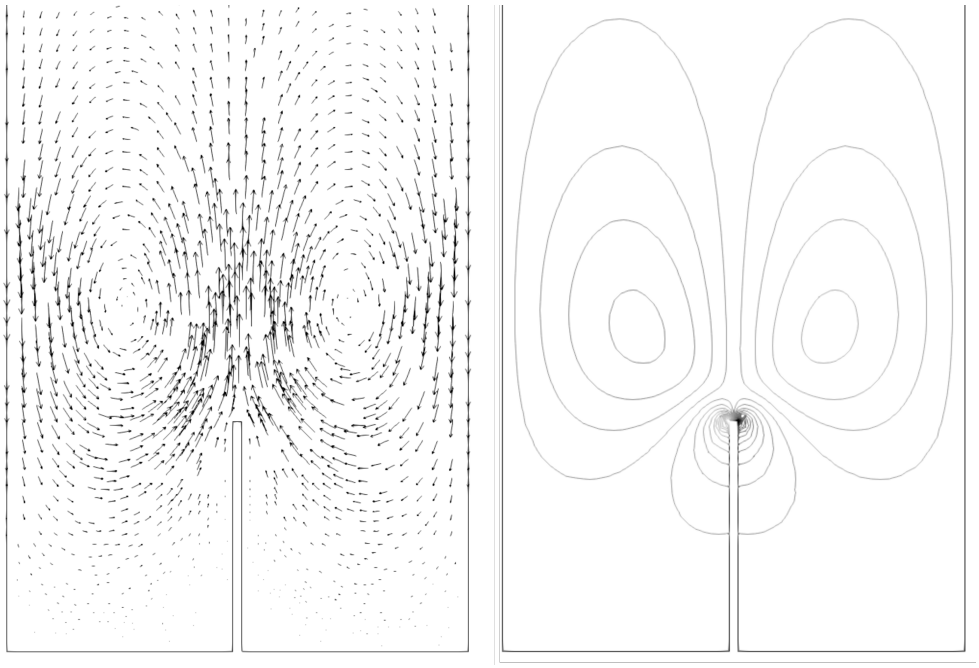

Figure 2.5: Synthetic near-wall vortices for blade riblets ($\mathcal{P} = 160$), displayed via velocity vectors of the (v_V^+, w_V^+) field and contours of the streamwise vorticity, ω_x.

Figure 2.5 shows the vortical structure in the case of blade riblets. In the left image, velocity magnitude vectors highlight the shape of the vortex pair in the case of the largest periodicity tested here ($\ell^+ = 40.6$), with a maximum vertical velocity equal to 0.11 (in plus units). On the

right frame, isolines of the streamwise vorticity are displayed. The intensity of ω_x is evaluated as:

$$\frac{\partial v_V^+}{\partial z^+} - \frac{\partial w_V^+}{\partial y^+} \tag{2.59}$$

equal to ± 0.023 at the vortex central position.
By the combination of equation (2.26) and the vortex field (v_V^+, w_V^+), the following microscopic system of equations is obtained by assuming that the $u_{ji}^\dagger$ field develops on top of a streamwise-invariant mean field plus a synthetic vortex pair which depends on only y and z:

$$-\delta\ell^+ \left(u_k^{(0)} \frac{\partial u_{ji}^\dagger}{\partial x_k} \right) = -\ell^+ \left(v_V^+ \frac{\partial u_{ji}^\dagger}{\partial y} + w_V^+ \frac{\partial u_{ji}^\dagger}{\partial z} \right), \tag{2.60}$$

It is crucial to notice that in the case of small ℓ^+, in the viscous regime, the equation just defined produces the same results as in the Stokes case. However, interestingly, the advective term becomes significantly important for larger periodicity.
This is quantitatively demonstrated in the following table that shows the results of the Navier slip and interface permeability coefficients, for the case of blade riblets, computing thisnew $u_{ji}^\dagger$ fields, setting $\mathcal{P} = 160$. Microscopic coefficients are calculated following the same procedure described before in the section 2.5..

Table 2.3: Effective coefficients for blade riblets, fig. 2.4(d), with the model for advection ($\mathcal{P} = 160$).

ℓ^+	ℓ_g^+	$\max(v_V^+)$	$\lvert\omega_x\rvert_{vortex\ center}$	λ_x	λ_z	$\mathcal{K}_{xy}^{itf}$	$\mathcal{K}_{zy}^{itf}$	$\Delta\lambda$
Stokes	-	-	-	0.1915	0.0784	0.0379	0.0046	0.1131
17.7	12.4	0.11	0.052	0.1730	0.0766	0.0400	0.0076	0.0964
27.9	19.5	0.11	0.034	0.1473	0.0740	0.0468	0.0097	0.0733
40.6	28.4	0.11	0.023	0.1038	0.0690	0.0599	0.0126	0.0348

Looking at the numerical results, it is interesting to observe how the coefficients change. Firstly, the streamwise slip coefficient, λ_x, decreases rapidly as ℓ^+ increases, explaining how much the streamwise flow has been affected by the presence of a fictitious vortex pair. In particular, comparing the Stokes result and the one for the largest ℓ^+, there is a difference of about 46 % between the two values of λ_x. On the other hand, the spanwise slip coefficient, λ_z, exhibits only a slight reduction (maximum reduction equal to 12 %).
In contrast to the slip-length coefficients, the interface permeability components exhibit a markedly different behavior as a function of the spanwise periodicity. Specifically, both $\mathcal{K}_{xy}^{itf}$ and $\mathcal{K}_{zy}^{itf}$ increase with increasing ℓ^+, highlighting the progressively dominant role of the advective (convective) term at larger riblet spacings in accurately capturing the flow dynamics. This trend indicates that the wall-normal (transpiration) velocity component becomes increasingly influential, as larger values of $\mathcal{K}_{xy}^{itf}$ and $\mathcal{K}_{zy}^{itf}$ enhance the coupling between the outer flow and the near-wall region. Unlike the slip-length coefficients, which remain comparatively close to their creeping-flow counterparts, the interface permeability components show a substantial deviation from the Stokes-limit values. In particular, $\mathcal{K}_{xy}^{itf}$ increases by approximately 58% when comparing the creeping-flow result to the value obtained at $\ell^+ = 40.6$, while $\mathcal{K}_{zy}^{itf}$ more than doubles

over the same range. This relevant growth in the interface permeability coefficients is directly associated with an intensification of wall transpiration at the virtual interface located at $Y = 0$. Physically, this reflects an enhanced exchange of momentum between the flow above the riblets and the flow within the grooves, mediated by wall-normal velocity fluctuations induced by the underlying vortical structures. The magnitude of this effect can be quantitatively assessed through direct numerical simulations of turbulent flow over the modeled surface, which provide detailed information on the near-wall transport mechanisms and their dependence on the geometrical parameters.

The slip coefficients have been quantitatively compared between the simple Stokes model, initially proposed, and the forced formulation, that model the vortex flow over riblets. The following figures present the principal contour plots for blade riblets without and with the advection vortex model, respectively. In particular, isocontours of auxiliary fields of $u^{\dagger}_{33}$, $u^{\dagger}_{23}$ and $u^{\dagger}_{11}$ as been shown, from left to right. The isolines of these relevant variables are plotted to guide the eye into the field, highlighting the formation of particular structures in the proximity of the blade riblet.
A comparison between the first and third contours for each case reveals no substantial differences. In all cases, the isolines display consistent behaviour near the blade riblets, conforming to the geometric features of the surface. Further away from the riblet region, the isolines gradually transition to a more regular pattern, becoming aligned and uniformly spaced, which suggests a more uniform distribution of the auxiliary quantity.
On the other hand, a substantial difference emerges in the isocontours of $u^{\dagger}_{23}$: the presence of two extra coherent regions appears above the ribs in the advection model results, an unequivocal signature of the presence of the vortex pair.

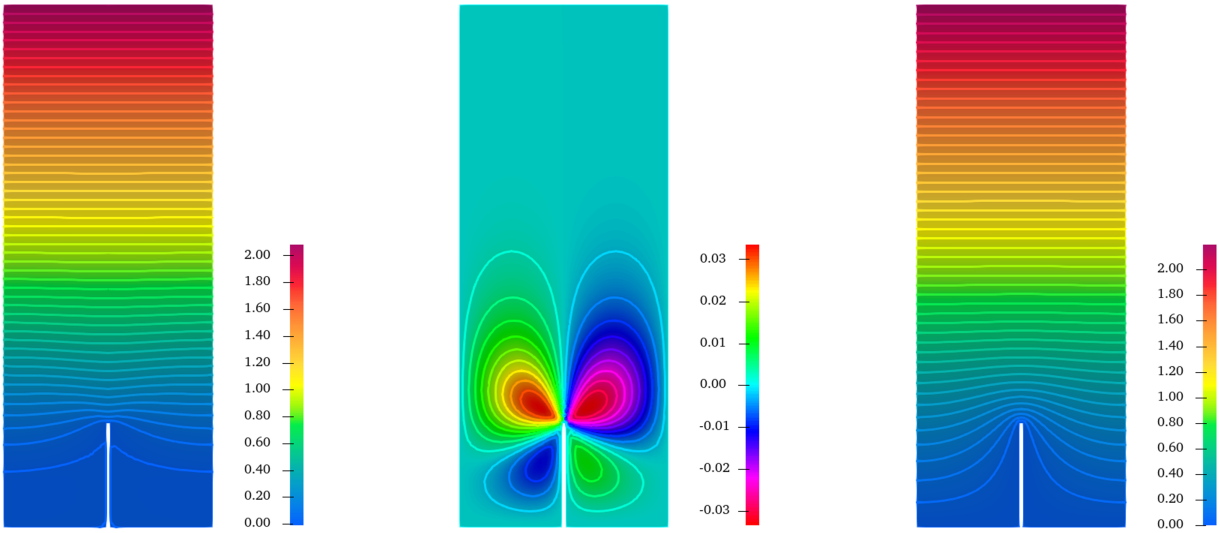

Figure 2.6: From left to right: auxiliary fields of $u^{\dagger}_{33}$, $u^{\dagger}_{23}$, and $u^{\dagger}_{11}$, in the Stokes limit.

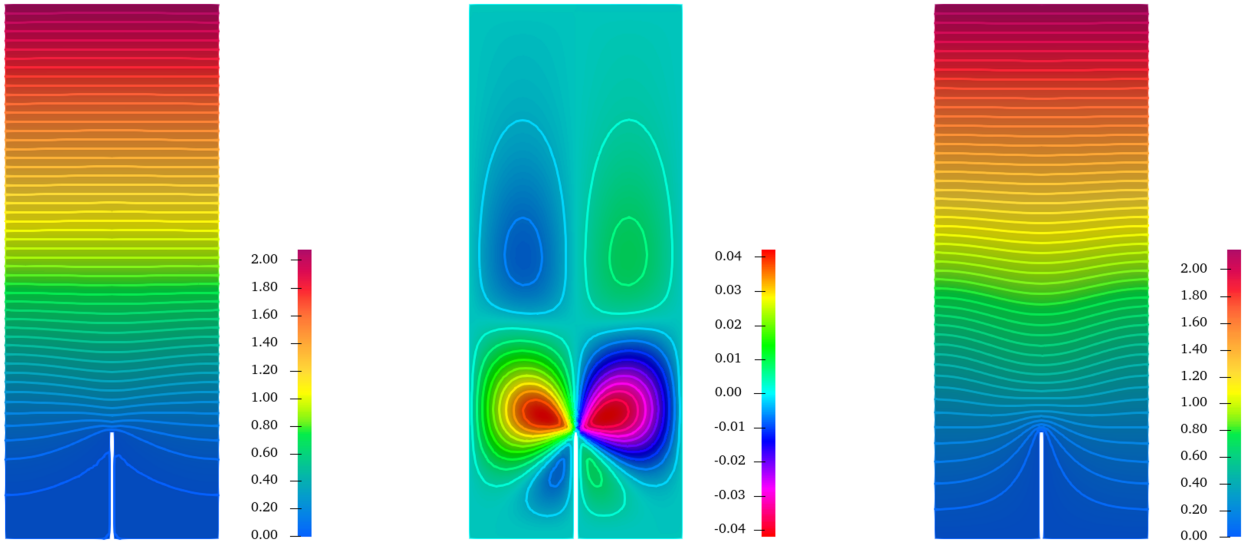

Figure 2.7: Same as Figure 2.6 for $\ell^+ = 27.9$ using the advection model ($\mathcal{P} = 160$).

2.7. The macroscale problem

2.7.1. Problem description and numerical setup

The macroscopic boundary conditions are now fully specified. The subsequent step consists of performing direct numerical simulations to assess the effectiveness of the proposed formulation and to systematically evaluate the contribution of each additional modeling term to the overall predictive capability of the model. Large-scale direct numerical simulations have been performed by applying the effective boundary conditions, defined in the equations:

$$\begin{aligned} U^{\mathcal{O}}(t,X,0,Z) &= \delta\,\lambda_x \frac{\partial U^{\mathcal{O}}}{\partial Y}\bigg|_{Y=0} + \mathcal{O}(\delta^2) \\ V^{\mathcal{O}}(t,X,0,Z) &= -\delta\,\frac{\mathcal{K}^{itf}_{xy}}{\lambda_x}\,\frac{\partial U^{\mathcal{O}}}{\partial X}\bigg|_{Y=0} - \delta\,\frac{\mathcal{K}^{itf}_{zy}}{\lambda_z}\,\frac{\partial W^{\mathcal{O}}}{\partial Z}\bigg|_{Y=0} + \mathcal{O}(\delta^3) \\ W^{\mathcal{O}}(t,X,0,Z) &= \delta\,\lambda_z \frac{\partial W^{\mathcal{O}}}{\partial Y}\bigg|_{Y=0} + \mathcal{O}(\delta^2) \end{aligned} \tag{2.61}$$

Both the Stokes coefficients and the coefficients calculated through the advection model (table 2.3) have been applied in macroscopic boundary conditions, for the case of blade riblets, to model the presence of microgrooves using the equivalent conditions. As previously discussed, the main idea of developing the present model is to enforce effective conditions on a fictitious smooth wall.

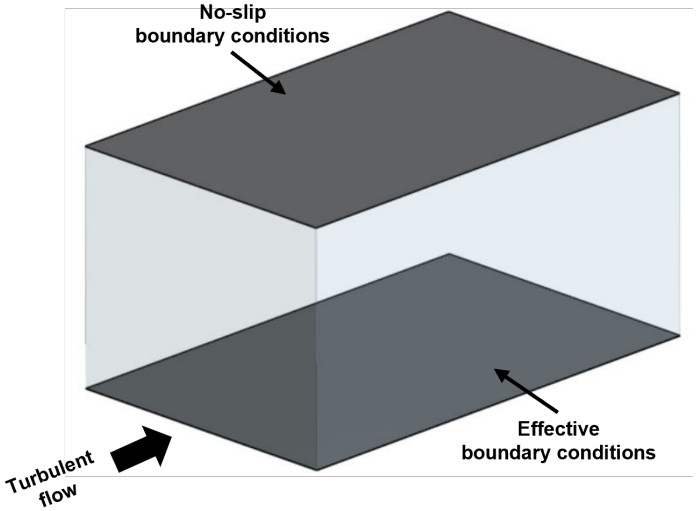

Figure 2.8: Sketch of the boundary conditions of the channel flow, highlighting the apparent smoothness of the bottom wall, while effectively accounting for the presence of grooves through equivalent boundary conditions. The top wall is enforced with no-slip boundary conditions.

In the present study, only the bottom wall is designed to emulate the influence of a grooved surface by equivalent boundary conditions; on the top wall, no-slip boundary conditions are applied.
The virtual corrugated wall, similar to the case sketched in Fig. 2.1, but with blade riblets characterized by periodic element, ℓ, with a height of $0.5\,\ell$, and thickness $0.02\,\ell$ (cf. Fig. 2.4(*d*)). The computational region of the macroscopic domain has the dimensions of:

- $L_X = 2\pi H$ for the streamwise direction;
- $L_Y = 2H$ along the vertical or wall-normal direction;
- $L_Z = \pi H$ along the spanwise direction.

with H half the channel height.
A turbulent flow is set through the channel thanks to the imposition of a macroscopic pressure gradient, $\mathcal{M}$, and, correspondingly, a bulk stress $\tau_{\mathcal{M}}$ can be defined as:

$$\mathcal{M} = |\Delta\hat{p}/L_X|, \qquad \tau_{\mathcal{M}} = \mathcal{M}H. \tag{2.62}$$

where $\Delta\hat{p}$ is the pressure difference between the inlet and the outlet along the streamwise direction of the channel.
From the momentum balance in the macroscopic domain, it can be established that $\tau_{\mathcal{M}} = (\tau_{\mathcal{F}} + \tau_{\mathcal{T}})/2$, where $\tau_{\mathcal{F}}$ and $\tau_{\mathcal{T}}$ are the total shear stresses at the fictitious boundary ($\hat{y} = 0$) and at the top, smooth wall ($\hat{y} = 2H$), respectively.
A shear velocity and a corresponding shear-velocity Reynolds number can be defined as:

$$u_{\tau(\mathcal{M})} = \sqrt{\tau_{\mathcal{M}}/\rho} \qquad Re_{\tau(\mathcal{M})} = \frac{\rho u_{\tau(\mathcal{M})} H}{\mu} \tag{2.63}$$

In particular, $Re_{\tau(\mathcal{M})}$ has a fixed value of about 193 for all the simulations carried out.
A range of riblet spacings has been systematically investigated in order to explore configurations from narrowly spaced geometries, characteristic of the viscous regime, to more widely spaced corrugated surfaces. As the periodicity increases, the flow progressively departs from this regime, and the interaction of secondary flow structures becomes increasingly pronounced. In particular, wider spacings promote stronger cross-stream motions and enhanced coupling between the outer flow and the groove region. Configurations characterized by larger riblet periodicity are of particular interest, as they provide an assessment for the validity and robustness of the proposed model. In this regime, the increasing relevance of advective effects and secondary flow interactions makes it especially suitable for evaluating whether the model is capable of accurately capturing the underlying physical mechanisms.
The riblet pitch $\ell^+_{\mathcal{M}}$ defined as:

$$\ell^+_{\mathcal{M}} = \frac{\rho u_{\tau(\mathcal{M})} \ell}{\mu} \tag{2.64}$$

has different values $\ell^+_{\mathcal{M}} = (13.5, 17.7, 27.9, 40.6)$.

To compare the present results with direct numerical simulations of[69], taken as reference, a shear stress τ_w has been defined to normalize the results.
The shear stress at the corrugated wall τ_w can be retrieved theoretically by applying momentum balance over the whole domain, yielding:

$$\tau_w \approx (2\tau_{\mathcal{M}} - \tau_{\mathcal{T}}) + \tau_{\mathcal{M}} \frac{\ell}{2H} = \tau_{\mathcal{F}} + \tau_{\mathcal{M}} \frac{\ell}{2H}. \tag{2.65}$$

Physically, it represents the drag evaluated per unit plan area for the bottom physical surface, with the thickness of the thin blades neglected.

Direct numerical simulations of the macroscale problem are run using the Simcenter STAR-CCM+, finite-volume-based software. The grid resolution and the numerical procedure are the same as in references[70,56].

Mesh size and settings

The computational mesh is uniform in both the streamwise and spanwise directions, while a non-uniform stretching is applied in the wall-normal direction. Specifically, the grid is refined in the proximity of the upper and lower walls - where the smallest grid spacing is imposed - and gradually it becomes coarser toward the channel centerline, where the largest spacing is reached.
Given that the highest level of accuracy near the walls, where the effects of the boundary conditions are most significant, is common in a numerical simulation context; so, the grid is deliberately refined in this region. Conversely, the grid resolution is progressively relaxed towards the central plane, in wall-normal direction, of the domain following a standard approach in wall-bounded turbulent flow simulations to optimize computational efficiency without compromising accuracy in the near-wall region. The resulting grid resolution in viscous units is $h^+_X = 9.47$, $h^+_Z = 6.32$, $h^+_Y|_{\min} = 0.27$, and $h^+_Y|_{\max} = 9.25$.

Numerical scheme

The convective fluxes are discretized using a third-order scheme formulated as a linear blend between *MUSCL* third-order upwind and a third-order central-differencing expression.
A second-order implicit scheme is employed for temporal discretization with 20 internal iterations performed at each time step.
The time step is set to $0.001H/u_{\tau(\mathcal{M})}$ for the maximum convective Courant–Friedrichs–Lewy (CFL) number to be maintained below 1, to ensure numerical stability and accuracy.
The averaging time, after the initial transient of the flow field in each simulation, is typically taken equal to $40\,H/u_{\tau(\mathcal{M})}$.

2.8. Results and discussion

The present model introduces a novel framework for predicting the behavior of turbulent flow over riblet-textured surfaces. The approach is based on a multiscale homogenization technique, through which effective boundary conditions are rigorously derived. In particular, the microscopic problem is solved both under the Stokes approximation and within an advection-inclusive formulation, enabling a more comprehensive characterization of the flow dynamics in the vicinity of riblets.

This section reports the results of direct numerical simulations (DNS) for the case of blade-type riblets. The findings demonstrate that the proposed model significantly outperforms existing wall models in reproducing the drag reduction curve, maintaining accuracy even at relatively large riblet spacings, where traditional approaches typically lose predictive capability.

The following figure represents a main outcome of the present study, as it synthesizes the complete set of numerical results. It clearly illustrates that incorporating both the transpiration velocity component and the advective term into the model formulation is essential for accurately predicting flow behavior at higher values of ℓ^+.

These results highlight the critical role of previously neglected physical mechanisms in extending the validity of riblet-based drag reduction models beyond viscous regime.

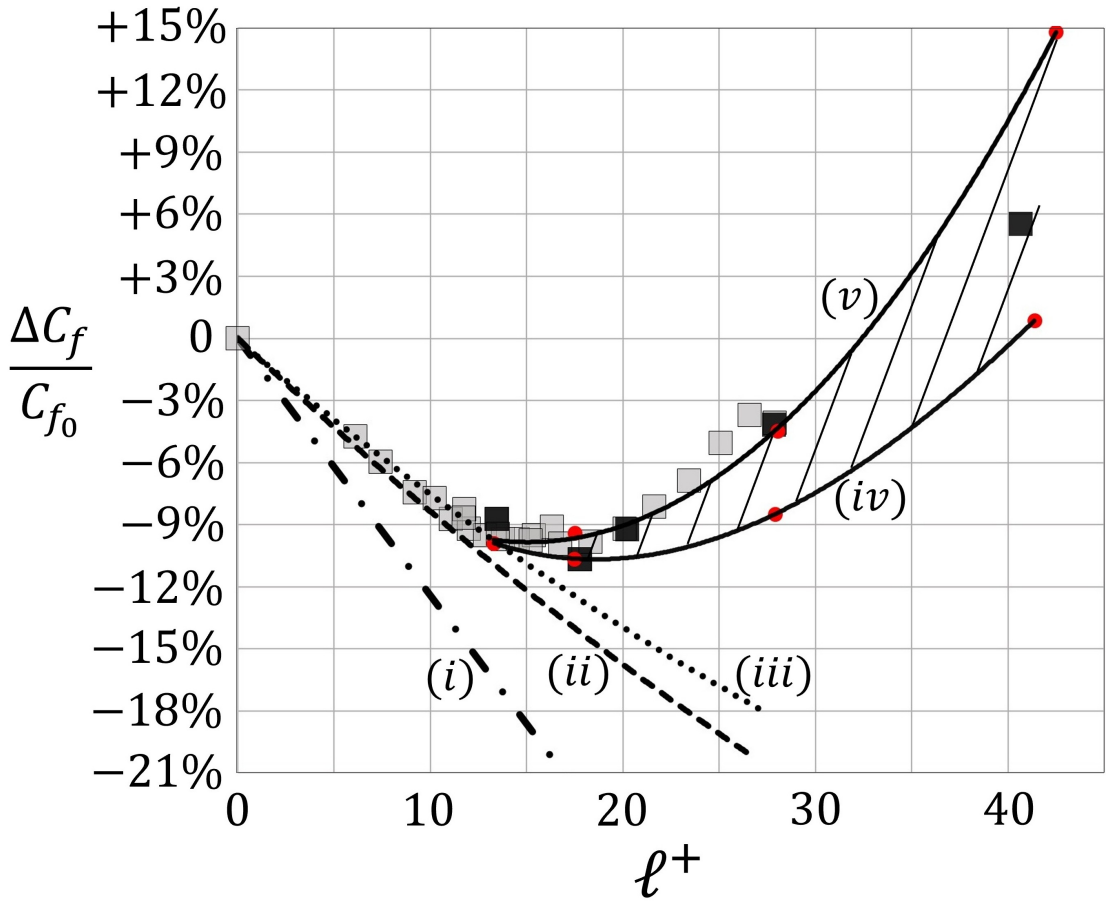

Figure 2.9: Drag reduction versus spacing for blade riblets.

A comprehensive set of data is presented in Fig. 2.9, including reference numerical and experimental results, the theoretical linear prediction for the viscous regime, and the outcomes of the present study.
The square markers denote reference data collected from previous investigations. In particular, the grey symbols correspond to the experimental measurements of Bechert et al.[23], obtained for blade-type riblets over a range of bulk Reynolds numbers between 4000 and $15,000$. The black symbols represent the direct numerical simulation (DNS) results of El-Samni et al.[69] (at $Re_{\text{bulk}} = 2821$, $Re_\tau = 180$), which fully resolve the microscopic geometry of the textured wall by explicitly modeling a corrugated surface composed of blade riblets.
The dot-dashed curve (i) corresponds to the analytical prediction for the viscous regime, as given by equation (1) with $\mu_0 = 1$. Comparison with the reference data indicates that this linear approximation accurately captures the flow behavior only up to $\ell^+ \simeq 5$, i.e., within the regime where $\Delta\lambda$ remains linearly proportional to the drag variation and higher-order effects are negligible.
The other curves represent the results obtained using effective boundary condition models.
The skin friction coefficient C_f can be defined as:

$$C_f = \frac{2\tau_w}{\rho\,(\hat{u}_{bulk})^2} \tag{2.66}$$

with $\hat{u}_{bulk}$ the temporally and spatially averaged velocity over the whole channel (of total height equal to $2H+h$). However, considering that the average velocity is only in the free-fluid region, there is a need to estimate the average velocity in the riblet layer $\hat{u}_R$, to correctly evaluate $\hat{u}_{bulk}$. From a theoretical point of view, the value of $\hat{u}_R$ is expected to lie between the velocity at the solid groove, equal to zero, and the slip velocity at the fictitious interface, $\hat{u}$slip. Accordingly, $\hat{u}_R$ satisfies:

$$0 < \hat{u}_R < \hat{u}_{slip} \tag{2.67}$$

In the present work, an intermediate estimation is adopted by assuming $\hat{u}_R \approx 0.5\,\hat{u}_{\text{slip}}$. Using the scaling $\hat{u}_{\text{slip}} \approx \lambda_x^+\, u\tau$, this leads to the following approximation:

$$\hat{u}_R \approx 0.5\,\hat{u}_{slip} \approx 0.5\,\lambda_x^+ u_\tau \tag{2.68}$$

The variable $\hat{u}_R$ can be evaluated precisely for each case, and the drag reduction coefficient can be estimated.
The dashed line, denoted (ii), corresponds to simulations based solely on Stokes-derived slip coefficients applied to the tangential velocity components, neglecting both advective effects and wall-normal (transpiration) velocity. This approach extends the predictive capability up to approximately $\ell^+ \simeq 10$, beyond which significant discrepancies arise.
The dotted curve (iii) incorporates, in addition to the Stokes slip coefficients, the transpiration velocity at the fictitious wall, as defined by equation (2.56), while still neglecting advective contributions. This model shows very good agreement with the reference data up to $\ell^+ \simeq 15$, which is the effect of incorporating the transpiration velocity, enabling a prediction of the maximum drag reduction. However, it fails to reproduce the characteristic parabolic trend of the drag reduction curve at larger riblet spacings. This limitation indicates that transpiration alone is insufficient to capture the onset of secondary flow effects responsible for the subsequent increase in drag.

Finally, the synthetic vortex pair model, which incorporates both transpiration and convective (advective) terms, yields results enclosed within the shaded region. Within the underlying microscopic formulation, a parameter $\mathcal{P}$ can be tuned around a nominal value of approximately 160. The boundaries of this region, indicated by the solid curves (iv) and (v), correspond to $\mathcal{P} = 140$ and $\mathcal{P} = 180$, respectively. The superimposed red circular markers represent simulation results obtained for these two parameter values. In this case, it is clear that the results increasingly depend on the vortex intensity as the riblets' spacing grows, and thus the choice of the forcing parameter $\mathcal{P}$ (cf. equation 2.58) becomes critical. Since the aim is not that of optimizing the agreement with previous experiments and simulations, but to develop and test practical boundary conditions which might apply to riblet configurations beyond the viscous regime, $\mathcal{P}$ has been chosen by considering the streamwise vortex pair that provides and sits above the rib, intensities in the expected range[55,54].

Figure 2.10 presents the results of the direct numerical simulations performed in the present study, employing vortex-model-based effective coefficients. The distributions of the mean streamwise velocity, $\overline{U}^+$, and the Reynolds shear stress, τ^R_{XY}, in the free-fluid region adjacent to the lower boundary are reported, and compared with the texture-resolving data of El-Samni et al.[69].

For $\ell^+ \approx 17.7$ and 27.9, the agreement between the proposed model and the reference data is overall satisfactory. Moreover, when $\ell^+ = 40.6$, the model—particularly with $\mathcal{P} = 180$ - is still able to accurately reproduce the logarithmic behavior of the mean velocity profile. A similarly good agreement is observed for the peak value of the Reynolds shear stress.

Conversely, the predictive capability of the present model deteriorates in the near-wall region, particularly in close proximity to the corrugated surface, as ℓ^+ increases.

One possible explanation for the discrepancy between the present results and those of El-Samni et al.[69] at large ℓ^+ lies in the behavior of the slip lengths (and the associated $\Delta\lambda$), which decrease with increasing riblet spacing (see Table 2.3 and the discussion in Section 2.6.).

Another possible reason concerns the spatial resolution of the DNS performed by El-Samni et al.[69]. Specifically, the number of grid points between adjacent riblets in their simulations ranges from 6 to 16 for the three values of ℓ considered. Such a resolution may be only marginally sufficient to fully capture the flow dynamics within the corrugations, potentially affecting the accuracy of the near-wall statistics.

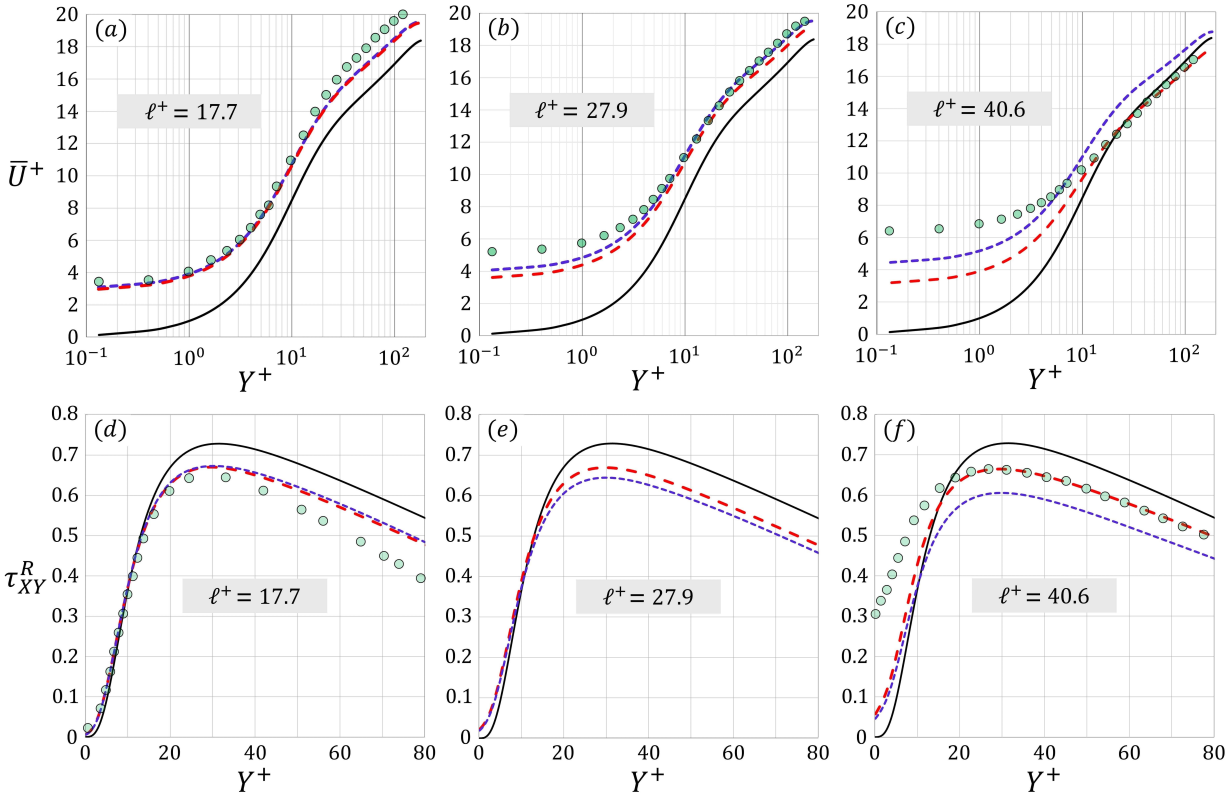

Figure 2.10: Mean velocity (top row) and Reynolds stress as a function of Y^+ for three values of ℓ^+. The solid black line reports the solution for the flow in a channel with two smooth walls. The blue and red dashed lines correspond to the results of the turbulent motion in a ribleted channel using, respectively, $\mathcal{P}$ = 140 and 180 in the model. The reference numerical data from El-Samni et al.[69] are plotted with small green circular symbols.

2.9. Conclusions and future developments

A multiscale homogenization framework has been developed to derive effective boundary conditions that accurately reproduce the flow behavior over grooved surfaces and enable reliable prediction of drag reduction. The approach begins with the definition of a microscopic near-wall domain under the Stokes approximation. It is then extended to incorporate advective effects by introducing a synthetic streamwise vortex pair above the corrugated wall.
To couple the microscopic and macroscopic descriptions, matching conditions on velocity and shear stress are formulated, ensuring consistency between the inner and outer regions. This procedure yields macroscopic boundary conditions for both the streamwise and spanwise velocity components, while also accounting for the transpiration velocity. Notably, neglecting wall-normal velocity fluctuations at the virtual wall can lead to significant inaccuracies, particularly in the modeling of riblets operating beyond the viscous regime.
The proposed framework is validated through direct numerical simulations of channel flow, where one wall is textured with blade-type riblets, demonstrating good agreement with the theoretical predictions.
The configuration with blades at the surface is probably the most difficult to simulate (in particular, with the growth of the pitch distance between blades), and previous attempts at modeling it have met with only partial success. The present model appears to be able to replicate the well-known parabolic shape of the drag curve with ℓ^+, typical of grooved patterns.
The key aspect relies on accounting for advection and transpiration, two crucial elements, especially when riblets' spacings become wider.
However, the model partially fail into predicting slip velocity and near-wall Reynolds stress when ℓ^+ is larger than 30. By improving the new model to predict the near-wall behavior of the flow by extending the model to higher orders, this inaccuracy could possibly be solved.
The central aim is to determine a universal coefficient that can effectively model diverse surface types - including rough, porous, stochastic, and realistic geometries - and reliably predict the resulting flow behavior over slip-enabled boundaries, avoiding full numerical simulations that require high numerical and computational demands.
Riblets offer significant potential for continued innovation across a wide range of applications. Promising research directions include the development of sinusoidal and converging–diverging micro-groove configurations, which may further enhance drag-reduction performance. In parallel, bio-inspired approaches provide valuable pathways for optimizing riblet geometry by drawing on naturally evolved surface structures.
Advances in material science are also expected to play a key role, enabling the design of adaptive or self-healing riblet surfaces capable of responding dynamically to varying flow conditions, thereby improving overall efficiency. In the context of growing environmental concerns and rising energy costs, riblet technology stands out as a compelling solution for reducing energy dissipation and enhancing performance across multiple industries.

Taylor-Couette instability

An experimental study has been conducted to assess the effect of circumferential periodic micro-patterns on the **onset** of Taylor-Couette **primary instability**, from an experimental and theoretical point of view. The experimental apparatus is composed of two coaxial cylinders, a stationary outer cylinder and a rotating inner cylinder, and in the gap, there is water. The outer cylinder is surrounded by 3D-printed skeletons, with micro-grooves of different shapes and dimensions. The primary instability occurs in laminar conditions, characterizing the flow by toroidal counter-rotating vortices elongated along the vertical directions. An asymptotic upscaling analysis, considering the micro-domain in the near-wall groove region and a macro domain represented by the gap, is then conducted to estimate the slip lengths (azimuthal and axial) of the axially-periodic microgrooves. A linear stability analysis is carried out to infer the critical parameters for the onset of Taylor vortices, under conditions of differential slip evaluated through the upscaling technique. The experimental-theoretical results are then compared, and they are in good agreement. The presence of grooves promotes the **delay** of primary instability, meaning that it occurs at higher speeds. This positive effect is highlighted only when *virtual* dimensions are introduced to account for the virtual origin of the mean azimuthal flow, and the parameters are properly rescaled.

3.1. Introduction

3.1.1. Taylor-Couette flow and instabilities

A Couette flow arises from the relative motion between two bounding surfaces separated by a viscous fluid. In its simplest configuration, this corresponds to flow between two infinite parallel planes, a canonical case that admits an analytical solution. An alternative and widely studied configuration is provided by the flow between two coaxial cylinders, commonly referred to as Taylor–Couette flow, which can be formulated and solved within the framework of the Navier-Stokes equations expressed in cylindrical coordinates.
In the cylindrical configuration, the inner and/or outer cylinders are set into steady rotation. Different flow regimes can be realized, including cases where the inner cylinder rotates while the outer one is stationary, the opposite configuration, or counter-rotation of both cylinders. This geometry is particularly convenient from an experimental standpoint, as it is commonly employed in rotational rheometers.
The choice of Taylor–Couette flow as the test configuration for the present study is motivated by two main considerations. First, it represents a hydrodynamic system for which an excellent level of agreement between theoretical predictions and experimental observations has been consistently demonstrated. Second, the presence of centrifugal effects promotes the formation of coherent vortical structures, known as Taylor vortices, even at relatively low rotation rates. These structures act as efficient mechanisms for the transport of momentum and energy, playing a role analogous to that of near-wall streaks and quasi-streamwise vortices in turbulent wall-bounded shear flows. Consequently, this configuration provides a suitable framework for investigating the influence of surface roughness, including riblet-like textures, even in regimes characterized by relatively low flow velocities.
The Taylor-Couette (TC) flow is characterized by the formation of flow instabilities between the two coaxial cylinders. The onset of instabilities across various flow regimes has been studied since the last decades of the 19th century by Mallock[71] and by Couette[72]. Lately, G.I. Taylor in 1923 largely investigated the Taylor-Couette flow instabilities[73], solving the problem of the linear stability of the Couette flow in a curved geometry. The study focuses on identifying, from an analytical and experimental point of view, that the flow becomes unstable when the inner cylinder exceeds a critical rotation speed, leading to the formation of toroidal vortices, so-called Taylor vortex. Subsequently, other instability phenomena emerged in this flow regime, such as the non-axially symmetric spirals identified by Coles in 1965[74]. An extensive research programme has been carried out investigating rotating cylinders; a collection of all the experimental and theoretical data culminated in 1986 with the publication by Andereck[75].
The following figure 3.1 summarizes the different flow regimes, the vortex configurations, and critical conditions. The appearance of these structures depends on the ratio of the cylinders' rotational speeds ω_o/ω_i and the ratio of the cylinders' radii r_i/r_o (where the subscript *i* denotes the inner cylinder, *inner*, and the subscript *o* denotes the outer cylinder wall, *outer*).

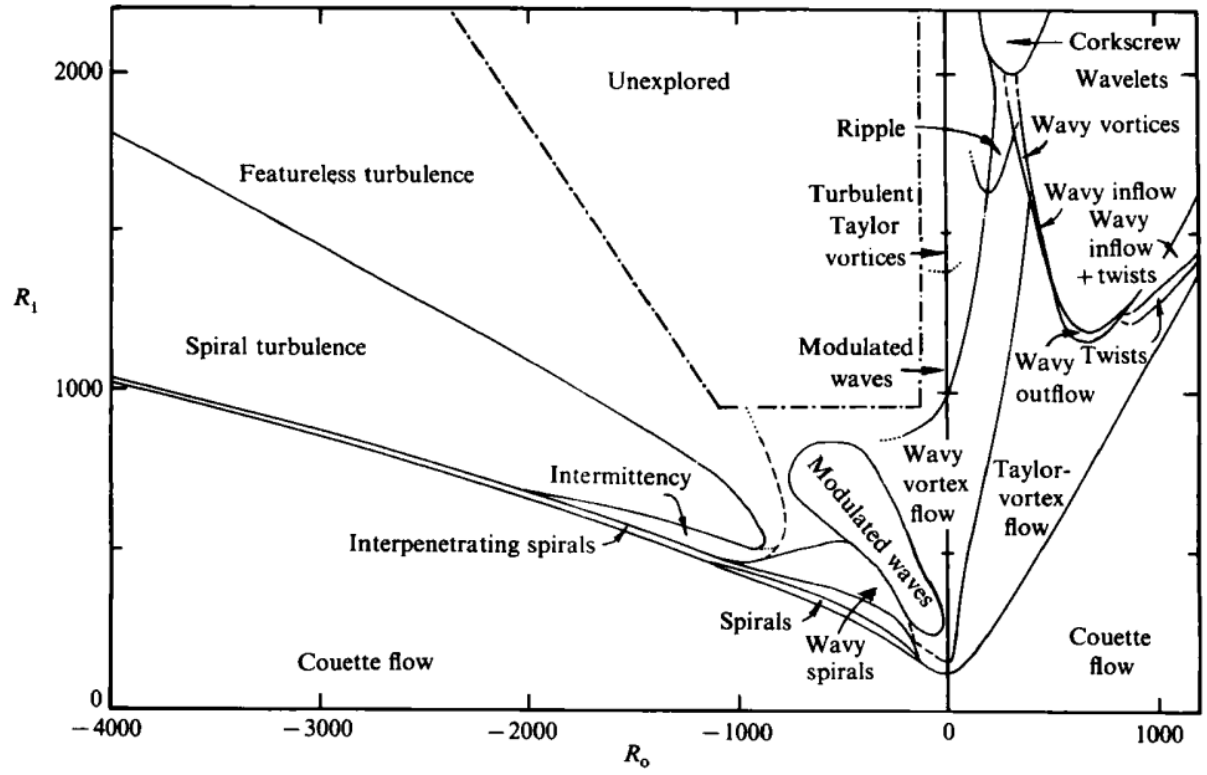

Figure 3.1: Flow regimes observed between independently rotating coaxial cylinders. The horizontal axis represents outer Reynolds number R_o, and the vertical axis shows inner Reynolds number R_i. Negative value of R_o stands for counter-rotating direction. Dashed lines indicate the transition boundaries, and the dotted-dashed lines indicate the expected continuation of several boundaries.[75]

When the outer cylinder is fixed, $R_o = 0$, so following the vertical solid line, the subsequent stages can be identified.
In laminar conditions, first of all, a Couette flow is created, then by increasing the inner rotational speed, the first instability occurs, creating Taylor-vortex flow, moving forward, then there is the secondary instability - Wavy vortex flow. Then, these vortical structures start to break, moving to a transitional flow that leads to turbulent Taylor vortices, characterized by chaotic mixing of the flow structure.
From an experimental point of view, vortical structure has been clearly identified, and the following images, taken by[75], show the early stage formation and the Taylor vortex and Wavy vortex flows. Starting from Fig. 3.2 and following the other images, the evolution of the flow structures is described from the first end effects and moving to the global vortical effects, in the case of counter-rotating concentric cylinders.

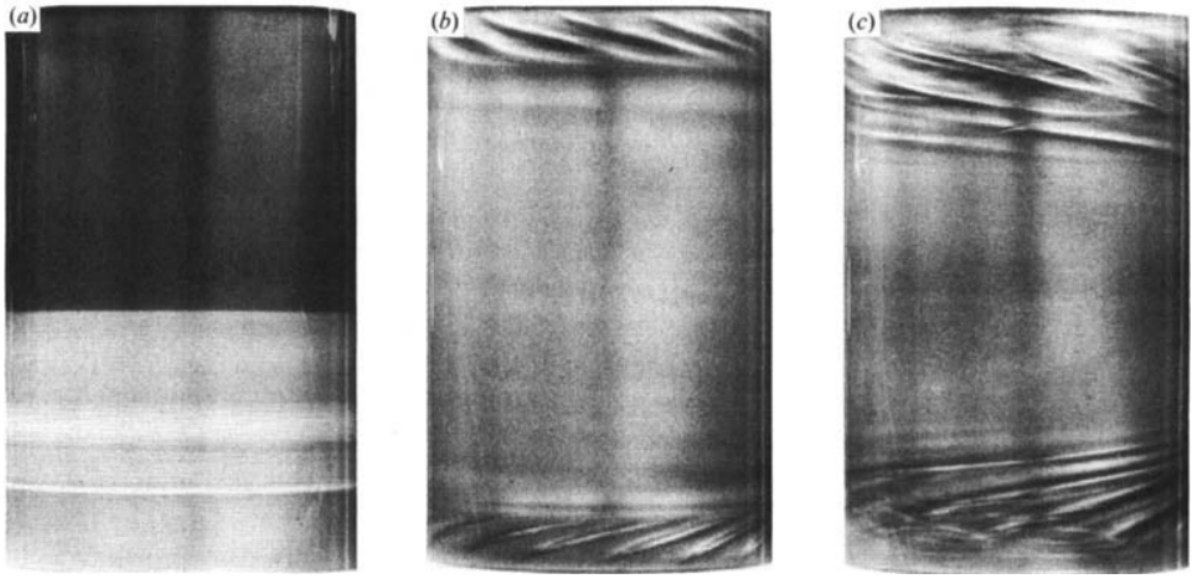

Figure 3.2: From left to right: (a) outer cylinder rotating, inner cylinder at rest: R_o = 1000, R_i = 0. Co-rotating cylinders: (b) R_0 = 1000, R_i = 1124; (c) R_0 = 4005, R_i = 4520. Kalliroscope flakes have been added to the cell in the lower half of the cylinder at rest, and then as both cylinders started rotating, end effects appear.[75]

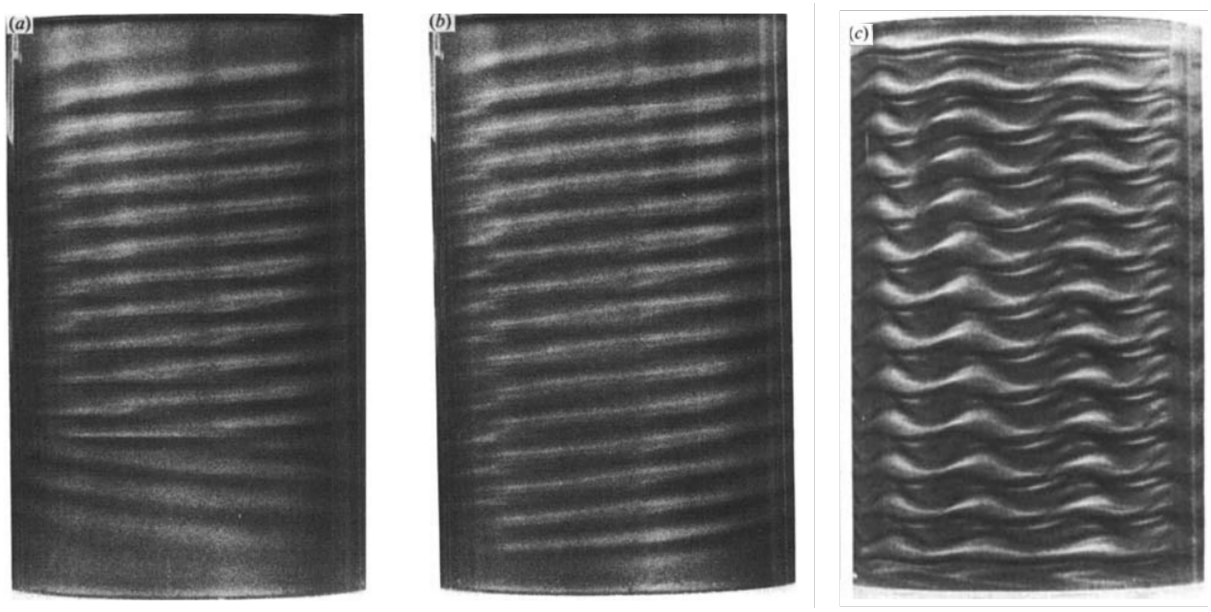

Figure 3.3: From left to right. Images (a) and (b) show Taylor vortex flow. The outer cylinder Reynolds number is R_o = -300, and for the inner cylinder is R_i = 240. Image (c) represents the Wavy vortex flow. Outer cylinder R_o = -100, inner cylinder R_i = 350.[75]

3.1.2. Literature review on slippery surfaces in TC flow

In the last few decades, much attention has been paid to non-smooth walls, rough or patterned surfaces, superhydrophobic or lubricant-impregnated material; the increasing attention has been driven by the potential for drag reduction application, provided by slippery surfaces and materials, in laminar and turbulent flow conditions.
Investigating superhydrophobic surfaces, several theoretical, numerical, and experimental studies have been developed. The main outcomes are listed below.
Naim and Baig[76] performed direct numerical simulations to assess the effect of superhydrophobic surface patterns on drag reduction in turbulent Taylor–Couette flow. Modeling the plastron–liquid interface as undeformable and shear-free, they found that streamwise-aligned microgrooves provide the highest drag reduction (up to 34% at $Re = 5,000$), whereas spiral grooves lead to a slight drag increase. The observed behavior was attributed to wall slip, which modifies near-wall turbulence and reduces the production of velocity fluctuations and turbulence kinetic energy.
Liu et al.[77] combined experiments and modeling to investigate air-filled V-shaped azimuthal microgrooves on the inner cylinder of a Taylor–Couette system. Drag reduction up to 62% has been reported at $Re = 2.79 \times 10^4$. The air-filled grooves induce wall slip, weakening Taylor vortices and reducing momentum transport. Increased groove width enhances this effect, and the dependence on groove spacing can be predicted.
[78] demonstrates a reduction in the wall shear stress that can be translated into drag reduction, in the turbulent Taylor-Couette flow regime. The maximum drag reduction registered has been up to 22 % at a Reynolds number of $Re = 8 \times 10^4$.
However, as previously discussed, superhydrophobic surfaces are more prone to fail under high shear flow conditions, because the gas plastron can be replaced by the external fluid and gradually fully replaced, exposing the rough surface directly to the flow and affecting the durability and efficacy of the SHS surface. This promotes the study of liquid-infused surfaces.
The case of corrugated surfaces impregnated with a liquid lubricant was considered by Van Buren and Smits[43]. The experimental setup is shown in the next figure. The outer cylinder rotates around the treated, stationary inner cylinder. Torque measurements have been in performed on the inner cylinder in the TC apparatus. The study reported a maximum drag reduction of approximately 35% at a Reynolds number of around 10^4, in the case of LIS inner cylinder; the reduction was found to be stable over time, indicating the potential for sustainable performance of lubricant-impregnated surfaces in practical applications.

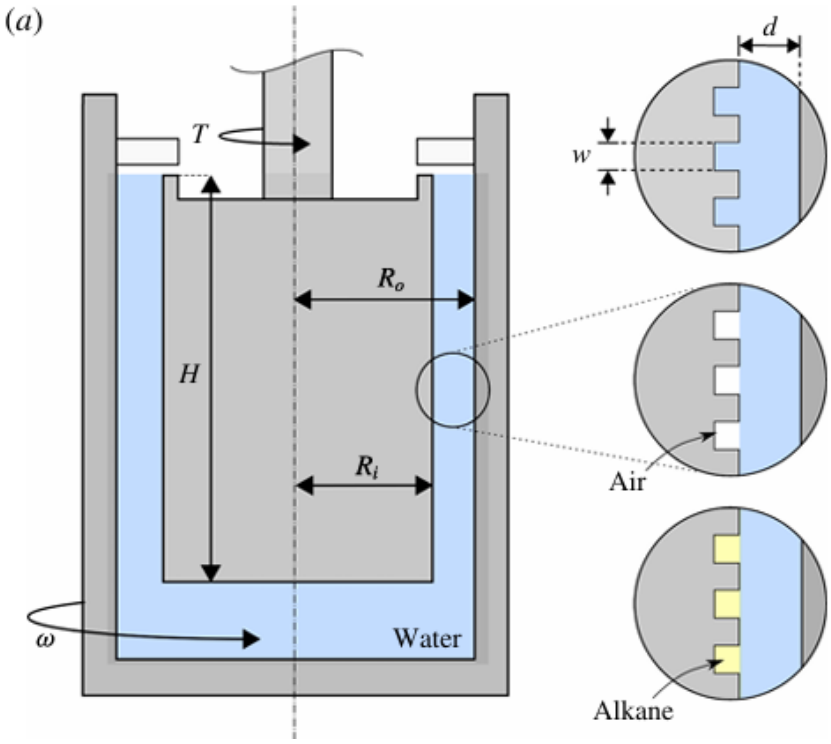

Figure 3.4: Sketch of the experimental apparatus of the Taylor–Couette facility, filled with water. Longitudinal grooves are tested in three different conditions: micro-grooved surface, superhydrophobic functionalization (air trapped within the microgrooves), liquid-infused surface - impregnated with alkane oil.[78]

In the absence of a lubricant, longitudinal microgrooves are commonly referred to as riblets[17,8,23]. Within Taylor–Couette (TC) flow, the investigation of V-shaped azimuthal riblets was initiated by Hall and Joseph[79], who examined their drag-reducing capability in a configuration with a corrugated inner cylinder and a rotating outer cylinder. A more detailed study by Greidanus et al.[80], including tomographic PIV measurements, introduced a model to separate the effects of riblets and cylinder rotation, showing that drag reduction depends strongly on the flow regime and can reach up to 3.4% beyond a threshold shear Reynolds number.
The experiments of Xu et al.[81] extend this analysis beyond the fully turbulent regime, covering Re from 160 to 18,700. Transition was identified at $Re_{\mathrm{trans}} \approx 1380$ (for $\eta = 0.7$). Below this threshold, drag reduction is associated with the weakening of primary Taylor vortices, with further reductions observed for increasing Re and groove size. Above transition, however, surface roughness leads to drag increase. These findings are consistent with the immersed-boundary DNS of Zhu et al.[82], which showed that, at higher Re, the boundary layer thickness becomes smaller than the groove height, promoting secondary flows and enhancing torque. While the effect of riblets on modal and non-modal instabilities in plane channel flow has been addressed[83], their influence on the Taylor-Couette flow has never been investigated.

3.1.3. Present study

The primary instability of Taylor–Couette flow remains largely unexplored. This is a crucial aspect to clarify whether specific roughness patterns can delay or promote the onset of centrifugal instabilities. Moreover, it provides a necessary foundation for more complex configurations involving higher rotation rates and advanced surface treatments, such as superhydrophobic or lubricant-infused coatings.
The present work aims to address this gap in the literature by a combined experimental/theoretical approach, investigating the primary TC instability in the presence of axially periodic, azimuthally invariant wall corrugations. The most innovative aspects of the study are:

I. torque-based measurements to quantify the onset of the primary instability for micro-grooved inner cylinders;

II. evaluation of anisotropic effective slip lengths, through an upscaling derivation, for realistic, three-dimensional printed grooves via asymptotic homogenization;

III. incorporation of these effective boundary conditions into a linear stability analysis;

IV. introduction of a virtual origin of the mean azimuthal flow to rescale the critical parameters of the problem, observing a systematic delay of the instability governed by the differential slip length.

The experiments are described in Section 3.2. and results in Section 3.3. are shown for a few wall groove shapes and dimensions. The experimental apparatus is a rheometer with a stainless steel inner rotating shaft surrounded by stereolithographic 3D-printed sleeves, each with different circumferential grooves. The effect of micro-grooved patterns is addressed in the present study.
The inner cylinder is forced to rotate at angular velocity $\Omega = \frac{\pi}{30}\dot{n}$ (with Ω denoting the angular velocity measured in radians per second and $\dot{n}$ the rpm velocity). Considering the smooth case of the inner cylinder and defining the inner and outer radii as, respectively, R_i and R_o, the control parameter is the Taylor number, Ta, conventionally defined as:

$$Ta = \frac{2\,\eta^2}{1-\eta^2}\frac{\Omega^2\,d^4}{\nu^2} = Re^2\,\frac{2\,d}{R_i+R_o}. \tag{3.1}$$

with $d = R_o - R_i$ is the gap between the cylinders, $\eta = R_i/R_o$ is the radius ratio, and ν is the kinematic viscosity of the fluid, evaluated based on the fluid temperature during the test. The parameter Re is the Reynolds number, defined as $Re = \Omega R_i\,d/\nu$. In the so-called narrow gap case, when $\eta \to 1$, the onset of steady toroidal vortices is found for the following *critical* parameters: $Ta_c = 1708$ and $\beta_c = 3.117$[84], with β the axial wavenumber.
The effect of inhomogeneities at the inner cylinder wall is addressed from a theoretical perspective: an asymptotic upscaling analysis is conducted for the purpose of estimating the realistic

and idealized slip lengths (azimuthal and axial) of the microgrooves (section 3.4.).
These conditions are then used in a linear stability analysis, described in Section **??**, performed to establish the critical parameters for the onset of Taylor rolls under conditions of differential slip.
Considering that the presence of grooves shifts the flow's virtual origin, virtual dimensions are introduced, and in combination with the proper rescaling of the parameters, demonstrate that the instability is delayed by the wall corrugations.
Good agreement between theory and experiments has been demonstrated, and it represents the starting point for further studies on more complex slippery surfaces (SHS and LIS), at even higher rotational speeds.

3.2. The experimental apparatus and the results

3.2.1. Description of the experimental apparatus

Rheometric setup

The experimental apparatus is shown in Figure 3.5. The core instrument of the experimental setup is the Anton Paar Physica MCR 301 rheometer. It is equipped with a highly precise rotational electric motor, shaft-connected to the inner cylinder, and supported by an air bearing. This allows the inner shaft to rotate almost frictionlessly; furthermore, it has high sensitivity for torque and angular displacement, allowing very accurate measurements for all conditions tested. In particular, the torque is measured using a strain-gauge-based transducer with a resolution in the $nN\,m$ range, while the angular velocity is imposed and monitored by an electronically commutated synchronous motor equipped with optical encoders. These encoders provide highly accurate angular position measurements, from which the angular velocity is precisely determined.

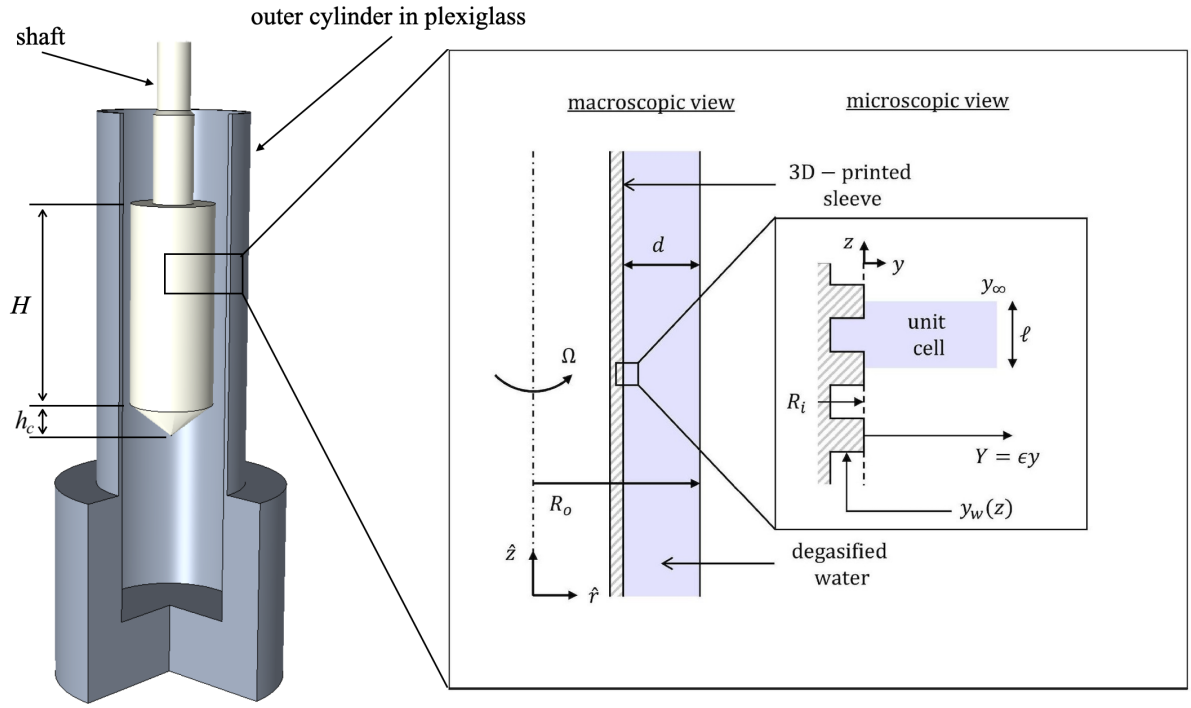

Figure 3.5: Left: schematic of the experimental apparatus in the smooth configuration, showing the stationary outer cylinder and the rotating inner cylinder, whose shaft is connected to the electric motor. Right: magnified view of the grooved sleeve, illustrating both the macroscopic and microscopic representations of the system.

The inner cylinder, made of stainless steel, has a diameter of $D_i = 25$ mm and a height equal to $H = 60$ mm. The inner cylinder is freely suspended, and it ends with a conical tip at the bottom, with a corresponding height of $h_c = 10$ mm. It is inserted coaxially into an outer fixed cylindrical plexiglass case, placed and blocked in a holder, which is part of the rheometer itself.
To investigate different micro-structured patterns and to study the effect of azimuthally-invariant surface structures on the onset of the instability, several polymeric sleeves have been 3D-printed with stereolithography technology and properly placed and fixed around the inner cylinder. Whereas the inner radius R_i of the cylinder–sleeve assembly is approximately 19 mm (the exact value, reported below, depends on the specific micro-pattern and on the corrugation pitch ℓ), the outer radius R_o is fixed at 20.64 mm.
In the right image of the Figure 3.5, a magnified view of the grooved skeleton is presented. In particular, the existence of two well-separated domains is pointed out. The macroscopic region has the gap dimensions $d = R_o - R_i$, as a characteristic length; the microscopic domain is instead characterized by the axial periodicity of the roughness ℓ. The ratio between the microscopic characteristic length and the macroscopic one, defines a small parameter ϵ, variable then used for the asymptotic expansion of Section 3.4.. The unit cell or representative element of volume (REV) is defined, and it includes one periodic element of roughness.
As the inner cylinder starts rotating, it drives the water in the gap around the central element, eventually leading to the formation of Taylor-Couette vortices.
The water has a free surface exactly in correspondence with the outer edge of the inner cylinder, which remains wet throughout each test; we have verified that the free surface remains flat and unperturbed when the angular velocity of rotation is sufficiently small, while low-amplitude surface waves develop at larger velocities.

The microstructured sleeves

Hollow cylinders are designed for later printing, with two types of azimuthally-invariant microgrooves on the lateral surface, a trapezoidal and a square shape (denoted respectively by "T" and "S"). The CAD design of microstructured skeletons has been done using Onshape.
The print has been realized by a laser-powered stereolithographic printer produced by Formlabs (Model Form3); it is an additive manufacturing technology for thermosetting polymers. The method is based on the photopolymerization of a liquid resin, which is sensitive to the ultraviolet radiation emitted by a laser source. The technique allows, in principle, greater geometric accuracy than normal extrusion 3D printing. The polymeric resin used (Clear Resin, also produced by Formlabs) is specifically designed for high-resolution models.
A black dye has been added to the liquid resin, colouring the batch in order to obtain black samples instead of white/grey ones. One of the main reason of adding a dark dye is to allow for a better visualization of the flow structure, enabling the visual tracking of Taylor-Couette flows. Beyond that, this modification permits the laser analysis of each 3D-printed sample to assess the exact shape and dimensions of the micro-patterns, leading to the characterization of the grooves.
The following Figure 3.6 shows the idealized shape of the unit cells. The axial periodicity ℓ of the periodic pattern is set to be either 1000 μm, 800 μm, or 400 μm. The different patterns are thus named $T1000$, $S800$, etc., to distinguish among them. These shapes are the idealized

shapes.

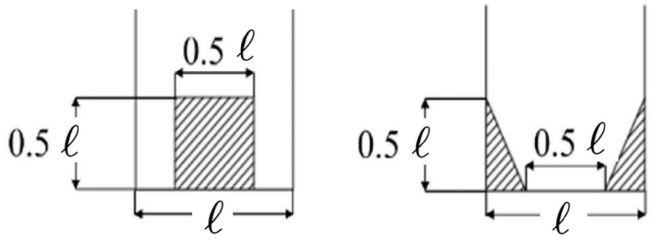

Figure 3.6: Idealized shape of the unit cells for S and T micro-grooves.

Minor printing artifacts and defects are observed in the fabricated samples, leading to deviations from the intended ideal geometries and resulting in real configurations that may not achieve the expected level of precision. Furthermore, the additive manufacturing process itself introduces uncertainties. In the case of stereolithography, although the nominal minimum printable feature size is approximately 25 μm, empirical observations indicate that larger discrepancies can occur in practice.
Given that the geometrical dimensions represent critical parameters for the present study, it is essential to accurately characterize the actual configuration of the 3D-printed components. Although the designs were based on ideal geometries, the presence of printing-induced artifacts led to measurable variations, which were systematically evaluated using laser profilometry and microscopy techniques.
Different approaches have been used to characterize the grooved surfaces, including high-resolution imaging with a camera, optical microscopy, and profilometry. The first technique allows the verification of the periodicity of the riblets and a more qualitative view of the patterns. The next image 3.7 shows an example of a picture, obtained using a high-resolution camera.

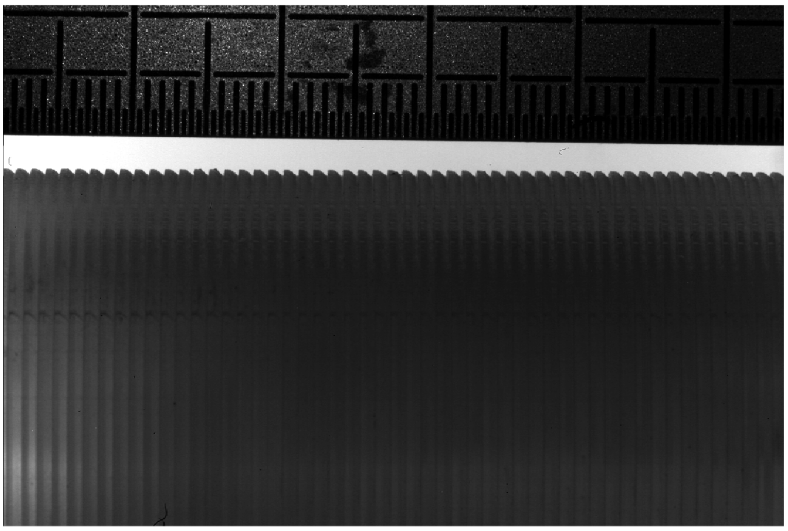

Figure 3.7: Image of sample S1000 captured with high resolution camera.

The second technique used is optical microscopy. In particular, looking at the sample from the top, to obtain and measure the riblets' spacing.

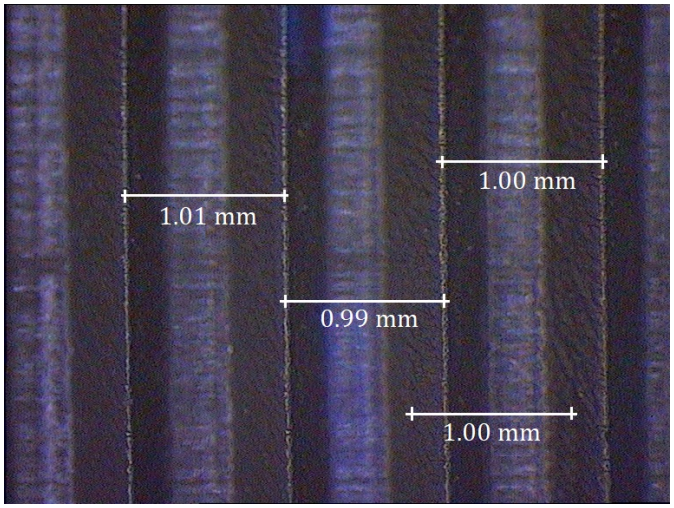

Figure 3.8: Optical microscopy of $T1000$ sample. Riblets' spacing is measured and the periodicity ℓ is indicated in the image.

Optical microscopy also enables the identification of surface defects in the fabricated samples. The occurrence of such defects may be attributed to various factors, including the printing process itself, post-curing procedures, the removal of polymeric supports, or other process-related variables.
The following image highlights a localized defect within the microstructure, most likely originating from the mechanical configuration of the 3D printer. This defect is observed in the sample featuring a trapezoidal geometry with a periodicity of 800.

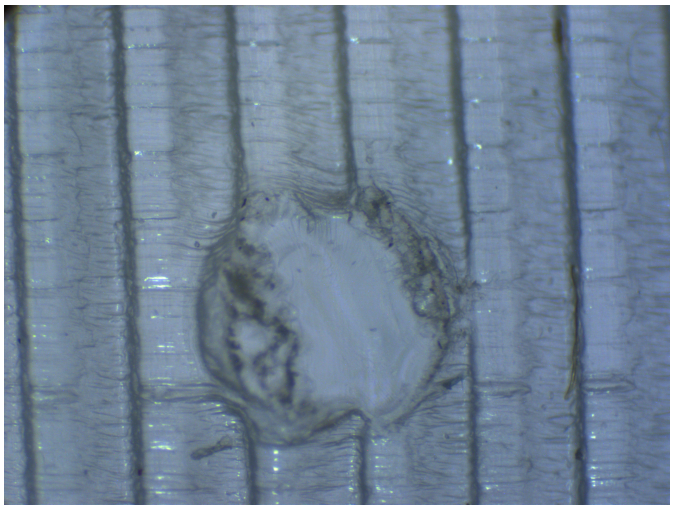

Figure 3.9: Optical microscopy of $S800$ skeleton with a defect.

However, both of these approaches are more concerned with the qualitative analysis of surface quality. To obtain a detailed reconstruction and an accurate model of the sample surfaces, the third technique has been used through the utilization of a *Taylor Hubson* laser profilometer (*Ametek's Ultra Precision Technologies Group*).
A surface profilometer is a metrological instrument employed to characterize the topography of a specimen, particularly for the reconstruction and quantification of surface roughness. The technique relies on multipoint laser-based measurements capable of resolving surface height variations at a sub-micrometer scale; in the present case, a vertical resolution of 0.159 μm was achieved. All the samples have been tested following the same procedure and adopting the same parameters and methods.
A surface equal to $\sim 3mm \times 3mm$ has been scanned by the laser and then reconstructed in three different possible ways: a y-diagram, a planar surface, and a 3D-reconstruction of the sample. Two examples are reported below for the case of T400 and S1000 samples.
An examination of the surface topography reveals that the trapezoidal structures, despite exhibiting a smaller periodicity compared to the square configuration in the example reported, maintain a highly regular pattern with well-defined peaks and valleys. In contrast, the square geometries appear less precise, particularly in the vicinity of the right-angle corners, where noticeable deviations from the intended shape are observed. These discrepancies are likely attributable to limitations inherent to the fabrication process. Specifically, the layer-by-layer nature of the printing technique may reduce accuracy in regions characterized by sharp geometrical transitions. Additionally, post-curing effects may have introduced further distortion or deformation, contributing to the observed imperfections in the final structures.

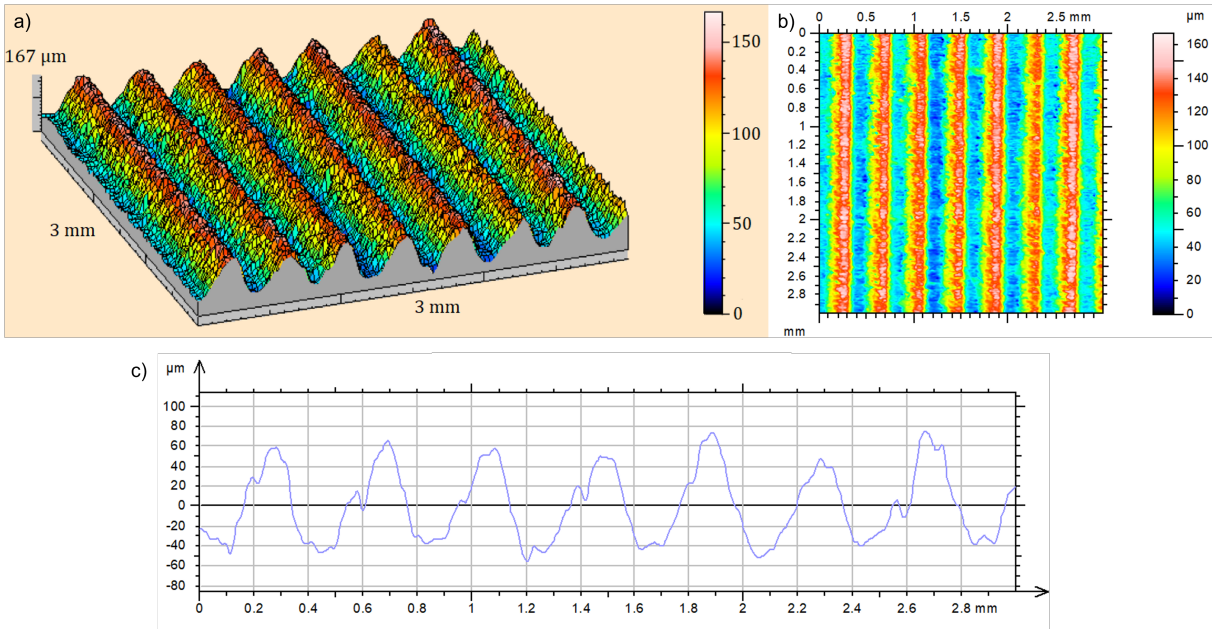

Figure 3.10: a) Three-dimensional reconstruction of the realistic shapes of $T400$ (color scale in μm). b) Planar plot of the top section captured. c) y-diagram, showing picks and valleys.

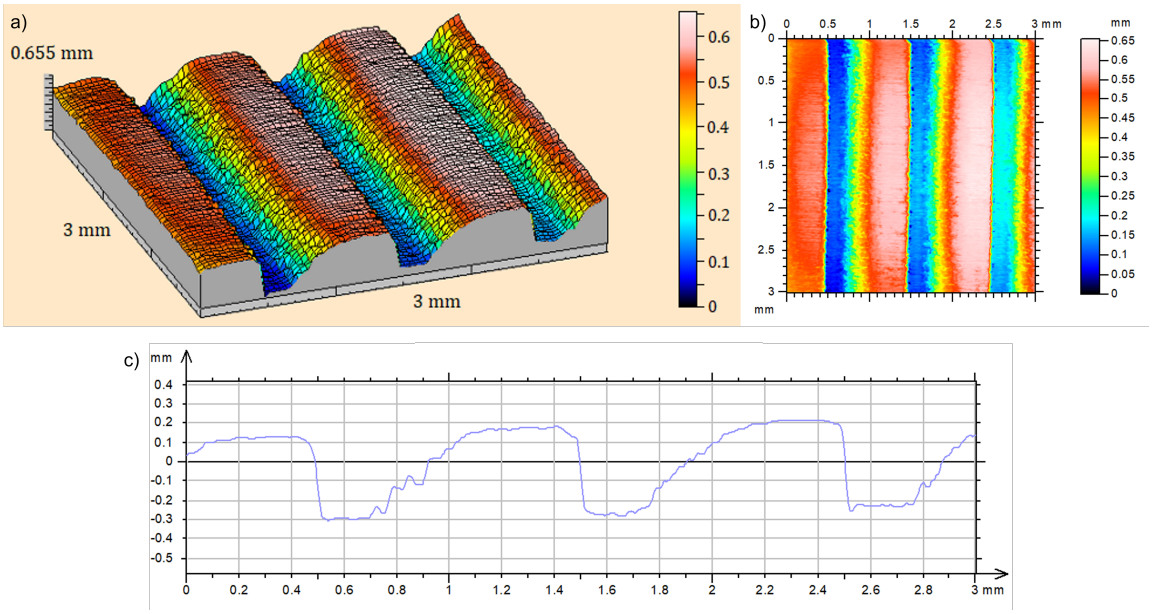

Figure 3.11: a) Three-dimensional reconstruction of the realistic shapes of $S1000$ (color scale in μm). b) Planar plot of the top section captured. c) y-diagram, showing picks and valleys.

The dimensions of the printed samples are reported in Table 3.1.
The measurements of ℓ are obtained directly from laser profilometry, whereas the dimensions R_i, R_o, and H are determined using a digital caliper with a resolution of 0.01 mm. To ensure statistical reliability and capture potential spatial variability - especially related to some coaxial misalignment - measurements are performed at multiple locations distributed along both the axial and azimuthal directions. This approach enabled the determination of representative mean values and the assessment of measurement dispersion. The root mean square (RMS) deviation associated with the measurement of H is consistently below 0.20 mm across all tested samples, while the RMS deviations for R_i and R_o remained below 0.08 mm. Concerning the rib periodicity ℓ, the deviation from the nominal value is found to be less than 0.01 mm in all cases.

	R_i [mm]	R_m [mm]	d [mm]	ℓ [mm]	$\eta = R_i/R_o$	$\delta = d/R_i$	$\epsilon = \ell/d$
smooth cylinder	18.36	19.50	2.28	–	0.890	0.124	–
$T400$	18.70	19.67	1.94	0.40	0.906	0.104	0.206
$T800$	18.85	19.74	1.79	0.80	0.913	0.095	0.447
$T1000$	18.95	19.79	1.69	1.00	0.918	0.089	0.592
$S800$	18.82	19.73	1.82	0.80	0.912	0.097	0.440
$S1000$	18.96	19.80	1.68	1.00	0.919	0.089	0.595

Table 3.1: Measurements of the 3D-printed micro-roughness elements. "smooth cylinder" stands for a smooth sleeve of thickness equal to 5.86 mm, positioned around the inner, stainless steel cylinder. Each sleeve is $H = 60$ mm high, within ± 0.20 mm, i.e., the inner cylinder is completely covered. $R_m = (R_i + R_o)/2$ is the mean radius; δ is the curvature parameter, and ϵ, used in the homogenization analysis, is the ratio of microscale to macroscale.

3.2.2. Experimental settings

Before each experimental test, water has been degassed and seeded with tracer particles. Hollow glass spheres (Dantec Dynamics HGS-10 Hollow Glass Spheres) of a mean diameter equal to 10 μm and density very close to the density of water have been added to visualize the vortices. The concentration of these particles in the water is always kept below 1%wt. Other particles have been tested, like PAS Polyamid Seeding Particles $1.03g/cm^3$ ϕ=50 μm and HGM Hollow Glass Microspheres $0.38g/cm^3$, but no one has the same efficacy as the one selected. Hollow glass spheres look like powder, but, if properly mixed in the sonicator for 5-10 minutes, they are uniformly distributed in the liquid.
Before running the test, the temperature of the water is measured using a thermocouple; once the test is finished, the measurement of temperature is repeated, and the average value is used to evaluate the flow properties for each experiment.
A systematic analysis of the thermal variations associated with water temperature is conducted, highlighting their significant influence on the evaluation of the critical parameter.
The stainless steel inner cylinder is fitted with the microstructured sleeves, ensuring precise alignment and continuity between adjacent elements. Particular care is taken to avoid the formation of geometric discontinuities, such as small steps at the top internal interfaces, which could otherwise act as sources of secondary flows or flow disturbances. The interference fit between the inner cylinder and the sleeves is minimal; the components are securely fixed, preventing any relative motion during the test. The final assembly constitutes the effective inner cylinder, which is subsequently connected to the rheometer shaft and properly mounted within the instrument for testing.
Subsequently, the Taylor-Couette setup is filled with the water + HGS liquid mixed solution, up to the top surface of the inner cylinder, carefully avoiding the formation of bubbles inside the setup, while the cell is filled.
The rotational speed settings are kept constant across all experiments. Each test is initiated by rapidly accelerating the shaft to an angular velocity of n = 20 rpm, followed by a waiting period of several minutes to ensure that steady-state conditions are reached. Subsequently, the rotational speed is increased in increments of 0.5 rpm and maintained at each step for 30 s, up to a maximum of 50 rpm, while continuously recording the torque. Then the test is stopped and the temperature of the water is immediately measured. It has been observed that the water temperature can vary partially during each experiment, by a maximum of 1 °C between the beginning and the end.

3.3. Results of the experiments

The experimental apparatus measures the torque while the rotational speed is increasing; in particular, one data point is recorded each 0.5 rpm step for a total of 61 data points collected. As expected, the torque increases with increasing angular velocity because of the increasing torque required to drive the inner cylinder at higher rotation rates.
At low speeds, the torque exhibits an approximately linear dependence on the rotation rate. However, beyond a critical threshold, a marked change in slope is observed. This deviation is indicative of the onset of secondary flows, which alter the distribution of shear stresses within the gap and consequently increase the torque required to maintain the imposed angular velocity. Transition is classically observed and identified by a sudden variation in the slope of the torque curve as a function of $\dot{n}$: this is a sign that vortical structures have appeared, modifying the shear stress at the wall. Similarly, the following instabilities can be detected and recognized in the same way. Secondary instability is characterised by wavy vortex flow. Vortical structure begins to wave, creating upward and downward velocity fluctuations that modify the shear stress at the inner wall. This leads to further changes in the torque response.
To ensure reproducibility and robustness of the measurements, each experimental run is repeated multiple times. Both increasing and decreasing angular velocity ramps are performed to assess and exclude potential hysteresis effects. Each experiment has a typical duration of approximately 30 minutes.
Different patterned configurations have been investigated: a smooth case, tested as reference, 3 different periodicities for the trapezoidal shape, and 2 configurations for the square shape. The following plot compares the smooth cylinder and the $S1000$ cases.

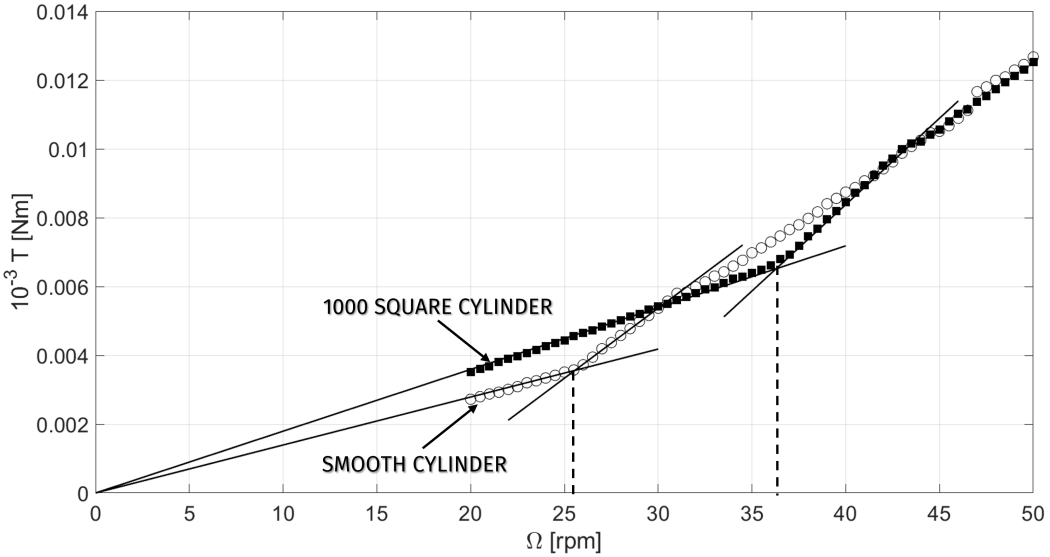

Figure 3.12: Torque as a function of rotational speed. Circular markers denote the smooth-cylinder configuration, while black square markers correspond to the $S1000$ case. The dashed lines indicate the critical rotational speed associated with the onset of the primary instability.

A preliminary assessment suggests that the grooved surface produces:

- an increase in shear stress at the inner wall, which leads to an increased of the required torque;
- a delay in the onset of the primary transition.

The apparent increase in wall shear stress can be explained by accounting for the difference in gap dimensions between the corrugated and smooth configurations. Regarding the transition, the angular velocity at the first bifurcation point shifts from 25.5 ± 0.3 rpm, in the smooth case, to 36.3 ± 0.3 rpm, in the corrugated configuration.
Before drawing any conclusions, the results must be suitably normalized. Variations in fluid viscosity, as well as in the effective geometrical parameters of the test section, exert a significant influence on the measurements.
Therefore, a consistent and appropriate normalization procedure is essential to enable meaningful comparison across different experimental conditions. The raw experimental data, both the torque and the angular velocity, have been normalized, defining a torque coefficient and the Reynolds number or Taylor number.
All the dimensionless numbers are consistently based on the mean density and kinematic viscosity corresponding to the specific experimental conditions. Within the temperature range of 24–26 °C, the fluid density ρ varies only slightly, from 997.3 to 996.8 kg,m^{-3}, while the kinematic viscosity ν decreases from 0.9132×10^{-6} to 0.8729×10^{-6} m^2,s^{-1}. The exact value of fluid properties is used to define the dimensionless parameters for each test.
The torque coefficient c_T is defined as:

$$c_T = \frac{\mathcal{C}}{\pi \rho \, \Omega^2 R_i^4 H} \tag{3.2}$$

and the Reynolds and Taylor numbers are defined as:

$$Re = \frac{\Omega \, R_i \, d}{\nu} \qquad Ta = \frac{2\,\eta^2}{1-\eta^2} \frac{\Omega^2 \, d^4}{\nu^2} = Re^2 \, \frac{2\,d}{R_i + R_o}. \tag{3.3}$$

Dimensionless results for both trapezoidal and square groove geometries are presented in Fig. 3.13.
For all the patterned configurations, the primary instability is clearly identified by a sharp change in the slope of the torque curve at $Ta \approx 1700$ (precise values are reported later). A secondary transition to wavy vortex flow is also discernible at Taylor numbers slightly above 2000. Interestingly, for the trapezoidal corrugations, the dependence of the primary instability threshold on the groove pitch is not strictly monotonic. In particular, the case with $\ell = 800, \mu$m (red curves) exhibits an earlier onset of the first bifurcation compared to the other configurations (see Table 3.5 for quantitative values). This apparent inconsistency can be rationalized by noting that dimensionless parameters such as Re and Ta can be meaningfully compared across configurations only when the radius ratio is held constant. In the present study, η varies slightly between cases (cf. Table 3.1). Moreover, each surface topology introduces a distinct *virtual origin* for the primary flow, thereby affecting the effective flow geometry. A detailed discussion of this concept and its implications is deferred to Section 3.5..

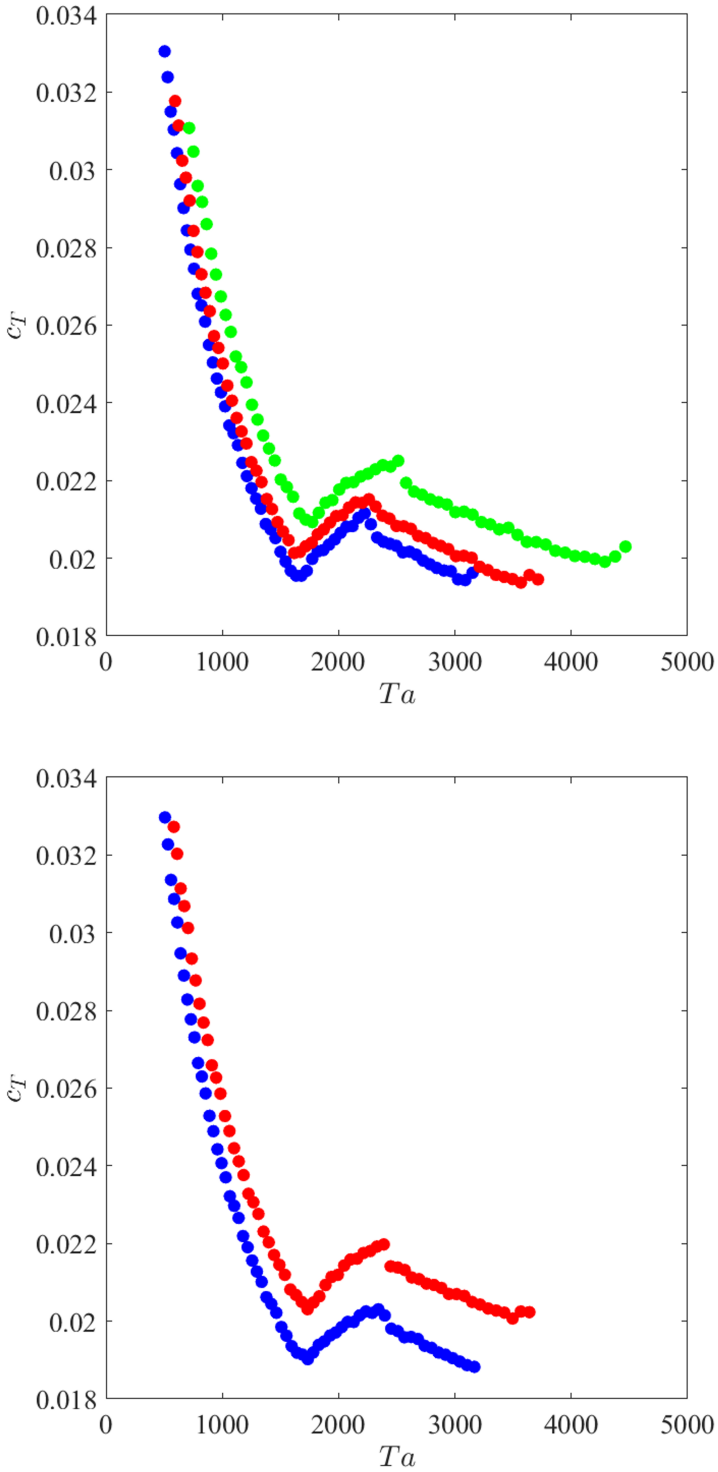

Figure 3.13: Torque coefficient versus the Taylor number for trapezoidal (top) and square (bottom) surface corrugations. The green markers correspond to $\ell = 400$ μm, the red markers represent the data of the cases $\ell = 800$ μm, and the blue ones $\ell = 1000$ μm.

Representative flow visualizations are presented in Figure 3.14 for the $T800$ configuration, captured slightly below and slightly above the onset of the primary instability.
In the left panel, only the surface grooves are visible, but it can be noticed by looking at the bottom part of the figure that the fluid has a white colour, because of the hollow glass spheres that are mixed with it. In the right panel, the addition of glass particles to the working fluid enables visualization of the emerging vortex structures.
In particular, inspection of the right panel reveals a series of regularly spaced, brighter bands, which mark the formation of sinks associated with regions of radially inward flow. The tracer particles tend to accumulate within the cavities formed by the grooves, leading to localized trapping. This phenomenon introduces significant challenges in accurately determining the spacing between adjacent vortical structures.
Moreover, the grooved geometry may exert a receptive influence on the selection of the instability wavenumber. To mitigate uncertainties in the wavelength estimation, the reported wavenumbers are obtained by averaging measurements over the six centrally located vortex pairs. Image acquisition is carried out using a Fujifilm X-T200 mirrorless camera equipped with an 18–35 mm lens, yielding 24-megapixel images. These are subsequently processed using ImageJ software, with a caliper serving as a spatial reference. Owing to the intrinsic difficulty in precisely identifying the boundaries of individual vortex pairs, the experimentally determined wavenumbers are reported with a precision limited to two significant digits.

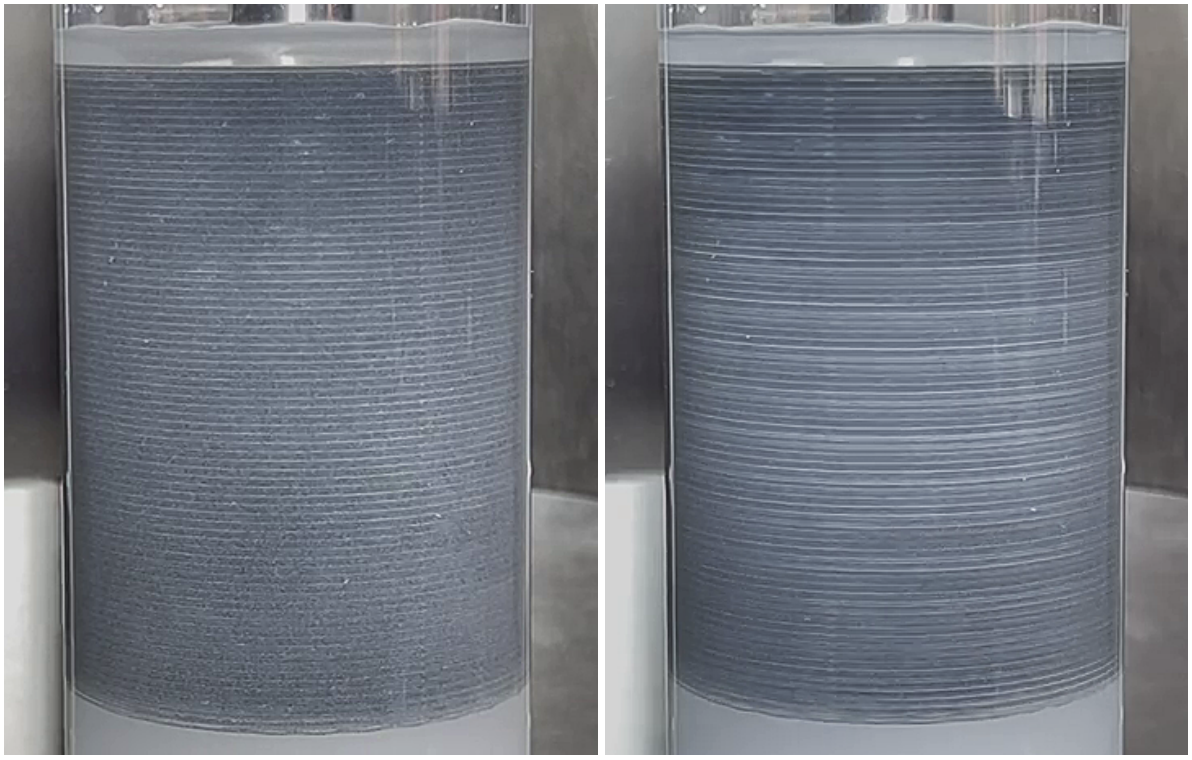

Figure 3.14: Visualizations of the motion before (left) and after (right) the onset of the first bifurcation for the case $T800$.

3.4. Asymptotic homogenization theory for *effective* boundary conditions

3.4.1. Domain decomposition, governing equations and definition of scales

As previously introduced and illustrated in Figure 3.5, the system is thus decomposed into an inner and an outer region, associated with characteristic length scales d and ℓ, respectively. The outer scale d corresponds to the macroscopic extent of the flow, physically represented by the gap between the two cylinders. The inner scale ℓ describes the periodicity of the microscopic corrugations, represented by the representative element of volume (REV), also known as the unit cell. In particular, the wall of the inner cylinder is patterned with microgrooves that are periodic in the axial direction and invariant in the azimuthal direction.
There is a clear separation between these two length scales; together with the periodic nature of the microstructure, it motivates the use of *homogenization theory*. This approach enables the derivation of effective boundary conditions at an idealized, fictitious interface, assumed here to coincide with $y = 0$.
Such effective boundary conditions are valid when the characteristic size of the surface corrugations is much smaller than the macroscopic length scale of the flow. Under this assumption, the detailed resolution of the rough surface can be avoided, thereby significantly reducing computational cost. Instead of solving the full macroscopic problem with no-slip conditions imposed along the actual corrugated boundary $y = y_w(z)$, difficult to capture because of the small-scale effects in the near wall region, a simplified problem can be solved with equivalent boundary conditions applied at the smooth fictitious interface.
Building on recent advances in the literature[15,85,61,86,87,88], this framework provides effective descriptions in terms of azimuthal and axial Navier slip lengths, which depend on the geometry and dimensions of the surface corrugations.

The analysis proceeds by considering the governing differential equations - mass conservation and the Navier–Stokes equations - formulated in cylindrical coordinates, under the assumption of axisymmetric flow ($\partial/\partial\theta = 0$):

$$\frac{\partial \hat{u}_r}{\partial \hat{r}} + \frac{\hat{u}_r}{\hat{r}} + \frac{\partial \hat{u}_z}{\partial \hat{z}} = 0, \tag{3.4}$$

$$\rho\left[\frac{\partial \hat{u}_r}{\partial \hat{t}} + \hat{u}_r\frac{\partial \hat{u}_r}{\partial \hat{r}} + \hat{u}_z\frac{\partial \hat{u}_r}{\partial \hat{z}} - \frac{\hat{u}_\theta^2}{\hat{r}}\right] = -\frac{\partial \hat{p}}{\partial \hat{r}} + \mu\left(\frac{\partial^2 \hat{u}_r}{\partial \hat{r}^2} + \frac{1}{\hat{r}}\frac{\partial \hat{u}_r}{\partial \hat{r}} - \frac{\hat{u}_r}{\hat{r}^2} + \frac{\partial^2 \hat{u}_r}{\partial \hat{z}^2}\right), \tag{3.5}$$

$$\rho\left[\frac{\partial \hat{u}_\theta}{\partial \hat{t}} + \hat{u}_r\frac{\partial \hat{u}_\theta}{\partial \hat{r}} + \hat{u}_z\frac{\partial \hat{u}_\theta}{\partial \hat{z}} + \frac{\hat{u}_\theta\,\hat{u}_r}{\hat{r}}\right] = \mu\left(\frac{\partial^2 \hat{u}_\theta}{\partial \hat{r}^2} + \frac{1}{\hat{r}}\frac{\partial \hat{u}_\theta}{\partial \hat{r}} - \frac{\hat{u}_\theta}{\hat{r}^2} + \frac{\partial^2 \hat{u}_\theta}{\partial \hat{z}^2}\right), \tag{3.6}$$

$$\rho\left[\frac{\partial \hat{u}_z}{\partial \hat{t}} + \hat{u}_r\frac{\partial \hat{u}_z}{\partial \hat{r}} + \hat{u}_z\frac{\partial \hat{u}_z}{\partial \hat{z}}\right] = -\frac{\partial \hat{p}}{\partial \hat{z}} + \mu\left(\frac{\partial^2 \hat{u}_z}{\partial \hat{r}^2} + \frac{1}{\hat{r}}\frac{\partial \hat{u}_z}{\partial \hat{r}} + \frac{\partial^2 \hat{u}_z}{\partial \hat{z}^2}\right). \tag{3.7}$$

with $\hat{u}_r, \hat{u}_\theta$ and $\hat{u}_z$ the three velocity components along the directions denoted by the respective subscripts, $\hat{p}$ the pressure, ρ the density, and μ the dynamic viscosity of the fluid contained within the two co-axial cylinders.
The flow in the microscopic (inner) region is dominated by viscous diffusion, whereas inertial effects become significant in the macroscopic (outer) domain. The two regions are characterized by different characteristic lengths and must be described using different scalings that reflect the underlying flow dynamics.

The *macroscopic scales* to normalize the outer region are the following:

- d: length scale
- $\Omega\, R_i$: velocity scale
- $\rho(\Omega\, R_i)\, R_i$: pressure scale
- $\dfrac{d}{\Omega\, R_i}$: time scale

The microscales in the near-wall domain, for a steady and creeping flow, are:

- $\ell = \epsilon\, d$: length scale
- $\epsilon\, \Omega\, R_i$: velocity scale
- $\dfrac{\mu\, \Omega\, R_i}{d}$: viscous pressure scale

The two domains are coupled by enforcing the continuity of both velocity and traction vectors across the interface. To rigorously formulate the homogenized (upscaled) model, it is necessary to derive the governing equations under the assumption of a clear scale separation, expressed by the small parameter $\epsilon \equiv \ell/d \ll 1$.
This asymptotic framework justifies the homogenization procedure and enables the systematic derivation of effective boundary conditions. Even for moderately small values of ϵ, the leading-order approximation typically provides an accurate representation of the flow.

3.4.2. The macroscopic problem

The dimensionless variables for the outer region are defined using capital letters,

$$Y = \frac{\hat{r} - R_i}{d}, \quad Z = \frac{\hat{z}}{d}, \quad (U, V, W) = \frac{(\hat{u}_\theta, \hat{u}_r, \hat{u}_z)}{\Omega\, R_i}, \quad P = \frac{\hat{p}}{\rho(\Omega\, R_i)\, R_i}, \quad \tau = \frac{\hat{t}}{d/(\Omega\, R_i)}. \tag{3.8}$$

that lead to the description of the outer macroscopic equations as:

$$\frac{\partial V}{\partial Y} + \delta V + \frac{\partial W}{\partial Z} = 0, \tag{3.9}$$

$$\frac{\partial V}{\partial \tau} + V\,\frac{\partial V}{\partial Y} - \delta\,U^2 + W\,\frac{\partial V}{\partial Z} = -\frac{\partial P}{\partial Y} + \frac{1}{Re}\left[\frac{\partial^2 V}{\partial Y^2} + \delta\frac{\partial V}{\partial Y} + \frac{\partial^2 V}{\partial Z^2}\right], \tag{3.10}$$

$$\frac{\partial U}{\partial \tau} + V\,\frac{\partial U}{\partial Y} + \delta\,U\,V + W\,\frac{\partial U}{\partial Z} = \frac{1}{Re}\left[\frac{\partial^2 U}{\partial Y^2} + \delta\frac{\partial U}{\partial Y} + \frac{\partial^2 U}{\partial Z^2}\right], \tag{3.11}$$

$$\frac{\partial W}{\partial \tau} + V\,\frac{\partial W}{\partial Y} + W\,\frac{\partial W}{\partial Z} = -\frac{\partial P}{\partial Z} + \frac{1}{Re}\left[\frac{\partial^2 W}{\partial Y^2} + \delta\frac{\partial W}{\partial Y} + \frac{\partial^2 W}{\partial Z^2}\right], \tag{3.12}$$

with the Reynolds number Re and the curvature parameter δ defined as:

$$Re = \frac{\rho\,\Omega\,R_i\,d}{\mu}, \qquad \delta = d/R_i \tag{3.13}$$

The system above is correct up to order δ, under the assumption that $\delta \ll 1$, meaning that the gap between the two cylinders is much smaller than the inner radius.
It is important to highlight that the variables (U, V, W, P) depend only on the macroscopic dependent variables Y and Z. The boundary at $Y = 1$ satisfies the simple no-slip condition.

3.4.3. The microscopic problem

At the microscopic scale, it is convenient to formulate the problem in Cartesian coordinates rather than in cylindrical coordinates. This simplification is justified by the strong separation of length scales characterizing the system. In fact, the characteristic size of the surface corrugations, denoted by ℓ, is assumed to be much smaller than the macroscopic length scale d associated with the curvature of the cylinder. Under this assumption, the flow within the microscopic domain can effectively be seen as "flat". Consequently, curvature effects are negligible at leading order and do not influence the dominant balance governing the flow in the inner region. As a result, the microscopic problem can be accurately approximated using Cartesian coordinates, described in this section.

The dimensionless variables for the inner region are defined below:

$$y = \frac{\hat{r} - R_i}{\epsilon\,d}, \quad z = \frac{\hat{z}}{\epsilon\,d}, \quad (u, v, w) = \frac{(\hat{u}'_\theta, \hat{u}_r, \hat{u}_z)}{\epsilon\,\Omega\,R_i}, \quad P = \frac{\hat{p}}{\mu\,\Omega\,R_i/d}, \tag{3.14}$$

with R_i radius of the inner cylinder, Ω rotational speed, $\hat{u}'_\theta = (\hat{u}_\theta - \Omega\,R_i)$, the azimuthal velocity deviation.
Considering a steady and incompressible flow, and through the definition of the microscales of the inner region, the microscopic problem can be defined as:

$$\frac{\partial v}{\partial y} + \epsilon\delta v\,(1 - \epsilon\delta y + ...) + \frac{\partial w}{\partial z} = 0 \tag{3.15}$$

$$-\frac{\partial p}{\partial y}+\frac{\partial^2 v}{\partial y^2}+\epsilon\delta\,(1-\epsilon\delta y+...)\frac{\partial v}{\partial y}+\frac{\partial^2 v}{\partial z^2}=0 \tag{3.16}$$

$$\frac{\partial^2 u}{\partial y^2}+\epsilon\delta\,(1-\epsilon\delta y+...)\frac{\partial u}{\partial y}+\frac{\partial^2 u}{\partial z^2}=0 \tag{3.17}$$

$$-\frac{\partial p}{\partial z}+\frac{\partial^2 w}{\partial y^2}+\epsilon\delta\,(1-\epsilon\delta y+...)\frac{\partial w}{\partial y}+\frac{\partial^2 w}{\partial z^2}=0 \tag{3.18}$$

and by neglecting terms of order δ^2, ϵ^2, $\epsilon\,\delta$ and higher, it leads to:

$$\frac{\partial v}{\partial y}+\frac{\partial w}{\partial z}=0, \tag{3.19}$$

$$-\frac{\partial p}{\partial y}+\frac{\partial^2 v}{\partial y^2}+\frac{\partial^2 v}{\partial z^2}=0, \tag{3.20}$$

$$\frac{\partial^2 u}{\partial y^2}+\frac{\partial^2 u}{\partial z^2}=0, \tag{3.21}$$

$$-\frac{\partial p}{\partial z}+\frac{\partial^2 w}{\partial y^2}+\frac{\partial^2 w}{\partial z^2}=0. \tag{3.22}$$

The boundary conditions for the inner problem are:

$$u=\delta\,y_w \quad v=0 \quad w=0 \tag{3.23}$$

3.4.4. Matching of velocity and traction vectors

At the outer boundary of the microscopic domain, located at $Y_\infty=\epsilon\,y_\infty$, the flow fields asymptotically lose their dependence on the microscopic coordinate z, provided that y_∞ is taken sufficiently far from the corrugated surface y_w.
In this limit, the solution approaches a locally uniform state, enabling consistent matching with the outer (macroscopic) region, by imposing continuity of the dimensionless velocity and traction vectors across the interface, then yields:

$$U\big|_{Y_\infty}=1+\epsilon\,u\big|_{y_\infty},\quad V\big|_{Y_\infty}=\epsilon v\big|_{y_\infty},\quad W\big|_{Y_\infty}=\epsilon w\big|_{y_\infty}, \tag{3.24}$$

$$\left.\frac{\partial U}{\partial Y}\right|_{Y_\infty}=\left.\frac{\partial u}{\partial y}\right|_{y_\infty}, \tag{3.25}$$

$$-Re\,P+2\left.\frac{\partial V}{\partial Y}\right|_{Y_\infty}=-p+2\left.\frac{\partial v}{\partial y}\right|_{y_\infty}, \tag{3.26}$$

$$\left.\frac{\partial V}{\partial Z}+\frac{\partial W}{\partial Y}\right|_{Y_\infty}=\left.\frac{\partial v}{\partial z}+\frac{\partial w}{\partial y}\right|_{y_\infty}. \tag{3.27}$$

By accounting for the forcing terms the problem, the problem for u is decoupled from the others, and the solution for the dimensionless azimuthal velocity can be readily expressed as:

$$u = u^\dagger(y,z)\left.\frac{\partial U}{\partial Y}\right|_{Y_\infty} + \delta\, y_w, \tag{3.28}$$

with the auxiliary variable $u^\dagger$ solution of

$$\frac{\partial^2 u^\dagger}{\partial y^2} + \frac{\partial^2 u^\dagger}{\partial z^2} = 0, \tag{3.29}$$

subject to $u^\dagger = 0$ at $y = y_w$ and $\dfrac{\partial u^\dagger}{\partial y} = 1$ at $y = y_\infty$.
The auxiliary variables $(v^\dagger, w^\dagger, p^\dagger)$ solve a Stokes system in the inner domain, subject to no-slip at $y = y_w$ plus $\dfrac{\partial w^\dagger}{\partial y} = 1$ and $v^\dagger = 0$ at $y = y_\infty$.

3.4.5. Slip lengths and virtual origin

The outer solution (first equation in 3.24) can be Taylor expanded,

$$U\big|_{Y_\infty} = U\big|_{Y=0} + \epsilon\, y_\infty \left.\frac{\partial U}{\partial Y}\right|_{Y=0} + \mathcal{O}(\epsilon^2) = 1 + \epsilon\, u^\dagger(y_\infty, z)\left[\left.\frac{\partial U}{\partial Y}\right|_{Y=0} + \mathcal{O}(\epsilon)\right] + \mathcal{O}(\epsilon\,\delta), \tag{3.30}$$

for the outer condition to be eventually transferred to the fictitious boundary in $Y = 0$; it reads at leading order

$$U\big|_{Y=0} = \epsilon\, \ell_x \left.\frac{\partial U}{\partial Y}\right|_{Y=0}, \tag{3.31}$$

with the slip length $\ell_x = u^\dagger(y_\infty, z) - y_\infty$. It is important to point out that $u^\dagger$ is independent of the height of the domain y_∞, consequently, ℓ_x does not vary with the choice of y_∞.
The solution for the remaining two components of the inner velocity field, which are coupled through the pressure, follows closely the approach developed for closely spaced planar riblets[8,60]. Provided that y_∞ is chosen sufficiently far from the corrugated boundary y_w, the flow in this region becomes effectively independent of the microscopic coordinate z, as will be demonstrated later. Under this assumption, the leading-order expressions for the outer velocity components can be written as:

$$V\big|_{Y=0} = 0, \quad W\big|_{Y=0} = \epsilon\, \ell_z \left.\frac{\partial W}{\partial Y}\right|_{Y=0}, \tag{3.32}$$

with the spanwise slip length defined as $\ell_z = w^\dagger(y_\infty, z) - y_\infty$, similarly to ℓ_x is independent of the choice of y_∞.

The boundary conditions on the inner radius $\hat{r} = R_i$ can be defined as:

$$\hat{u}_\theta\big|_{r=R_i} = \Omega(R_i + \hat{y}_w) + \left.\hat{\ell}_x \frac{\partial \hat{u}_\theta}{\partial \hat{r}}\right|_{r=R_i}, \quad \hat{u}_r\big|_{r=R_i} = 0, \quad \hat{u}_z\big|_{r=R_i} = \left.\hat{\ell}_z \frac{\partial \hat{u}_z}{\partial \hat{r}}\right|_{r=R_i}. \tag{3.33}$$

In particular, the azimuthal slip length, $\ell_x = \hat{\ell}_x/\ell$, plays a central role in characterizing the effect of the different surface patterns. As mentioned before, the effect of rough surface, as microgrooves, is often to shift the origin of the mean flow into a new origin, a *virtual* one. Considering the slip length ℓ_x, it determines the virtual origin of the mean flow and, consequently, both the *virtual* inner radius,

$$R_{i\,\mathrm{vrt}} = R_i - \hat{\ell}_x, \tag{3.34}$$

and the corresponding *virtual* gap thickness,

$$d_{\mathrm{vrt}} = d\,(1 + \epsilon\,\ell_x)\,, \tag{3.35}$$

in accordance with (**??**) (see also the schematic in Figure 2.7).

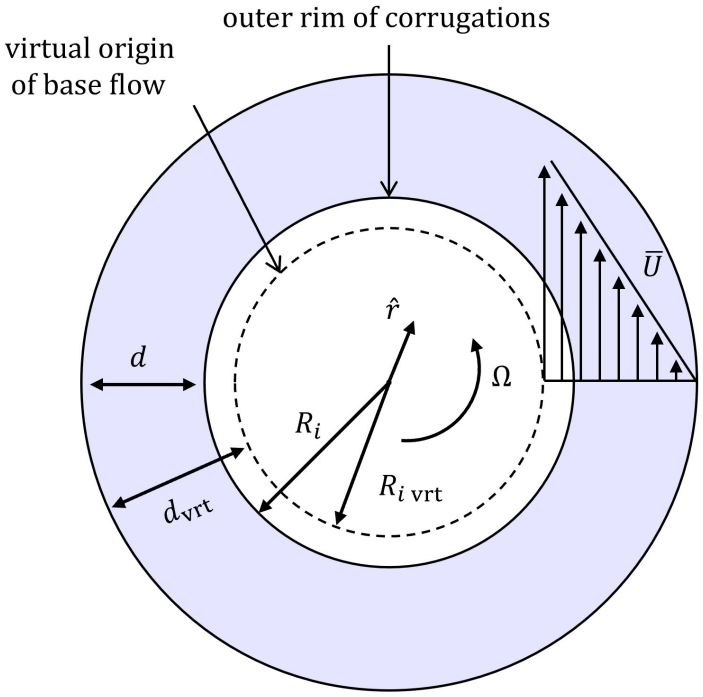

Figure 3.15: Sectional sketch of the rotating system. The dashed circumference highlights the inner-wall virtual origin, where the dimensionless mean azimuthal velocity is $\bar{U} = 1$.

The presence of a virtual radial gap in the case of grooved walls has also been discussed by Xu et al.[81], who referred to it as the *actual gap*. In their work, the actual (or virtual) gap thickness has been assumed, somewhat arbitrarily, to be equal to half the riblet height for all configurations considered. This approximation is subsequently incorporated into the definition of the total uncertainty, encompassing both modelling assumptions and experimental measurement errors, in their assessment of drag reduction (or increase) induced by azimuthal riblets on the inner cylinder of a Taylor-Couette apparatus. However, the idea in the present study is to precisely determine the fictitious positions of the virtual origin, based on the shapes and dimensions of the rough element.

3.4.6. Microscopic results: idealized and realistic geometry

Numerical solutions of the two auxiliary microscopic systems of equations, $u^\dagger$ and $(v^\dagger, w^\dagger, p^\dagger)$, are obtained using the freefem++ solver[89]. Using this open-source software to solve partial differential equations, the Stokes system has been solved, with the boundary conditions previously described applied.
All variables have been discretized by continuous piecewise quadratic finite elements, except for $p^\dagger$, which is approximated using continuous piecewise-linear elements. The resulting formulation is implemented on an unstructured mesh comprising up to 200000 triangular elements. Local mesh refinement is introduced in the vicinity of the solid boundary to adequately resolve steep gradients and ensure grid-independent (converged) solutions.
Two different configurations have been investigated in the present study: an idealized shape, derived from the nominal design of the surface grooves, and a realistic geometry, reconstructed from the measured profile of the 3D-printed surface. For the idealized micro-corrugations case, figure 3.6 illustrates the contour of the auxiliary variables.

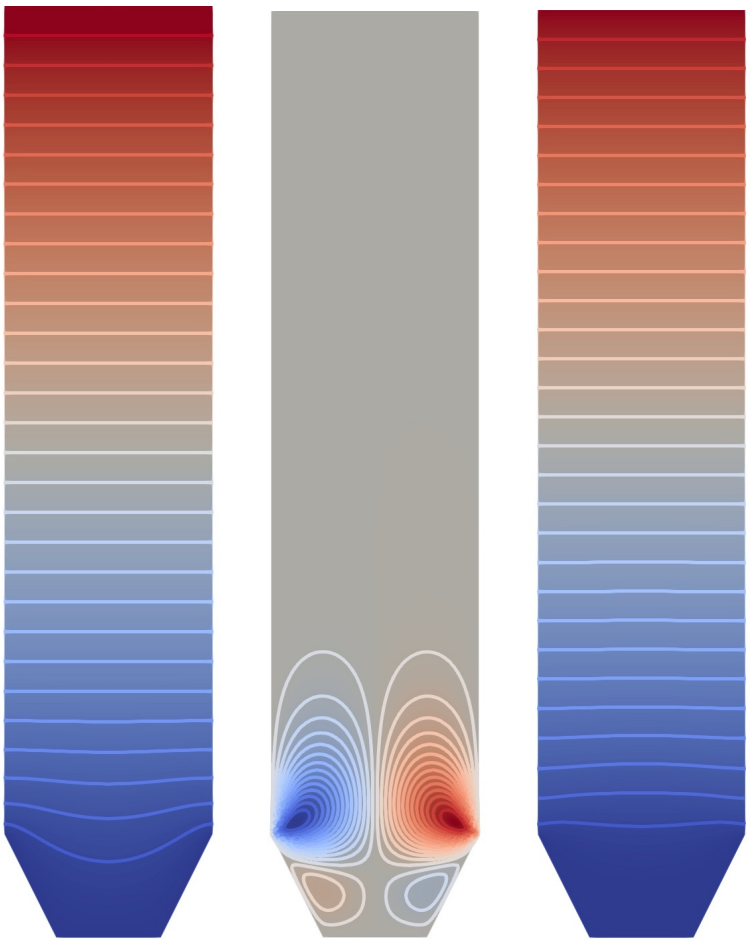

Figure 3.16: Auxiliary fields for the idealized trapezoidal micro-corrugations. From the left, $u^\dagger$ (with values in the dimensionless range [0, +4.175]), $v^\dagger$ [-0.037, +0.037], and $w^\dagger$ $[0, +4.081]$.

The dimensionless values found for the slip coefficient are given in Table 3.2. On account of arguments presented by Luchini et al.[8], it is not the individual value of ℓ_x (origin of the mean flow) or ℓ_z (origin of the cross-stream flow) which affects drag reduction (or, in the present case the onset of the instability), but their difference, since the origin of the wall-normal axis is set arbitrarily. In the case of idealized grooves, $\Delta\ell$ can be evaluated: for the square S-type, $\Delta\ell = \ell_x - \ell_z = 0.023$, while T-riblets have $\Delta\ell = 0.094$. The expectation is that, for the case of trapezoidal micro-structures at the wall, a stronger effect on the onset of Taylor vortices is expected.

micro-groove type	ℓ_x	ℓ_z
S	0.041	0.018
T	0.175	0.081

Table 3.2: Dimensionless slip lengths for the idealized S and T grooves of Figure 3.6.

As previously observed (cf. Figure 3.9), the real geometry can be affected by errors and technical problems during printing, manufacturing, and the realization process, and final geometries can differ significantly from their idealized designs. One of the most innovative aspects of the present study is to take into account the real profile of the microstructured sleeves in both the theoretical and numerical approaches. An example is shown in Fig. 3.17 that presents the auxiliary fields for the $S1000$ configuration. In the model, the effective patterned profile is approximated using piecewise-linear or parabolic segments using MATLAB code. In this case, the resulting slip coefficients are slightly larger than those reported for the idealized grooves in Table 3.2, with their dimensionless values given by $\ell_x = u^\dagger\big|_{y_\infty} - y_\infty = 0.051$ and $\ell_z = w^\dagger\big|_{y_\infty} - y_\infty = 0.027$.
The next table 3.3 summarizes the dimensional slip lengths from the upscaling technique, both identifying the realistic and idealized geometries. The 3D-printed trapezoidal grooves exhibit smaller slip lengths compared to their idealized versions. On the other hand, the square grooves show slightly larger slip coefficients. Furthermore, the observation that T-riblets produce larger slip coefficients than S-riblets with the same spanwise pitch agrees with findings reported in the literature[8,23,63].

Case	$\hat{\ell}_x$ [mm]	$\hat{\ell}_z$ [mm]	$\Delta\hat{\ell}$ [mm]	$R_{i\,\mathrm{vrt}}$ [mm]	d_{vrt} [mm]	R_m [mm]	η_{vrt}
$T400$	0.046 (0.070)	0.026 (0.032)	0.020 (0.038)	18.65	1.99	19.64	0.904
$T800$	0.107 (0.140)	0.055 (0.065)	0.052 (0.075)	18.74	1.90	19.69	0.908
$T1000$	0.134 (0.175)	0.069 (0.081)	0.065 (0.094)	18.82	1.82	19.73	0.912
$S800$	0.041 (0.033)	0.021 (0.014)	0.020 (0.019)	18.78	1.86	19.71	0.910
$S1000$	0.051 (0.041)	0.027 (0.018)	0.024 (0.023)	18.91	1.73	19.77	0.916

Table 3.3: Dimensional slip lengths and differential slip ($\Delta\hat{\ell} = \hat{\ell}_x - \hat{\ell}_z$) from the homogenization calculations for the reconstructed, *realistic* geometries, together with *virtual* dimensions of the different microstructured surfaces. The *idealized* slip values are given within round brackets for each shape and periodicity examined. The *virtual* mean radius, $R_m = (R_{i\,\mathrm{vrt}} + R_o)/2$, and radius ratio, η_{vrt}, are also defined.

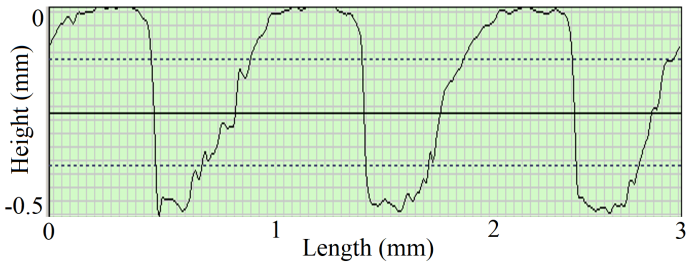

(a) Laser scan of small portion of S1000 grooves

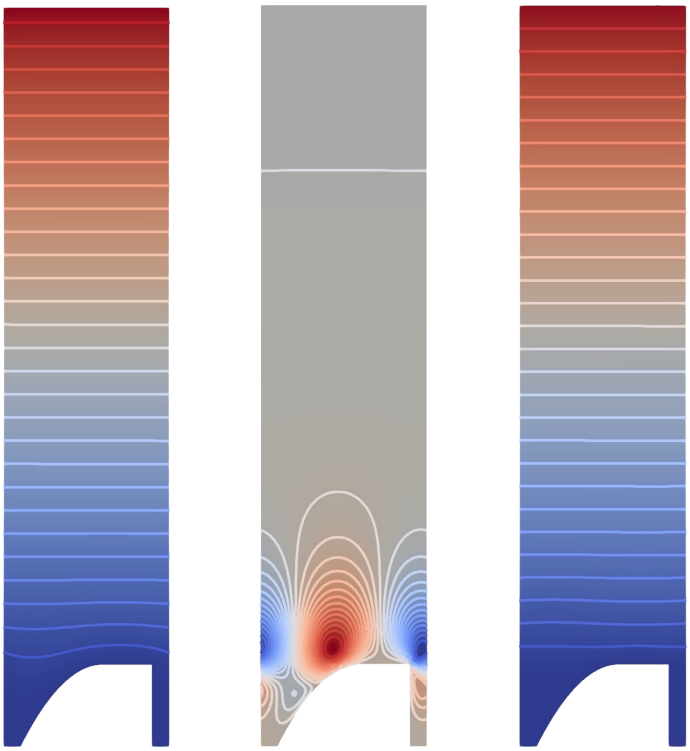

(b) $u^{\dagger}$[0 mm, +4.051mm]

(c) $v^{\dagger}$[−00233 mm, +0.0204 mm]

(d) $w^{\dagger}$[0 mm, +4.027 mm]

Figure 3.17: On the top, laser scan of a small portion of the $S1000$ grooves; the vertical size of the *real* corrugations is measured to be 476 μm instead of the imposed value $\ell/2 = 500$ μm. From left to right, the bottom three images display auxiliary fields of $u^{\dagger}$, $v^{\dagger}$, and $w^{\dagger}$ for the model in the case of *real* corrugations.

The results obtained from the upscaling homogenization procedure serve as input for the following step of the present analysis. In particular, the Navier slip lengths are employed to formulate effective macroscopic boundary conditions, which are then incorporated into a linear stability framework to determine the critical parameters governing the Taylor–Couette flow.

3.5. The stability theory

The outcomes of the upscaling homogenization procedure provide the starting point for the next stage of the study, followed by a linear stability analysis. Specifically, the Navier slip lengths, evaluated both for an idealized and a realistic shape, have been integrated into a linear stability theory to define the slip boundary condition and identify the critical parameters governing Taylor–Couette flow. The stability analysis can be found in Innocenti et al.[90]; the calculations have been carried out by Jan O. Pralits.

Some considerations need to be made about the classical, no-slip case. In particular, results for smooth cylinders[84,91] show that the critical Taylor number, Ta_c, that represents the onset of instability, increases as the radius ratio $\eta = R_i/R_o$ decreases. In contrast, the critical wavenumber, β_c, exhibits only a slight increase with decreasing η. As reported in Table 3.1, the radius ratio η for the micro-structured configurations grows with the pattern periodicity, because the outer radius is fixed and the inner one depends on the periodicity ℓ. It can be observed, relative to the smooth case, that a reduction in the critical Taylor number (along with a mild decrease in the wavenumber) is expected.
Numerical results are shown for all configurations considered, including both idealized and realistic corrugations. The geometric parameters adopted for the idealized model are summarized in Table 3.4. In particular, corrugations with height $\ell/2$ and periodicity ℓ are assumed to be located directly above the sleeve of the smooth configuration. For example, in case $T400$ (with $\ell = 0.4$ mm), the inner radius is taken as $(18.36 + 0.4/2)$ mm, same for the other cases.

	R_i [mm]	d [mm]	ℓ [mm]	$\eta = R_i/R_o$	$\delta = d/R_i$	$\epsilon = \ell/d$
smooth cylinder	18.36	2.28	–	0.890	0.124	–
$T400$	18.56	2.08	0.40	0.899	0.112	0.192
$T800$	18.76	1.88	0.80	0.909	0.100	0.426
$T1000$	18.86	1.78	1.00	0.914	0.094	0.562
$S800$	18.76	1.88	0.80	0.909	0.100	0.426
$S1000$	18.86	1.78	1.00	0.914	0.094	0.562

Table 3.4: Geometrical dimensions and dimensionless parameters used for the stability analysis of idealized micro-undulations. In all configurations R_o is fixed and equal to 20.64 mm.

The critical conditions for the onset of Taylor vortices are summarized in Table 3.5.

Case	Theory: idealized shapes (η, Re_c, Ta_c, β_c)	Theory: realistic shapes (η, Re_c, Ta_c, β_c)	Laboratory results (η, Re_c, Ta_c, β_c)
Smooth cylinder	(0.890, 121.8, 1735, 3.143)	(0.890, 121.8, 1735, 3.143)	(0.890, 122.2, 1746, 3.1)
$T400$	(0.899, 127.1, 1714, 3.050)	(0.906, 131.1, 1696, 3.070)	(0.906, 134.1, 1772, 2.8)
$T800$	(0.909, 133.4, 1698, 2.983)	(0.913, 136.0, 1675, 3.010)	(0.913, 134.6, 1618, 3.1)
$T1000$	(0.914, 137.3, 1699, 2.950)	(0.918, 139.9, 1670, 2.983)	(0.918, 140.2, 1679, 3.5)
$S800$	(0.909, 134.5, 1726, 3.090)	(0.912, 135.7, 1700, 3.077)	(0.912, 137.0, 1732, 2.9)
$S1000$	(0.914, 138.2, 1721, 3.084)	(0.919, 140.8, 1683, 3.070)	(0.919, 143.3, 1731, 3.2)

Table 3.5: Onset conditions for both theoretical and experimental results. The former are computed for both idealized and modelled micro-grooves, using the values of δ and ϵ from Table 3.4 (*idealized* case) and Table 3.1 (*realistic* case), together with the slip coefficients in Table 3.3.

The reference case corresponds to a smooth inner cylinder, which in the present case consists of the stainless steel core and a smooth sleeve, with radius ratio $\eta = 0.890$. In the case of a smooth cylinder, classical results available in the literature report a critical Taylor number $Ta_c = 1839$ and a critical axial wavenumber $\beta_c = 3.129$[91]. These values provide a well-established benchmark for assessing the accuracy of the present stability analysis, a crucial requirement to check before investigating all cases.
Numerical computations for the smooth configuration under no-slip boundary conditions yield $Ta_c = 1735$ and $\beta_c = 3.143$. The predicted critical Taylor number is approximately 5.7% lower than the reference value, while the critical wavenumber differs by less than 0.5%. This discrepancy in Ta_c may be attributed to the approximations inherent in the perturbation framework, in which second-order contributions (i.e., ϵ^2, $\epsilon\delta$, and δ^2) are neglected, as well as to possible uncertainties in the reference data. Moving to the micro-structured configurations, the results obtained with slip boundary conditions indicate a consistent trend in the critical Reynolds number Re_c. In particular, Re_c exhibits a mild increase with the pattern periodicity ℓ, in agreement with the qualitative predictions of the virtual origin model. This behavior is observed for both square and trapezoidal groove geometries. Furthermore, for all values of ℓ, the critical Reynolds numbers associated with realistic groove shapes are systematically higher than those obtained for the corresponding idealized configurations. The behavior of the critical wavenumber β_c is comparatively less sensitive to the surface structuring. Variations in β_c across the different configurations remain modest, with no pronounced or systematic dependence on the geometrical parameters. This observation is consistent with classical results for smooth cylinders, where β_c is known to vary only weakly with the radius ratio. It can also be related to uncertainties in the visualization process. To observe critical parameter trends versus radius ratio, two figures are obtained by plotting Reynolds and Taylor numbers, at critical conditions, as functions of the radius ratio η while it increases with the pattern periodicity. In particular, the T geometry is represented with triangles, the S geometry with squares. A comparison of experimental and numerical data is performed. The experimental data points are in black, the realistic shapes are drawn with red symbols, while the idealized grooves are shown in blue. The solid lines are the computed values of Re_c and Ta_c for smooth walls. The uncertainty on the critical Reynolds numbers measured in the laboratory is of ± 1, leading to an error bar on the experimental Taylor

number of ± 25. These trends are in qualitative agreement with expectations based on smooth-cylinder studies, although the dependence of the critical Taylor number on ℓ is not strictly monotonic.

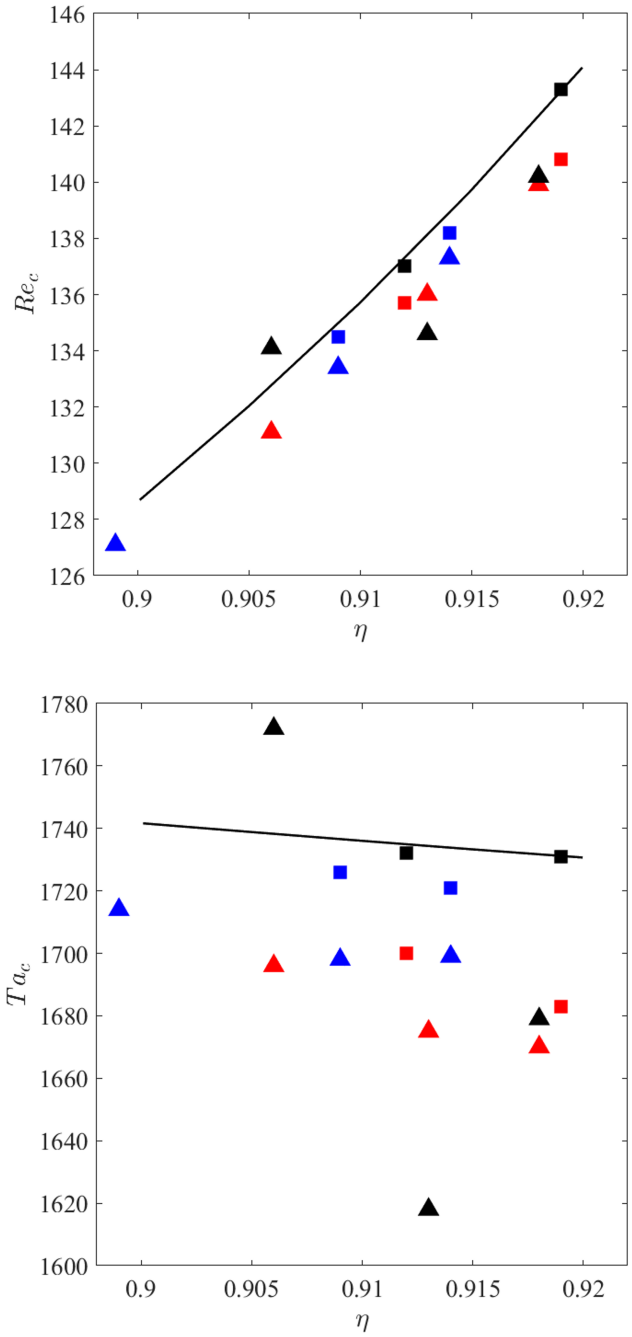

Figure 3.18: Critical parameters - Re_c and Ta_c - versus radius ratio η.

3.5.1. Is the instability postponed or anticipated?

An analysis of the data suggests that the introduction of grooved surfaces tends to promote an earlier onset of the primary instability. However, a rigorous comparison between the experimental cases remains challenging, as key geometric parameters - the inner radius R_i and the gap width d - vary from one configuration to another. Consequently, with this expression of the flow parameter, it is not possible to isolate the effect of patterned surface from that of the underlying geometric differences, and any interpretation of the results must be considered with this limitation in mind.
By observing figure 3.15, a virtual origin can be defined taking into account differences of microstructured grooves, leading to a unique model that can equally compare results.
The idea is to use an appropriate scale based on the virtual origin, thus defining a virtual gap of the system and a virtual inner radius with the following definitions:

$$R_{i\,\mathrm{vrt}} = R_i - \hat{\ell}_x, \qquad d_{\mathrm{vrt}} = d + \hat{\ell}_x \tag{3.36}$$

Both Reynolds and Taylor numbers need to be rescaled using virtual dimensions, by denoting the new parameter by the subscript *vrt*:

$$Re = \frac{\Omega\, R_{i\,\mathrm{vrt}}\, d_{\mathrm{vrt}}}{\nu} \qquad Ta = {Re_{vrt}}^2\, \frac{2\, d_{\mathrm{vrt}}}{R_{i\,\mathrm{vrt}} + R_o} \tag{3.37}$$

and similarly, the virtual radius ratio, η_{vrt}, and the torque coefficient, c_T, are rescaled:

$$c_T = \frac{\mathcal{C}}{\pi \rho\, \Omega^2 R_{i\,\mathrm{vrt}}^4 H} \tag{3.38}$$

The experimental results of Figure 3.13, virtual rescaled as indicated above, are plotted in Figure 3.19. Green marker corresponds to periodicity ℓ of $400\,\mu m$, the red markers represent the data of the cases $\ell = 800$ μm, and the blue ones $\ell = 1000$ μm.
The top figure corresponds to the trapezoidal case, where an almost perfect collapse of the curves can be observed, particularly in the subcritical regime (i.e., for Taylor numbers below the critical value). The change in the slopes of the curves enables a straightforward extrapolation of the critical parameters and facilitates comparison: increasing the groove dimensions leads to a delay in the onset of Taylor instability.
On the other hand, the bottom figure shows square groove results. As it can be observed, there isn't a perfect collapse like the trapezoidal case, most probably related to the less-than-perfect manufacturing of the microstructures.
Generally, by characterizing the rough surface, it has been noticed that the square shapes present more irregularities and imperfections if compared to the trapezoidal case.
Larger defect, as the one shown in Figure 3.13, results in a local alteration of the regular pattern with a consequent disruption of the base motion, leading to a modification of the wall shear stress.

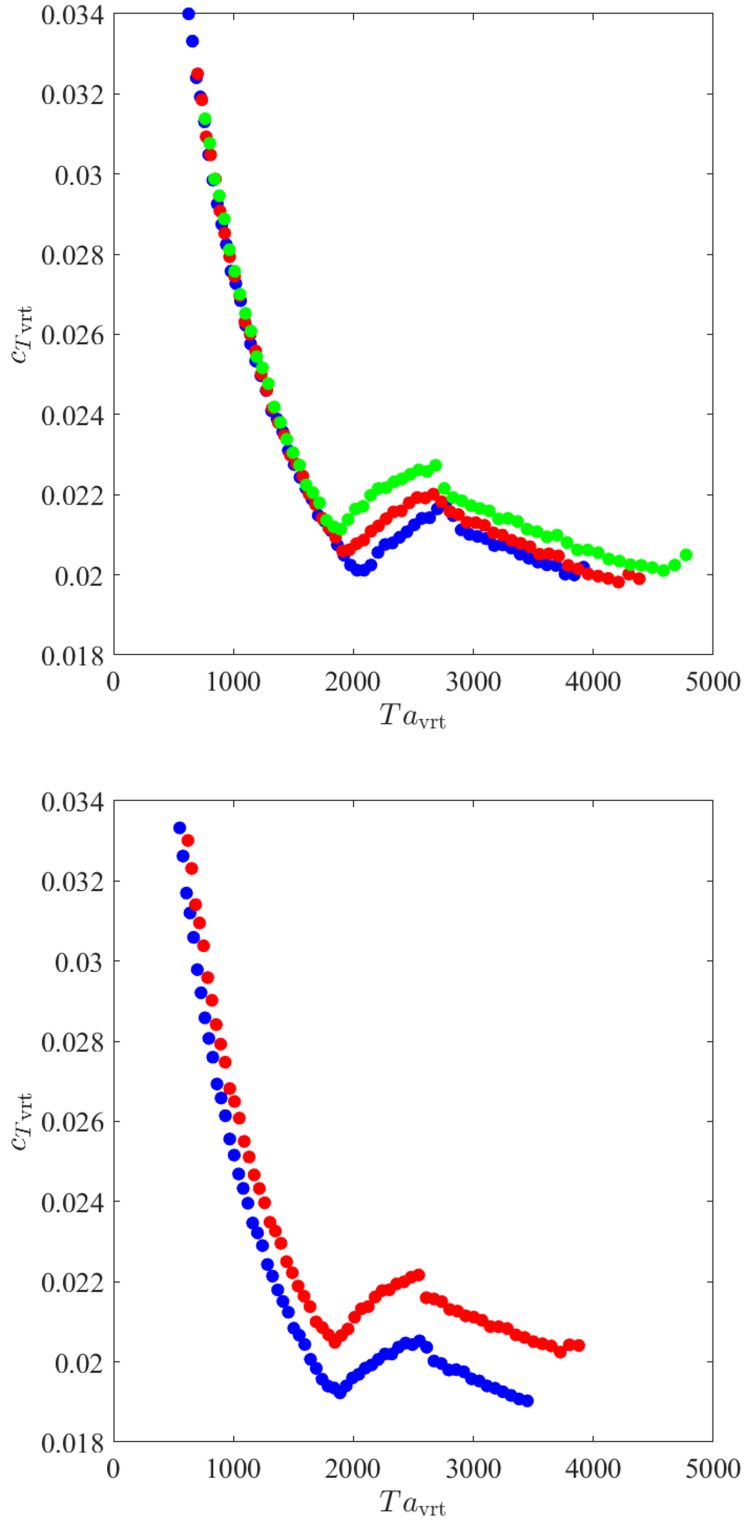

Figure 3.19: Torque coefficient versus the Taylor number for trapezoidal (top) and square (bottom) surface corrugations in virtual coordinates.

Figure 3.19 permits to extrapolate the critical values of Ta_{vrt} (and Re_{vrt}) for each case, and the virtual results are summarized in Table 3.6, for both experimental and theoretical cases. The agreement between theory and laboratory is good, particularly for T-shaped corrugations, with the rescaled, critical Reynolds and Taylor numbers which consistently increase with the length scale ℓ of the wall inhomogeneities.

	Theory: idealized shapes $(\eta_c, Re_c, Ta_c, \beta_c)_{\mathrm{vrt}}$	Theory: realistic shapes $(\eta_c, Re_c, Ta_c, \beta_c)_{\mathrm{vrt}}$	Laboratory results $(\eta_c, Re_c, Ta_c, \beta_c)_{\mathrm{vrt}}$
$T400$	(0.896, 130.9, 1882, 3.153)	(0.904, 133.9, 1812, 3.143)	(0.904, 136.9, 1894, 3.0)
$T800$	(0.902, 142.3, 2083, 3.205)	(0.908, 143,3, 1979, 3.190)	(0.908, 141.0, 1915, 3.5)
$T1000$	(0.905, 149.4, 2219, 3.240)	(0.912, 149.9, 2078, 3.220)	(0.912, 150.3, 2088, 4.1)
$S800$	(0.907, 136.6, 1814, 3.144)	(0.910, 138.5, 1810, 3.146)	(0.910, 139.8, 1846, 3.1)
$S1000$	(0.912, 141.1, 1837, 3.155)	(0.916, 144.7, 1832, 3.163)	(0.916, 146.7, 1887, 3.4)

Table 3.6: Onset conditions based on the rescaled (virtual) dimensions of gap and inner radius.

The rescaled critical values, $Re_{c\,\mathrm{vrt}}$ and $Ta_{c\,\mathrm{vrt}}$, are found to be consistently higher than their no-slip counterparts for all values of the radius ratio, meaning that an actual delay of the primary TC instability is observed. The reference values for the smooth-wall configuration are reported in Figure 3.13 (see solid lines). This observation leads to two main conclusions:

- azimuthally invariant grooves are effective in delaying the onset of the instability;

- trapezoidal corrugations exhibit a greater stabilizing effect than square-shaped geometries.

The latter result is consistent with the theoretical expectation that the leading-order variation in the critical Taylor (or Reynolds) number depends on the difference between the two effective protrusion heights, $\Delta\ell = \ell_x - \ell_z$. This behavior is analogous to that observed for riblets in turbulent channel and boundary layer flows, where physically relevant quantities must remain invariant under a shift of the reference origin (here chosen at the groove tip). As a consequence, the only meaningful geometric parameter is not the absolute value of the protrusion heights, but rather their difference, which represents the effective separation between the virtual walls perceived by the azimuthal and axial flow components.
The stabilizing influence of differential slip arises from the multiple mechanisms rather than from a single dominant effect. In particular, anisotropic slip alters the effective geometry of the system, modifies the centrifugal balance, and changes the boundary conditions experienced by flow perturbations. Among these contributions, the leading-order effect can be identified as an effective widening of the gap perceived by the instability.
In classical Taylor-Couette flow with inner-cylinder rotation, an increase in the gap width is known to result in higher critical Reynolds and Taylor numbers, due to a reduction in centrifugal destabilization per unit radial distance and a weaker confinement of Taylor vortices.
In the present configuration, the separation between the virtual origins associated with azimuthal and axial motion produces an analogous effect, increasing the distance over which the instability develops.

Additional effects, such as local modifications of the base-flow shear and the anisotropic nature of the perturbation boundary conditions, provide secondary contributions. While these mechanisms may influence the detailed structure of the unstable modes and their subsequent nonlinear evolution, they do not play a primary role in determining the onset threshold of the instability.

For the critical Reynolds number, and analogously for the Taylor number, the results can be expressed as a function of the smooth-wall critical value $Re_{c\,\mathrm{smooth}}$, by introducing this new definition:

$$Re_{c\,\mathrm{vrt}} = Re_{c\,\mathrm{smooth}} + \zeta \left.\frac{\partial Re_c}{\partial \zeta}\right|_{\zeta=0} + \mathcal{O}(\zeta^2), \tag{3.39}$$

with a dimensionless parameter ζ:

$$\zeta = \frac{\Delta\hat{\ell}}{d_{\mathrm{vrt}}} = \epsilon_{\mathrm{vrt}} \Delta\ell, \tag{3.40}$$

with $\epsilon_{\mathrm{vrt}} = \ell / d_{\mathrm{vrt}} \ll 1$.
Next figure 3.20 shows both $\Delta Re_c = Re_{c\,\mathrm{vrt}} - Re_{c\,\mathrm{smooth}}$ and $\Delta Ta_c = Ta_{c\,\mathrm{vrt}} - Ta_{c\,\mathrm{smooth}}$ versus ζ for all cases treated numerically: the trapezoidal geometry is represented with triangles, the square one with squares. The realistic shapes are represented with red symbols, while the idealized grooves are shown in blue.
It confirms that, provided that ζ is small enough, the variations in Reynolds and Taylor numbers follow a linear trend. The scatter in the data is very low, as expected, since the variation in radius ratio among the different cases is not large, especially in the Reynolds plot, since the Taylor definition is based on the Reynolds to the second power.
Larger critical Reynolds (or Taylor) numbers can be achieved by maximizing $\Delta\ell$, obtaining a later appearance of the primary instability, with circumferential microgrooves which maximize $\Delta\ell$. This occurs for very thin blade riblets[8,23].

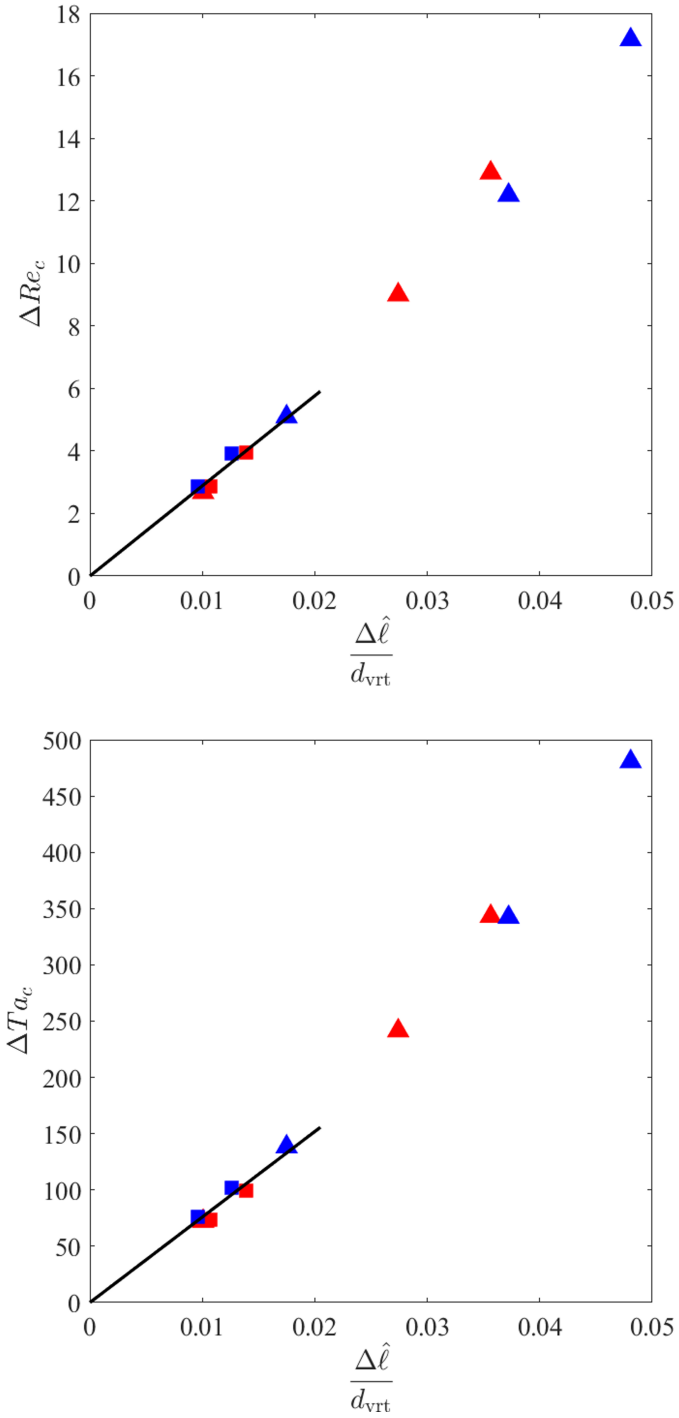

Figure 3.20: Variations of the critical Reynolds and Taylor numbers (with respect to the corresponding smooth-wall cases) versus $\Delta\hat{\ell}/d_{\mathrm{vrt}}$ for all the configurations simulated. The straight, solid lines are plotted only to guide the eyes.

3.6. Conclusions and future developments

A comprehensive investigation has been carried out to assess the influence of circumferential microgrooves on the onset of the primary Taylor–Couette instability. Microstructured sleeves with trapezoidal and square grooves have been fabricated via stereolithographic printing to investigate different configurations. The effect of periodic patterned elements has been characterized both experimentally, by measuring the torque against the rotational speed and by visualizing flow vortical structures, and theoretically, by defining equivalent slippery boundary conditions, obtained through an upscaling technique, to be applied to a linear stability analysis. In particular, governing equations defined through the asymptotic homogenization approach have been defined up to leading order in ϵ (yielding effective slip boundary conditions). Higher-order homogenization corrections are not expected to significantly alter the macroscopic behavior, as demonstrated by Bottaro & Naqvi[61].

Previous studies explain that the presence of microgrooves creates a virtual origin of the mean flow. In order to properly compare the results obtained from different geometries tested, critical parameters have been redefined and expressed considering the virtual origin. It leads to the demonstration that azimuthally invariant microgrooves alter the stability characteristics of the system, promoting a delay of instability, leading to an earlier onset of Taylor vortices compared to smooth-wall configurations (cf. Figure 3.18). However, upon introducing the concept of a virtual origin for the mean azimuthal flow and rescaling the governing parameters accordingly, it becomes evident that the instability is, in fact, delayed. This stabilizing effect increases with groove pitch and is more pronounced for trapezoidal geometries than for square ones, in agreement with the larger slip-length differences ($\Delta\ell$) associated with the former.

These findings highlight two key points. First, mildly corrugated surfaces can be effectively modeled using Navier slip boundary conditions within a homogenization framework, providing a robust and computationally efficient approach to account for surface roughness in stability analyses. Second, microgroove geometry design offers a practical way to control the onset of centrifugal instabilities. This has direct implications for delaying transition in rotating shear flows, with potential applications spanning rotating machinery and journal bearings - where early vortex formation can increase energy losses and induce vibrations - to cylindrical mixers and reactors, where controlled centrifugal instabilities can be leveraged to regulate momentum and heat transport.

Future work should extend the present analysis beyond the primary instability to regimes where advection and nonlinear effects become significant. In particular, the proposed homogenization–stability framework could be applied to the onset of wavy vortex flow and other non-axisymmetric instabilities, where wall-induced anisotropy may play a more prominent role.

Additional extensions include higher rotation rates and weakly turbulent regimes, in which effective slip models may still provide valuable insights into near-wall dynamics. Finally, the framework could be generalized to azimuthally non-uniform surface textures—such as helical or staggered grooves—as well as to superhydrophobic or lubricant-infused surfaces, enabling systematic comparisons of different surface designs within a unified virtual-origin perspective.

3.7. Ongoing experiments

From the perspective of future developments of the present study, a series of experimental activities has been carried out to extend the investigation toward more complex slippery surfaces under higher rotational regimes. These efforts are motivated by the need to assess the robustness and durability under more realistic and technologically relevant conditions.
Two main research projects have been undertaken to address this purpose.
The first activity focuses on the functionalization of the previously described 3D-printed microstructured sleeves to create a superhydrophobic coating and then a liquid-impregnated surface. The next figure schematizes the slippery surfaces: a superhydrophobic and a liquid-infused configurations.

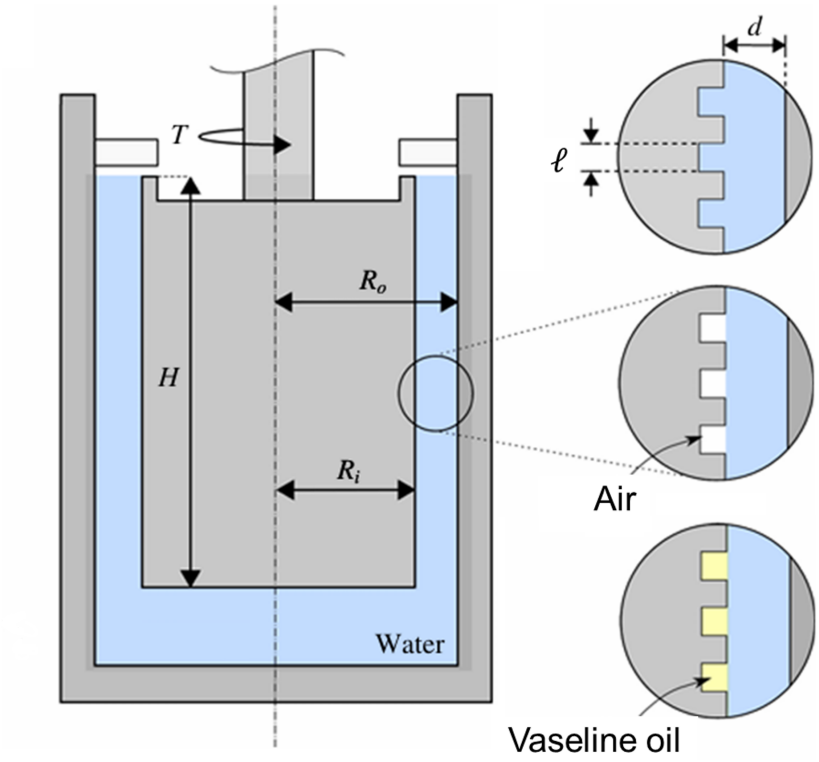

Figure 3.21: Schematic of the Taylor–Couette setup. On the right, a magnified view of the tested microgrooved surface is shown. The top panel illustrates the baseline configuration, consisting of azimuthally periodic grooves only. The central panel depicts the superhydrophobic case, highlighting air pockets trapped within the surface texture. The bottom panel shows the same microstructured surface after lubricant infusion, with the grooves filled by the lubricating oil.

This treatment is intended to impart water-repellent properties to the surface, thereby promoting slip and reducing viscous drag at the fluid-solid interface. After the coating process, obtained through the application via spray of a commercial superhydrophobic coating (Soft Glaco Mirror Coat Zero[92]), the modified sleeves are subjected to experimental characteriza-

tion using the same protocol described previously, in order to quantify the resulting changes in torque response and flow structure. The only modification to the procedure concerns the operating range: rather than ending the rotational tests at 50 rpm, the experiments are extended up to 80 rpm, thereby enabling the exploration of higher rotational regimes.
Subsequently, these superhydrophobic textures are impregnated with a lubricant oil (Petroleum jelly - Vaseline oil) to create lubricant-infused surfaces (LIS). This additional level of complexity introduces a thin liquid layer within the surface texture, which can significantly enhance effective slip and potentially modify the stability characteristics of the flow.
The following figure highlights the most promising results obtained in this preliminary investigation. The $T800$ cylinder has been selected as the reference configuration for functionalization and subsequent testing. The plot compares the performance of superhydrophobic (SHS) and lubricant-infused surface (LIS) treatments over an extended range of operating conditions.

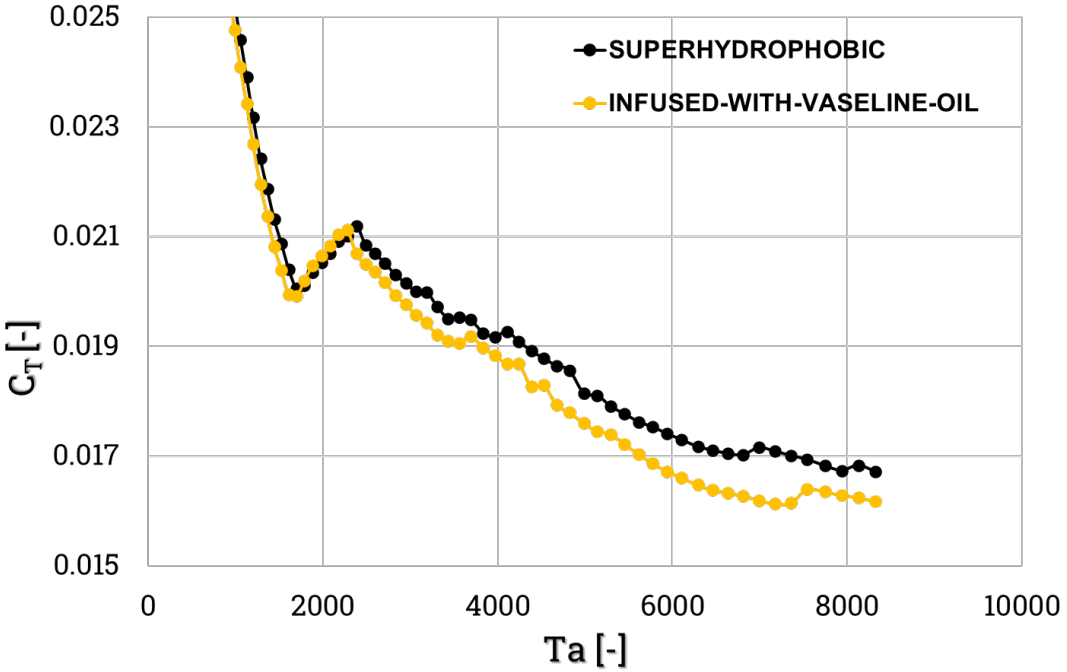

Figure 3.22: Torque coefficient against Taylor number. $T800$ cylinder in the case of superhydrophobic coating (black symbols) and liquid-infused surface (yellow ones).

For Taylor numbers up to approximately $Ta \simeq 2200$, the flow remains in the laminar regime. Within this range, two distinct changes in slope can be clearly identified, corresponding to the onset of the primary instability - namely, Taylor vortex flow - and the subsequent transition to secondary instabilities, characterized by wavy vortex flow. As the rotational speed increases further, the system enters the turbulent regime, where coherent wavy vortices progressively break down and exhibit oscillations. This results in complex velocity and pressure fluctuations, which interact with the slippery boundary provided by the surface treatment.
In the laminar regime, no appreciable differences are observed between the SHS and LIS configurations. This suggests that the presence of an air plastron in the superhydrophobic case, as well as the lubricating liquid layer in the LIS case, does not significantly influence either

the onset of Taylor instabilities or the wall friction, under these conditions. In contrast, a significantly different behavior emerges in the turbulent regime. The LIS configuration exhibits a pronounced drag reduction effect, which becomes increasingly significant with rising Taylor number. This trend is clearly evidenced by the growing discrepancy in the torque coefficient between the SHS and LIS cases.
These findings are particularly encouraging, as they point out the potential of lubricant-infused surfaces to enhance flow performance in high-shear, turbulent conditions. They also provide strong motivation for further investigations, including the exploration of surface geometries, different lubricant types, and a broader range of operating parameters, to optimize and better understand the underlying mechanisms governing drag reduction in such systems.
The second research line is motivated by the well-known limitations of conventional LIS coatings, such as their tendency to lubricant depletion and degradation under sustained flow conditions, which impact the durability and functionality. In this context, an alternative strategy has been explored, aimed at improving the robustness and longevity of lubricant-infused configurations without altering the underlying microstructured geometry.
Specifically, the approach consists of developing a combined coating, formed by inorganic-organic layers, capable of enhancing oil affinity and retention within the surface features. These coatings are designed to promote strong physico-chemical interactions with the lubricant, thereby mitigating oil losses and depletion, even under high shear.
These coatings have been realized in collaboration with CNR-ISSMC - Istituto di Scienza e Tecnologia dei Materiali Ceramici- on an aluminum disk of 50 mm in diameter and 1.5 mm in thickness, which has been selected as substrate to investigate these new coatings. The disk has been sandblasted to reach a roughness average Ra of 5-10 μm. The samples have been cleaned with soapy water and ethanol, then dip-coated in alumina Al_2O_3 solution. After drying, they have been annealed at 400 °C for 1 h to form an amorphous Al_2O_3 layer, followed by boiling water treatment and a final thermal stabilization (10 min). The next figure shows the Alumina flower-like hierarchical structures.

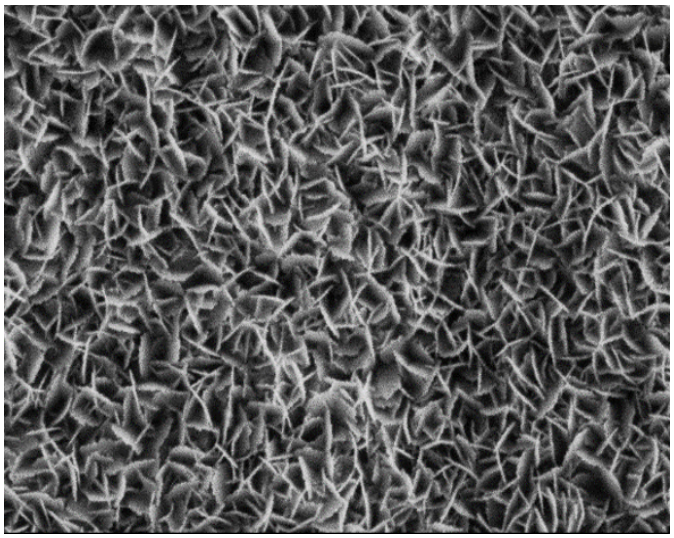

Figure 3.23: SEM image of the inorganic layer of Al_2O_3.

Superhydrophobicity has been achieved by depositing an organic layer using hexadecyltrimethoxysilane (HTS, C16) or triethoxy(octyl)silane (OTS, C8), both diluted to 6% in ethanol and applied via dip-coating. After drying, samples were annealed at 150 °C for 30 min. Different coatings have been obtained by combining the inorganic and organic layers.
The sample, shaft-connected with the Anton Paar rheometer, is immersed in a tank of distilled water, sufficiently large to avoid the wall effects on the measurement and to simulate an infinite volume of water. Moreover, the rectangular shape of the tank minimizes the possibility of the formation of two vortices around the disk, leading to a corruption of the evaluation of the torque, and thus helps to break the symmetry. Several tests have been carried out to assess the best combination of layers and the best lubricant oil affinity. Preliminary observations suggest that these advanced coatings may provide a promising way to achieve more durable and reliable liquid-infused surfaces.
Overall, these ongoing experimental efforts are paving the way toward a more comprehensive framework capable of addressing realistic surface conditions, higher Reynolds numbers, and long-term operational stability. Following this purpose, the next chapter builds on this foundation by presenting an experimental investigation of a complex LIS under highly turbulent flow conditions, looking at the mechanisms responsible for the degradation of its durability and functional performance.

Effect of the flow on lubricant depletion

One of the most promising applications of slippery liquid-infused surfaces (LIS) lies in the marine environment, where reducing biofouling and hydrodynamic drag is of critical importance. However, under realistic operating conditions — particularly in the presence of sustained shear flow — the stability of the infused lubricant layer is progressively compromised. The shear stress promotes lubricant drainage, leading to a gradual loss of surface slipperiness. As the lubricant layer depletes, the protective liquid interface can no longer effectively prevent the adhesion of microorganisms, thereby facilitating the onset of fouling. The primary mechanism responsible for this deterioration in performance is **lubricant depletion**. To systematically investigate this phenomenon, a collaborative study is conducted with the University of Sydney, focusing on the mechanisms governing lubricant depletion under controlled shear flow conditions. Teflon-based wrinkled nanoscale surfaces are fabricated as structured substrates, infused with silicone oil to create stable LIS. In order to directly visualize oil dynamics and quantitatively assess lubricant loss, a custom-designed meso-scale Taylor–Couette flow cell is developed. The LIS sample is attached to the device, inside the annular gap, subject to a shear flow field. The experimental protocol consisted of applying a rotational speed profile to the inner cylinder using a stepper motor, thereby imposing progressively increasing shear stresses on the surface. Simultaneously, high-resolution optical imaging is performed to monitor the evolution of the lubricant layer in real time. This setup enabled direct correlation between the applied shear conditions and the rate and mechanisms of lubricant depletion.

4.1. Introduction

4.1.1. Degradation of Liquid-Infused surface under shear flow

In a real environment, especially under shear flow conditions relevant to maritime applications, the infused lubricant layer is progressively depleted. As the lubricant drains, the surface gradually loses its lubricating properties, leading to a decline in slipperiness and promoting the onset of fouling.
In order to investigate the mechanisms that lead to lubricant depletion, it is fundamental to deeply analyze the physics related to the retention of oil, studying the phenomena in terms of mechanical forces. Capillarity and Van der Waals forces keep the lubricant in the scaffold cavities, thanks to the intermolecular forces, characterized by both adhesive and cohesive natures, that produce the interaction between atoms or molecules and act to keep the lubricant trapped and well-fixed to the substrate. The equilibrium of this condition could be destroyed if the order of magnitude of external force sources becomes even slightly higher than the force that keeps the fluid trapped between the textured solid substrates, breaking the intermolecular interactions. It can cause depletion of the lubricant. Then the adhesive and cohesive forces balance will be restored to a new stable state.
The nature of the external forces varies depending on the operating conditions and the specific application. These forces can arise from different physical mechanisms, each contributing in distinct ways to lubricant depletion. The following figure illustrates the primary mechanisms responsible for the progressive loss of the lubricating layer.[93]

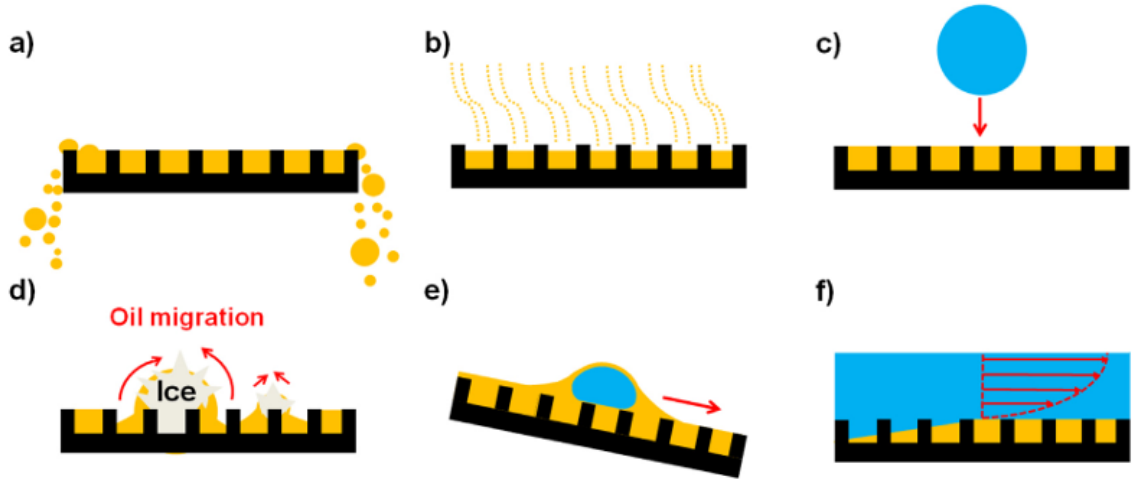

Figure 4.1: Gravitational drainage **a)** Evaporation **b)** Drop impact **c)** Frost growth via drop condensation and frosting **d)** Formation of wetting ridge and cloaking layers **e)** Shear flow conditions **f)**.[93]

Focusing on shear flow conditions, beyond the mechanisms previously outlined, external shear flow induces shear stresses on the lubricant film, which present a significant challenge. The capillary forces should keep the lubricant within the textured surface. However, when lubricant-impregnated surfaces are subjected to dynamic fluid environments, such as wind, water, or any working fluids that move across, the applied shear forces can lead to lubricant depletion, driven by shear-induced mechanisms, which gradually degrades the slippery property. At the interface between the lubricant oil and the working fluid, a non-zero slip velocity arises as a result of the external shear flow acting on the system. Due to the continuity of interfacial velocities, depletion occurs at the contact surface between the two fluids.
Previous studies have highlighted that even in the absence of physical barriers, a finite portion of the surface can remain stably wetted under flow conditions. Based on these experimental observations, from a theoretical point of view, it has been explained through an analytical model by[94], which attributes lubricant retention to capillary-driven trapping within the surface texture. Furthermore, the study identifies the critical role of geometric surface parameters in governing fluid retention, providing a framework that applies to both structured and randomly patterned substrates.
From an experimental point of view, Kim and Rothstein (2016)[95] observed that the presence of a slip velocity results in a fast depletion of the lubricant from between the microfeatures of liquid-infused surfaces. The viscosity ratio is one of the keys to understanding depletion mechanisms. Its role is fundamental as it determines the magnitude of the equivalent oil-water interfacial velocity, which governs the mass flux of lubricating oil within liquid-infused surfaces.
In the study conducted by H.N. Kim et al (2021)[48], the lubricant depletion phenomenon was experimentally investigated in a single spherical-shaped microcavity exposed to an external shear flow. The shape variation of the lubricant interface, subjected to a laminar channel flow, was directly observed in time.

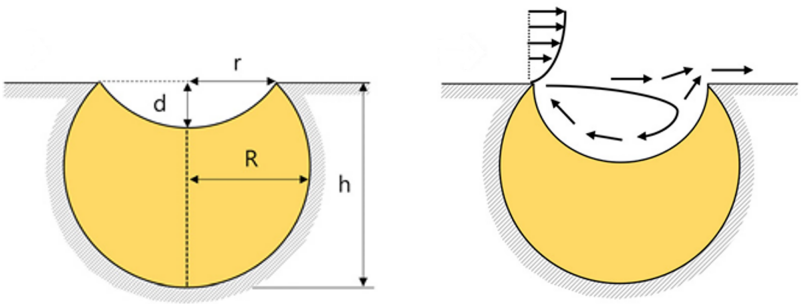

Figure 4.2: Left: Geometry sketch of the spherical cavity. Right: Large-scale vortex.[48]

The previous figure (4.2) illustrates two crucial aspects that demonstrate the potential for regulating and postponing the depletion mechanism. Close to the lubricant meniscus, the formation of a large-scale vortex can weaken the slippery layer by exerting shear stress on the interface, thereby reducing the depletion rate. Secondly, the ”opening ratio” is a geometric factor, with a smaller ratio conferring greater resistance against lubricant depletion.

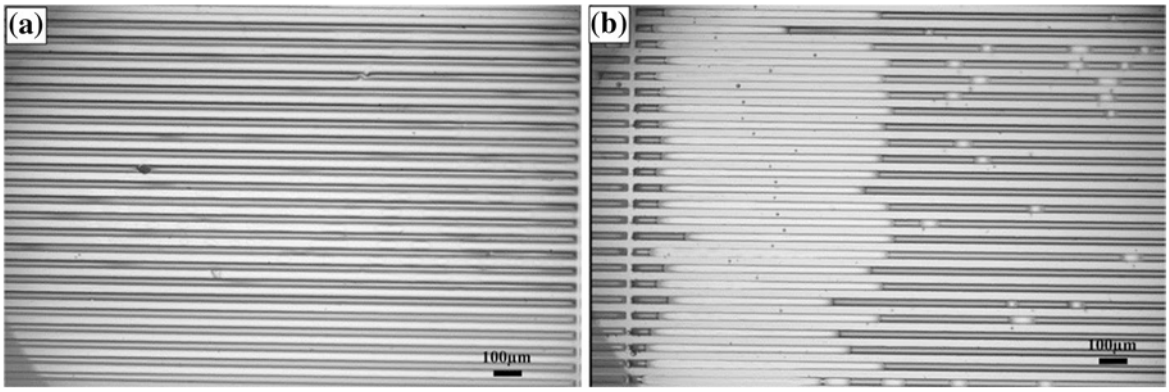

Figure 4.3: Microscope images of a microstructured surface, patterned with elongated grooves filled with lubricating oil. Right: partially-impregnated riblets after an external shear flow.[95]

Using a microchannel, Kim and Rothstein[95], investigated pressure drop behavior on liquid-infused superhydrophobic surfaces. They experimentally tested three different textured surfaces: a sandblasted surface, one with pillars, and one with micro ridges.
The figure 4.3 represents two images, obtained using the microscope, showing the system before and after the application of a flow rate of U = 0.4 mm/s with a viscosity ratio between the working fluid and lubricating layer of $\frac{\mu_w}{\mu_0} = 9.2$ across the liquid-infused surfaces. The shear stress induces recirculation within the microgrooves, leading to lubricant losses and leaving the surfaces partially oil-filled. First, a rapid depletion occurs, followed by a slow pressure drop that increases the depletion rate until a steady state is reached. Interestingly, a microstructured random surface provides an important delay in terms of slippery failure properties, enforcing the importance of three-dimensional random surface roughness for establishing and maintaining liquid-infused surface drag reduction.
Saoncella et al,[96] investigate lubricant-impregnated longitudinal grooves subjected to turbulent flow conditions. Their results indicate that the chemical compatibility between the lubricant and the working fluid is not a dominant factor in mitigating lubricant depletion. Instead, interfacial and geometric effects play a more critical role.

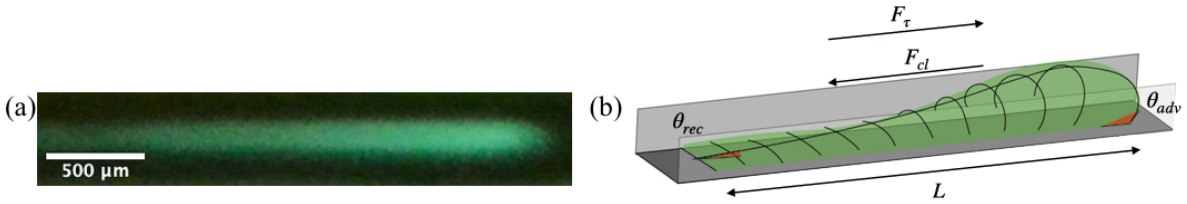

Figure 4.4: (a) Fluorescence intensity feedback of a lubricant droplet pinned within the groove of a partially wetting LIS. (b) Schematic representation of the lubricant interface, showing the advancing θ_{adv} and receding θ_{rec} contact angles, the lubricant length L, the external shear stress F_τ, and the pinning force F_{cl}.[96]

The experiments have been conducted in a turbulent water channel designed to provide a fully developed, high-Reynolds-number flow over the test section. The facility allows precise control of flow rate and shear conditions, with optical access to visualize lubricant behavior within longitudinal micro-grooves. To rationalize experimental observations, the authors develop a mathematical model that predicts the maximum streamwise elongation of a lubricant droplet under shear.
Their analysis shows that the stability and retention of macroscopic droplets are governed primarily by contact-angle hysteresis: the pinning of the triple-phase contact lines at substrate heterogeneities generates a capillary resisting force that counteracts shear-induced deformation and entrainment. As a result, this pinning mechanism provides a key stabilizing effect, significantly delaying or preventing lubricant depletion even under turbulent conditions.

4.1.2. Challenge of overcoming lubricant depletion

Liquid-infused surfaces (LIS) exhibit significantly greater stability than superhydrophobic surfaces (SHS) against pressure-driven and diffusive failure mechanisms, primarily due to the incompressibility of the infused liquid lubricant. Consequently, LISs have emerged as a promising alternative to SHS for applications operating under harsh conditions. Enhancing LIS performance and optimizing their drag-reduction capabilities requires a comprehensive understanding of the mechanisms governing lubricant depletion. This includes elucidating the interactions between the external working fluid and the surface, as well as establishing quantitative relationships between wettability characteristics and depletion dynamics. In addition, reliable methods for mapping lubricant thickness and accurately characterizing surface properties are essential.[97]
Nevertheless, when exposed to external flow, LIS are susceptible to shear-induced drainage of the infused lubricant. The imposed shear stress can progressively deplete the lubricant layer, leading to significant surface degradation and ultimately limiting practical applicability, particularly in submerged environments.
To overcome lubricant depletion, several appropriate techniques can be developed. The choice of lubricant viscosity μ_l is one of the keys to increasing the longevity of the lubricant layer, starting from the selection of a proper lubricant viscosity that must be much smaller than the outer working fluid ($\frac{\mu_w}{\mu_l} \gg 1$).
The hierarchical surface, characterized by the combination of micro and nanocavities, is widely regarded as one of the most promising textured surfaces for improving the durability of slippery properties. Recently, the presence of nanostructured elements has been shown to reinforce the lubricant film by enhancing intermolecular capillary forces, thereby improving performance in high shear conditions.[98,99]
Therefore, addressing shear-driven depletion and developing a robust physical understanding of the underlying mechanisms are crucial steps toward fully exploiting the potential of LIS.

4.1.3. Present study

This study focuses on the fabrication and characterization of liquid-infused surfaces (LIS), with evaluation of their slippery properties under static and dynamic conditions. A custom-built mesoscale Taylor–Couette cell is employed to investigate their durability under flow, while lubricant motion is visualized to better understand performance degradation and inform strategies for long-term improvement.

The present research aims to bridge the gap of the weak knowledge about lubricant depletion phenomena by building an innovative setup able to visualize lubricant oil dynamics under real flow conditions on a complex hierarchical substrate.

The research begins with the fabrication of Teflow-Wrinkles, the hierarchical substrate chosen for developing the study, subsequently infused with Silicone lubricant oil, followed by preliminary characterization to assess their initial properties. A key aspect of this phase is the measurement of wetting properties, particularly through contact-angle analysis, which provides insight into the surface's slippery behavior.

Simultaneously, a novel TC flow cell is designed, built, developed, and validated. This setup has been selected to test the LIS surface, able to reach turbulent flow conditions, and to reproduce desired flow conditions, while investigating through a visualization system the lubricant behavior under dynamic conditions.

The study focuses on visualizing lubricant losses through fluorescent feedback captured by the camera. This allows direct observation of depletion mechanisms and the spatial distribution of the lubricant.

The aim is to investigate the mode and dynamics of lubricant losses under turbulent flow conditions and focus on correlating wettability properties with lubricant viscosity.

4.2. Materials and Methods

4.2.1. Liquid Infused Surface: Teflon-Wrinkles fabrication

Teflon-Wrinkles (TW) are double-nanoscale surfaces fabricated and subsequently infused with silicone oil, following the methodology previously developed by[100]. There are five main steps to follow to fabricate a wrinkled surface, schematically summarized in the next figure:

1. Substrate preparation and cutting;
2. Substrate cleaning and surface preparation;
3. Thin film deposition via spin coating;
4. Thermal annealing;
5. Impregnation with lubricant oil.

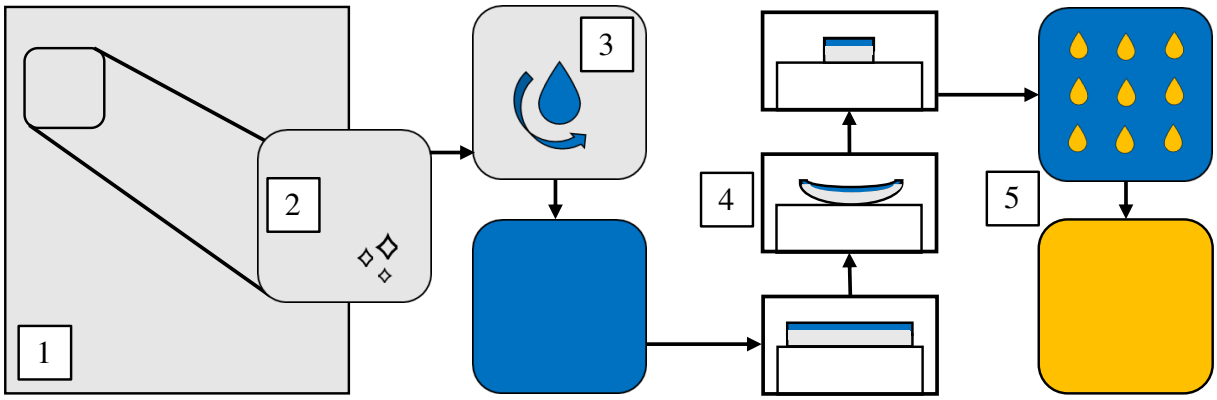

Figure 4.5: Schematic illustration of the five-step fabrication process.

The substrate consists of shrinkable polystyrene films (Grafix Shrink Film), a highly transparent plastic material fabricated from polystyrene resin and characterized by excellent shrinkage properties. The polymeric sheet is cut into square samples using a precision cutting machine. To accurately determine the dimensional variation of the substrate, a shrinkage factor, R, is defined as the ratio between a characteristic length measured before and after thermal annealing. Based on the obtained shrinkage factor ($R = 2.5$), the initial substrate dimensions are selected as 84×84 mm to achieve final dimensions of 34×34 mm, after thermal annealing. Additionally, corner fillets with a radius are incorporated into the square substrate design to reduce internal stress concentration within the material, thereby promoting improved flatness of the final sample. A parametric study has been developed to identify the best configuration. Three different corner radii have been designed (5, 10, 20 mm). By measuring the contact angle hysteresis, the difference between advancing and receding contact angles, as an indicator of the wettability property, and by evaluating the flatness of the sample, the 10 mm radius has been selected as the

best compromise to be as close as possible to the square shape ensuring a flat sample, and able to maintain good slippery property. Results and observations are summarized in the following table.

Fillet radius $[mm]$	$\overline{CAH}$ [°]	Flatness
5	9.0	$\sim$
10	10.3	✓
20	4.8	✓

Table 4.1: Fillet radius design dimensions of the substrate. Contact angle hysteresis to evaluate the wettability property. Flatness of the sample.

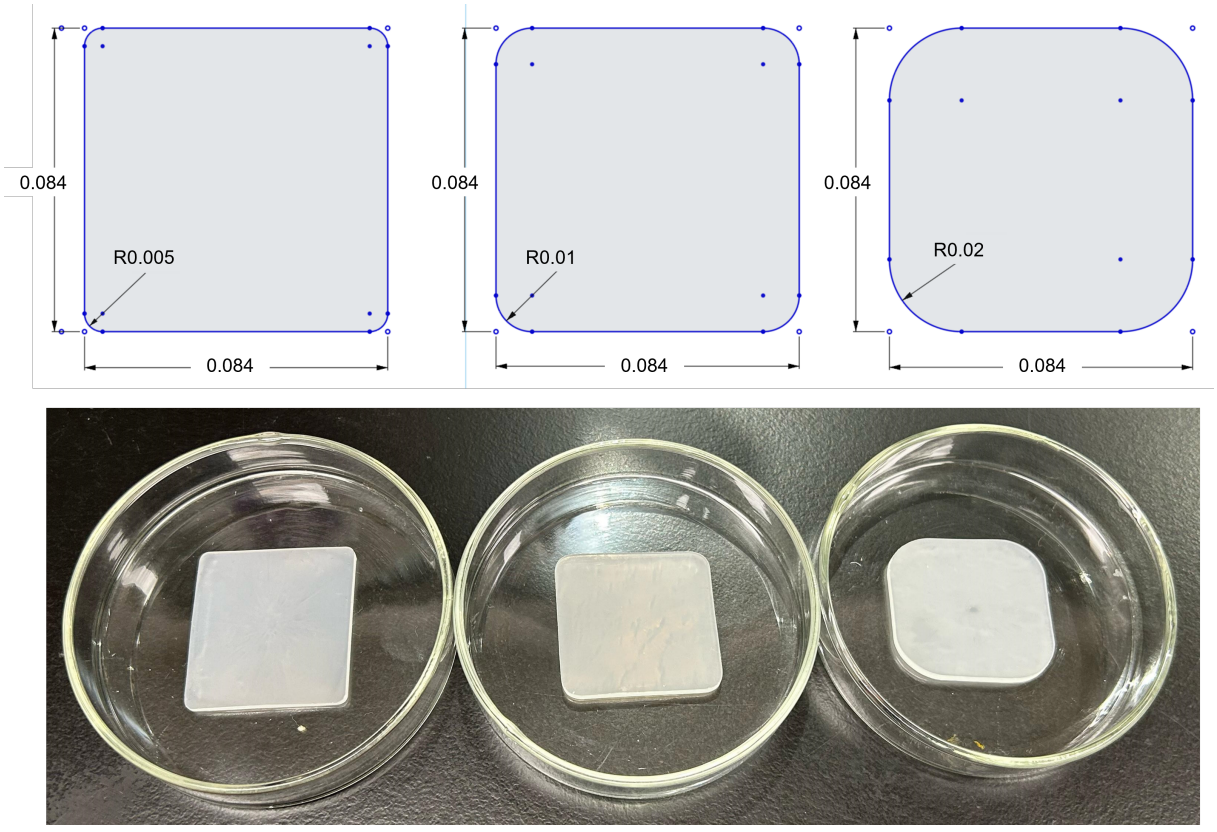

Figure 4.6: Flatness optimization by modifying the corner's radius.

Subsequently, the substrate is thoroughly cleaned by sonication in high-purity ethanol, followed by nitrogen blow-drying, in order to remove any contaminants and particulate matter from the surface. This cleaning step is of primary importance, as any residual contamination may lead to defects in the subsequent processing stages. A volume of 150 μl of Teflon AF 1% (Amorphous Fluoropolymer) in FC-40 (Fluoro-Carbon) is deposited on the substrate by spin-coating (speed

= 3000 rpm, time = 60 s). The solution spreads all over the substrate, creating a thin layer of Teflon; the thickness is about 36.5 nm (standard deviation 1.2 nm), by measurements conducted by an ellipsometer. The following step is the one that actually makes the surface; it creates the hierarchical structure, leading to the formation of the superhydrophobic and highly oil-wettable material. The sample is annealed in the oven at 135 °C for 1 hour.

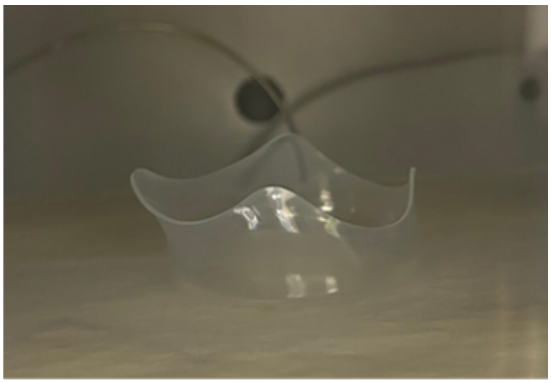

Figure 4.7: Wrinkles formation process by thermal annealing phase is in the oven.

The thermal annealing process induces wrinkling due to the modulus mismatch between the Young's modulus of Polyshrink and Teflon AF. The previous figure 4.7 shows a TW sample in the oven, which starts to shrink, modifying its shape and dimensions. Uniform heating is crucial, especially in the first 15 minutes, to ensure a flat and effective surface. The last 45 minutes properly cure all the nanostructured cavities and porosities. The final sample measures approximately 34 x 34 mm. The final step is impregnation with lubricant oil; the infusion consists of approximately $90\,\mu l$ of Silicone oil (10 and 50 cSt, Sigma-Aldrich), mixed with Nile Red (Sigma-Aldrich), a fluorescent dye pre-dissolved in acetone. The lubricant density is the same for the two fluids, $\rho_{lub} \simeq 940\,kg/m^3$, and the dynamic viscosity is for the case of 10 cSt $\mu_{lub}^{10} \simeq 9.3 \times 10^{-3}\ Pa\,s$ and for the case of 50 cSt $\mu_{lub}^{50} \simeq 4.65 \times 10^{-2}\ Pa\,s$. The oily solution is dropped out in 9 droplets of 10 μl each, then the oil is spread with the micropipette tip all over the surface. After leaving it on infusion, it has been placed vertically to drain away the excess oil. The role of the dye, crucial in the visualisation process, is discussed in detail in Section 4.3.1.

4.2.2. Surface characterization: wettability properties and surface topography.

The slippery behaviour of the fabricated LIS is characterised based on contact angle hysteresis, roll-off angle, and droplet mobility measurements[97]. All the contact angle measurements have been performed by a contact angle goniometer, following a well-defined procedure and settings. In particular, the advancing and receding contact angle measurements have been performed by increasing the volume of a Milli-Q water droplet, with a constant rate, up to about 13 μl, and then decreasing it, while recording several images of the droplet. Following the common definition, the contact angles have been evaluated as the angle between the baseline of the droplet and the tangent. The next plot is an example of the trend. Increasing the volume, the

contact angle follows the top line, and then after reaching a maximum volume value, it starts to slowly and linearly decrease. By averaging the values around 10 μl, for both cases, and evaluating the difference between advancing and receding contact angles, the contact angle hysteresis is evaluated.

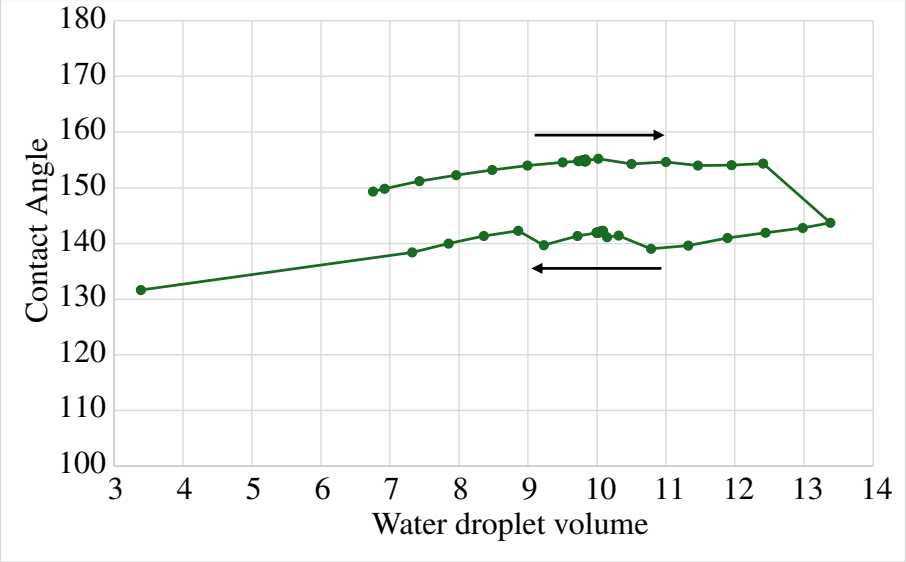

Figure 4.8: Contact angle measurements [°] vs Water droplet volume $[\mu l]$ to evaluate the hysteresis contact angle.

Teflon wrinkles exhibit significant superhydrophobic behavior. The hierarchical nano-cavity structure promotes the trapping of an air plastron beneath the droplet, significantly reducing the liquid–solid contact area. As a result, the droplet remains in a Cassie–Baxter wetting state and tends to adopt a nearly spherical shape on the surface (Fig. 4.9).

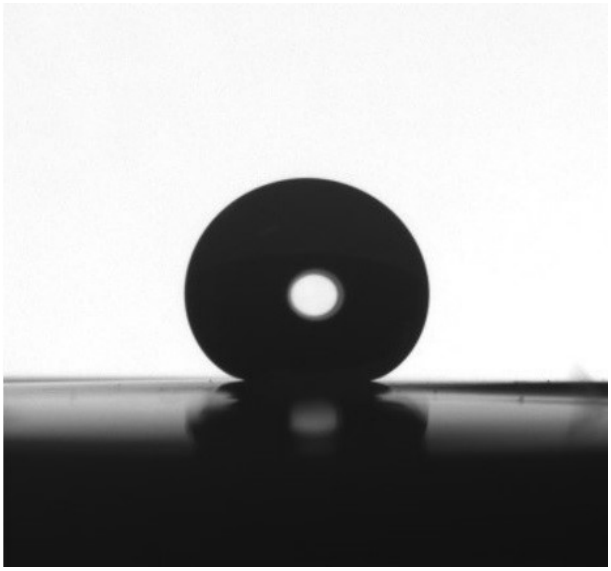

Figure 4.9: 10 μl Milli-Q water droplet on uninfused Teflon-Wrinkles sample.

The following table 4.2) presents the average wettability properties over all the Teflon-Wrinkles samples; in particular, showing the overall average values of advancing, receding, and hysteresis contact angle and its standard deviation. By looking at the results, the surface presents good superhydrophobic properties. The advancing contact angle should generally be larger than 150° for a superhydrophobic surface, and the hysteresis should be lower than 10°. However, in the case of TW surfaces, it is close to 10°, but slightly larger. The superhydrophobic performances aren't excellent, CAH could reach even a value lower than 5°.

$\overline{ACA}$ [°]	$\overline{RCA}$ [°]	$\overline{CAH}$ [°]
158 ± 2	145 ± 5	13 ± 2

Table 4.2: Advancing Contact Angle (ACA), Receding Contact Angle (RCA), and Contact Angle Hysteresis (CAH) of uninfused Teflon-Wrinkles surfaces.

However, TW samples have been selected as highly promising liquid-infused surfaces thanks to the exhibition of high oil wettability and excellent capability of retaining the lubricant due to their chemical composition and hierarchical nanostructure, as described by[52]. The nanowrinkle morphology efficiently traps the silicone lubricant oil, since Teflon exhibits a positive spreading parameter in water that promotes lubricant spreading and retention.

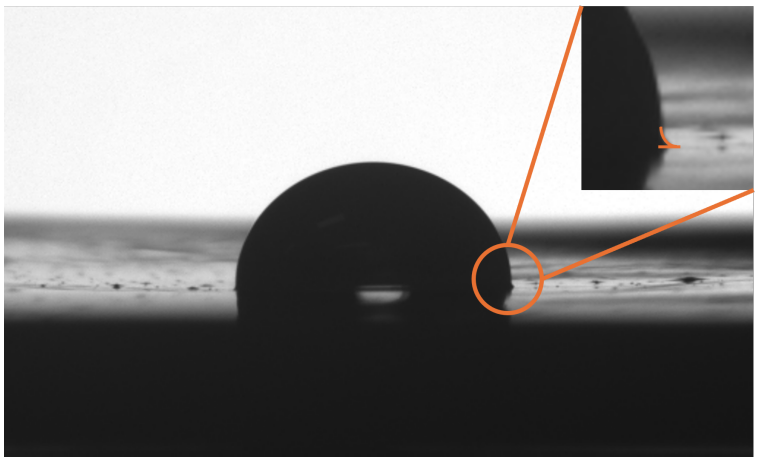

Figure 4.10: 10 μl Milli-Q water droplet on infused TW sample with 10 cSt Silicone oil.

After lubricant infusion, the $\overline{CAH}$ decreases to approximately $\sim 3°$, resulting in reduced liquid–surface friction. Achieving high droplet mobility requires an optimal oil volume. This can be verified by observing a limited droplet meniscus. Excessive oil may form a thin lubricating film that partially cloaks the droplet, thereby reducing its mobility.
The structure is composed of smaller nano-cavities of approximately 200 nm in width and height and larger ones of about 1 μm, together forming a multi-scale architecture that enhances lubricant stability. The surface topography is characterized by atomic force microscopy (AFM) over a scan area of 10×10 μm^2. Measurements were performed in tapping mode, a high-resolution imaging technique in which a microcantilever oscillates near its resonance frequency

$\overline{ACA}$ [°]	$\overline{RCA}$ [°]	$\overline{CAH}$ [°]
116	113	3

Table 4.3: Wettability properties of Silicon-oil infused Teflon-Wrinkles surfaces.

and intermittently contacts the sample surface. This operational mode minimizes lateral forces and reduces the risk of structural damage while preserving high spatial resolution. The figure 4.11 shows surface characterization obtained by AFM. The image on the left qualitatively reveals the wrinkled morphology of the surface, including the presence of localized defects, such as darker voids and linear features, indicating a degree of structural heterogeneity. By selecting one line (dashed red line), through a specific software is possible to obtain the corresponding height profile. The y-diagram on the right shows a representative cross-sectional line extracted from the scan area, providing quantitative information on the amplitude and spatial distribution of the surface features.

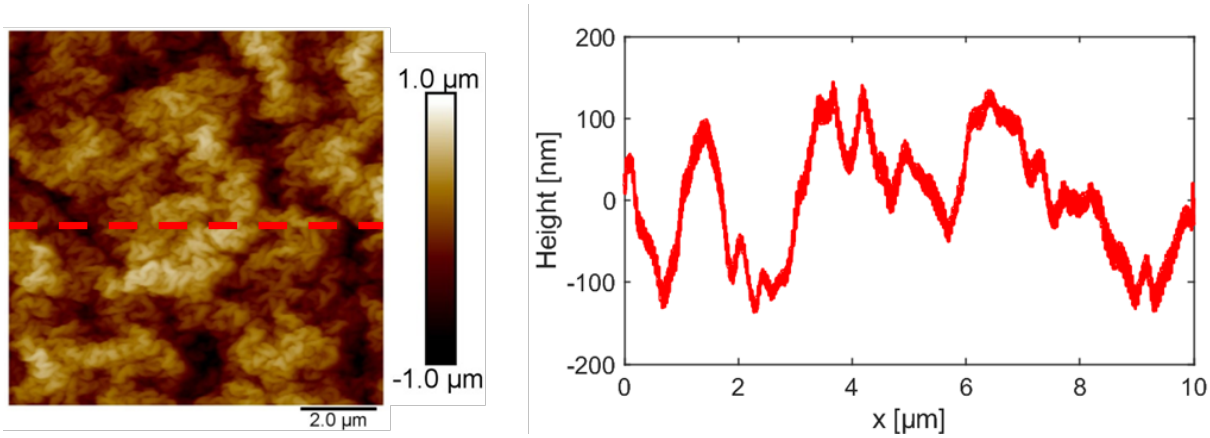

Figure 4.11: On the left, an Atomic Force Microscopy image shows TW topography. On the right, y-diagram representation presents the surface profile with valleys and peaks.

4.3. Experimental apparatus

4.3.1. Taylor-Couette flow cell and visualization system

The experimental apparatus is a custom-built meso-scale Taylor-Couette flow cell. The main part of the design consists of two coaxial cylinders: a stationary outer cylinder and a rotating inner cylinder. The outer cylinder, fabricated from transparent acrylic, enables visual observation of the interior. The inner cylinder is made of opaque black anodized aluminum to avoid light reflections. It is shaft-connected to a stepper motor (ISV-57T) that rotates up to 3000 rpm, supported by two precision ball bearings. A 3D-printed substrate holder is designed to properly keep the sample in place, avoiding leakages and resisting fluid motion, even under high pressure, and to ensure tangential alignment of the substrate with the internal lateral surface, allowing a correct interaction between the rotating flow and the LIS. The sample is placed at half the cylinder's height to minimize the effects of the upper and lower walls.

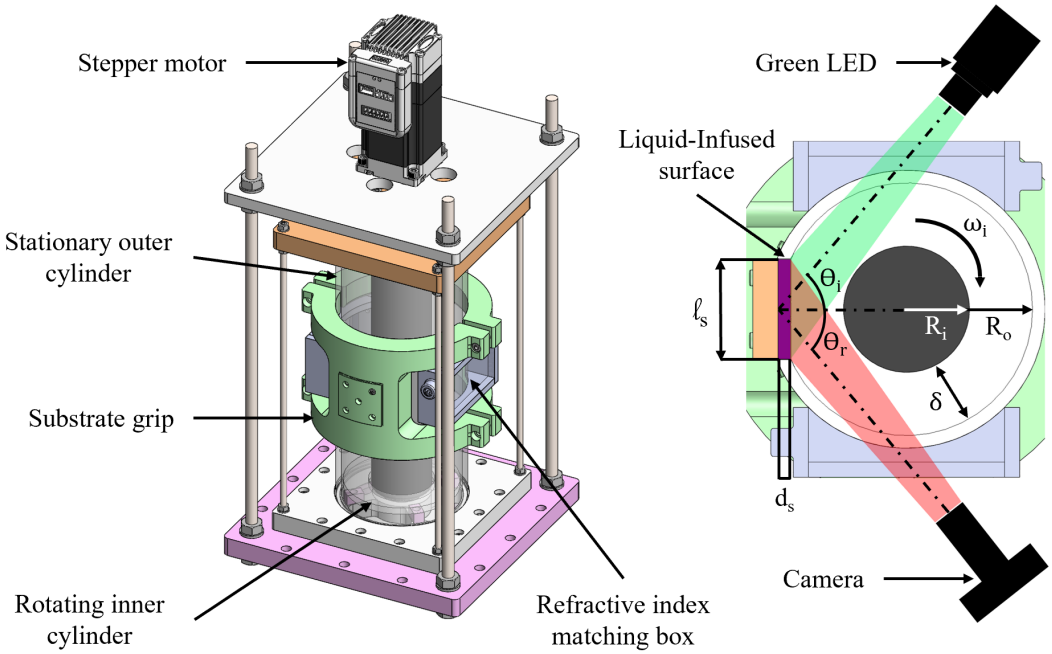

Figure 4.12: Schematic of the Taylor-Couette flow cell built in this project. On the right, a magnified view of the liquid-infused surface's location and a representative sketch of the visualisation system.

R_i [mm]	R_o [mm]	δ [mm]	ℓ_s [mm]	d_s [mm]	θ_i [°]	θ_r [°]
25.0	50.0	25.0	35.0	1.8	-	-

Table 4.4: Experimental setup dimensions.

The visualization system (Fig. 4.12) is mainly composed of two objects: the green LED, a light source device, and a camera. The Light Emitting Diode (LED) provides green light, filtered by using an optical bandpass filter (Edmund Optics - Filter BD OD4 $525 \pm 25\,nm$), to exclude lower and upper light wavelengths, ensuring to enlighten the sample. The illumination passes through the refractive index-matching box to minimize diffraction effects before reaching the sample. The green light excites the Nile Red, dissolved in the lubricant oil, leading to an orangish-emission light, absorbed by a coloured camera (Panasonic Lumix DC-GH5) equipped with a red filter installed (BrightLine Basic Fluorescence Filter, Central Wavelength CWL of 620 nm and a Guaranteed Minimum Bandwidth GMBW of 52 nm). The filter suppresses all the other wavelengths, enabling selective imaging of the thin lubricant layer. The dye plays a crucial role in capturing oil dynamics during the test, whose oil film thickness, $\sim$ 1-2 μm, would otherwise be undetectable by an optical system.

The following figure shows the final experimental apparatus developed for this study. The system is entirely designed and built from scratch, in order to perform controlled experiments on lubricant depletion from Teflon-wrinkled surfaces. The apparatus is specifically developed and engineered to investigate lubricant depletion on Teflon-wrinkled surfaces, in real conditions, using a complex hierarchical surface. Figure 4.13 shows five transparent rectangular overlays highlighting the main components of the experimental setup, which are described below.

- **Green box:** The *Taylor–Couette cell* represents the core of the system. It generates the desired flow conditions, hosts the liquid-infused sample, and its design enables the visualization of the lubricant motion.

- **Orange box:** A *colour camera* used to acquire high-quality videos of the experiments. The picture 4.14 shows the camera's point of view through the observation window of the Taylor–Couette cell, providing a direct view of the test section inside the apparatus.

- **Blue box:** The *LED illumination system* provides green light that illuminates the surface and excites the dye within the lubricant.

- **Purple box:** The *control system* consists of a *function generator*, which produces a periodic electrical signal (a square wave in this study) to modulate the LED brightness, and a *computer* interfaced with an Arduino and the stepper motor. This setup enables control of the motor rotational speed while simultaneously recording the electrical intensity feedback and other experimental signals.

- **Yellow box:** *Additional auxiliary devices* required to perform the experiments, including a *peristaltic pump* used to fill the cell, a *scientific digital thermometer* to monitor the temperature of the solution, and *adhesives* used to secure the sample inside the cell.

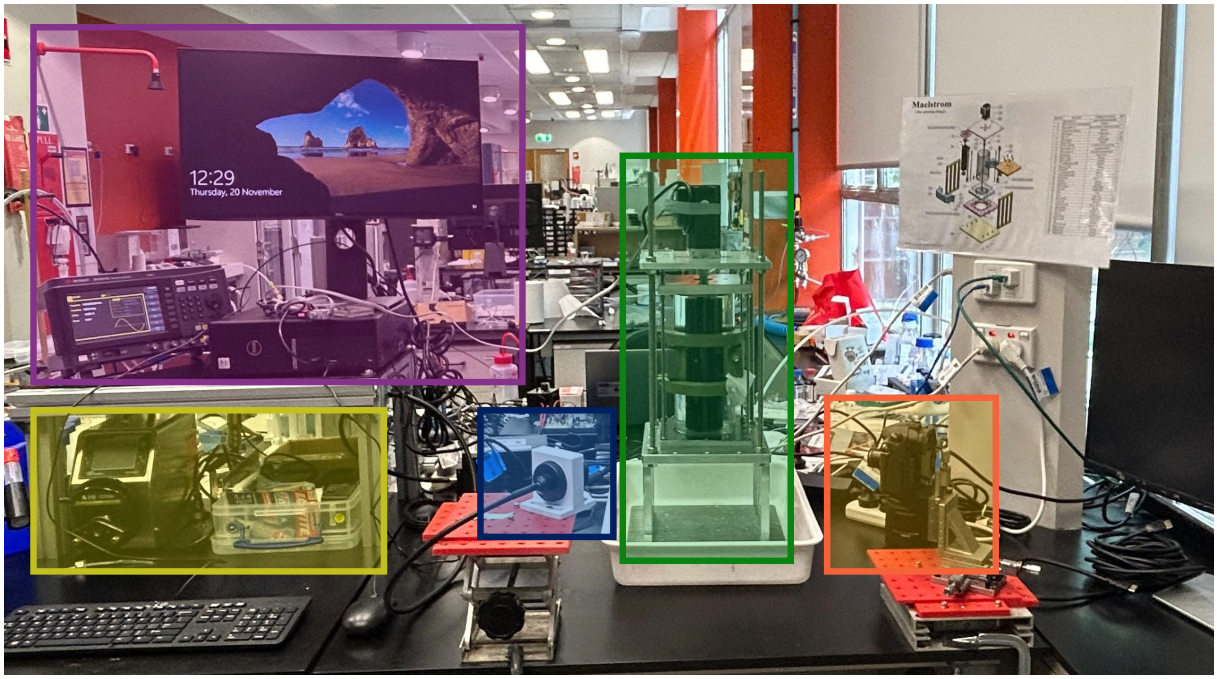

Figure 4.13: Picture of experimental apparatus, with coloured rectangle to indicate the main components.

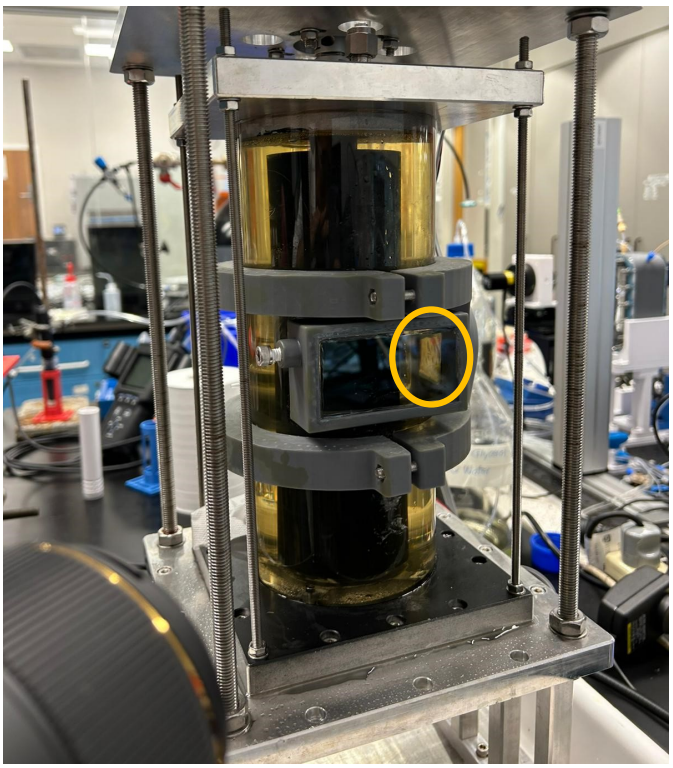

Figure 4.14: Photograph of the Taylor–Couette apparatus used in the experiments. The camera is oriented with the lateral window, providing optical access to the test section (yellow circle) and enabling the recording of lubricant distribution and redistribution on the sample surface under shear flow.

4.3.2. Refractive Index Matching solution

A refractive index matching (RIM) box filled with a solution is placed around the outer cylinder to correct the optical distortion and eliminate refraction caused by the curvature of the outer cylinder. The solution has a refractive index RI of 1.4893, closely matching the acrylic one, equal to RI = 1.49. The solution consists of 45 wt% of Ammonium Thiocyanate (Sigma-Aldrich), 30 wt% of Glycerol (Thermo Fisher Scientific), and 25 wt% of Milli-Q Water.[101,102] The Ammonium Thiocyanate solution presents two issues: it tends to decolorize, due to iodine precipitation, it is acidic (pH $\simeq$ 5), and it can corrode some cell materials. To overcome these problems, $\sim$ 0.2 wt% of Sodium molybdate is added as a corrosion inhibitor to protect metallic components in contact with the RIM solution. $\simeq$ 0.05 wt% of Ascorbic acid is included as an agent to stabilize and neutralize the solution, limit oxidative degradation, and maintain long-term optical clarity and transparency. Solution properties, such as density ρ and viscosity μ, are essential for defining the flow regime conditions. Density measurements are performed using a Density Meter DMA 4100 M (Anton Paar), with the temperature increased stepwise from 10 °C to 40 °C in 2 °C increments. The density decreases by approximately 0.05 % at each step, following the expected linear trend with temperature. Dynamic viscosity is measured using an Anton Paar rheometer as a function of shear rate, γ, at fixed temperatures. The measurements are then averaged to obtain a single representative viscosity value for each temperature. In particular, the test is run by increasing γ from 1 $[\frac{1}{s}]$ to 750 $[\frac{1}{s}]$, at a static temperature, performed between 10 °C and 40 °C, with 5 °C steps. The chosen bottom plate is PLS55-C0147-SS, and the top cone-plate is CP4/40-SR0730-SS. For each temperature, the average dynamic viscosity is calculated.

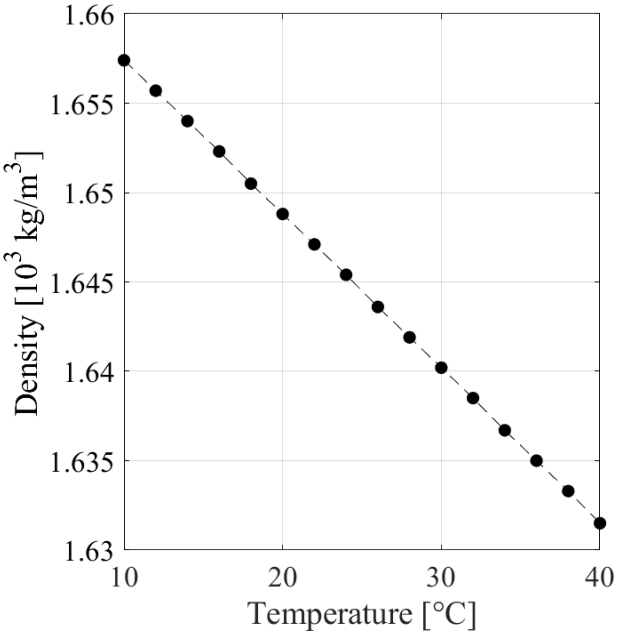

Temperature [°C]	Density [$\mathrm{kg/m^3}$]
10	1657.4
12	1655.7
14	1654.0
16	1652.3
18	1650.5
20	1648.8
22	1647.1
24	1645.4
26	1643.6
28	1641.9
30	1640.2
32	1638.5
34	1636.7
36	1635.0
38	1633.3
40	1631.5

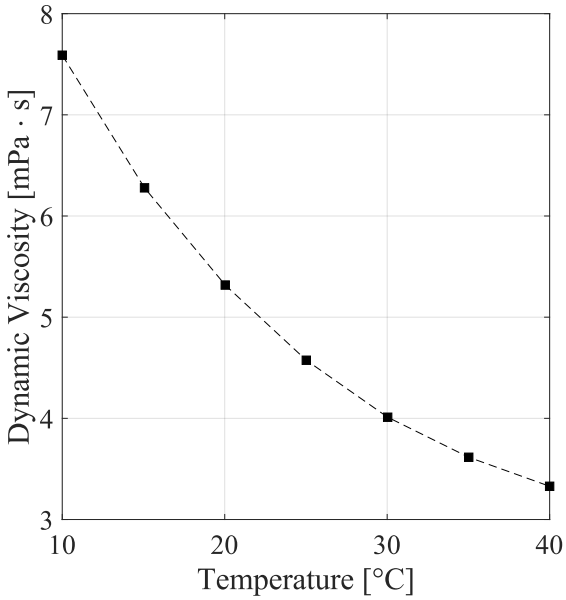

Temperature [°C]	Viscosity $[mPa \cdot s]$
10	7.59
15	6.28
20	5.32
25	4.57
30	4.01
35	3.62
40	3.33

Figure 4.15: RIM solution properties, density and viscosity, as a function of temperature. The figures on the left show the experimentally measured trends, while the tables report the values.

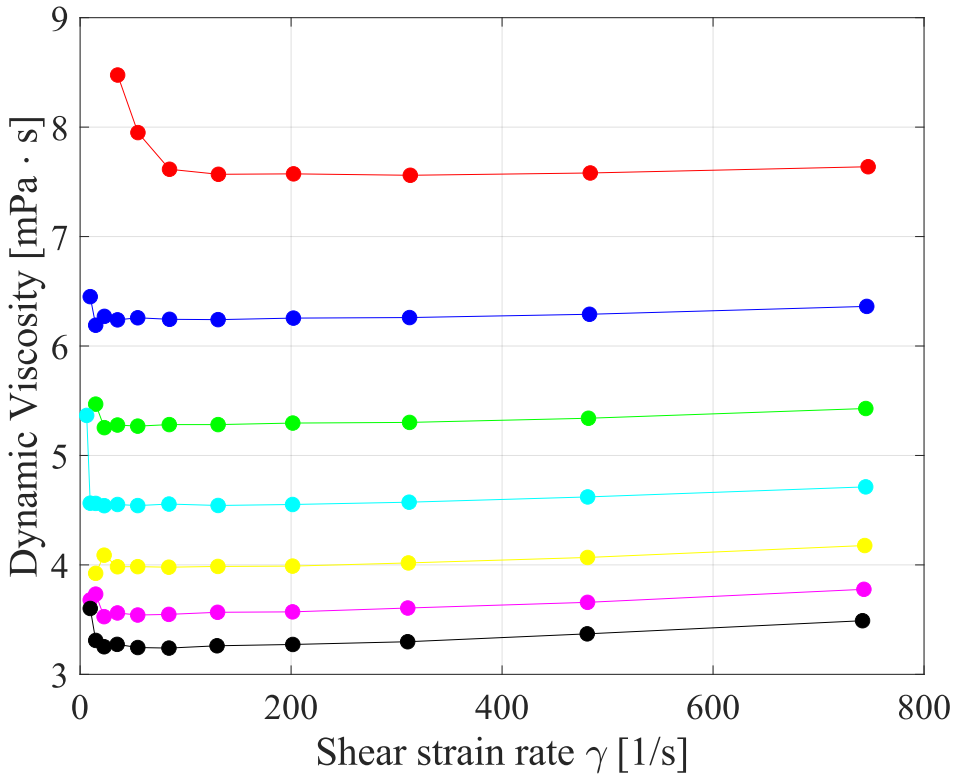

Figure 4.16: Constant temperature rheometric test: dynamic viscosity vs shear strain rate.

4.3.3. Setup and operating conditions

Before the experiments, both the laboratory ambient temperature and the temperature of the solution are recorded. The sample is permanently glued to a removable component of the substrate grip, which is designed to accommodate different samples. Once the substrate holder is correctly mounted, sealing the outer opening, the cell is filled with the refractive index matching (RIM) solution up to the top plate. Particular care is taken to avoid trapping air inside the cell, as this would generate bubbles during the test. After filling, the Taylor–Couette cell is ready for operation. The next step involves setting up the visualization system. Specifically, the position and orientation of the green LED and the camera are adjusted to ensure proper light emission, reflection, and capture through the optical windows. Both the light intensity and the camera settings, including the aperture, are kept constant throughout the experiment. The stepper motor is controlled via the StepperOnline iSV software. The rotational speed can be defined either manually, by specifying the acceleration ramp and the final rotational velocity, or automatically via an Arduino, appropriately programmed and electrically connected to the motor. Once the stepper motor is programmed and ready, the camera begins recording to capture the initial condition. The experiment is then started, and the camera continues recording until the end of the test. All experiments are recorded at a constant frame rate of 50 fps.

The experimental campaign can therefore be divided into two main categories.
In the first experimental investigation, a constant rotational speed is imposed in order to study the quasi–steady-state behaviour of the lubricant at a fixed shear rate. It aims to reproduce operating conditions in which a slippery surface is exposed to a constant shear flow, allowing the investigation of how the lubricant layer evolves and adapts to steady external forcing. To investigate long-term lubricant depletion, experiments are performed at constant rotational speeds: low shear-condition (500 rpm) and high-shear condition (1500 rpm), corresponding to two distinct flow regimes. These tests aim to characterize the lubricant response under moderate/sustained and extreme shear conditions and to identify the primary effects induced by the flow. In particular, the analysis focuses on the existence of transitional and quasi–steady states, the duration of the transient phase, and the dependence of these features on the imposed flow regime.
In the second, a stepwise rotational speed protocol is applied to investigate the dynamic response of the liquid-infused surface under progressively increasing shear-rate conditions. The stepwise velocity protocol starts from 0 rpm and increases up to 2000 rpm in increments of 250 rpm, with an acceleration ramp of 200 $\frac{rpm}{s}$. Each speed step is maintained for 1 minute. This experimental investigation aims to mimic situations in which the surface is subjected to progressively increasing shear conditions, as would occur for a body accelerating in a fluid, thereby enabling the study of the transient response of the liquid-infused surface. Finally, in order to investigate lubricant depletion under dynamic conditions, experiments are performed using two different lubricant viscosities. This comparison enables assessment of the role of viscosity in governing the response of the liquid-infused surface under progressively increasing speed.

Two distinct surface types are investigated in this study: a liquid-infused surface, specifically the previously described Teflon-wrinkles material, and a regular grooved surface. To evaluate the effectiveness of the lubricant system, a grooved sample is specifically designed and impregnated with lubricant oil. The geometry and dimensions of the periodic elements are illustrated in the following figure. This well-defined and easily recognizable geometry is intentionally chosen to facilitate the observation and analysis of lubricant distribution throughout the tests. By providing clear visual images of oil retention and motion, the design ensures that the experimental results are both reproducible and interpretable, enhancing confidence in the reliability of the lubricant visualization method. Moreover, the regular pattern allows for a systematic assessment of how the lubricant behaves under different shear conditions, providing quantitative and qualitative insights into the performance of the liquid-infused system.

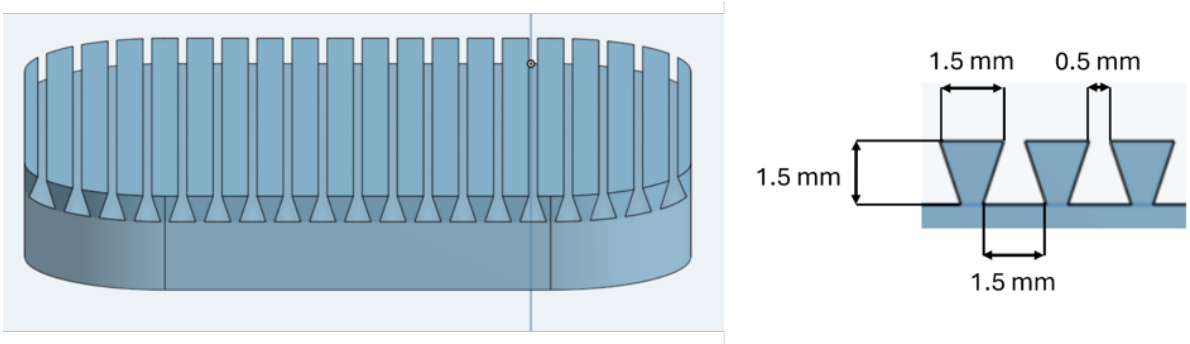

Figure 4.17: Left: grooved sample design. Right: Magnified side-view of the periodic element, with the geometric dimensions.

4.4. Results and Discussion

4.4.1. Data Postprocessing

The fluorescence intensity emitted by the lubricant-infused sample is assumed to be proportional to the local lubricant thickness. The measured light intensity results from a combination of fluorescence emission from the dye dissolved in the lubricant and reflections from both the oil and the substrate surface. However, the analysis procedure is developed to remove the contribution of surface reflections, as their intensity remains constant throughout the experiment. Based on this signal, the lubricant motion is investigated by tracking and quantitatively evaluating the fluorescence intensity averaged in both time and space. The objective of this analysis is not to determine the absolute lubricant volume from fluorescence intensity, as the imaging system is not calibrated for quantitative thickness measurements; rather, the intensity is used as a relative indicator of lubricant distribution. Instead, the analysis focuses on two main aspects: quantifying lubricant loss at different rotational speeds and tracking depletion phenomena by examining the raw image sequences. In particular, the recordings allow observation of the lubricant structures and their interaction with the external flow, which leads to the formation of vortices, streaks, and rounded bubble-like structures.
A MATLAB script was developed to analyze the recorded videos. Figure 4.18 shows the selected region of interest (ROI): a rectangular area corresponding to the textured surface.

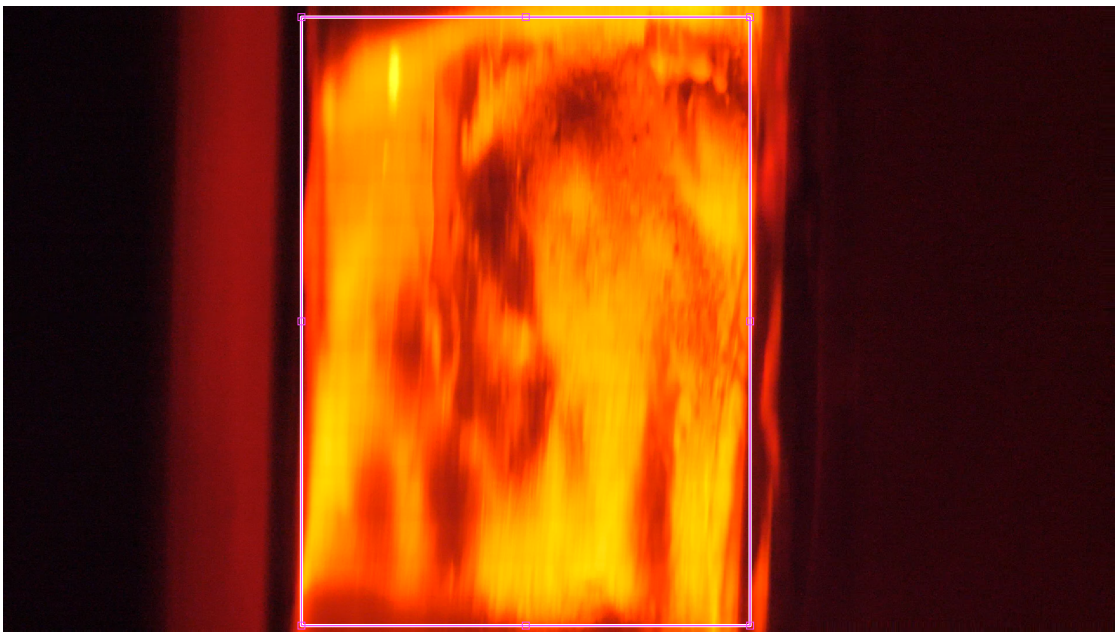

Figure 4.18: Screenshot of the full recorded image displayed in MATLAB. The magenta rectangle indicates the region selected for cropping.

This region is manually defined before running the code and is applied consistently to all frames of the video. Each frame is initially imported as an RGB image, where each pixel is characterized by three color channels representing the intensities of red, green, and blue. The MATLAB function *rgb2gray* converts the RGB image into a grayscale image by combining the three channels into a single intensity channel that represents pixel brightness. As a result, each frame is converted into a grayscale image. This step is commonly performed in image processing to facilitate the analysis of pixel intensity values.

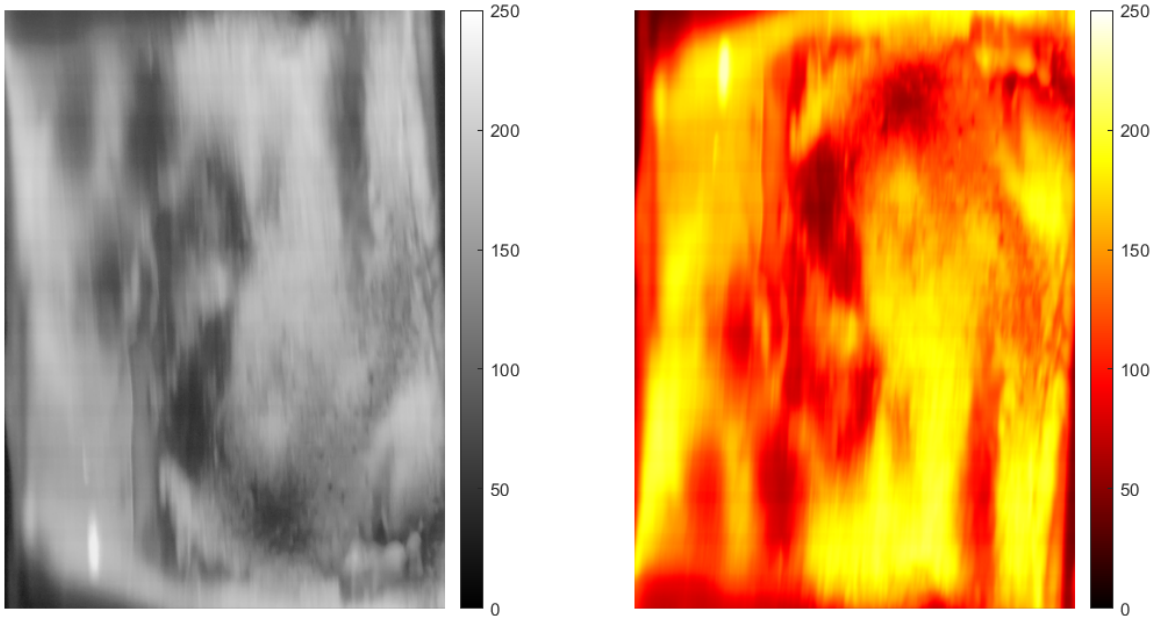

Figure 4.19: Left: Instantaneous image in grayscale. Right: mean initial image as reference state - average of the first 100 images.

A reference state is defined by averaging the first $n_0 = 100$ frames acquired under stagnant conditions. A *mean initial intensity* field $I_o(x, z)$ is generated by summing the first n_0 frames and then dividing them by the total number, obtaining the image on the right in the following Figure 4.19. This reference image depicts the undepleted lubricant distribution; it shows the initial oil distribution, highlighting its non-uniformity due to surface inhomogeneities. Darker regions indicate areas where the lubricant has been partially depleted, for example, during the filling of the cell with the RIM solution, or locations where the surface topography retains less lubricant within the nano-wrinkled cavities. In contrast, lighter regions correspond to areas where the lubricant layer is thicker. It interestingly provides a direct visualization, a realistic snapshot, of the oil distribution over a hierarchical structure in contact with an external fluid, thereby revealing the complexity of a liquid-infused surface.
For each subsequent frame, the instantaneous intensity field $I_i(x, z, t)$ is processed, and the mean intensity over time, the average along the flow and axial direction have been computed.
There are various ways to represent, analyze, and visualize the results. First, a list of them is provided below.

- **Instantaneous images** - a representative frame extracted from the video. The lubricant distribution is effectively frozen at a specific moment in time. This allows for a direct comparison between different stages of the experiment by examining how the main oil distribution and structural patterns evolve.

- **Spatial-temporal field** - intensity fields averaged along the streamwise (x) and axial (z) directions to characterise spatial configuration, yielding spatiotemporal depletion maps. These contours are visualised using diverging colour scales centred at zero, which allows for clear differentiation between lubricant depletion (negative values) and accumulation or redistribution (positive values).

- **Global depletion percentage rate** DR - global parameter to evaluate the global lubricant depletion effect. It is quantified by, firstly, averaging over time (t) and space (x, z) each frame, yielding a single representative value, and secondly subtracting the initial condition $I(x, z, t) = I_i(x, z, t) - I_o(x, z)$ and normalising the intensity difference by the initial condition:

$$DR\,[\%] = \frac{I(x,z)}{I_o(x,z)} \cdot 100\,[\%] = \frac{I_i(x,z) - I_o(x,z)}{I_o(x,z)} \cdot 100\,[\%] \tag{4.1}$$

The flow regime is determined by the Reynolds number, which is defined as:

$$Re = \frac{\omega R_i d}{\nu} \tag{4.2}$$

The following sections summarize the main results, organized by surface type (grooved sample or Teflon-wrinkles) and by speed conditions (constant shear or stepwise-increasing shear flow).

4.4.2. Grooves sample case

The grooved sample is designed as a reference case to demonstrate the correct operation of the system. The objective is not to develop an optimized groove design, but rather to select dimensions and geometries capable of retaining the oil. Therefore, the purpose is to demonstrate the effectiveness of the system rather than to evaluate the intrinsic performance of the surface. Three consecutive tests, at a constant shear rate, have been run, all starting from 0 rpm up to three different speeds: 100 rpm, 900 rpm, and 1800 rpm, in order to investigate low, moderate, and high shear conditions.

Instantaneous images

The initial and final images are captured by the code, corresponding to the beginning and the end of the video recording. By observing the lubricant configuration on the 3D-printed grooved sample, lighter lines can be identified where the oil is retained, showing a higher concentration in the central region of the sample. In contrast, the darker and wider lines correspond to the groove tips, which are likely covered only by a thin lubricant layer. A comparison between the two images reveals the presence of oil at the start of the test and its almost complete depletion

by the end, mainly due to the shear stress exerted on the surface. A particularly relevant aspect is the presence of linear patterns, clearly visible to the naked eye, which provide a direct interpretation of the fluorescence signal captured by the camera. The following three groups of images present snapshots of the initial and final conditions for all the investigated flow regimes. These images represent the evolution of the sample at key moments of the experiment, qualitatively illustrating the lubricant's resistance under low and moderate shear conditions, while also highlighting the collapse of the liquid-infused surface when subjected to high shear stresses. The quantitative results will be presents in the following sections.

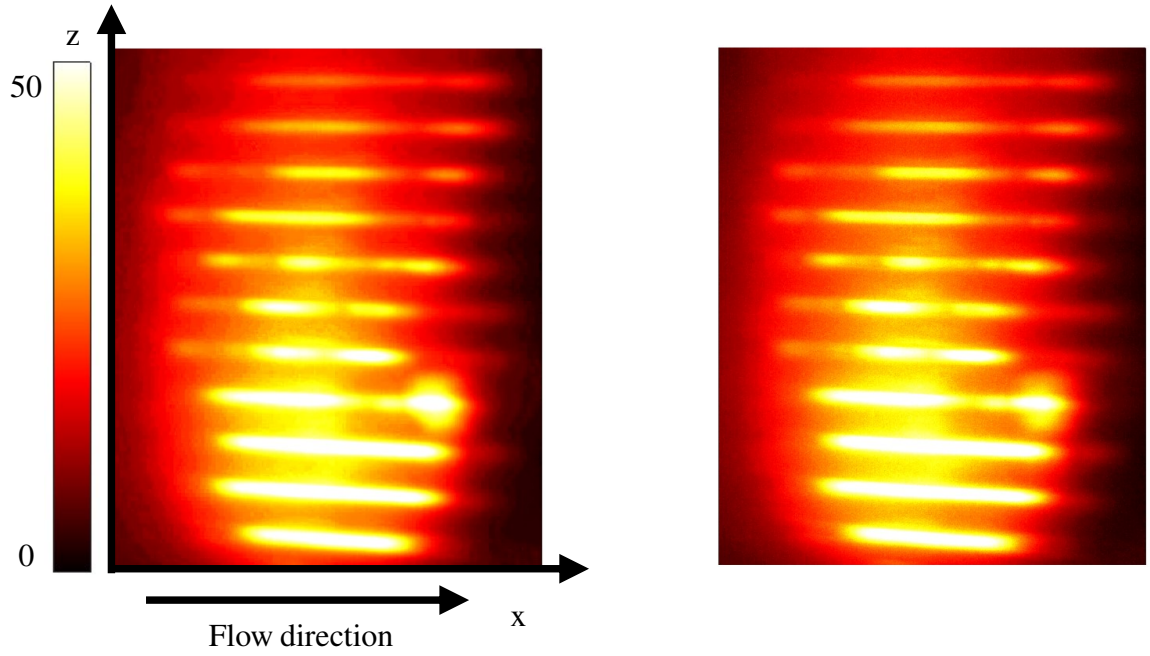

Figure 4.20: Initial (left) and last (right) instantaneous images for a grooved sample. Inner cylinder's rotational speed = 100 rpm.

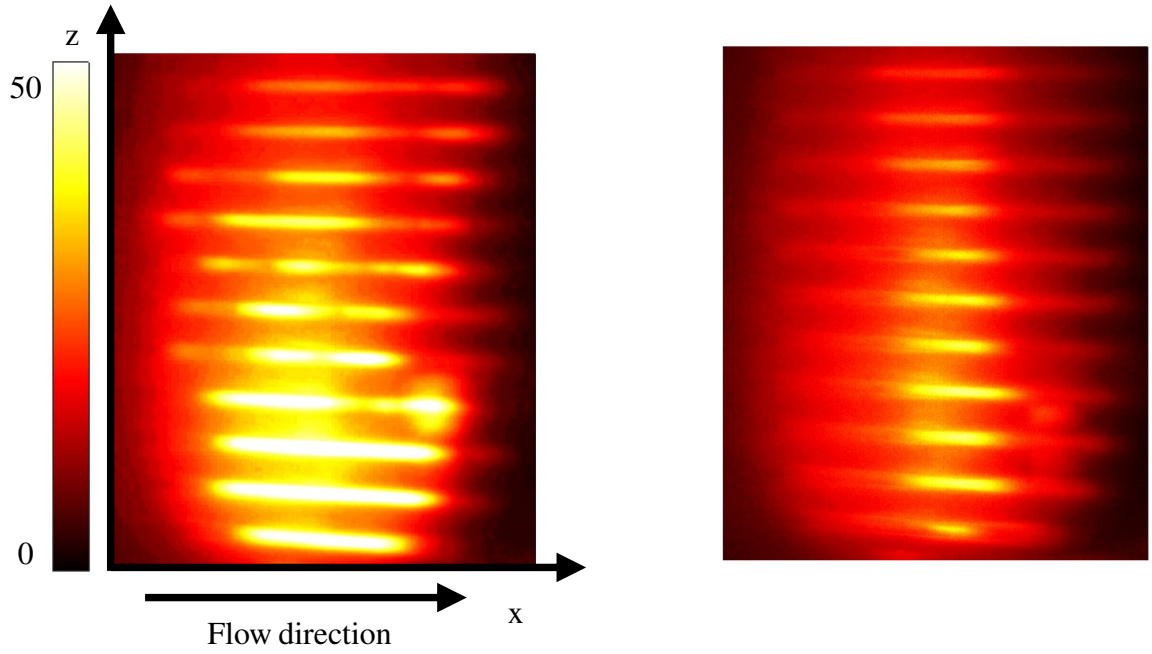

Figure 4.21: Initial (left) and last (right) instantaneous images for a grooved sample. Inner cylinder's rotational speed = 900 rpm.

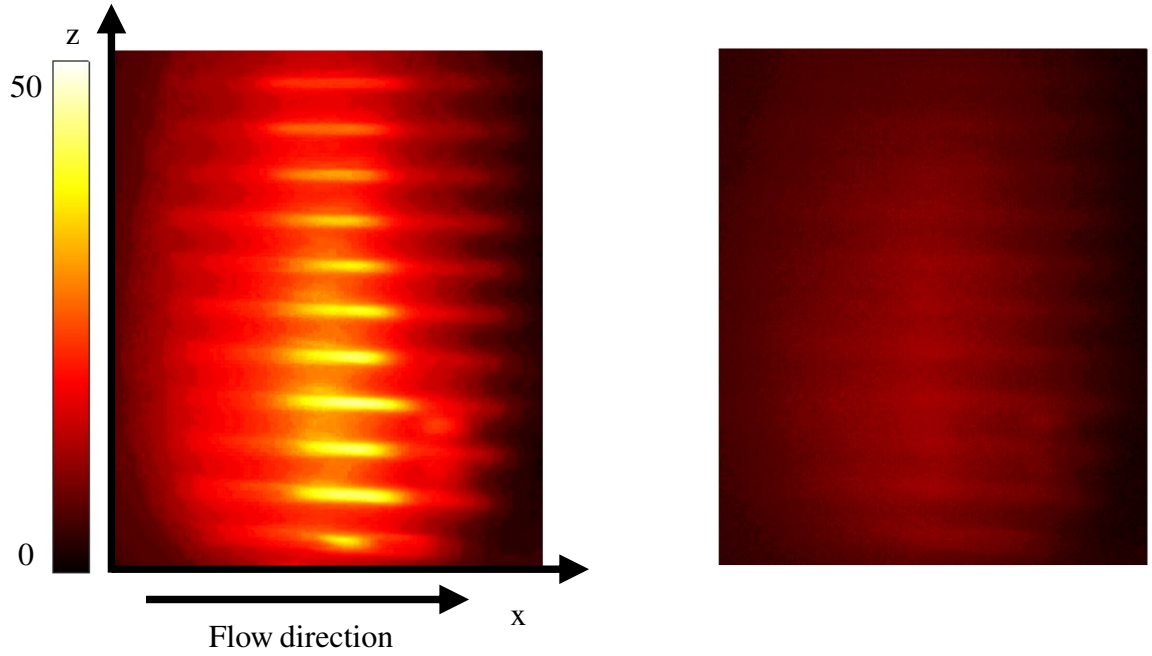

Figure 4.22: Initial (left) and last (right) instantaneous images for a grooved sample. Inner cylinder's rotational speed = 1800 rpm.

Spatial-temporal field

The intensity fields are averaged along both the streamwise and axial directions, allowing the temporal evolution of lubricant depletion to be observed. When examining the plots from left to right, the effect of low, moderate, and high shear conditions becomes evident. At the lowest rotational speed, the intensity values remain close to zero, with small positive and negative fluctuations that can be attributed to the intrinsic measurement uncertainty of the system. In the central contour, corresponding to 900 rpm, two main regions of pronounced depletion gradually expand over time, resulting in significant lubricant loss. Finally, under the highest speed setting, representing the most extreme flow condition, an almost complete loss of oil is observed. In this case, the sample appears to be nearly entirely drained by the flow.

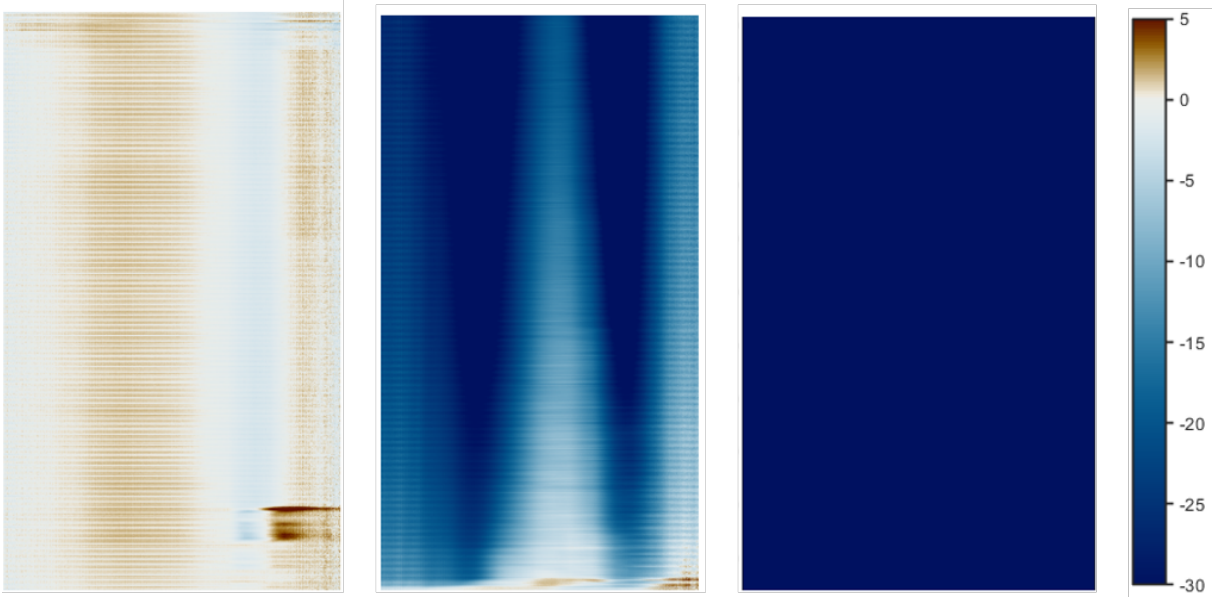

Figure 4.23: Spatiotemporal evolution of the axial z-averaged intensity in time, three different shear conditions while moving from left to right.

Global depletion percentage rate

Considering the results from a more quantitative perspective, the following plot shows the temporal evolution of the lubricant depletion rate, DR, combining all the experimental data in a single graph. The reference parameter I_o is determined from the sample configuration before the experiments begin. The duration of the individual tests varies because, during the first experimental campaign, the objective is to investigate the lubricant's evolution over time and identify the point at which the system appears to reach a stable condition. Under the low-speed regime, at 100 rpm, the recorded depletion rate remains nearly constant. Small fluctuations are observed; however, considering the uncertainty associated with the camera acquisition and image processing, these variations are within an acceptable range. Under these low shear conditions, the lubricant remains stable, as capillary forces are sufficiently strong to retain it within the grooves and counteract the shear stress applied at the oil–solution interface. Moving to the moderate shear flow regime, a transitional phase is observed. At the beginning of the test,

the depletion percentage rate decreases more rapidly, as indicated by a steeper slope, and then gradually approaches a more stable condition. From the surface perspective, during this transitional phase the upper lubricant layer is progressively removed by the action of the rotating flow, exposing the deeper oil regions to shear. As a result, the system eventually reaches a new equilibrium state, characterized by a more stable configuration between the remaining lubricant and the external fluid. During this second stage, the global lubricant loss is about -30 %. Finally, under high shear conditions, at 1800 rpm, an even steeper and faster depletion is observed, resulting in nearly an 80 % loss of lubricant—potentially even greater if the test has been extended. The strong external shear almost completely removes the oil, exposing the grooved surface directly to the rotational flow. As a consequence, the surface progressively loses its slippery properties, highlighting the limitations of this rough configuration under extreme shear conditions.

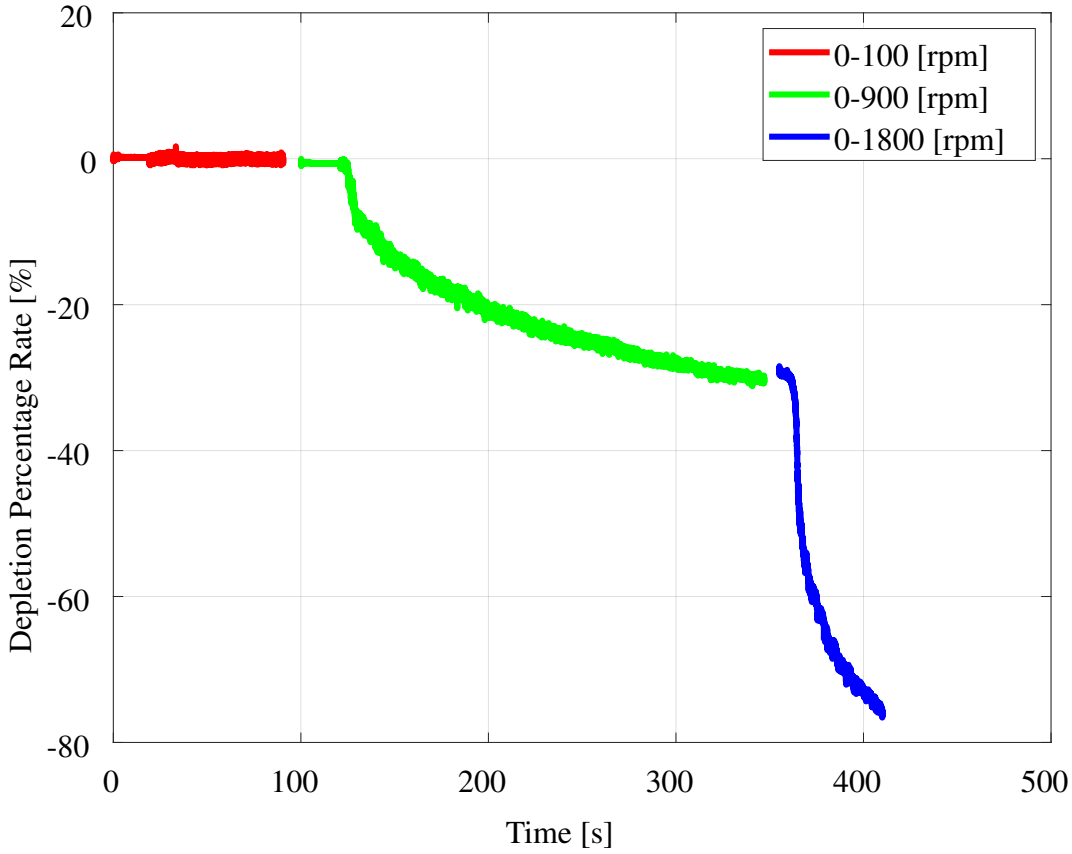

Figure 4.24: Lubricant depletion rate as a function of time under three constant rotational speed regimes (from 0 to 100 rpm, from 0 to 900 rpm, and from 0 to 1800 rpm).

4.4.3. Teflon-Wrinkles case: constant shear flow conditions

This section presents the results obtained for the Teflon-Wrinkles surface, which constitute the core contribution of this research project. Building upon the observations previously reported for the regular grooved sample, the objective is to investigate the behaviour of a more complex hierarchical surface when subjected to two different shear conditions. Particular attention is devoted to understanding how the multiscale topography influences lubricant redistribution and stability. In the following sections, the oil distribution within the surface texture, the structure and evolution of lubricant depletion, and the overall behaviour of a realistic slippery surface are analysed and discussed.
Several consecutive tests are performed on the same sample infused with 10 cSt silicone oil. The surface is progressively stressed by exposing it to different shear-rate conditions, while monitoring the oil dynamics and the redistribution of the lubricant over the textured surface. The velocity values adopted for the constant-shear-flow experiments can be summarized as: low speed (100 rpm), intermediate speed (500 rpm), and high speed (1500 rpm). These tests can be divided into two main categories.
The first group, referred to as **depletion data**, includes experiments in which the system starts from rest, and the inner cylinder is accelerated up to a constant rotational speed.
The second group, referred to as **recovery/displacement data**, includes experiments that begin at a prescribed rotational speed; the inner cylinder is then stopped while the camera continues recording, allowing observation of the subsequent lubricant redistribution and relaxation processes occurring on the surface.
Based on these two types of experimental campaigns, the two main datasets—detailing the velocity settings and the corresponding purpose of each test—are listed below. These datasets are analysed and discussed in the subsequent sections. In particular, the first dataset consists of six different experimental conditions designed to explore the lubricant response to consecutive shear-rate variations imposed on the surface.

- from 0 to 100 rpm
- from 0 to 500 rpm
- from 500 to 0 rpm
- from 0 to 1500 rpm
- from 1500 to 0 rpm

The second dataset consists of four experimental conditions defined by different rotational speed sequences:

- from 0 to 1500 rpm - clockwise rotation
- from 1500 to 0 rpm
- from 0 to 1500 rpm - counterclockwise rotation

- from 1500 to 0 rpm

These tests are designed to investigate the lubricant behaviour under high-shear conditions. In addition, reversing the rotation direction allows a qualitative assessment of how the shear orientation influences the oil distribution and redistribution across the surface.

Instantaneous images

Through a selection of instantaneous images, two representative and particularly relevant phenomena are illustrated in this section. These examples provide a qualitative insight into the governing mechanisms of lubricant redistribution on the textured surface under external shear conditions.

Figure 4.25 presents a sequence of consecutive snapshots acquired during a depletion test performed at high shear rate (inner cylinder's rotational speed equal to 1500 rpm), taken from the first dataset. The images illustrate the temporal evolution of the lubricant distribution on the surface. As the flow develops, the oil is displaced in the direction of the imposed shear, from left to right, progressively reorganizing into a different spatial configuration. This process leads to the formation of localized regions of lubricant accumulation, redistribution within the surface texture, and partial disruption of previously stable oil features. A noticeable decrease in the overall image intensity is also observed throughout the sequence. This change is clearly visible upon visual inspection: darker regions progressively expand and become more pronounced, occupying areas that were initially characterized by brighter tones. This behaviour suggests a progressive depletion or thinning of the lubricant layer in certain regions of the surface.

On the other hand, Fig. 4.26 presents a sequence of consecutive snapshots acquired during a recovery/displacement test. In this experiment, the system initially operates at a high shear rate, corresponding to an inner cylinder rotational speed of 1500 rpm. The rotation is then stopped, while image acquisition continues to monitor the subsequent lubricant motion and redistribution on the surface. The recording is maintained until no further visible changes can be detected. As time progresses, the darker regions observed in the images gradually become less pronounced, indicating a partial redistribution of the lubricant. In particular, the oil that accumulated on the right side of the sample during the high-shear phase slowly migrates back across the surface, gradually approaching the initial configuration.

A comparison between the first image in Fig. 4.25 and the final snapshot in Fig. 4.26 reveals that several characteristic features of the original lubricant distribution reappear over time. This behaviour suggests that, once the external shear is removed, the lubricant tends to reorganize into a configuration that is more favourable and consistent with the underlying surface topography. In other words, the initial state appears to represent a relatively stable equilibrium configuration for the oil within the textured surface.

Finally, Fig. 4.27 shows a sequence of representative snapshots from the counterclockwise high-speed test (from right to left in the snapshot). By observing the evolution of the lubricant distribution, it can be seen that the region of accumulated oil initially located on the right side of the sample progressively migrates toward the left, following the direction of the imposed rotation. The images also highlight the presence of an end effect, which appears to limit the displacement of the lubricant. In particular, this boundary condition acts as a physical constraint that prevents the oil from being further swept along the surface, leading to a localized accumulation near the edge of the sample.

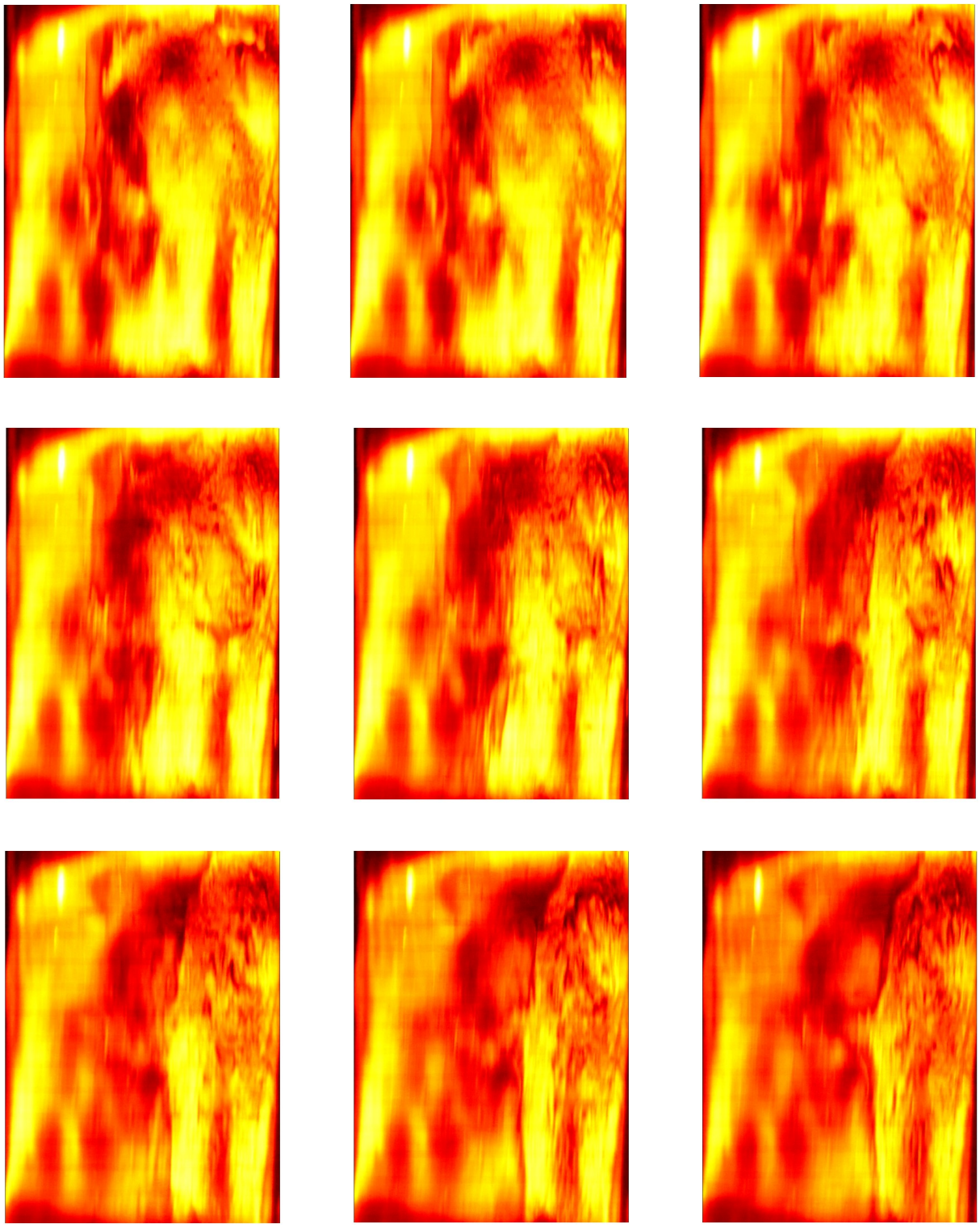

Figure 4.25: Nine instantaneous images from high shear **depletion** test (dataset 1). Starting from the top left images, those snapshots have been recorded at consecutive times, in particular: 0 s, 4 s, 6 s, 10 s, 30 s, 60 s, 90 s, 120 s, 260 s.

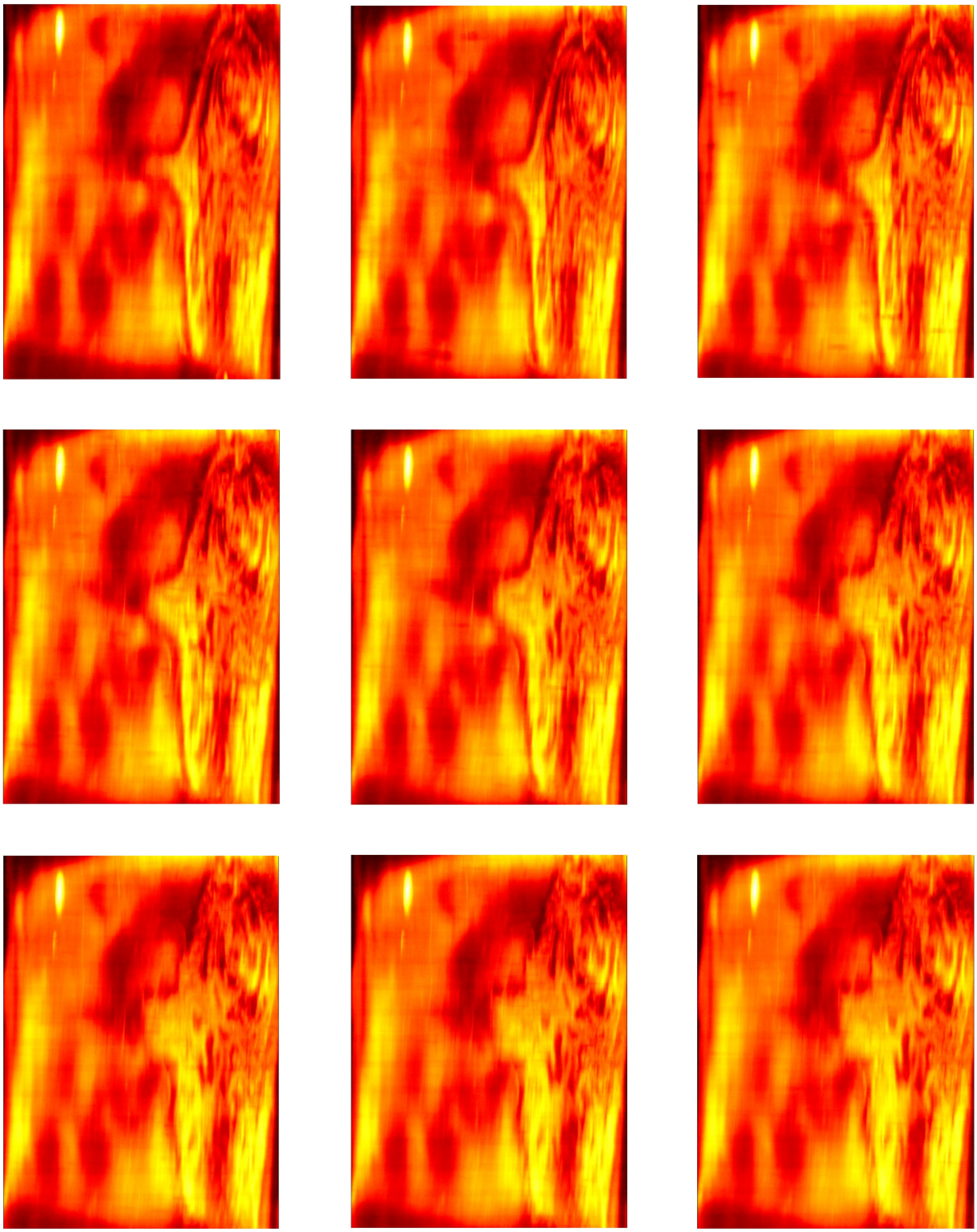

Figure 4.26: Nine instantaneous images from high shear **recovery/displacement** test (dataset 1). Starting from the top left images, those snapshots have been recorded at consecutive times, in particular: 0 s, 4 s, 6 s, 10 s, 30 s, 60 s, 90 s, 120 s, 260 s.

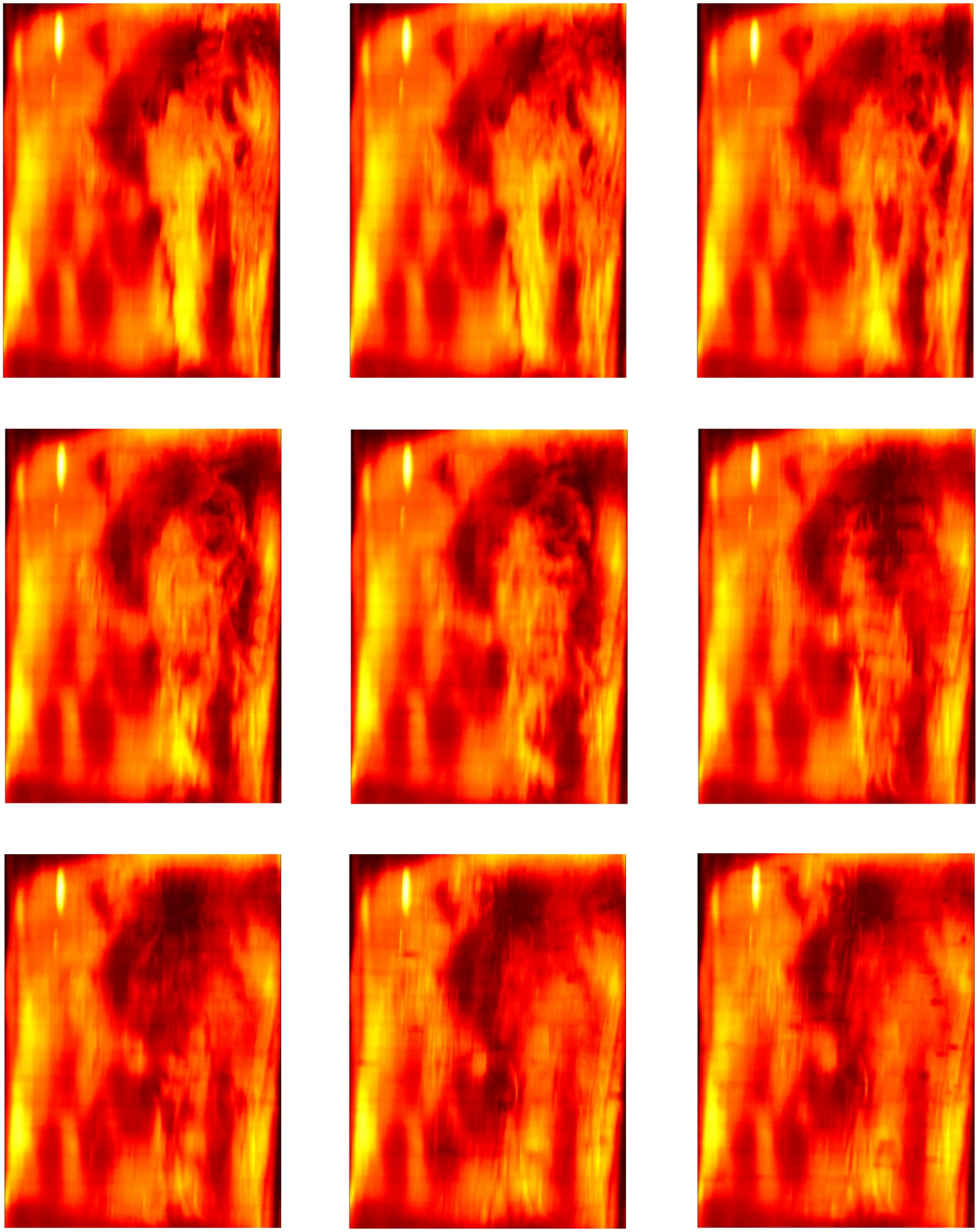

Figure 4.27: Nine instantaneous images from high shear **depletion** test (dataset 2) in counter-clockwise rotation direction. Starting from the top left images, those snapshots have been recorded at consecutive times, in particular: 0 s, 3 s, 6 s, 8 s, 10 s, 20 s, 30 s, 45 s, 50 s.

Global depletion percentage rate

The following results show the global depletion rate over time quantitatevely analyzing the behaviour of the lubricant in two consecutive cases. Both depletion and recovery/displacement at different flow regimes have been investigated in the first dataset (Fig. 4.28), and at high speed different rotation directions in dataset 2 (Fig. 4.29).
The results are obtained using the same initial reference condition, I_o, recorded at the beginning of each experimental campaign. As expected, each dataset starts from the final state reached in the previous test, since the experiments are performed consecutively on the same sample.
The plot presented below shows that low and moderate shear conditions do not significantly affect the overall lubricant quantity on the surface. The observed fluctuations remain within the experimental uncertainty range, indicating that the lubricant distribution is relatively stable under these shear levels. The most pronounced effect is observed during the fourth test, conducted under high-shear conditions, where a rapid decrease in the measured signal indicates significant lubricant depletion.

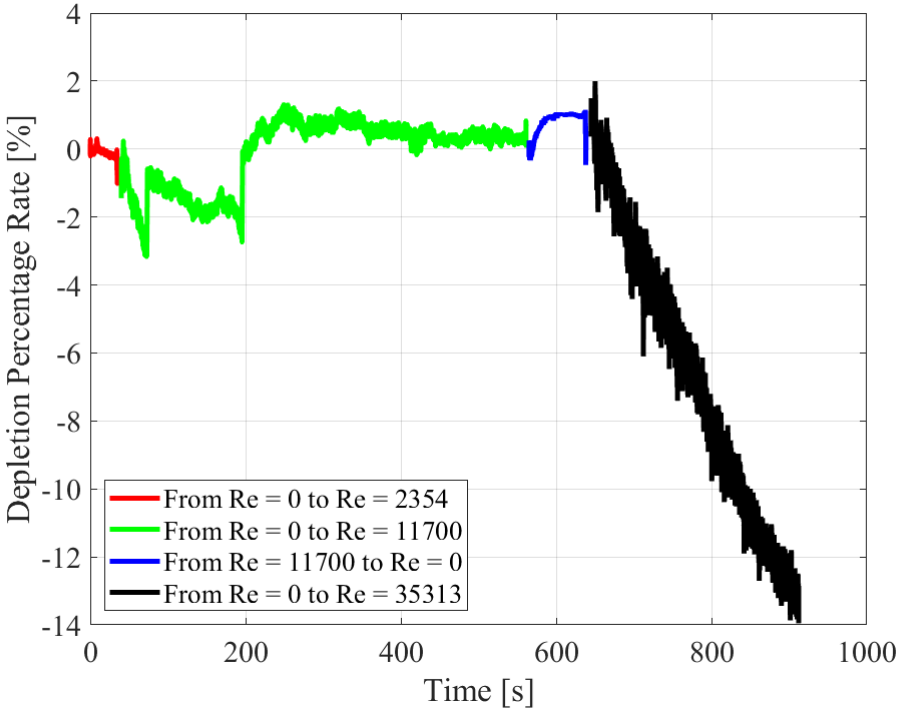

Figure 4.28: Lubricant depletion rate as a function of time - dataset 1.

The final dataset does not perfectly match the previous measurements. This discrepancy arises because an additional recording was performed in the meantime, and by error, using different acquisition settings. In particular, the video was recorded at 2 fps and the image intensity was adjusted during acquisition, preventing a direct quantitative comparison with the previous datasets. Nevertheless, the sequence remains qualitatively relevant, as it shows a clear positive trend, indicating an effective redistribution of the lubricant even after exposure to extreme shear conditions.

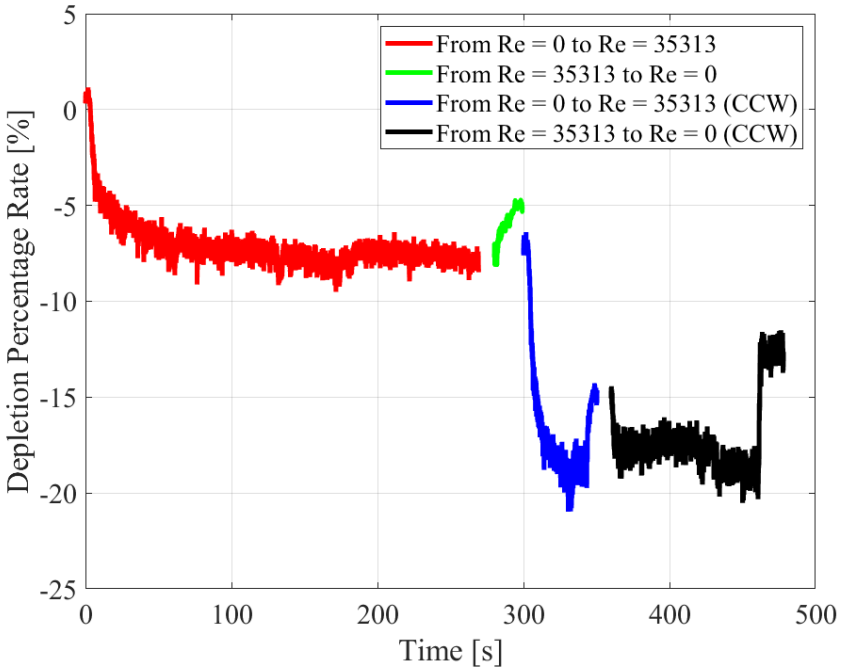

Figure 4.29: Lubricant depletion rate as a function of time - dataset 2.

The first test shows an initial decrease in the measured quantity associated with lubricant depletion, followed by the establishment of an approximately constant rate, suggesting that the system reaches a new quasi-stable condition under the imposed shear. The second recording begins at high shear; the inner cylinder is then suddenly stopped while image acquisition continues. During this phase, the measured signal gradually increases, indicating a partial redistribution of the lubricant and a limited recovery of the oil layer across the surface. The third test again subjects the system to a high-speed regime, but with the rotation direction reversed (counterclockwise). A similar qualitative behaviour is observed during both the third and the fourth tests. It is important to emphasize that, before the data presented here, several additional experiments had already been performed on the same sample (dataset 1). Consequently, the actual cumulative lubricant depletion is greater than what is directly indicated by the present measurements.

4.4.4. Teflon-Wrinkles case: stepwise increasing shear flow conditions

Several consecutive tests are performed on two different samples infused with 10 cSt and 50 cSt Silicone oil, each one is reinfused before running another test. A stepwise rotational speed protocol is implemented to examine the dynamic response of the liquid-infused surface under progressively increasing shear conditions. The protocol begins at 0 rpm and increases in 250 rpm steps up to 2000 rpm, with an acceleration rate of 200 rpm/s. Each speed step is maintained for 60 seconds, which is much larger than the capillary time scale. The corresponding Reynolds numbers for each rotational speed are summarized in the table below.

Rotational speed [rpm]	Reynolds number [-]
250	5885
500	11771
750	17656
1000	23542
1250	29427
1500	35313
1750	41198
2000	47084

Table 4.5: Corresponding Reynold numbers at different rotational speeds.

The surface is progressively subjected to increasing shear-rate conditions while the lubricant dynamics and its redistribution across the textured surface are continuously monitored. This experimental campaign is designed to replicate scenarios in which a surface experiences gradually increasing shear, such as a body accelerating in a fluid, allowing for the investigation of the transient behavior of the liquid-infused surface. The influence of lubricant viscosity is also an insight studied by looking at the surface's response as the shear rate increases. Each horizontal line represents the lubricant intensity extracted from a single frame, collapsed into a one-dimensional profile and stacked sequentially to show its temporal evolution.

Spatial-temporal field

Figure 4.30 presents the spatiotemporal representation describing the behavior of a sample infused with 50 cSt silicone oil. The vertical axis corresponds to time, while the horizontal axis represents the streamwise direction.

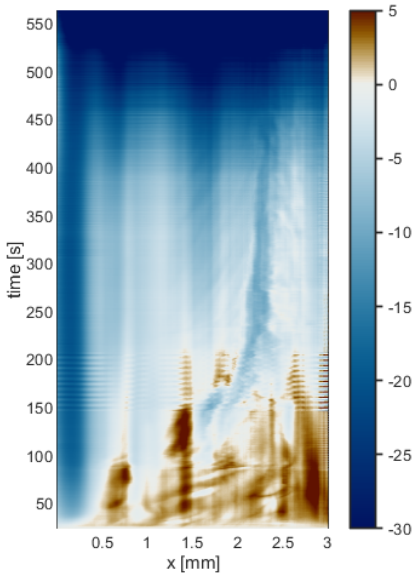

Figure 4.30: Spatiotemporal evolution of the axial z-averaged intensity.

Each horizontal line represents the lubricant intensity extracted from a single frame, collapsed into a one-dimensional profile and stacked sequentially to show its temporal evolution. There is an initial phase of lubricant motion on the surface, redistribution and accumulation, lead to a "virtual" increase of the intensity. It is important to emphasise that the formation of new lubricant on the surface is physically impossible. Therefore, a positive intensity value does not represent the generation of additional oil, but rather the local accumulation of lubricant that has been redistributed during testing. Conversely, negative intensity values indicate a net loss of lubricant from the surface. Observing the spatial-temporal contours, there are several spots of accumulation up to $t \simeq 150\,s$. This time corresponds to a Reynolds number $Re = 17\,656$, rotational speed of 750 rpm, and defines what appears to be a threshold above which intense lubricant depletion occurs. This then progressively increases as the velocity rises. Notably, the colour distribution shifts towards progressively darker blue tones at higher rotational speed regimes, reflecting severe lubricant depletion under these conditions.

Global depletion percentage rate

The depletion rate behaviour is plotted in the next figure, showing the temporal evolution across different speed regimes by comparing two cases of study.

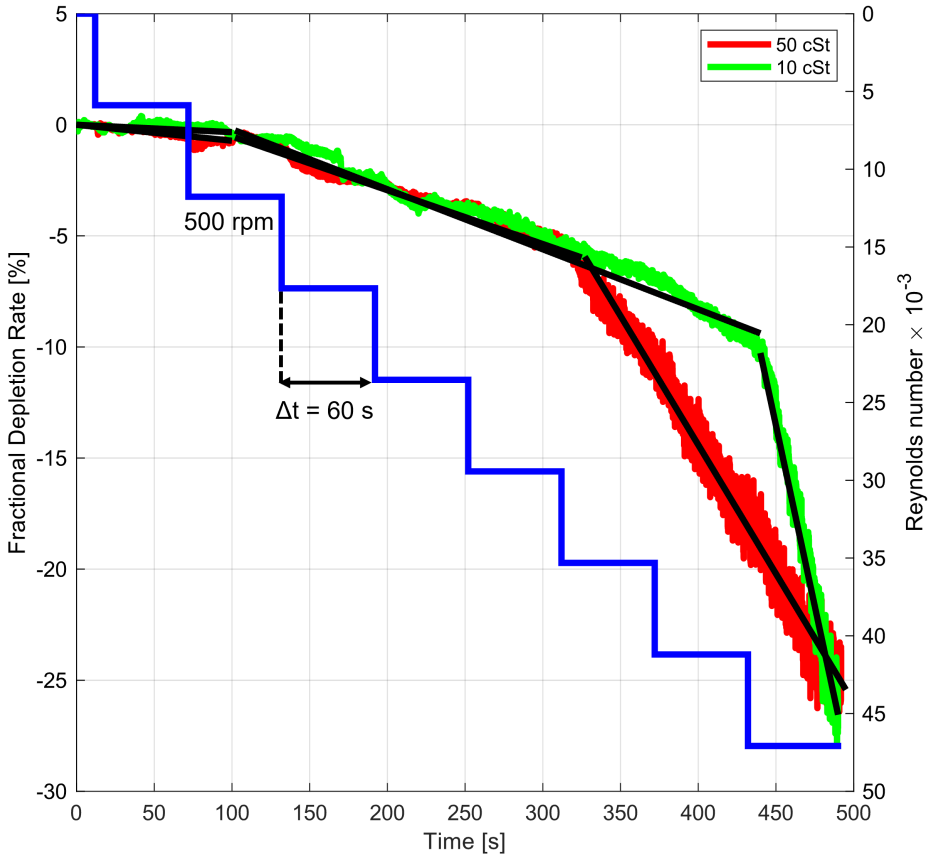

Figure 4.31: Lubricant depletion rate as a function of time under stepwise speed increase (from 0 to 2000 rpm, 250 rpm step for 1 minute long). On the right y-axis, there is the Reynolds number, defined as $Re = \frac{\omega R_i d}{\nu}$ - corresponding values for each step are reported in Tab. 4.5. The RIM solution properties are taken for a temperature of 24 °C. Red data: 50 cSt Silicone oil. Green data: 10 cSt Silicone oil.

Lubricant viscosity is investigated by testing two different samples, one infused with 10 cSt Silicone oil and the other with 50 cSt. Each test has been repeated two times, to assess experimental reproducibility.
Interestingly, three distinct regions can be defined in both cases and clearly detected by observing the next plot 4.31.
During the first phase, the average intensity decreases by only 2–3%, which is effectively negligible when considering the experimental uncertainty. Although local motion and bubbling are observed, the lubricant film remains in a stable state, almost completely retained within the sample's cavities, up to Re = 11771. In this regime, capillary forces are sufficient to retain the lubricant on the surface, counteracting the external shear stresses imposed by the moving fluid.
The onset of depletion characterizes the second phase. As a result of continuous exposure to the rotating fluid and the progressively increasing shear rate, the lubricant — previously redistributed across the surface during the stable regime — begins to detach. The locally accumulated regions become excessively thick and are no longer able to resist the imposed shear stresses, ultimately leading to lubricant removal from the surface.
The last regime is a depletion-dominated phase. Lubricant losses prevail over retention and redistribution. The equilibrium is broken by the external shear flow that becomes strongly higher than the forces that keep the fluid trapped between the micro and nano-cavities of the surface.
Surprisingly, both viscosities exhibit three distinct regimes characterized by a similar rate of decrease in the first two regions. Later, the effect of viscosity starts to play a role in the lubricant depletion phenomenon.
The primary distinction lies in the onset of the transition from the second to the third regime. In particular, for the 10 cSt case, the final regime is reached at higher operating conditions compared to the 50 cSt case, indicating a delayed transition. This behavior can be attributed to differences in surface topography: although both samples are fabricated following the same procedure, variations in the distribution and morphology of the hierarchical micro- and nanocavities are inevitable. Such differences can lead to varying levels of efficiency in sustaining the lubrication mechanism, thereby influencing the transition between regimes.
The slopes associated with the three regimes can be evaluated to quantify the transition rate between successive phases. These values are summarised in the next table.

Oil viscosity	10 cSt	50 cSt
I regime	$-4.0 \cdot 10^{-5}$	$-7.0 \cdot 10^{-5}$
II regime	$-2.7 \cdot 10^{-4}$	$-2.5 \cdot 10^{-4}$
III regime	$-3.3 \cdot 10^{-3}$	$-1.2 \cdot 10^{-3}$

Table 4.6: Slope values (unit s^{-1}) associated with the three lubricant depletion regimes. From one regime to the next, there is one order of magnitude difference in fractional depletion rate, highlighting the fact that the transition is sharp.

They show how the depletion rate changes over time and, from a physical point of view, the fractional depletion rate represents how fast lubricant losses happen in each regime.
The first and second regimes exhibit comparable slopes, indicating that oil viscosity does not affect the rate of lubricant depletion during this stage. In contrast, the third regime displays a

significantly different behaviour: the characteristic fractional depletion rate for the 10 cSt lubricant is approximately three times higher than that observed for the 50 cSt case.
Interestingly, analysis of the characteristic speed associated with the onset of the third regime shows that lower viscosity delays the transition between the second and third phases. For the 50 cSt silicone oil, the transition point of the third regime corresponds to Reynolds numbers approximately between $[29400; 35300]$. On the other hand, for the 10 cSt lubricant, the corresponding onset condition occurs at higher Reynolds numbers, approximately in the range of $[41200; 47000]$. However, once the system enters the depletion-dominated regime, higher viscosity becomes more effective in mitigating the rate of lubricant loss.

4.4.5. Physical interpretation of experimental results

Three distinct depletion regimes were identified during stepwise-increase tests at the two viscosities. Each regime can be characterized and named based on the physical interpretation of the measured lubricant depletion rates, as summarized below. The first phase is a capillary-stabilised regime, characterized by negligible depletion; then, an intermediate regime occurs with viscosity-independent, approximately linear depletion; and, at high Reynolds numbers, the third regime with enhanced linear depletion and pronounced viscosity dependence. The purpose of this section is to explain these experimental observations from lubrication theory, turbulent near-wall pressure statistics, and thin-film capillary physics.
First of all, it is crucial to determine and describe the flow. Considering the gap width of the Taylor-Couette apparatus, the critical Reynolds number for the onset of Taylor vortices is $Re_c = 68$.[91] This value corresponds to a rotational speed of approximately 3 rpm, which is exceeded almost immediately under the operating conditions investigated in the present study. Consequently, turbulent Taylor vortices are present from the very beginning of the experiments, with a characteristic axial length scale on the order of the gap width. In 1933, Wendt investigated the dimensionless torque both below and above a threshold Reynolds number of approximately 10^4, observing a strong dependence of the torque coefficient on the Reynolds number relative to this threshold.[103] This behavior was associated with the formation and evolution of Taylor-Couette cells. Subsequent studies confirmed these findings, and Lathrop *et al.* further demonstrated that, for $Re_T > 10000$, the flow exhibits characteristics typical of turbulent wall-bounded shear flows.[104]
In summary, turbulent Taylor vortex structures are observed to dominate the flow throughout all experimental conditions. Nevertheless, when the Reynolds number exceeds a critical threshold - identified here as $Re = 11700$ - smaller-scale turbulent structures progressively emerge and become increasingly dominant in terms of intensity relative to the large-scale Taylor vortices, ultimately promoting the onset of wall-bounded turbulence. This flow regime is further characterized by the occurrence of high-pressure peaks.
To provide a rational interpretation of the observed scaling behavior, a characteristic timescale analysis is required to identify the dominant physical mechanisms governing each regime, taking into account the underlying flow structures and their relative interactions.
Under the assumption of a thin liquid film, the pressure may be considered uniform across the film thickness, while inertial effects within the film are neglected. Furthermore, the wall is as-

sumed to be impermeable, and the external fluid imposes both an interfacial shear stress, τ_o, and an interfacial pressure, p_o.
Under these assumptions, the governing equations reduce to the Stokes-flow formulation of the momentum and mass conservation equations. Their combination yields the Reynolds lubrication equation, which enables the identification of three characteristic timescales governing the system dynamics:

$$\frac{\partial \delta}{\partial t} + \Delta \cdot \mathbf{q} = S \tag{4.3}$$

where δ is the local thickness of a thin viscous film, $\mathbf{q}$ is a depth-integrated flux per unit length, and S is a sink term representing volume (per unit area and time) removed by turbulent extraction events. The term $\mathbf{q}$ can be defined as a sum of a pressure-driven and a shear-driven flux:

$$\mathbf{q} = -\frac{\delta^3}{3\mu_{lub}} \nabla p + \frac{\delta^2}{2\mu_{lub}} \tau_{\mathbf{o}} \tag{4.4}$$

Three timescales can be defined as:

$$\tau_{visc} \sim \frac{\rho_{lub}\, \delta^2}{\mu_{lub}}, \qquad \tau_{print} \sim \frac{r_{HAPP}}{u_c}, \qquad \tau_{lub} \sim \frac{\mu_{lub}\, \Lambda^4}{\gamma\, \delta^3} \tag{4.5}$$

The τ_{visc} is the time required for the velocity profile to adjust to a change in the boundary conditions; it physically represents the viscous equilibration across the film. The τ_{print} is the representative timescale of High Amplitude Pressure Peaks (HAPP), a term introduced by Ghaemi and Scarano[105], considering a speed of propagation $u_c \sim 10\, u_\tau$.[106] The τ_{lub} is the time needed for the film to redistribute laterally across one cell, and it is obtained by balancing the pressure-driven lubrication flux against the capillary pressure terms over the characteristic length of a cell Λ.
To give an estimation of the timescale factors, the film thickness has been set to $\delta \approx 200$ nm, $\Lambda \approx 10\mu m$, $\gamma \approx 4 \times 10^{-3}\, N/m$; over the range of Reynolds numbers considered, the following ordering is found:

$$\tau_{visc} \ll \tau_{print} \ll \tau_{lub} \tag{4.6}$$

This leads to two main observations: the first one is that since $\tau_{visc} \ll \tau_{print}$, the velocity profile across the film is re-established instantaneously on the timescale of any outer-flow event and since $\tau_{print} \ll \tau_{lub}$ during a high peak pressure event, the film does not have the time to redistribute laterally, it is laterally frozen and only the interface can be deformed.

Regime I - Capillary Stabilisation

During the first phase, the micro- and nano-scale cavities of the surface are filled with lubricating oil. In this condition, the surface is effectively impregnated, leading to the formation of a thinner lubricant overlayer that sits on the tip of the solid elements, and a thicker lubricant layer contained in the hierarchical structure, as schematized in the following image.
The interface is stably pinned at the crest edges by capillarity. This continuous film ensures that the external flow interacts primarily with the lubricant rather than the underlying solid features.

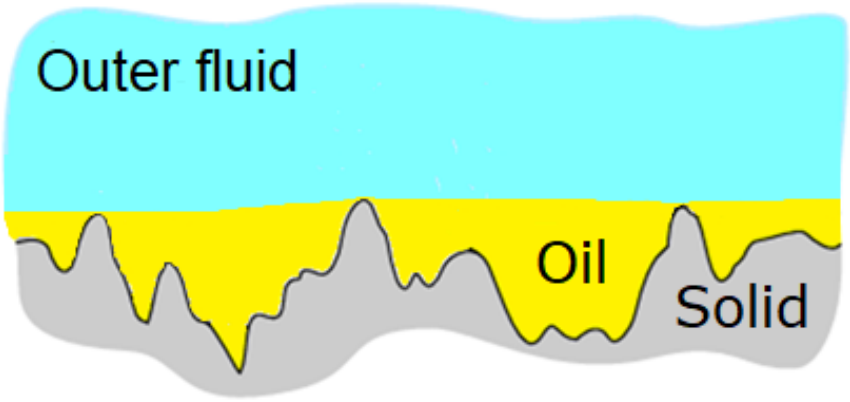

Figure 4.32: Schematic of a lubricant-infused surface (LIS): a hierarchical solid substrate (grey) fully impregnated with lubricant oil (yellow) and in contact with an outer fluid (light blue). The surface is completely infused, with a thin lubricant overlayer that not only fills the micro- and nano-scale roughness but also forms a continuous film above the structure.

The first regime is characterized by quasi-periodic turbulent Taylor-vortices that act on the interface without disrupting it, thereby preventing the external fluid from penetrating the LIS structure.
An analysis of the depletion rate behavior (see Figure 4.31) and the data reported in Table 4.6 indicates that this initial regime is not affected by oil viscosity.
Minimal variations are observed up to a Re = 11771, suggesting that viscous effects play a marginal role at this stage. Instead, the capillary restoring forces dominate the system, providing sufficient resistance to counteract the imposed external shear stress and thereby stabilizing the lubricant within the surface structure.
As mentioned before, a Reynolds number of $Re_T \sim 10000$ corresponds to the critical parameter associated with the beginning of the disruption of turbulent Taylor vortices, creating a more chaotic and unsteady environment. In fact, the depletion first threshold - that marks the end of the first regime and the beginning of the second one - therefore coincides with Re_T because turbulence acquires an intermittent behaviour, required to produce HAPP.

Regime II - Constant-Rate Turbulent Extraction

As the system transitions to the subsequent regime, the depletion process begins to dominate the overall behavior under moderate shear flow conditions. In this phase, at approximately Re $\simeq$ 10000, shear turbulence dominates the near-wall dynamics, starting to be characterized by chaotic, irregular, and unsteady motion, with rapid fluctuations in both velocity and pressure. These fluctuations enhance the interaction with the lubricant interface, which progressively develops ripples and instabilities. In particular, small ripple-like interface deformations are driven by pressure bursts.
Due to positive and negative high-pressure peaks, the interface is locally deformed, and the mean film level has receded below the higher crests, while the outer turbulent shear then sweeps the entrained volume away.
Following the removal of the oil film, the solid asperities of the higher wrinkles' tips begin to come into direct contact with the external fluid. The second regime can be summarized as the phase characterised by extraction events followed by complete capillary recovery of the lubricant interface before the next burst arrives.
From a hydrodynamic perspective, the interface is no longer homogeneous; instead, the flow experiences an alternating pattern of lubricant-covered regions and exposed solid areas. This spatial heterogeneity translates into a combination of slip and no-slip boundary conditions, which significantly alter the overall flow behavior and contribute to the progressive degradation of the surface performance.

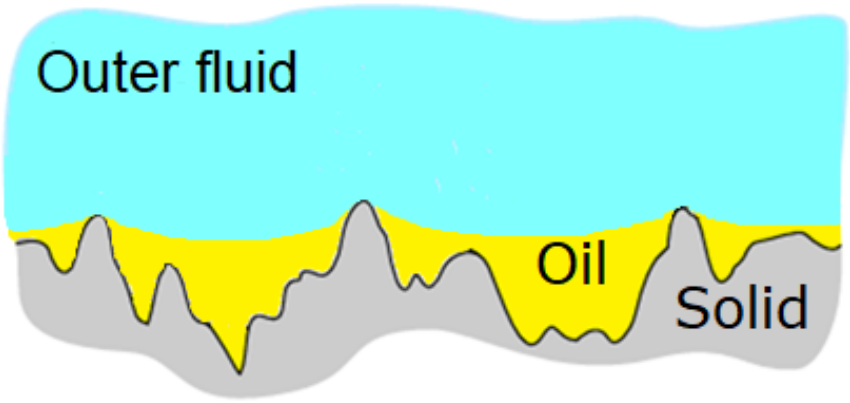

Figure 4.33: LIS is partially infused: the thin lubricant overlayer has been removed by the external water flow, exposing the roughness tips to the surrounding liquid.

Interestingly, the second regime appears to be independent of lubricant viscosity. As shown by the values reported in the previous table, the depletion rates for both 10 cSt and 50 cSt silicone oils are comparable throughout this phase.
Viscosity doesn't play a primary role during this phase, because it is mainly governed by the turbulent fluctuations that started to locally interact with the oil interface, breaking and modifying it. Moreover, the mean lubricant level is shifted below.

Regime III - Thin-Film Softening and Enhanced Linear Depletion

When the third regime is reached, τ_{lub} starts to become very close to τ_{burst}, and over time, these disturbances cause the pinning points to start moving, there is a gradual removal of the lubricant layer over the wrinkles, and the film is very thin. At this point, molecular van der Waals forces enter the picture to rupture the film and create molecular clusters, leading to the end of the validity of the continuum vision. Moreover, disjoining pressure reduces the interfacial stiffness, enlarging the extracted packet per event and increasing the depletion slope.
In the final regime, the role of lubricant viscosity becomes increasingly significant. An analysis of the previously reported data reveals a marked difference between the two cases considered: the fractional depletion rate for the 10 cSt oil is approximately three times higher than that of the 50 cSt oil. This clearly indicates that lower-viscosity lubricants are more susceptible to shear-induced depletion, while higher-viscosity oils provide enhanced resistance to depletion.
Furthermore, the onset of the third regime occurs at two distinct rotational speeds for the two cases considered. Interestingly, the lower-viscosity lubricant exhibits a delayed transition. This behavior can be analyzed by considering that $\tau_{lub} \propto \mu_{lub}$, indicating that an increase in lubricant viscosity leads to a corresponding delay in the onset of the final threshold.

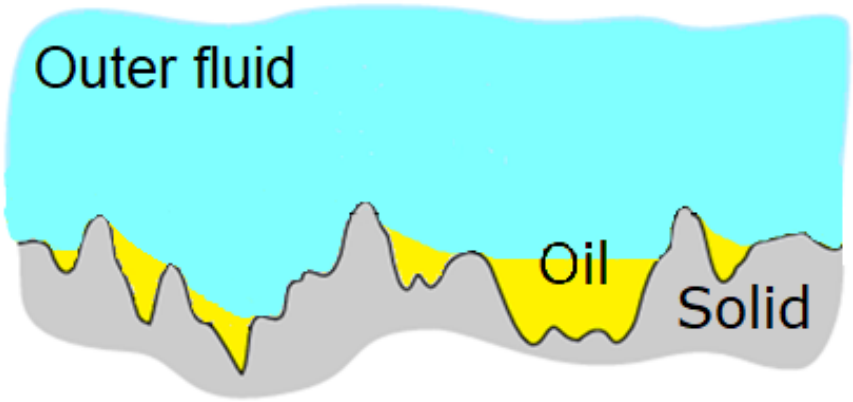

Figure 4.34: Most of the lubricant has been removed by the external shear, leaving the majority of the solid surface exposed to the liquid, while some cavities still retain residual oil.

Furthermore, as the intensity of the external flow increases, a progressively larger portion of the solid surface becomes exposed. The outer fluid begins to penetrate into the surface cavities and porosities, actively displacing and emulsifying the lubricant trapped within them and moving the lubricant through the hierarchical structure itself, accumulating it on the edge side. The strong, rapid, and more frequent turbulent fluctuations interact with the remaining oil layers, promoting their breaks and consequent losses. Overall, this regime is characterized by a coupled mechanism of lubricant displacement and depletion, ultimately leading to a substantial loss of lubrication and a significant degradation of surface performance.

4.5. Conclusions and future developments

Lubricant-infused surfaces (LIS) are among the most promising passive technologies for reducing friction between a solid surface and an external fluid. Inspired by natural adaptations in animals and plants, hierarchical materials infused with lubricant oil have demonstrated significant potential, both in numerical simulations and experimental studies.
However, the effectiveness, durability, and functionality of LIS decrease when lubricant depletion occurs. As the viscous fluid trapped in surface cavities drains, the underlying rough solid is exposed to the external flow, compromising performance. Despite its importance, the physical mechanisms of lubricant depletion are not yet fully understood, leaving unclear several aspects and limiting the ability of researchers to optimize LIS designs.
This chapter first highlights the critical role of lubricant retention in determining LIS performance. It then proposes an innovative approach to investigating lubricant dynamics under shear flow conditions. Establishing a clear correlation between lubricant behavior and flow is a key step toward designing more robust and durable surfaces capable of maintaining functionality under realistic operating conditions.
Through the investigation of the relation between lubricant properties and flow dynamics, the results demonstrate that the proposed hierarchical surface maintains high efficacy even under high-speed flow conditions. This confirms the potential of such architectures for applications in demanding fluid dynamic environments.
Moreover, the choice of lubricant viscosity becomes increasingly critical at high shear rates, eventually becoming the dominant mechanism over others. Furthermore, the evolution of oil flow structures, including streaks and vortical formations, has been observed over time.
Finally, this work reports, for the first time to the best of our knowledge, the real-time observation of lubricant motion on an anisotropic and complex surface. This achievement provides valuable insights into the dynamic behavior of lubricants and offers a powerful tool for future studies aimed at optimizing LIS performance.
Overall, this study represents a starting point for future investigations of LIS, toward a quantitative correlation between surface topography and lubricant properties, and enabling the identification of optimal configurations for drag reduction.

Summary

The global challenge posed by climate change necessitates coordinated research efforts and multidisciplinary approaches, integrating different scientific and technological perspectives to develop effective, scalable, and sustainable solutions.
Addressing this complex challenge requires not only the development of novel solutions but also the critical reassessment and adaptation of existing systems. Enhancing and optimizing current technologies - rather than systematically replacing them - allows for a more sustainable approach that accounts for the entire life cycle. In this perspective, drawing inspiration from natural systems, which have evolved over millions of years under constraints of efficiency, adaptability, and resilience, provides a powerful paradigm for guiding such improvements.
In this context, nature represents an insightful source of inspiration. Biological systems have been optimized through evolutionary processes to achieve remarkable properties. Consequently, the study of the natural world offers a valuable framework for identifying strategies that can be translated into engineering applications.
Researchers have long been fascinated by the capabilities of both animals and plants to adapt and improve themselves, and they started investigating natural complex systems. From the aerodynamic efficiency of insects and birds to the hydrodynamic adaptations of marine animals, and from the microstructural properties of leaves to the macroscopic features of trees, these natural systems exhibit optimized solutions for minimizing resistance, enhancing performance, and achieving specific functional objectives.
The primary motivation of the present research arises from the pursuit of strategies to reduce drag across various engineering applications, with particular emphasis on the marine environment. This focus is driven by the increasing need to comply with progressively stringent environmental regulations, which demand improved energy efficiency and reduced emissions in maritime operations. By drawing inspiration from nature, this work aims to contribute to the development of innovative, sustainable, and passive approaches to drag reduction.
In this context, one of the most appealing solutions to address this aim is slippery surfaces. This field is wide, and many different solutions and approaches can be included, such as rough walls, ribleted and patterned surfaces, superhydrophobic and lubricant-impregnated materials.
The present thesis has described, through three main projects, three different types of slippery surfaces: ribleted, superhydrophobic, and liquid-infused surfaces. In particular, through an integrated theoretical, numerical, and experimental study, it aims to bridge some literature gaps in this field.
Within the framework of ribleted surfaces, this work aims to advance toward the definition of a universal scaling and a corresponding functional description capable of capturing the microscopic behavior of structured slippery interfaces and translating it into the performance of the macroscopic domain. In particular, the objective is to predict and quantify the influence of regular and periodic patterned surface features on drag reduction, thereby enabling their systematic design and optimization across different flow regimes.
To investigate the mechanisms through which riblets, superhydrophobic surfaces (SHS), and lubricant-infused surfaces (LIS) interact with fluid dynamic instabilities and modulate hydro-

dynamic resistance, a Taylor-Couette apparatus has been designed and constructed. This experimental platform provides a controlled environment to isolate and analyze the relevant physical processes, thereby laying the groundwork for subsequent studies targeting more complex configurations and increasingly extreme flow conditions.
Finally, particular attention is focused on one of the less understood aspects of LIS technology: its degradation under shear flow conditions over time, which compromises durability and functionality of the infused material. The progressive loss of effectiveness, primarily associated with lubricant depletion, remains largely unexplored. In this context, the present work seeks to investigate the underlying failure mechanisms, identify the physical processes responsible for lubricant loss, and determine the key parameters governing the durability and long-term performance of these surfaces.

Over the past three years, this work has provided me with the opportunity to observe, explore, make mistakes, design, and learn, while allowing me the freedom to express creativity and to develop my own approach to research. Engaging with the same topic from multiple perspectives and through a range of methodologies has been deeply enriching, broadening my scientific understanding, my curiosity, and my way of thinking.

REFERENCES

[1] V. Eyring and H. W. Köhler. Emissions from international shipping: The last 50 years. *Journal of Geophysical Research*, 110:D17305, 2005. doi: 10.1029/2004JD005619.

[2] V. Eyring, I.S.A. Isaksen, T. Berntsen, W.J. Collins, J.J. Corbett, O. Endresen, R.G. Grainger, J. Moldanova, H. Schlager, and D.S. Stevenson. Transport impacts on atmosphere and climate: Shipping. *Atmospheric Environment*, 44:4735–4771, 2010. doi: 10.1016/j.atmosenv.2009.04.059.

[3] A.F. Molland, S.R. Turnock, and D.A. Hudson. Ship resistance and propulsion: Practical estimation of ship propulsive power. *Cambridge Univ. Press*, 2011.

[4] Wärtsilä Encyclopedia of Ship Technology. Ship resistance. `[wartsila.com](https://www.wartsila.com/encyclopedia/term/ship-resistance)`, 2024. Accessed: February 2025.

[5] Apostolos Papanikolaou. *Ship design: methodologies of preliminary design*. Springer, 2014.

[6] Equasis - electronic quality shipping information system. Technical report, European Commission, 2022.

[7] Y.F. Fua, C.Q. Yuana, and X.Q. Bai. Marine drag reduction of shark skin inspired riblet surfaces. *Biosurface and Biotribology*, 3:11–24, 2017. doi: 10.1016/j.bsbt.2017.02.001.

[8] P Luchini, F Manzo, and A Pozzi. Resistance of a grooved surface to parallel flow and cross-flow. *Journal of Fluid Mechanics*, 228:87–109, 1991. doi: 10.1017/S0022112091002641.

[9] M. Ahmadzadehtalatapeh and M. Mousavi. A review on the drag reduction methods of the ship hulls for improving the hydrodynamic performance. *International Journal of Maritime Technology*, 4:51–64, 2015.

[10] W.U. Hao, O. Yongpeng, and Y.E. Qing. Experimental study of air layer drag reduction on a flat plate and bottom hull of a ship with cavity. *Ocean Engineering*, 183:236–248, 2019. doi: 10.1016/j.oceaneng.2019.04.088.

[11] F. Gentile, N. Coppedè, and G. et al. Tarabella. Microtexturing of the conductive pedot:pss polymer for superhydrophobic organic electrochemical transistors. *BioMed Research International*, 2014. doi: 10.1155/2014/302694.

[12] Shutao Wang, Kesong Liu, Xi Yao, and Lei Jiang. Bioinspired surfaces with superwettability: new insight on theory, design, and applications. *Chemical reviews*, 115(16): 8230–8293, 2015.

[13] Bharat Bhushan. Biomimetics inspired surfaces for drag reduction and oleophobicity/philicity. *Beilstein Journal Nanotechnol*, 2:66–84, 2011. doi: 10.3762/bjnano.2.9.

[14] University of Minnesota. Lotus leaf and superhydrophobicity (lotus effect), 2011. URL https://www.cems.umn.edu/. Educational material on surface texture and low surface energy.

[15] A Bottaro. Flow over natural or engineered surfaces: an adjoint homogenization perspective. *Journal of Fluid Mechanics*, 877:P1, 2019. doi: 10.1017/jfm.2019.607.

[16] E. Alinovi and A. Bottaro. Apparent slip and drag reduction for the flow over superhydrophobic and lubricant-impregnated surfaces. *Phys. Rev. Fluids 3*, page 124002, 2018. doi: 10.1103/PhysRevFluids.3.124002.

[17] D W Bechert and M Bartenwerfer. The viscous flow on surfaces with longitudinal ribs. *Journal of Fluid Mechanics*, 206:105–129, 1989. doi: 10.1017/S0022112089002247.

[18] M. D. Ibrahim, S.N.A. Amran, Y.S. Yunos, M.R.A. Rahman, M.Z. Mohtar, L. K. Wong, and Zulkharnain A. The study of drag reduction on ships inspired by simplified shark skin imitation. *Ocean Engineering*, 2018. doi: 10.1155/2018/7854321.

[19] Susheel Kumar, Krishna Murari Pandey, and Kaushal Kumar Sharma. Advances in drag-reduction methods related with boundary layer control – a review. *Materials Today: Proceedings*, 45:6694–6701, 2021. doi: 10.1016/j.matpr.2020.12.150. International Conference on Mechanical, Electronics and Computer Engineering 2020: Materials Science.

[20] M J Walsh and L M Weinstein. Drag and heat transfer characteristics of small longitudinally ribbed surfaces. *AIAA Journal*, 17(7):770 – 771, 1979.

[21] M I Walsh. Drag characteristics of v-groove and transverse curvature riblets. In *In Viscous Flow Drag Reduction, G. R. Hough, Ed., AIAA Washington, DC*, pages 168–184, 1980.

[22] M I Walsh and A M Lindemann. Optimization and application of riblets for turbulent drag reduction. *AIAA Paper 84–0374*, 1984.

[23] D W Bechert, M Bruse, W Hage, J G T Van der Hoeven, and G Hoppe. Experiments on drag-reducing surfaces and their optimization with an adjustable geometry. *Journal of Fluid Mechanics*, 338:59–87, 1997. doi: 10.1017/S0022112096004673.

[24] The New York Times. Stars & stripes finds a groove. [nytimes.com](https://www.nytimes.com/1987/01/13/sports/scouting-stars-stripes-finds-a-groove.html), 1987. Section A, page 25. Published January 13, 1987.

[25] Zhoukun He, Linpeng Mu, Na Wang, Jie Su, Zhuo Wang, Mingdong Luo, Chunle Zhang, Guangwen Li, and Xiaorong Lan. Design, fabrication, and applications of bioinspired slippery surfaces. *Advances in Colloid and Interface Science*, 318:102948, 2023. ISSN 0001-8686. doi: https://doi.org/10.1016/j.cis.2023.102948.

[26] P Luchini. Reducing the turbulent skin friction. In J A Désidéri, editor, *European Congress on Computational Methods in Applied Sciences and Engineering — Proceedings of 3rd ECCOMAS CFD Conference*. Wiley, Chichester, England, U.K., pp. 466–470, 1996.

[27] J Jiménez. Turbulent flows over rough walls. *Annual Review of Fluid Mechanics*, 36: 173–196, 2004. doi: 10.1146/annurev.fluid.36.050802.122103.

[28] M R Pakatchian, J Rocha, and L Li. Advances in riblets design. *Applied Sciences*, 13 (19):10893, 2023. doi: doi.org/10.3390/app131910893.

[29] Bionic Surface Technologies GmbH. Riblets solutions for drag reduction. [bionicsurface.com](https://www.bionicsurface.com/riblets-solutions/), 2024. Accessed: February 2025.

[30] S. Stille, J. Pöplau, T. Beck, M. Bambach, G. Hirt, and L. Singheiser. Very high cycle fatigue behavior of riblet structured alclad 2024 thin sheets. *International Journal of Fatigue*, 63:183–190, 2014. doi: https://doi.org/10.1016/j.ijfatigue.2014.01.023.

[31] Huawei Chen, Xin Zhang, Lingxi Ma, Da Che, Deyuan Zhang, and T.S. Sudarshan. Investigation on large-area fabrication of vivid shark skin with superior surface functions. *Applied Surface Science*, 316:124–131, 2014. doi: https://doi.org/10.1016/j.apsusc.2014.07.145.

[32] S. Supriadi, G. Yanuar1, and H.S. Budhi. The replication of micro-riblets on ship hulls for drag reduction applications. *International Journal of Technology*, 5:983–989, 2015. doi: 10.14716/ijtech.v6i5.1880.

[33] National Aeronautics and Space Administration (NASA). Stars and stripes boat race project report. [ntrs.nasa.gov](https://ntrs.nasa.gov/api/citations/20020087761/downloads/20020087761.pdf), 2002. NASA Technical Report Server (NTRS); Accessed: February 2025.

[34] Robert N Wenzel. Resistance of solid surfaces to wetting by water. *Industrial & engineering chemistry*, 28(8):988–994, 1936.

[35] ABD Cassie and SJToTFS Baxter. Wettability of porous surfaces. *Transactions of the Faraday society*, 40:546–551, 1944.

[36] Alberto Giacomello, Simone Meloni, Mauro Chinappi, and Carlo Massimo Casciola. Cassie–baxter and wenzel states on a nanostructured surface: phase diagram, metastabilities, and transition mechanism by atomistic free energy calculations. *Langmuir*, 28(29): 10764–10772, 2012.

[37] Wilhelm Barthlott and Christoph Neinhuis. Purity of the sacred lotus, or escape from contamination in biological surfaces. *Planta*, 202(1):1–8, 1997.

[38] José Bico, Uwe Thiele, and David Quéré. Wetting of textured surfaces. *Colloids and Surfaces A: Physicochemical and Engineering Aspects*, 206(1-3):41–46, 2002.

[39] David Quéré. Wetting and roughness. *Annu. Rev. Mater. Res.*, 38:71–99, 2008.

[40] Aurélie Lafuma and David Quéré. Superhydrophobic states. *Nature materials*, 2(7): 457–460, 2003.

[41] H. Dong, M. Cheng, Y. Zhang, H. Wei, and F. Shi. Extraordinary drag-reducing effect of a superhydrophobic coating on a macroscopic model ship at high speed. *The Royal Society of Chemistry*, 1:5886–5891, 2013. doi: 10.1039/c3ta10225d.

[42] Subodh Barthwal, Surbhi Uniyal, and Sumit Barthwal. Nature-inspired superhydrophobic coating materials: drawing inspiration from nature for enhanced functionality. *Micromachines*, 15(3):391, 2024.

[43] T Van Buren and A J Smits. Substantial drag reduction in turbulent flow using liquid-infused surfacess. *Journal of Fluid Mechanics*, 827:448–456, 2017. doi: 10.1017/jfm.2017.50.

[44] François J Peaudecerf, Julien R Landel, Raymond E Goldstein, and Paolo Luzzatto-Fegiz. Traces of surfactants can severely limit the drag reduction of superhydrophobic surfaces. *Proceedings of the National Academy of Sciences*, 114(28):7254–7259, 2017.

[45] Tak-Sing Wong, Sung Hoon Kang, Sindy KY Tang, Elizabeth J Smythe, Benjamin D Hatton, Alison Grinthal, and Joanna Aizenberg. Bioinspired self-repairing slippery surfaces with pressure-stable omniphobicity. *Nature*, 477(7365):443–447, 2011.

[46] J David Smith, Rajeev Dhiman, Sushant Anand, Ernesto Reza-Garduno, Robert E Cohen, Gareth H McKinley, and Kripa K Varanasi. Droplet mobility on lubricant-impregnated surfaces. *Soft Matter*, 9(6):1772–1780, 2013.

[47] Tommi Huhtamäki, Xuelin Tian, Juuso T Korhonen, and Robin HA Ras. Surface-wetting characterization using contact-angle measurements. *Nature protocols*, 13(7):1521–1538, 2018.

[48] Hae Nyeok Kim, Seung Joong Kim, Woorak Choi, Hyung Jin Sung, and Sang Joon Lee. Depletion of lubricant impregnated in a cavity of lubricant-infused surface. *Phys. Fluids*, 33(2):022005, 2021.

[49] P. Juuti and J. et al Haapanen. Achieving a slippery, liquid-infused porous surface with anti-icing properties by direct deposition of flame synthesized aerosol nanoparticles on a thermally fragile substrate. *Applied Physics Letters*, 110:161603, 2017. doi: 10.1021/nl4003969.

[50] International Towing Tank Conference. Standard skin-friction correlation line. In *ITTC-1957 model-ship correlation line*, 1957.

[51] P Stott, PNH Wright, and A Bakalees. Typical ship principal dimensions. 2011.

[52] Cameron S. Ware, Truis Smith-Palmer, Sam Peppou-Chapman, Liam R. J. Scarratt, Erin M. Humphries, Daniel Balzer, and Chiara Neto. Marine antifouling behavior of lubricant-infused nanowrinkled polymeric surfaces. *ACS Appl. Mater. Interfaces*, 10: 41734182, 2018.

[53] M Kadivar, D Tormey, and G McGranaghan. A review on turbulent flow over rough surfaces: Fundamentals and theories. *International Journal of Thermofluids*, 10:100077, 2021. doi: 10.1016/j.ijft.2021.100077.

[54] D B Goldstein and T.-C. Tuan. Secondary flow induced by riblets. *Journal of Fluid Mechanics*, 363:115–151, 1998. doi: 10.1017/S0022112098008921.

[55] S Endrikat. *Effects of riblet shape on drag reduction in turbulent flow*. PhD thesis, University of Melbourne, 2020.

[56] E N Ahmed and A Bottaro. Exploring the nexus among roughness function, apparent slip velocity and upscaling coefficients for turbulence over porous/textured walls. In press *Journal of Fluid Mechanics*, 2025.

[57] S K Robinson. Coherent motions in the turbulent boundary layer. *Annual Review of Fluid Mechanics*, 23:601–639, 1991. doi: 10.1146/annurev.fl.23.010191.003125.

[58] J Jiménez. On the structure and control of near wall turbulence. *Physics of Fluids*, 6(2): 944–953, 1994. doi: 10.1063/1.868327.

[59] M Thakkar, A Busse, and N D Sandham. Direct numerical simulation of turbulent channel flow over a surrogate for Nikuradse-type roughness. *Journal of Fluid Mechanics*, 837:R1, 2018. doi: 10.1017/jfm.2017.873.

[60] A Bottaro, G Innocenti, and E N Ahmed. A slip-transpiration-vortex model for riblets past the viscous regime. *Meccanica*, 60:2487–2506, 2025. doi: 10.1007/s11012-025-01962-y.

[61] A Bottaro and S B Naqvi. Effective boundary conditions at a rough wall: a high-order homogenization approach. *Meccanica*, 55:1781–1800, 2020. doi: 10.1007/s11012-020-01205-2.

[62] P Luchini and A Bottaro. Görtler vortices: a backward-in-time approach to the receptivity problem. *Journal of Fluid Mechanics*, 363:1–23, 1998. doi: 10.1017/S0022112098008970.

[63] R García-Mayoral and J Jiménez. Drag reduction by riblets. *Philosophical Transactions of the Royal Society A: Mathematical, Physical and Engineering Sciences*, 369:1412–1427, 2011. doi: 10.1098/rsta.2010.0359.

[64] P Orlandi and S Leonardi. DNS of turbulent channel flows with two- and three-dimensional roughness. *Journal of Turbulence*, 7:N73, 2006. doi: 10.1080/14685240600827526.

[65] P Orlandi, S Leonardi, and R A Antonia. Turbulent channel flow with either transverse or longitudinal roughness elements on one wall. *Journal of Fluid Mechanics*, 561:279–305, 2006. doi: 10.1017/S0022112006000723.

[66] P Orlandi and S Leonardi. Direct numerical simulation of three-dimensional turbulent rough channels: parameterization and flow physics. *Journal of Fluid Mechanics*, 606: 399–415, 2008. doi: 10.1017/S0022112008001985.

[67] P Modesti, S Endrikat, N Hutchins, and D Chung. Dispersive stresses in turbulent flow over riblets. *Journal of Fluid Mechanics*, 917:A55, 2021. doi: 10.1017/jfm.2021.310.

[68] S Endrikat, D Modesti, R García-Mayoral, N Hutchins, and D Chung. Influence of riblet shapes on the occurrence of Kelvin–Helmholtz rollers. *Journal of Fluid Mechanics*, 913: A37, 2021. doi: 10.1017/jfm.2021.2.

[69] O A El-Samni, H H Chun, and H S Yoon. Drag reduction of turbulent flow over thin rectangular riblets. *International Journal of Engineering Science*, 45:436–454, 2007. doi: 10.1016/j.ijengsci.2007.03.002.

[70] E.N. Ahmed, S.B. Naqvi, L. Buda, and A. Bottaro. A homogenization approach for turbulent channel flows over porous substrates: Formulation and implementation of effective boundary conditions. *Fluids*, 7(5):178, 2022. doi: 10.3390/fluids7050178.

[71] Arnulph Mallock. Iii. experiments on fluid viscosity. *Philosophical Transactions of the Royal Society of London. Series A, Containing Papers of a Mathematical or Physical Character*, (187):41–56, 1896.

[72] M Couette. Distinction de deux régimes dans le mouvement des fluides. *J. Phys. Theor. Appl.*, 9(1):414–424, 1890.

[73] G I Taylor. Stability of a viscous liquid contained between two rotating cylinders. *Philosophical Transactions of the Royal Society of London. Series A*, 223(605-615):289–343, 1923. doi: 10.1098/rsta.1923.0008.

[74] Donald Coles. Transition in circular couette flow. *Journal of Fluid Mechanics*, 21(3): 385–425, 1965.

[75] C David Andereck, SS Liu, and Harry L Swinney. Flow regimes in a circular couette system with independently rotating cylinders. *Journal of Fluid Mechanics*, 164:155–183, 1986.

[76] M S Naim and M F Baig. Turbulent drag reduction in Taylor-Couette flows using different super-hydrophobic surface configurations. *Physics of Fluids*, 31:095108, 2019. doi: 10.1063/1.5116316.

[77] Xiaochao Liu, Chenxi You, Yanlin Cao, Baorui Xu, Yantao Yang, Hongyuan Li, Pengyu Lv, Chao Sun, and Huiling Duan. Friction drag reduction of Taylor–Couette flow over air-filled microgrooves. *Journal of Fluid Mechanics*, 999:A63, 2024. doi: 10.1017/jfm.2024.948.

[78] Siddarth Srinivasan, Justin A. Kleingartner, Jonathan B. Gilbert, Robert E. Cohen, Andrew J. B. Milne, and Gareth H. McKinley. Sustainable drag reduction in turbulent Taylor-Couette flows by depositing sprayable superhydrophobic surfaces. *Physical Review Letters*, 114:014501, Jan 2015. doi: 10.1103/PhysRevLett.114.014501. URL https://link.aps.org/doi/10.1103/PhysRevLett.114.014501.

[79] T Hall and D Joseph. Rotating cylinder drag balance with application to riblets. *Experiments in Fluids*, 29:215–227, 2000. doi: 10.1007/s003489900075.

[80] A J Greidanus, R Delfos, S Tokgoz, and J Westerweel. Turbulent Taylor–Couette flow over riblets: drag reduction and the effect of bulk fluid rotation. *Experiments in Fluids*, 56:107, 2015. doi: 10.1007/s00348-015-1978-7.

[81] B Xu, H Li, X Liu, Y Xiang, P Lv, X Tan, Y Zhao, C Sun, and H Duan. Effects of micro-grooves on drag reduction in Taylor-Couette flow. *Physics of Fluids*, 35:043608, 2023. doi: 10.1063/5.0145900.

[82] Xiaojue Zhu, Rodolfo Ostilla-Mónico, Roberto Verzicco, and Detlef Lohse. Direct numerical simulation of Taylor–Couette flow with grooved walls: torque scaling and flow structure. *Journal of Fluid Mechanics*, 794:746–774, 2016. doi: 10.1017/jfm.2016.179.

[83] Antoine Jouin, Jean-Christophe Robinet, and Stefania Cherubini. Modal and non-modal stability of the laminar flow in a channel with longitudinal riblets. *Phys. Rev. Fluids*, 9:073903, Jul 2024. doi: 10.1103/PhysRevFluids.9.073903. URL https://link.aps.org/doi/10.1103/PhysRevFluids.9.073903.

[84] S Chandrasekhar. *Hydrodynamic and Hydromagnetic Stability*. Dover Publications, Inc., New York, N.Y., 1981.

[85] G A Zampogna, J Magnaudet, and A Bottaro. Generalized slip condition over rough surfaces. *Journal of Fluid Mechanics*, 858:407–436, 2019. doi: 10.1017/jfm.2018.780.

[86] U Lācis, Y Sudhakar, S Pasche, and S Bagheri. Transfer of mass and momentum at rough and porous surfaces. *Journal of Fluid Mechanics*, 884:A21, 2020. doi: 10.1017/jfm.2019.897.

[87] S B Naqvi and A Bottaro. Interfacial conditions between a free-fluid region and a porous medium. *International Journal of Multiphase Flow*, 141:103585, 2021. doi: 10.1016/j.ijmultiphaseflow.2021.103585.

[88] Y Sudhakar, U Lācis, S Pasche, and S. Bagheri. Higher-order homogenized boundary conditions for flows over rough and porous surfaces. *Transport in Porous Media*, 136: 1–42, 2021. doi: 10.1007/s11242-020-01495-w.

[89] F Hecht. New development in freefem++. *Journal of Numerical Mathematics*, 20(3-4):251–265, 2012. ISSN 1570-2820. doi: 10.1515/jnum-2012-0013. URL https://freefem.org/.

[90] Giulia Innocenti, Edoardo Maestri, Giovanni Bestoso, Alberto Lagazzo, Marina Delucchi, Enzo Santoromito, Nicolas Mazellier, Jan O. Pralits, and Alessandro Bottaro. Taylor-couette instability with differential slip at one boundary. *Chinese Journal of Aeronautics*, in press.

[91] E L Koschmieder. *Bénard Cells and Taylor Vortices*. Cambridge University Press, New York, N.Y., 1993.

[92] Soft99 GLACO coating user manual. *https://www.glaco.eu/en/*.

[93] P. Baumli, M. D'Acunzi, and Hegner K.I. The challenge of lubricant-replenishment on lubricant-impregnated surfaces. *Advances in Colloid and Interface Science*, 287:102329, 2021. doi: 10.1016/j.cis.2020.102329.

[94] Jason S Wexler, Ian Jacobi, and Howard A Stone. Shear-driven failure of liquid-infused surfaces. *Physical review letters*, 114(16):168301, 2015.

[95] J.H. Kim and J.P. Rothstein. Delayed lubricant depletion on liquid-infused randomly rough surfaces. *Physics of Fluids*, 57:81, 2016. doi: 10.1007/s00348-016-2171-3.

[96] Sofia Saoncella, Si Suo, Johan Sundin, Agastya Parikh, Marcus Hultmark, Wouter Metsola Van Der Wijngaart, Fredrik Lundell, and Shervin Bagheri. Contact-angle hysteresis provides resistance to drainage of liquid-infused surfaces in turbulent flows. *Physical Review Fluids*, 9(5):054002, 2024.

[97] Sam Peppou-Chapman and Chiara Neto. Mapping depletion of lubricant films on antibiofouling wrinkled slippery surfaces. *ACS Appl. Mater. Interfaces*, 10(39):33669–33677, 2018.

[98] S. Adera, J. Alvarenga, and A.V. Shneidman. Depletion of lubricant from nanostructured oil-infused surfaces by pendant condensate droplets. *American Chemical Society Nano*, 14:8024–8035, 2020. doi: 10.1021/acsnano.9b10184.

[99] P. Kim, M.J. Kreder, J. Alvarenga, and J. Aizenberg. Hierarchical or not? effect of the length scale and hierarchy of the surface roughness on omniphobicity of lubricant-infused substrates. *ACS Publications Nano Letters*, 13:1793–1799, 2013. doi: 10.1021/nl4003969.

[100] Liam RJ Scarratt, Ben S Hoatson, Elliot S Wood, Brian S Hawkett, and Chiara Neto. Durable superhydrophobic surfaces via spontaneous wrinkling of teflon af. *ACS Appl. Mater. Interfaces*, 8(10):6743–6750, 2016.

[101] Kunlun Bai and Joseph Katz. On the refractive index of sodium iodide solutions for index matching in piv. *Experiments in fluids*, 55(4):1704, 2014.

[102] Dajun Fan, Rongjie Li, Minghan He, Xianwen Li, Jinyang Li, Jun Wen, Yongping Hu, Yanan Li, Yue Li, Long Gu, et al. Review of refractive index-matching techniques of polymethyl methacrylate in flow field visualization experiments. *International Journal of Energy Research*, 2023(1):3413380, 2023.

[103] Fritz Wendt. Turbulente strömungen zwischen zwei rotierenden konaxialen zylindern. *Ingenieur-Archiv*, 4(6):577–595, 1933.

[104] Daniel P Lathrop, Jay Fineberg, and Harry L Swinney. Transition to shear-driven turbulence in couette-taylor flow. *Physical Review A*, 46(10):6390, 1992.

[105] S Ghaemi and F Scarano. Turbulent structure of high-amplitude pressure peaks within the turbulent boundary layer. *Journal of Fluid Mechanics*, 735:381–426, 2013.

[106] John Kim and Fazle Hussain. Propagation velocity of perturbations in turbulent channel flow. *Physics of Fluids A: Fluid Dynamics*, 5(3):695–706, 1993.